

Reinforced Concrete Shear Walls with Improved Self-Centering and Damage Resistance  
Properties: Experimental Testing and Numerical Modeling

by

Mohammad Javad Tolou Kian

A thesis submitted in partial fulfillment of the requirements for the degree of

Doctor of Philosophy

in

Structural Engineering

Department of Civil and Environmental Engineering  
University of Alberta

© Mohammad Javad Tolou Kian, 2020

## Abstract

Performance objectives in the seismic design of reinforced concrete (RC) buildings require buildings to survive their maximum considered earthquakes (MCE) with a low probability of total or partial collapse. Often, RC structures require costly retrofitting or demolition and reconstruction after the MCE. A building structure shall also withstand its design basis earthquake (DBE) with a low likelihood of causing life-threatening injuries to the individuals inside or outside.

The current research aims to improve the post-earthquake state of multi-story RC shear walls to decrease their rehabilitation costs after strong earthquakes. Current building codes require that essential structures such as hospitals remain serviceable after strong earthquakes. However, post-earthquake serviceability is not necessary for non-critical structures, such as apartments, which often comprise most buildings in every city. According to current seismic codes, the damage of RC structures can be characterized through their permanent drift ratios and concrete damage. These damage indicators are also intercorrelated to some degrees. For example, higher permanent drift ratios correspond to larger flexural crack openings in shear walls. One option to decrease these damage indicators is to use innovative materials and details with improved performance compared to conventional concrete and steel reinforcement.

In this study, the performance of three innovative shear walls is investigated through experimental testing. In this regard, the cyclic response parameters of the innovative walls are investigated and compared with the response parameters of a conventional RC wall designed to the latest seismic guidelines. Then, the following response parameters of the walls were compared between the conventional and innovative walls – failure mode, permanent drift ratio, concrete damage, stiffness, strength, and energy dissipation.

High-performance reinforced cementitious composites, such as engineered cementitious composite (ECC) and steel fiber reinforced concrete (SFRC) were used to minimize the damage in concrete. Also, to promote self-centering, shape memory alloy (SMA) bars, glass fiber reinforced polymer (GFRP) bars, and high-strength steel strands were used in the innovative walls. It was shown through experimental testing that the drift ratio recovery of a conventional RC shear wall could be improved by more than 90% when some of the longitudinal steel reinforcement of the wall is replaced with self-centering reinforcement.

In the next stage of the study, analysis models of the tested specimens were developed using finite-element methods and were verified with the obtained experimental results. Then, the models were used to study the response of large-scale innovative RC shear walls under cyclic and seismic loads. It was shown that the inelastic rotational capacity in the innovative and conventional RC walls is comparable. The study also showed that the extent of the plastic hinge region in steel-GFRP reinforced walls could be larger compared to conventional RC walls, while it is generally smaller in steel-SMA reinforced and partially post-tensioned concrete walls.

The results from this study demonstrate the feasibility of using innovative materials and details in the design of damage-resistant RC shear walls. It is expected that the analysis models and the design insights produced as part of this investigation assist engineers and building owners toward the adoption of high-performance materials in RC shear walls. The use of high-performance materials in shear walls can lead to more sustainable building structures, which require smaller amounts of time and money for repairing. Also, these buildings are less likely to need demolition and reconstruction after strong seismic events.

## Preface

This thesis is an original work by Mohammad Javad Tolou Kian.

Chapter 3 of this thesis has been published as M.J. Tolou Kian, and C. Cruz-Noguez as “Reinforced Concrete Shear Walls Detailed with Innovative Materials: Seismic Performance,” *Journal of Composites for Construction*, vol. 22, issue 6. I, Mohammad Javad Tolou Kian, was responsible for the data collection, performing analyses, writing the original manuscript of the paper, and concluding the revisions provided by all of the authors. C. Cruz-Noguez was the supervisory author and was involved with concept formation and manuscript composition of the paper.

Chapter 4 of this thesis has been accepted to be published in *Engineering Structures* as M.J. Tolou Kian and C. Cruz-Noguez “Seismic Design of Three Damage-Resistant Reinforced Concrete Shear Walls Detailed with Self-Centering Reinforcement.” I, Mohammad Javad Tolou Kian, was responsible for the data collection, performing analyses, writing the original manuscript of the paper, and concluding the revisions provided by all the authors. C. Cruz-Noguez was the supervisory author and was involved with concept formation and manuscript composition of the paper.

## **Acknowledgments**

The author would like to express his highest gratitude to his supervisor Dr. Cruz-Noguez whose guidance and insight were invaluable over the course of this research. The author would like to extend his thanks to Dr. Robert Driver, Dr. Ming Lu, Dr. Lijun Deng, Dr. Yong Li, and Dr. Doug Tomlinson for their guidance as supervisory committee members of my project.

## Table of Contents

1. CHAPTER 1 INTRODUCTION .....	1
1.1 Introduction .....	1
1.2 Problem Statement .....	1
1.3 Scope .....	3
1.4 General and Specific Objectives .....	3
1.4.1 Objective 1 .....	4
1.4.2 Objective 2 .....	4
1.5 Thesis Outline .....	5
2. CHAPTER 2 LITERATURE REVIEW .....	6
2.1 Introduction .....	6
2.2 Advanced Materials .....	8
2.2.1 Shape Memory Alloy .....	9
2.2.2 Fiber Reinforced Polymer (FRP) .....	11
2.2.3 Fiber Reinforced Concrete .....	13
2.2.4 Engineered Cementitious Composite (ECC) .....	16
2.2.5 Partially Post-Tensioned Systems .....	20
2.3 High-Performance Shear Walls .....	22
2.3.1 SMA Reinforced Concrete Shear Wall .....	22
2.3.2 GFRP Reinforced Concrete Shear Walls .....	26
2.3.3 Post-Tensioned Shear Walls .....	30
2.3.4 ECC Shear Walls .....	36
2.3.5 SFRC Shear Walls .....	39
2.3 Testing Methods .....	41
2.3.1 Shaking Table Testing .....	41

2.3.2 Hybrid Testing .....	43
2.3.3 Cyclic Testing.....	46
2.3.3.1 General considerations .....	46
2.3.3.2 Axial Load.....	48
2.4 Conclusion.....	50
<b>3. CHAPTER 3 REINFORCED CONCRETE SHEAR WALLS DETAILED WITH INNOVATIVE MATERIALS: PERFORMANCE .....</b>	<b>51</b>
3.1 Abstract .....	51
3.2 Introduction .....	51
3.3 Experimental Program.....	53
3.3.1 Material Properties .....	53
3.3.2 Test Specimens .....	58
3.3.3 Testing procedure and loading protocol .....	63
3.4 Experimental Results.....	64
3.4.1 Load-displacement hysteretic response .....	64
3.4.2 Damage Propagation and Failure Modes.....	66
3.4.3 Damage Propagation.....	67
3.4.4 Self-Centering.....	70
3.4.5 Energy Dissipation .....	72
3.5 Performance Assessment.....	73
3.6 Conclusions .....	75
<b>4. CHAPTER 4 SEISMIC DESIGN OF THREE DAMAGE-RESISTANT CONCRETE SHEAR WALLS DETAILED WITH SELF-CENTERING REINFORCEMENT .....</b>	<b>77</b>
4.1 Abstract .....	77
4.2 Introduction .....	78
4.3 Experimental Program.....	80

4.3.1 Test Specimens .....	80
4.3.2 Material Properties .....	82
4.3.3 Testing .....	83
4.4 Response Parameters.....	85
4.4.1 Post-Testing State and Cracking.....	85
4.4.2 Hysteretic Response .....	87
4.4.3 Curvature Distribution.....	88
4.4.4 Shear Strain Distribution .....	89
4.4.5 Wall Deformation Decoupling .....	91
4.5 Design Parameters.....	93
4.5.1 Stiffness .....	93
4.5.2 Inelastic Rotational Capacity.....	94
4.5.3 Plastic Hinge Length .....	95
4.5.4 Self-Centering Moment .....	99
4.6 Implications for Design.....	103
4.6.1 Reinforcement Layout .....	103
4.6.2 Rotational Capacity .....	105
4.6.3 Drift Ratio Recovery .....	107
4.7 Conclusions.....	109
5. CHAPTER 5 ANALYSIS MODEL FOR INNOVATIVE SHEAR WALLS.....	111
5.1 Abstract .....	111
5.2 Introduction .....	111
5.3 Analysis Model .....	114
5.3.1 Modified Compression Field Theory (MCFT).....	115
5.3.2 Innovative Walls.....	117

5.3.3 Additional Validation .....	128
5.4 Conclusions .....	131
6. CHAPTER 6 PARAMETRIC STUDY .....	133
6.1 Abstract .....	133
6.2 Introduction .....	134
6.3 Parametric Analysis.....	136
6.3.1 Fixed parameters.....	136
6.3.2 Independent parameters .....	137
6.3.3 Dependent parameters .....	137
6.3.4 Shear walls.....	137
6.3.5 FE Modeling.....	143
6.3.6 Cyclic Response .....	146
6.4 Cyclic Response Parameters .....	149
6.4.1 Lateral Resistance.....	149
6.4.2 Effective Stiffness.....	151
6.4.3 Ultimate Drift Ratio.....	152
6.4.4 Energy Dissipation .....	154
6.4.5 Effects of Independent Parameters on Cyclic Response Parameters .....	155
6.5 Design Parameters.....	157
6.5.1 Ductility .....	157
6.5.2 Inelastic Rotational Capacity .....	160
6.5.3 Plastic Hinge Analysis.....	163
6.5.4 Plastic Hinge Length .....	167
6.5.5 Self-Centering Analysis.....	171
6.5.6 Effects of Independent Parameters on Design Parameters.....	175

6.6 Seismic Response.....	176
6.6.1 Response History.....	178
6.6.2 Peak Drift Ratio.....	179
6.6.3 Residual Drift Ratio.....	180
6.6.4 Energy Dissipation.....	180
6.6.5 Effects of Independent Parameters on Seismic Properties.....	181
6.7 Conclusions.....	182
7. CHAPTER 7 CONCLUSIONS.....	185
7.1 Conclusions.....	185
7.1.1 Experimental Study.....	185
7.1.2 Numerical Study.....	186
7.2 Suggestions for Further Studies.....	188
7.2.1 Experimental Studies.....	188
7.2.2 Numerical Study.....	188
REFERENCES.....	190

## List of Tables

Table 3.1. Mechanical properties of self-centering reinforcements .....	54
Table 3.2. Mechanical properties of mild steel reinforcement .....	56
Table 3.3. Seismic performance of specimens in terms of permanent drift ratio .....	74
Table 4.1. Properties of different types of cementitious material.....	82
Table 4.2. Mechanical properties of different types of reinforcement .....	83
Table 6.1. Nomenclature of the walls .....	139
Table 6.2. Self-centering reinforcement layouts.....	142
Table 6.3. Self-centering reinforcement ratio in S2 and S3 relative to S1 .....	143
Table 6.4. Mechanical properties of different types of reinforcement .....	146
Table 6.5. Specifications of the earthquakes. ....	177

## List of Figures

Figure 2.1. ‘Examples of buildings with residual displacements leading that typically lead to demolition (left photo by M. Bruneau, MCEER; right photo by A. Whittaker, NISEE, EERC, UC Berkeley)’ (Ramirez and Miranda 2012).....	7
Figure 2.2. Probability of having to demolish a building that has not collapsed as a function of peak residual inter-story drift in the building. EDP, engineering demand parameter; RIDR, residual inter-story drift ratio (Ramirez and Miranda 2012) .....	8
Figure 2.3. Stress-strain relationship of NiTi (Desroches et al. 2004) .....	10
Figure 2.4. Tensile stress-strain relationship of different types of FRP in comparison to steel (Mohamed 2013).....	12
Figure 2.5. Cement composites (Kunieda and Rokugo 2006).....	14
Figure 2.6. Tensile stress-strain curves of concrete, SFRC, and ECC.....	15
Figure 2.7. Cracks in ECC and concrete (Li 2003).....	16
Figure 2.8. An ECC slab under four-point-load test (Nagai et al. 2002).....	17
Figure 2.9. Deformed shape of ECC beams (Fischer et al. 2002) .....	18
Figure 2.10. Hysteretic response of specimens (Fischer et al. 2002) .....	18
Figure 2.11. Damaged state in a pier of SMA/ECC bent (Cruz Noguez et al. 2012).....	19
Figure 2.12. Damaged state partially post-tensioned bent (Cruz Noguez et al. 2012) .....	21
Figure 2.13. Shear wall test performed by Abdulridha (a) test setup, (b) steel reinforced wall, (c) steel-SMA reinforced wall (Abdulridha 2013).....	23
Figure 2.14. Hysteretic response of shear walls: (a) steel-reinforced, (b) steel-SMA reinforced (Abdulridha and Palermo 2014).....	23
Figure 2.15. Response characteristics of shear wall specimens (Abdulridha 2013).....	24
Figure 2.16. Response characteristics of shear wall specimens (Abdulridha 2013).....	24
Figure 2.17. Post-test state of conventional (left) and steel-SMA reinforced shear wall (right) (Abdulridha 2013).....	25
Figure 2.18. Specimens tested by Mohamed (2013) (a) dimensions, (b) test setup .....	26
Figure 2.19. Reinforcement layouts of GFRP reinforced specimens (Mohamed 2013) .....	27
Figure 2.20. Cyclic behavior of specimens (Mohamed et al. 2014b).....	28
Figure 2.21. State of shear wall after testing (Mohamed 2013).....	29

Figure 2.22. Reinforcement layout of specimens (Ghazizadeh 2017).....	29
Figure 2.23. Hysteretic response of specimens (Ghazizadeh 2017) .....	30
Figure 2.24. Damaged state of specimens (Ghazizadeh 2017).....	30
Figure 2.25. Cyclic response of reinforced concrete walls (Holden et al. 2003).....	31
Figure 2.26. Test specimen (Schultz et al. 1998).....	32
Figure 2.27. Hysteretic result (Schultz et al. 1998) .....	32
Figure 2.28. Post-tensioned specimen at test setup (Holden et al. 2003) .....	33
Figure 2.29. Hysteretic response of specimens (Holden et al. 2003) .....	33
Figure 2.30. Residual drift of specimens (Holden et al. 2003).....	34
Figure 2.31. (a) Equivalent viscous damping of specimens, (b) cracking of unit 1 at drift ratio of 2.5%, (c) cracking of unit 2 at drift ratio of 3% (Holden et al. 2003) .....	34
Figure 2.32. Shear wall PP6-BO scheme and cross-section (Kurama 2005).....	35
Figure 2.33. PP6-BO wall (a) hysteretic response, (b) relative energy dissipation ratio (Kurama 2005).....	36
Figure 2.34. Hysteretic response of specimens (Nagai et al. 2002).....	37
Figure 2.35. Cracking pattern of specimens (Nagai et al. 2002) .....	37
Figure 2.36. Stress-strain relationship for ECC (Li et al. 2014).....	38
Figure 2.37. Cyclic behavior of (a) SW4 wall detailed with concrete and ECC, (b) SW13 wall detailed with concrete and ECC (Li et al. 2014).....	38
Figure 2.38. Reinforcement layout of specimens (a) detailed with concrete (b) detailed with SFRC (Athanasopoulou and Parra-montesinos 2014) .....	39
Figure 2.39. Hysteresis of (a) concrete wall, (b) SFRC wall (Athanasopoulou and Parra-montesinos 2014).....	40
Figure 2.40. Damage to (a) concrete wall, (b) SFRC wall (Athanasopoulou and Parra-montesinos 2014).....	40
Figure 2.41. Seismic testing of a full-scale 4-story structure on shaking table (Nagae et al. 2015) .....	42
Figure 2.42. Hysteretic response of structure under JMA-Kobe record scaled to (a) 25%, (b) 50%, (c) 100% (Nagae et al. 2015).....	42
Figure 2.43. Damage in walls of structure (Nagae et al. 2015) .....	42

Figure 2.44. Experimental and analytical response history results of seven-story structure (Martinelli and Filippou 2009).....	43
Figure 2.45. Hybrid testing of a frame structure (Del Carpio Ramos et al. 2014) .....	44
Figure 2.46. Hybrid testing method (Whyte and Stojadinovic 2012).....	44
Figure 2.47. Hybrid testing of a shear wall specimen (Whyte and Stojadinovic 2012) .....	45
Figure 2.48. Response of specimens under (a) DBE aftershock 1, (b) BDBE records .....	45
Figure 2.49. Test setup used in (Hidalgo et al. 2002) to study shear failure of shear walls .....	47
Figure 2.50. Applying axial force with (a) hydraulic actuators (Zhang and Wang 2000), (b) post-tensioning rods (Escolano-Margarit et al. 2012).....	48
Figure. 2.51. Cyclic response and failure mode of two shear walls with axial load ratios (a) of 25%, (b) 50%. (Su and Wong 2007).....	50
Figure 3.1. Tensile stress-strain relationships of various types of concrete reinforcement .....	54
Figure 3.2. Cyclic stress-strain relationship of a #4 NiTi bar and a 10M steel bar .....	55
Figure 3.3. Compressive stress-strain relationships of cementitious materials .....	57
Figure 3.4. Tensile stress-strain relationships of three ECC prism specimens corresponding to GFRP-ECC wall.....	57
Figure 3.5. Flexural tensile stress-CMOD relationships of three SFRC notched beam specimens corresponding to PPT-SFRC wall.....	58
Figure 3.6. Geometry of shear wall specimens.....	59
Figure 3.7. Reinforcement details of control wall (a) CW elevation, (b) CW cross-section.....	60
Figure 3.8. Reinforcement details of innovative shear walls (a) SMA-SFRC elevation, (b) GFRP-ECC elevation, (c) PPT-SFRC elevation, (d) SMA-SFRC cross-section, (e) GFRP-ECC cross-section, (f) PPT-SFRC cross-section .....	61
Figure 3.9. Test setup.....	63
Figure 3.10. Hysteretic response and idealized bilinear behavior of each shear wall (a) control wall, (b) GFRP-ECC, (c) PPT-SFRC, (d) SMA-SFRC .....	65
Figure 3.11. Ductility indices of shear walls .....	66
Figure 3.12. Backbone curves and damage resilience milestones of shear walls.....	66
Figure 3.13. Damaged walls after $\delta=0.45\%$ (a) CW(b) GFRP-ECC, (c) PPT-SFRC, (d) SMA-SFRC.....	68

Figure 3.14. Damaged walls after $\delta=1.35\%$ (a) CW(b) GFRP-ECC, (c) PPT-SFRC, (d) SMA-SFRC.....	68
Figure 3.15. Damaged walls after $\delta=3.25\%$ (a) CW(b) GFRP-ECC, (c) PPT-SFRC, (d) SMA-SFRC.....	68
Figure 3.16. Residual drift ratio of each innovative wall vs. control wall (a) GFRP-ECC, (b) PPT-SFRC, (c) SMA-SFRC .....	70
Figure 3.17. (a) Reduction in residual drift ratio in each innovative wall with respect to control wall, (b) ratio of residual drift ratio of each innovative wall to that of control wall .....	71
Figure 3.18. Normalized dissipated energy of each innovative wall vs. control wall (a) GFRP-ECC, (b) PPT-SFRC, (c) SMA-SFRC.....	72
Figure 3.19. Ratio of normalized dissipated energy of each innovative wall to that of control wall .....	73
Figure 4.1. Reinforcement detailing of (a) CW, (b) GFRP-ECC, (c) PT-SFRC, (d) SMA-SFRC	81
Figure 4.2. Test setup.....	84
Figure 4.3. Drift ratio at top point of control wall panel measured with cable transducer and DIC system. ....	84
Figure 4.4. Response measurement tools (a) DIC system, elevation measurement for CW, (b) strain gauge layout of CW.....	85
Figure 4.5. Sustained concrete damage in (a) CW at $\delta=4.0\%$ , (b) GFRP-ECC at $\delta=4.0\%$ , (c) PT-SFRC at $\delta=3.3\%$ , (d) SMA-SFRC at $\delta=6.0\%$ .....	86
Figure 4.6. Crack width measured at loading .....	87
Figure 4.7. Hysteretic response of (a) CW, (b) GFRP-ECC, (c) PT-SFRC, (d) SMA-SFRC .....	87
Figure 4.8. Recovery of drift ratios after unloading .....	88
Figure 4.9. Distribution of average curvature for (a) CW, (b) GFRP-ECC, (c) PT-SFRC, (d) SMA-SFRC walls.....	89
Figure 4.10. Distribution of average shear strains for (a) CW, (b) GFRP-ECC, (c) PT-SFRC, (d) SMA-SFRC.....	90
Figure 4.11. Average shear strain at base of walls .....	90
Figure 4.12. Decomposition of flexural and shear drift ratios for (a) CW, (b) GFRP-ECC, (c) PT-SFRC, (d) SMA-SFRC .....	91
Figure 4.13. Ratio of shear to flexural displacements .....	93

Figure 4.14. Peak-to-peak stiffness (a) calculated, (b) relative to CW.....	94
Figure 4.15. Inelastic rotational deformations at top points of walls.....	95
Figure 4.16. Plastic hinge analysis (a) idealized cantilever wall (b) true curvature distribution, (c) idealized curvature distribution.....	96
Figure 4.17. Longitudinal strain along outmost boundary reinforcement (R1) in (a) CW, (b) GFRP-ECC, (c) PT-SFRC, (d) SMA-SFRC .....	97
Figure 4.18. Curvature distribution along (a) CW, (b) GFRP-ECC, (c) PT-SFRC, (d) SMA-SFRC.....	98
Figure 4.19. Plastic hinge length.....	99
Figure 4.20. Distance of neutral axis from extreme compression fiber at bases of walls normalized to lengths of walls .....	100
Figure 4.21. Self-centering moment .....	101
Figure 4.22. Ratio of self-centering over resisting moments for specimens .....	102
Figure 4.23. Longitudinal strain at 50 mm above foundation in (a) R1, (b) R3 .....	103
Figure 4.24. Refined calculations for (a) strain along SMA bars, (b) yield curvature (c) ultimate curvature and inelastic rotational capacity.....	106
Figure 4.25. Required drift ratio recovery for different self-centering objectives.....	108
Figure 4.26. Drift ratio recovery of shear walls.....	109
Figure 5.1. Average strains in cracked element (Vecchio and Collins 1986).....	115
Figure 5.2. Modified compression field theory: (a) stresses applied to cracked elements, (b) calculated average stresses, (c) Local stresses at a crack (Vecchio and Collins 1986).....	116
Figure 5.3. Stress-strain relationship of cracked concrete (Vecchio and Collins 1986).....	116
Figure 5.4. Aggregate interlock and transmission of shear stresses (Vecchio and Collins 1986) .....	117
Figure 5.5. Reinforcement layouts: (a) CW vertical layout, and cross-sections for (b) CW, (c) GFRP-ECC, (d) PT-SFRC, (e) SMA-SFRC (Tolou Kian and Cruz-Noguez, 2018).....	118
Figure 5.6. Stress-strain response of cementitious materials: (a) measured, (b) calculated .....	119
Figure 5.7. Tensile stress-strain relationship of ECC .....	120
Figure 5.8. Stress-strain relationships of steel and SMA bars: (a) measured, (b) calculated .....	120
Figure 5.9. Stress-strain relationship of post-tensioned high-strength steel strands.....	121
Figure 5.10. Bond-slip relationship for different types of reinforcement.....	121

Figure 5.11. FE models of control wall using (a) M1, (b) M2, and, (c) M3.....	122
Figure 5.12. Lateral load-displacement response of FE models of control wall with mesh (a) M1, (b) M2, (c) M3 .....	123
Figure 5.13. FE models of shear walls: (a) CW, (b) GFRP-ECC, (c) PT-SFRC, (d) SMA-SFRC .....	123
Figure 5.14. Calculated and measured hysteretic responses of shear walls (a) CW, (b) GFRP-ECC, (c) PT-SFRC, (d) SMA-SFRC .....	124
Figure 5.15. Calculated cracking patterns of specimens at 2.7% drift (a) CW, (b) GFRP-ECC, (c) PT-SFRC, (d) SMA-SFRC .....	125
Figure 5.16. Recorded cracking patterns of specimens at a drift of 2.7% (a) CW, (b) GFRP-ECC, (c) PT-SFRC, (d) SMA-SFRC .....	125
Figure 5.17. Vertical displacements measured with DIC system .....	126
Figure 5.18. Strain distributions of shear wall specimens and FE models for (a) CW, (b) GFRP-ECC, (c) PT-SFRC, (d) SMA-SFRC .....	127
Figure 5.19. Strain distribution of shear wall specimens and FE models for (a) CW, (b) GFRP-ECC, (c) PT-SFRC, (d) SMA-SFRC .....	127
Figure 5.20. Curvature distribution of shear wall specimens and FE models of (a) CW, (b) GFRP-ECC, (c) PT-SFRC, (d) SMA-SFRC .....	128
Figure 5.21. Innovative shear wall tested by Ghazizadeh and Cruz-Noguez (2018) (a) reinforcement layout, (b) FE model, (c) experimental and numerical results.....	129
Figure 5.22 Innovative shear wall tested by Abdulridha (2013) (a) reinforcement layout, (b) FE model, (c) experimental and numerical results .....	130
Figure 5.23 Shear wall tested by Holden et al. (2003) (a) reinforcement layout, (b) FE model (c) experimental and numerical results. ....	131
Figure 6.1. Shear walls (a) schematics (b) regions with different reinforcement.....	138
Figure 6.2. Reinforcement layout of (a) CWA1L1S1, (b) CWA1L2S1, (c) CWA1L3S1 .....	141
Figure 6.3. Reinforcement layout of (a) GWA1L1S1, (b) PWA1L1S1 walls.....	142
Figure 6.4. Reinforcement layout of SWA1L1S1 wall.....	142
Figure 6.5. CWA1L2S1 wall discretized with (a) mesh M1, (b) mesh M2.....	144
Figure 6.6. Lateral load-displacement response of FE model of CWA1L2S1 wall discretized with mesh (a) M1, (b) M2.....	144

Figure 6.7. FE models (a) steel-GFRP reinforced and partially post-tensioned walls, (b) steel-SMA reinforced walls .....	145
Figure 6.8. Loading protocol .....	146
Figure 6.9. Hysteretic response of innovative walls (a) GWA1L1S3, SWA1L1S3, PWA1L1S3, (b) GWA1L2S3, SWA1L2S3, PWA1L2S3, (c) GWA1L3S3, SWA1L3S3, PWA1L3S3.....	147
Figure 6.10. Hysteretic response of innovative walls (a) GWA2L1S3, SWA2L1S3, PWA2L1S3, (b) GWA2L2S3, SWA2L2S3, PWA2L2S3, (c) GWA2L3S3, SWA2L3S3, PWA2L3S3.....	148
Figure 6.11 Lateral Resistance in shear walls with ALRs of (a) 0%, (b) 5%.....	150
Figure 6.12. Relative lateral resistance to CW in shear walls with ALRs of (a) 0%, (b) 5%.....	150
Figure 6.13 In-plane effective stiffness in shear walls with ALRs of (a) 0%, (b) 5%.....	151
Figure 6.14. Relative effective stiffness to CW for shear walls with ALRs of (a) 0%, (b) 5%..	152
Figure 6.15. Ultimate drift ratio in shear walls with ALRs of (a) 0%, (b) 5%.....	153
Figure 6.16. Relative ultimate drift ratio to CW for shear walls with ALRs of (a) 0%, (b) 5%.	154
Figure 6.17. Normalized dissipated energy in shear walls with ALRs of (a) 0%, (b) 5%.....	154
Figure 6.18. Normalized dissipated energy in the second cycle of hysteretic response of shear walls relative to CW walls when ALR is (a) 0%, (b) 5%.....	155
Figure 6.19. Idealized back-bone curves using reduced stiffness equivalent elasto-plastic model for shear walls with an ALR of 0% (a) CW, (b) GW, (c) SW, (d) PW .....	157
Figure 6.20. Idealized back-bone curves using reduced stiffness equivalent elasto-plastic model for shear walls with an ALR of 5% (a) CW, (b) GW, (c) SW, (d) PW .....	158
Figure 6.21. Yield and ultimate drift ratios in shear walls with ALRs of (a) 0%, (b) 5%.....	158
Figure 6.22. Displacement ductility in shear walls with ALRs of (a) 0%, (b) 5%.....	159
Figure 6.23. Relative ductility in shear walls to CW with an ALR of (a) 0%, (b) 5%.....	160
Figure 6.24. Yield Rotation in shear walls with ALRs of (a) 0%, (b) 5%.....	161
Figure 6.25. Inelastic rotational capacity in shear walls with an ALR of (a) 0%, (b) 5%.....	162
Figure 6.26. Relative Inelastic rotational capacity in the innovative shear walls to CW for ALRs of (a) 0%, (b) 5%. .....	163
Figure 6.27. Curvature distribution of shear walls with an ALR of 0% (a) CW, (b) GW, (c) SW, (d) PW.....	163
Figure 6.28. Curvature distribution of (a) CW, (b) GW, (c) SW, (d) PW under an ALR of 5%. .....	164

Figure 6.29. Cracking pattern at 2.0% drift in (a) CWA1L2S3, (b) GWA1L2S3, (c) PWA1L2S3, (d) SWA1L2S3, (e) CWA2L2S3, (f) GWA2L2S3, (g) PWA2L2S3, (h) SWA2L2S3 .....	165
Figure 6.30. Base curvature calculation in shear walls (a) theory, (b) calculated values .....	165
Figure 6.31. Base curvature in shear walls with ALRs of (a) 0%, (b) 5% .....	166
Figure 6.32. Relative base curvature to CW in shear walls with an ALR of (a) 0%, (b) 5% .....	167
Figure 6.33. Plastic hinge length of (a) CW, (b) GW, (c) SW, (d) PW, with an ALR of 0% ....	168
Figure 6.34. Plastic hinge length of (a) CW, (b) GW, (c) SW, (d) PW, with an ALR of 5% ....	168
Figure 6.35. Relative plastic hinge length in the innovative walls with an ALR of 0% to CW walls for (a) GW, (b) SW, (c) PW .....	169
Figure 6.36. Relative plastic hinge length in the innovative walls with an ALR of 5% to CW walls for (a) GW, (b) SW, (c) PW .....	170
Figure 6.37. Plastic hinge length of shear walls (a) compared to $0.5L_w$ (b) normalized to $0.5L_w$ .....	170
Figure 6.38. Drift ratio recovery of shear walls with 0% ALR (a) CW (b) GW (c) SW (d) PW	171
Figure 6.39. Drift ratio recovery of shear walls with 0% ALR (a) CW, (b) GW, (c) SW, (d) PW .....	171
Figure 6.40. Distance between neutral axis to the extreme compression fiber in the shear walls normalized to wall lengths for (a) CW, (b) GW, (c) SW, (d) PW .....	172
Figure 6.41. Increase in drift ratio recovery of innovative shear walls with an ALR of 0% compared to their control walls with 0% ALR for (a) GW, (b) SW, (c) PW .....	173
Figure 6.42. Increase in drift ratio recovery of CW walls with 5%ALR of compared to the control walls with ALR 0% .....	174
Figure 6.43. Increase in drift ratio recovery of innovative shear walls with an ALR of 5% compared to the control walls with 0% ALR for (a) GW (b) SW (c) PW.....	174
Figure 6.44. Acceleration history of (a) 1989 Loma, (b) 1985 Nahanni, (c) 1994 Northridge, (d) 1978 Tabas earthquakes. ....	177
Figure 6.45. Selected earthquake (a) pseudo-spectral acceleration (b) spectral displacement... ..	178
Figure 6.46. Response histories under (a) Loma Prieta (b) Nahanni (c) Northridge (d) Tabas..	178
Figure 6.47. Peak drift of walls under seismic loads and an ALR of (a) 0%, (b) 2.5%, (c) 5%.	179
Figure 6.48. Residual drift of walls under seismic loads and an ALR of (a) 0%, (b) 2.5%, (c) 5% .....	180

Figure 6.49. Dissipated energy of walls under seismic and an ALR of (a) 0% (b) 2.5% (c) 5% 181

# CHAPTER 1 INTRODUCTION

## 1.1 Introduction

According to FEMA 365 (2000), the permanent drift ratio and the extent of damage a shear wall sustains during an earthquake can be used to estimate the post-earthquake performance level of the shear wall. In the immediate occupancy performance level (IO), negligible permanent drift ratios and damage are acceptable. In the life safety (LS) level, in which significant damage with a margin to collapse can be sustained. In the LS level, limited degrees of crushing, reinforcement buckling, and flexural cracking with permanent drift ratios of 0.5% or smaller are allowed for shear walls. In the collapse prevention (CP) level, beyond which structural elements are considered to have no structural integrity, shear walls are expected to have severe boundary element damage, including crushing, reinforcement buckling, and major shear and flexural cracking. The permanent drift ratio at this level must be less than 2%.

Non-critical structures designed to the latest seismic codes and standards are effective in resisting strong earthquakes. However, this is usually achieved at the cost of suffering significant damage, as shown by Nagae et al. (2015). The sustained damage by RC structural elements can be classified based on the amount of permanent drift ratio and the damaged states of them, according to FEMA 365 (2000). The current research project is one of the first studies which aims to reduce permanent residual drift ratio and concrete damage in RC shear walls without compromising their energy dissipation capabilities. For that reason, it was decided to incorporate steel rebars as well as innovative reinforcement into the study. This study also draws a map for future studies in the realm of damage-resistant RC shear walls.

## 1.2 Problem Statement

In recent years, several studies have been conducted on the application of high-performance materials in the improvement of seismic performance of structural elements. Regarding reinforced concrete bridges, Saiidi et al. (2007, 2009) and Saiidi and Wang (2006), showed that bridge piers detailed with engineered cementitious composite (ECC) and reinforced with shape memory alloy (SMA) bars along their plastic hinge regions had notably reduced residual deformations and levels

of damage after withstanding earthquakes. Cruz Noguez et al. (2012) studied the seismic performance of a four-span bridge specimen detailed with high-performance materials such as ECC, SMA, and high-strength (HS) steel under seismic loads. The study showed that innovative materials could minimize damage and effectively reduce permanent displacements in bridge piers.

Regarding reinforced concrete (RC) shear walls, Holden et al. (2003) performed a study on the seismic performance of a precast concrete shear wall detailed with two un-bonded tendons and two bonded energy dissipating steel rebars. In addition, the precast wall was cast with steel fiber reinforced concrete (SFRC) for damage mitigation purposes. The shear wall illustrated substantial self-centering and damage mitigation with a very limited energy dissipation capability due to the lack of bonded reinforcement. Abdulridha and Palermo (2014) studied the seismic performance of a shear wall specimen reinforced with steel and SMA. The wall showed superior self-centering properties while maintaining comparable levels of stiffness, strength, and energy dissipation to a conventional RC wall. However, the wall sustained extensive damage in the plastic hinge, which was followed by the buckling and rupture of SMA bars at the extremities of the shear wall. Mohamed et al. (2014) studied the seismic performance of concrete shear walls, which were purely reinforced with glass fiber reinforced polymer (GFRP) bars. The study showed that GFRP reinforced shear walls could achieve satisfactory levels of deformability, stiffness, and strength while illustrating substantial self-centering. The energy dissipation capacity in GFRP reinforced walls, however, was insignificant due to the linear response of GFRP bars.

Considering the literature on innovative shear walls, a lack of systematic investigation on different types of innovative shear walls is seen. Also, the research projects performed on innovative walls have been focused on the merits of such walls and overlooked the design parameters of innovative shear walls. As a result, there are no recommendations and guidelines available for the design and construction of innovative shear walls. Thus, this research tries to answer the following questions. What are the merits of different types of innovative shear walls compared to each other and to conventional RC construction? What are the design parameters of different types of innovative shear walls compared to traditional RC construction?

### **1.3 Scope**

This study is comprised of two parts – an experimental and a numerical part. The scope of the experimental part of the study is limited to the seismic performance of cantilever, slender shear walls reinforced with steel rebars and a type of self-centering reinforcement, such as SMA bars, GFRP bars, or high-strength steel strands. The walls will be subject to ascending, pseudo-static, displacement reversals up to failure. Axial loads are not applied to the wall specimens, as it is desired to investigate the self-centering capacity of the innovative materials independently. This is because axial loads provide a re-centering mechanism to shear walls subjected to lateral loads (Maciel et al. 2016).

The scope of the numerical part of the study is limited to the seismic properties of cantilever, slender shear walls reinforced with steel rebars accompanied by a type of self-centering reinforcement consisting of SMA bars, GFRP bars, or high-strength steel strands. The study will be performed on shear walls with different aspect ratios, axial load ratios, and reinforcement ratios. The walls will be analyzed under cyclic displacement reversals and different ground motion acceleration histories.

### **1.4 General and Specific Objectives**

The current research was defined to reduce damage susceptibility of RC shear wall elements in terms of permanent drift ratio and concrete damage, which results in lower retrofitting costs after major earthquakes. This research intends to develop innovative RC wall systems that enable non-critical shear wall buildings to withstand strong ground motions with small permanent deformations and mitigated damage.

The general objective is to investigate the feasibility of using innovative materials and details to reduce damage and permanent deformations in several types of damage resilient shear wall systems. Reliable numerical models which can capture the response of the walls, and design methods suitable for inclusion in seismic codes will be developed afterward. The specific objectives are as follows.

### **1.4.1 Objective 1**

- The first objective of the study is to develop new types of damage-resistant shear walls and to conduct a systematic investigation of their merits.

In this regard, four shear wall specimens are designed, built, and tested to failure. The walls consist of one conventional reinforced concrete wall (used as the reference specimen) and three the shear walls incorporating advanced materials and details. The materials used in the hybrid vertical reinforcing schemes of the innovative walls are (steel/GFRP bars, steel/SMA, and steel bars/post-tensioning strands) to achieve self-centering. In addition, damage-resistant fiber-reinforced concrete is used in the walls to reduce crushing, spalling and cracking of concrete. The merits of the innovative materials will be assessed through the comparison of the advanced shear walls with a control wall built with conventional steel-reinforced concrete.

The innovative walls were designed to have comparable reinforcement layouts to the reinforcement layout of the control wall. To design the reinforcement layout of each innovative wall, first, the reinforcement layout of the control wall was adopted. Then, some of the steel reinforcement of the adopted reinforcement layout was substituted by a type of innovative reinforcement. This was to provide each innovative wall with a meaningful increase in the self-centering compared to the control wall while maintaining comparable levels of energy dissipation and deformation capacity to the control wall.

### **1.4.2 Objective 2**

- The second objective is to provide some recommendations for the design and construction of innovative shear walls.

In this regard, reliable finite-element analysis models for the experimented conventional and innovative shear walls are developed. The models are developed using off-the-shelf materials and elements of research-oriented finite-element (FE) packages. Then, the analysis models are verified and used to study the effect of high-performance materials on the design variables of the innovative shear walls. Then, some recommendations will be developed for the design of innovative shear walls.

In addition, a parametric study is performed to investigate the effects of the variables, such as axial force, aspect ratio, and reinforcement ratio, which are not investigated in the experimental study of the innovative shear walls. The finite-element modeling techniques developed through the analysis of tested walls are used to investigate the response of large-scale shear walls incorporating advanced materials and details under cyclic and seismic loads.

## **1.5 Thesis Outline**

The structure of this thesis is as follows. In Chapter 1, the problem statement, the scope, and the objectives of the thesis are defined. Chapter 2 reviews the literature on innovative materials and their application in innovative structural elements. Different methods of testing for structural elements are also explained in this chapter. Chapter 3 explains the experimental tests performed on four shear wall specimens in this study. This chapter also compares the performance of the tested innovative wall in terms of self-centering and energy dissipation capacity. In Chapter 4, the design parameters of the tested walls are calculated and compared. Chapter 5 explains the finite element models developed for the tested walls and other innovative walls from the literature. Chapter 6 discusses the implementation and the results of a parametric study performed on innovative walls. And finally, Chapter 7 concludes the results of the study.

## CHAPTER 2 LITERATURE REVIEW

### 2.1 Introduction

Many cities around the world are located in regions with moderate to high seismicity. Buildings designed in these regions must comply with minimum performance objectives set by seismic design guidelines and codes. In accordance to seismic design codes such as FEMA 356 (2000) or ASCE 7-10, non-critical buildings (most buildings including residential, commercial, and industrial buildings) are to meet collapse prevention limits when subjected to maximum considered earthquakes (MCE), which are earthquakes with a recurrence period of 2475 years, or a likelihood of occurrence of 2% in 50 years. Non-critical buildings must comply with the life safety definition when withstanding earthquakes with a recurrence period of 475 years, or a likelihood of occurrence of 10% in 50 years, which are called the design basis earthquakes (DBE).

Using reinforced concrete shear walls is an efficient way to resist lateral forces and provide stiffness to buildings. Under lateral loads produced by wind or seismic events, shear walls can deform in a ductile way and dissipate energy while maintaining sufficient load-carrying capacities. Ductile behavior of shear walls becomes possible through yielding of steel reinforcement and being adequately detailed, such as having confinement to the concrete at the wall boundaries. Ductility, however, comes with its intrinsic consequences, such as damage in concrete such as cracking, spalling and crushing, and residual deformations, which occur due to permanent elongations in the reinforcement. Therefore, after an extreme loading incident, the structure may need costly repairs and rehabilitation procedures, even if it has not collapsed. If the damage is extensive, the structure may even need to be demolished and replaced. According to Ramirez and Miranda (2012), after the 1985 Mexico City, and 1995 Kobe earthquakes, it was indicated that the main cause of the demolition of even moderately damaged structures was the high levels of permanent lateral deformations (Fig. 2.1).

Ramirez and Miranda (2012) performed a study on the significance of residual drifts in the loss estimation of post-earthquake buildings. The research was conducted on four RC frame buildings located in Los Angeles, California. Two of the buildings (a 4-story and a 12-story), which did not have the required details for ductile behavior, represented pre-Northridge seismic codes. On the

other hand, the other two, including one 4-story and one 12-story building, were equipped with the required detailing according to the current US seismic design codes. The results indicated that despite the non-ductile buildings, the economic losses in the ductile buildings were mainly due to the residual inter-story drift of them. In this regard, Fig. 2.2 shows the probability of demolition for a not-collapsed RC frame building against its peak inter-story residual drift ratio. According to the figure, for a permanent drift ratio of 1% or less, the probability of demolition is about 10% or smaller. For a permanent drift ratio of 2%, the probability of demolition rises to above 80%, and finally, demolition will be inevitable if the permanent drift ratio becomes more than 3%. The study also showed that estimating economic losses for DBE with consideration of forced demolition due to permanent drift inter-story ratios was 45% more than the estimates overlooking permanent drifts. The study, then, suggests that the current economic loss estimates which do not account for residual inter-story drift ratios may hugely be underestimating the reality.



Figure 2.1. ‘Examples of buildings with residual displacements leading that typically lead to demolition (left photo by M. Bruneau, MCEER; right photo by A. Whittaker, NISEE, EERC, UC Berkeley)’ (Ramirez and Miranda 2012)

To lower the probability of forced demolition in RC structures, their permanent inter-story drift ratios must be lowered. In this regard, the present study was defined to mitigate post-earthquake damage of RC shear wall structures in terms of permanent drift ratios and concrete damage. The general objective of the research is to investigate and compare three different types of innovative shear wall systems to reduce concrete damage and residual deformations. To reduce permanent deformations, high-performance materials and details such as SMA bars, GFRP bars, and unbonded post-tensioning strands were used. Also, in order to mitigate concrete damage, including

cracking, spalling, and crushing two types of fiber reinforced concrete (FRC), engineered cementitious composite (ECC) and steel fiber reinforced concrete (SFRC), were utilized.

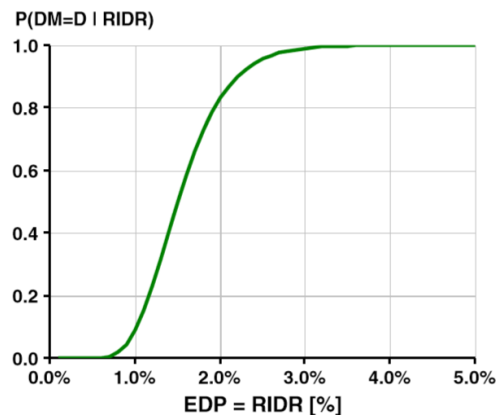


Figure 2.2. Probability of having to demolish a building that has not collapsed as a function of peak residual inter-story drift in the building. EDP, engineering demand parameter; RIDR, residual inter-story drift ratio (Ramirez and Miranda 2012)

Steel-reinforced concrete shear walls with especial reinforcement detailing have higher levels of ductility than ordinary walls. However, they are more expensive. In this regard, (Aly et al. 2018) studied the impact of detailing on the performance and the cost of RC shear walls. Detailing shear walls with different types of self-centering reinforcement also increases the construction cost of RC shear walls. However, this additional cost can drastically decrease the amount of time and money required to rehabilitate or even demolish and reconstruct a building after extreme seismic events, which are not insignificant in cities with high seismicity. For instance, the construction of the first prototype innovative bridge, which was detailed with SMA bars and ECC and constructed in Seattle in 2017 (Ge et al. 2019), is justifiable with the same rationale.

## 2.2 Advanced Materials

In recent years, high-performance materials such as SMA, GFRP, and FRC have become feasible alternatives to conventional construction materials such as steel and concrete to overcome their limitations. These limitations can be outlined as low tensile strength and negligible strain ductility in tension (concrete) as well as significant residual deformations and susceptibility to corrosion (steel). A literature review on the use of advanced materials and their application in structural engineering, with an emphasis on buildings, is presented next. In this section, the application of

advanced reinforcing materials such as SMA, FRP, and post-tensioning steel, together with fiber reinforced concrete and composite materials in structural engineering is discussed.

### **2.2.1 Shape Memory Alloy**

Shape Memory Materials (SMM) form a category of smart materials comprising a variety of materials, including alloys, ceramics, polymers, and gels with specific properties as shape memory effect and super-elasticity. These properties enable SMMs to recover large amounts of strain and return to their original shapes after being heated or the release of applied stress (Wei et al. 1998).

Among the shape-memory materials, shape memory alloys (SMA) have become suitable alternatives to conventional steel for certain applications in recent years. Although different types of SMAs are available, NiTi (Nickel-Titanium alloy), which is also called Nitinol, has become one of the most widely used SMA materials due to its superior mechanical properties, easier manufacturing, and significant shape memory effect (Cederstrom and Humbeeck 1995; Desroches et al. 2004; Nemat-Nasser and Guo 2006; Wei et al. 1998).

As shown in Fig. 2.3 the behavior of NiTi is a function of stress, strain, and temperature as the crystal structure of NiTi can transform between two phases: austenite and martensite. Austenite is the crystal structure of NiTi in which the atoms of the material have cubic structure, while in martensite, atoms are placed in a new structure taking more space (Nemat-Nasser and Guo 2006). According to Desroches et al. (2004), in low temperatures and high-stress levels, the stable crystal phase of NiTi is martensite, while the stable phase is austenite in high temperatures and low-stress levels. As illustrated in Fig. 2.3, at temperatures below the martensite finish temperature, or  $M_f$ , the material can recover its original shape upon heating. This is the so-called shape memory effect. The super-elastic behavior occurs when the temperature of NiTi is above the austenite finish temperature, or  $A_f$ , yet below the temperature in which the martensite behavior is no longer stress-induced (martensite deformation temperature or  $M_d$ ). This condition translates into a temperature range between  $-20\text{ }^\circ\text{C}$  and  $+100\text{ }^\circ\text{C}$ , according to Tehrani et al. (2015), indicating that NiTi exhibits super-elastic effects in temperature ranges found in common structural applications. And finally, at temperatures above  $M_d$ ,  $100\text{ }^\circ\text{C}$  (Tehrani et al. 2015), the material behaves as a usual metal.

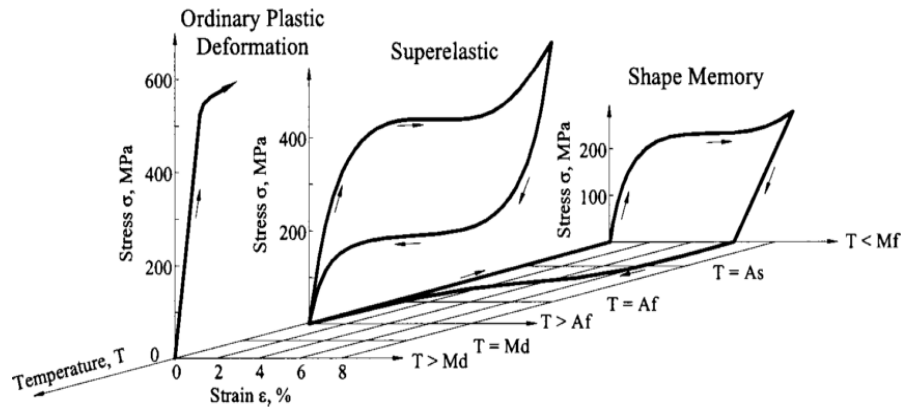


Figure 2.3. Stress-strain relationship of NiTi (Desroches et al. 2004)

Saiidi et al. (2007, 2009) and Saiidi and Wang (2006) performed exploratory studies on RC bridge columns detailed with advanced materials such as SMA and ECC. The studies showed that structural elements reinforced with SMA have notably reduced residual deformations after being subjected to strong earthquakes. It was also found that damage in elements incorporating ECC was substantially reduced in comparison to the conventional structural elements.

Cruz Noguez et al. (2012) studied the damage characteristics of innovative piers through shake-table testing of a four-span bridge specimen. The bridge had three, two-column piers, each of which implemented advanced materials at their bottom plastic hinges, while the top plastic hinges were made of conventional steel-reinforced concrete for comparison purposes. The bridge model was subjected to two horizontal components of the 1994 Northridge earthquake simultaneously. The results showed reduced damage in enhanced plastic hinges with the one made of ECC and reinforced with SMA remained almost undamaged. In terms of residual deformations also, enhanced hinges showed huge improvements in comparison to the plastic hinges made of conventional materials.

Tazarv and Saiidi (2015) proposed a set of design specifications for SMA bars as concrete reinforcement. First, a procedure was proposed to identify the different mechanical properties of an SMA bar from its standard tensile test. Then, through a parametric study, the effect of each mechanical properties on the load-deformation relationship of a bridge column was investigated. Then some design specifications for SMA reinforced piers were proposed. Based on the results of these seminal projects, SMA reinforcement has been used for the first time in a bridge structure.

As part of the RS99 tunnel project in Seattle, a damage resilient steel-SMA bridge is under construction (Kerry Clines (2016)). The piers of the bridge are detailed with ECC and SMA to have minimal damage and residual deformations under strong earthquakes. Over time, this innovative design is expected to result in substantial savings in repair costs, well beyond a 5% to 7% increase in cost is being made during construction (Kerry Clines (2016)).

Shahria Alam et al. (2009, 2012) explored the use of SMA at critical locations (plastic hinges) of RC frame buildings by investigating the seismic performance of two 8-story RC frames – one with SMA at beam joints and one pure steel reinforced frame. The results showed that the two frames had comparable performance, while the steel-SMA frame could effectively recover its inter-story and top-story residual drift ratios. Then, the study was expanded to 3, 6, and 8-story buildings with steel-SMA reinforced 3D frames.

Abdulridha and Palermo (2014) explored the application of SMA bars as in reinforced concrete shear walls by testing two RC shear walls – one purely reinforced with steel and the other reinforced with steel and SMA bars. The results showed that the wall with the hybrid reinforcing system had notable self-centering while having comparable strength and maximum drift ratio to the control specimen.

### **2.2.2 Fiber Reinforced Polymer (FRP)**

FRP is a type of composite material consisting of an arrangement of polymer fibers within a resin matrix. FRPs are manufactured as sheets and bars and are widely used in the construction and rehabilitation of structures. Some of the unique properties of FRPs are high-strength to weight ratio, ease of installation, high durability, and magnetic and thermal non-conductivity.

Based on the type of fibers used in the composite material, FRPs are termed as CFRP (carbon fiber), AFRP (aramid fiber), or GFRP (glass fiber). Since the fibers control the mechanical properties of the final composite, the properties of different types of FRP vary accordingly (Fig. 2.4). FRP materials have a quasi-linear stress-strain relationship in tension. They generally have high tensile strengths and exhibit a brittle mode of failure when the tensile strength is reached. In regards to the compressive capacity, FRP materials are not as efficient as in tension, since the

buckling strength of the fibers is low due to the negligible lateral support provided by the resin matrix (Mallick 2007).

Due to the unique properties and benefits of FRPs, their application in construction and retrofitting of structures has widely been explored. Wrapping is one of the most common retrofitting techniques used to strengthen vulnerable structural elements, such as columns or beams. The use of FRP wrapping in strengthening reinforced concrete columns is a well-studied subject. A literature review showed that FRP wrapping in the transverse (horizontal) direction of the columns could effectively increase the shear capacity of circular and rectangular columns. FRP horizontal wrapping has been proven to delay lap-splice brittle failures and concrete crushing effectively. It can also be used for increasing the confining stress and promote ductility in RC columns. Vertical wrapping has been used in flexural retrofitting and repair applications. In terms of efficiency, horizontal wrapping is more effective in circular columns than it is in rectangular cross-sections (Yu-Fei Wu, Tao Liu 2006).

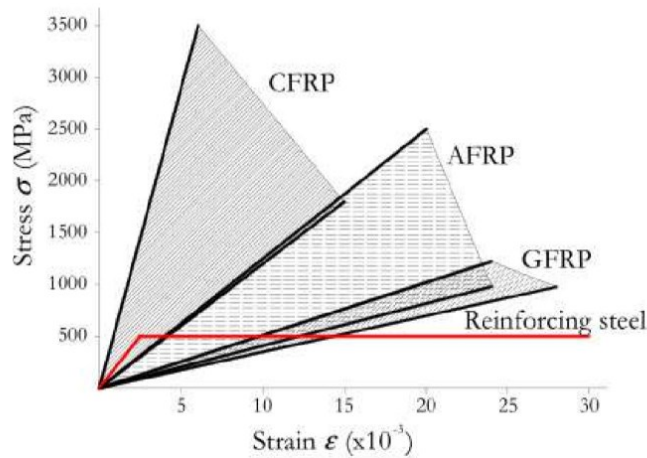


Figure 2.4. Tensile stress-strain relationship of different types of FRP in comparison to steel (Mohamed 2013)

De Luca et al. (2009) studied the response of 14 full-scale circular columns reinforced with longitudinal and transverse FRP (GFRP and CFRP) bars under concentric axial forces. The study investigated the effect of different transverse reinforcement configurations (stirrups versus spirals), volumetric ratio, and the type of FRP reinforcement on the confinement of concrete. The study illustrated that RC columns reinforced with GFRP and CFRP had similar behavior to the

conventional steel RC columns and behaved linearly up to 85% of the peak strength. Both CFRP and GFRP stirrups and spirals complying with CSA S608-12 were able to adequately prevent buckling of the longitudinal FRP bars and confine the core of the columns after the peak load. The GFRP and CFRP RC columns incorporating spirals attained less than 3% more strength in comparison to the identical specimens of them reinforced with circular stirrups. That shows the circular stirrups were as efficient as spirals in confining the core of the specimens. In terms of the longitudinal bars, GFRP and CFRP longitudinal bars underwent up to 0.4% and 0.7% of compressive strains. The bars resisted compression until after the crushing of the concrete.

Mohamed et al. (2014) explored the application of GFRP bars in concrete shears. The study included testing four cantilever shear wall specimens – three fully GFRP reinforced and one steel-reinforced shear walls. The walls were tested under a cyclic lateral load while carrying 7% of their axial capacities as gravity loading. The results showed that the GFRP walls reached satisfactory levels of drift ratio while reducing shear strains at the base of the walls and addressing the brittle shear failure.

### **2.2.3 Fiber Reinforced Concrete**

Concrete is composed of fine and coarse aggregates bound together by a cement-based paste. The composition of concrete results in high compressive and low tensile strengths. Damage mechanisms in concrete are related to cracking propagation in concrete related to its reduced tensile strength. Under an arbitrary load, cracks form and develop in the cement paste due to the occurrence of tensile strains caused by tension and shear forces. After cracking, the tensile strength of plain concrete is zero. Cracking in concrete leads to spalling, loss of concrete cover, and can even reduce the compressive capacity of concrete, producing crushing, due to compression softening. One solution to improve the tensile behavior of concrete is to reinforce the material with randomly oriented fibers made of materials with high tensile strength, which results in the composite exhibiting post-cracking tensile strength. Such materials are termed fiber reinforced cement composites (FRCC). Two of the most widely used types of FRCC are SFRC and ECC.

A more general classification of cement composites is depicted in Fig. 2.5. Fiber-reinforced cement composites (FRCC) incorporate metallic, polymeric, or other types of fiber to enhance different aspects of the composite response. According to Kunieda and Rokugo (2006), a class of

FRCCs designed to exhibit a ductile behavior in both compression, tension, or both, they are termed ductile fiber reinforced concrete (DFRCC). DFRCC materials are classified into two sub-classes – composites with or without tensile strain hardening. DFRCC materials with tensile strain hardening are called high-performance fiber-reinforced cement composite (HPFRCC). HPFRCCs achieve tensile ductility through the development of multiple micro-cracks in tension. One example of HPFRCCs is ECC, which is a mix of cement, sand, fly ash, and polyvinyl alcohol fibers.

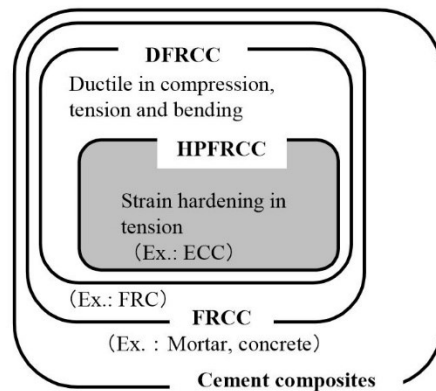


Figure 2.5. Cement composites (Kunieda and Rokugo 2006)

### 2.1.3.1 Steel Fiber Reinforced Concrete (SFRC)

In terms of the mixture, SFRC and concrete have similar components except for the steel fibers, which are usually provided as a fraction of the SFRC mix volume. SFRC materials are produced with different fiber contents; however, in order to maintain suitable levels of workability and fiber dispersion, it is suggested that the fraction of fibers should be limited to 2% (Parra-montesinos 2005). Apart from the fiber dosage, fiber properties, including the geometry, aspect ratio, and strength, play major roles in the tensile properties of the mix (Thomas and Ramaswamy 2007). In general, hook-ended or crimped fibers are more effective than straight fibers due to their higher pullout strength.

In regions under tensile straining, fibers contribute to resisting tensile stresses through the bridging of the crack, which results in enhancement on the post-cracking response in comparison to plain concrete. As the crack grows, the fibers are pulled out, and the material resists less tensile stresses

and finally fails in a quasi-brittle manner (Fig. 2.6). Beyond the cracking point, SFRC experiences a reduction in tensile strength as tensile strain increases (Li 1998).

It has been shown through several experimental studies that fiber reinforcement has a significant contribution to the response of the structural elements cast with FRCC. Canbolat et al. (2005) conducted an experimental study on the seismic response of coupling beams detailed with HPFRCC. The study consisted of testing four coupling beams under displacement reversals. One of the specimens was made of normal concrete. The other specimens were detailed with fiber reinforcement and different reinforcement configurations. The types of fiber used in the study were ultra-high molecular weight polyethylene (PE) with a volume fraction of 2% and twisted steel fibers with a 1.5% volume fraction. The study showed that detailing coupling beams with HPFRCC eliminates the need for the stirrups around the diagonal reinforcement in the coupling beams due to the adequate confinement provided by the HPFRCC. It was shown that the coupling beams detailed with diagonal reinforcement and HPFRCC were able to maintain their load-bearing capacity up the drift ratio of 4%. The study also suggested a pre-cast construction method for HPFRCC coupling beams. With precast construction methods and relaxed reinforcement details, it is possible to save time and workforce since the conventional construction of coupling beams requires substantial reinforcement detailing.

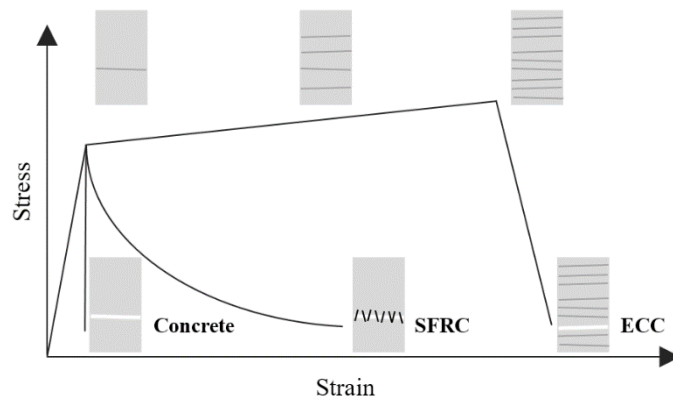


Figure 2.6. Tensile stress-strain curves of concrete, SFRC, and ECC

Parra-Montesinos and Kim (2004) also studied the HPFRCC low-rise shear walls (aspect ratio of 1.5). The walls had lower web reinforcement ratios than required by ACI 318-02 (2002) and were designed to have a diagonal tension failure. Two types of fiber reinforcement were used in the

HPFRCC materials used in the study. One was ultra-high molecular weight polyethylene with a volume fraction of 1.5%, and the other was hooked steel fibers at 2% of volume fraction. According to the test results, up to 70% of the specimen strength came from the contribution of the fiber-reinforced concrete. Failure of the specimens occurred at a drift ratio of 2.5%, as the fibers were pulled out, and a diagonal crack opened. The results suggested that HPFRCC shear walls exhibited enhanced damage resilience, superior strength, and displacement capacities than walls made of conventional concrete. Regarding shear walls, Athanasopoulou and Parramontesinos (2014) performed a complete study on low-rise SFRC specimens through exploring experimental results of nine low-rise shear wall specimens. Henager (1977) also studied a beam-column connection made of SFRC with a volume fraction of 1.7%. As the test result indicated, the joint illustrated an increase in strength and stiffness with less damage even though none of the column stirrups were extended in the connection region.

#### 2.2.4 Engineered Cementitious Composite (ECC)

Engineered cementitious composite (ECC), which was developed by Li (1993), is a class of HPFRCC material with tensile strain capacities ranging between 1% to 5%. ECC achieves ductile behavior through the development of multiple micro-cracks as opposed to the formation of a single, dominant crack. Figure 2.7 shows the difference between the cracks formed in ECC and concrete. In ECC, which is tailored through micromechanics, the formation of new cracks requires less energy than breaking the fibers that bridge an already formed crack. As a result, multiple micro-cracks with uniform widths, called steady-state flat cracks, are formed in the material. Figure 2.8 illustrates the ductile behavior of an ECC slab specimen during a four-point load test. In contrast, for plain concrete crack propagation and enlargement needs less energy than that required to form a new crack (Li 2003).

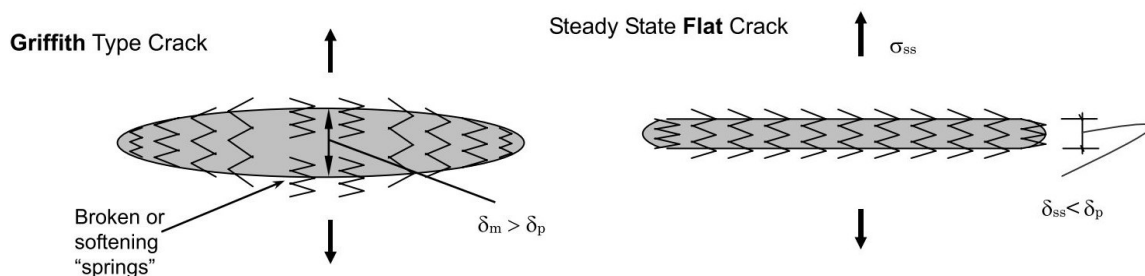


Figure 2.7. Cracks in ECC and concrete (Li 2003)

In terms of mixture components, ECC consists of cement, water, fine aggregate, fly ash, and polyvinyl alcohol (PVA), filling 2% of the mix volume (Li 1998). Only fine aggregates are used in ECC since course aggregates do not participate in tension and reduce the tensile strength and ultimate strain of the ECC.

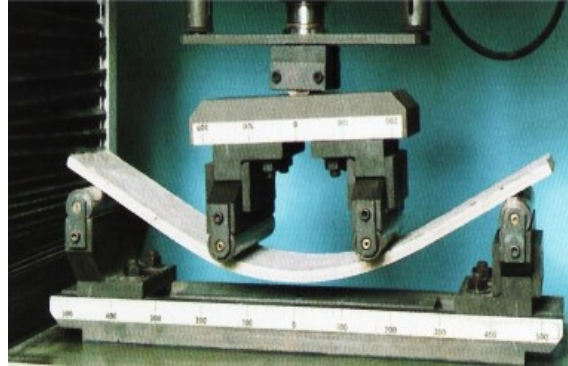


Figure 2.8. An ECC slab under four-point-load test (Nagai et al. 2002)

Fischer et al. (2002) performed a study on reinforced ECC beams under cyclic loading. The study included the testing of four small-scale cantilever specimens consisting of one reinforced concrete and three reinforced ECC beams. The control specimen (S1), was an RC beam with a longitudinal reinforcement ratio of 3.14%. The specimen also had a transverse reinforcement ratio of 0.57% below the height of 150 mm, and a ratio of 0.17% above the height of 150 mm. The second specimen (S2) was a reinforced ECC specimen with the same reinforcement ratios to those of the control beam. The third (S3) and the fourth (S4) specimens were ECC reinforced beams with the same longitudinal reinforcement ratio as the other two specimens; however, no transverse reinforcement was provided for them. The fourth specimen was the only specimen that carried an axial load of 80 kN while the specimens were tested under lateral reversed cyclic displacements.

The study showed a superior damage tolerance and hysteretic properties of the ECC beams regardless of the presence of transverse reinforcement. Figure 2.9 illustrates the cracking pattern of the specimens. As shown in the figure, several flexural cracks formed along the heights of the ECC reinforced specimens reducing the demand and damage in the plastic hinge region on the beams. In addition, bond slipping, cover spalling, and composite disintegration did not take place in the ECC specimens. The failure mode of ECC beams S2 and S3 was due to the low-cycle fatigue failure of longitudinal steel bars, while the control specimen S1 failed because of concrete

crushing. Regarding the S4, the decline in strength was because of ECC compression failure, although the specimen maintained its axial capacity up to the end of the test. The fourth specimen failed at the drift ratio of 14% when its longitudinal reinforcement buckled.

According to Fig. 2.10, the hysteresis of the specimens, each of the ECC beams illustrated an improved lateral load resisting, energy dissipation, and drift ratio capacity in comparison to those of the control specimen.

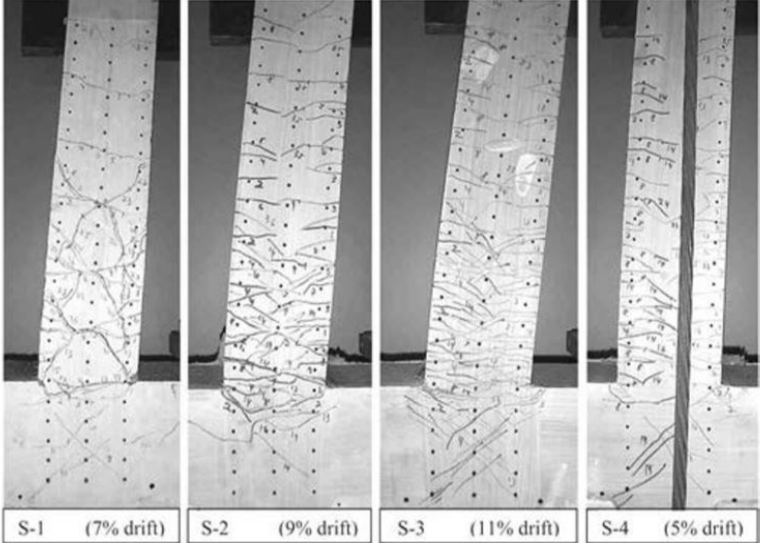


Figure 2.9. Deformed shape of ECC beams (Fischer et al. 2002)

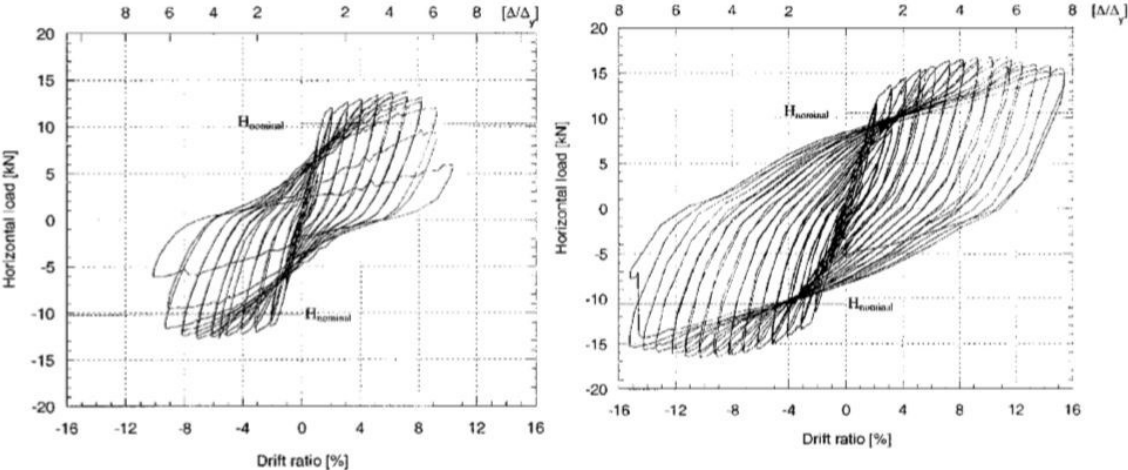


Figure 2.10. Hysteretic response of specimens (Fischer et al. 2002)

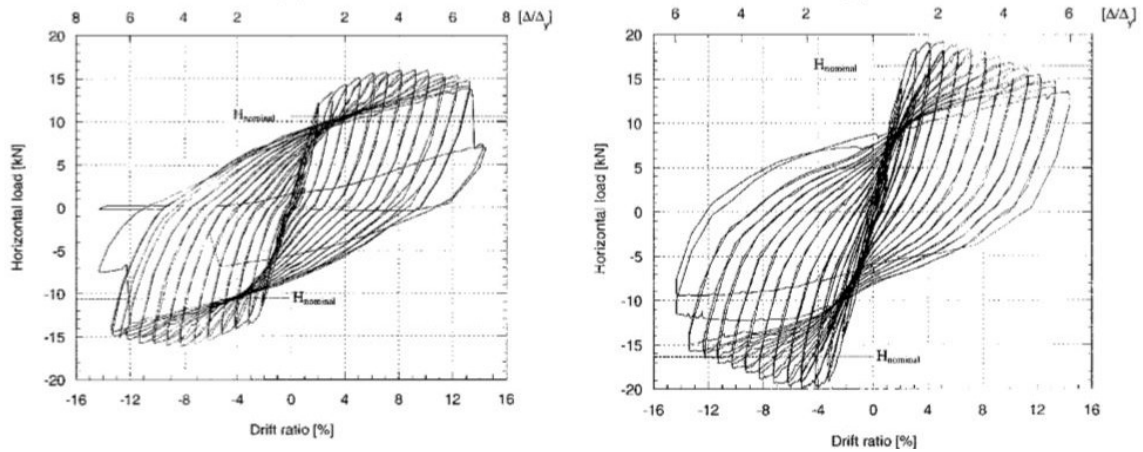


Figure 2.10. Continued

Saiidi and Wang (2006) investigated bridge piers detailed with ECC and SMA reinforcement at their plastic hinge locations. The test results indicated that the proposed detailing results in minimal sustained damage and residual deformation. Cruz Noguez et al. (2012) studied the seismic behavior of a quarter-scale, four-span bridge, which was special in utilizing advanced materials. One of the bents of the bridge model was detailed with NiTi bars and ECC. The ECC was incorporated in the lower parts of the bridge columns, where the bottom plastic hinges were expected to be formed. The rest of the columns, including the top plastic hinges, were detailed with steel and normal concrete. Figure 2.11 illustrates the state of the top and the bottom plastic hinges formed in the forgoing bent. As shown, the ECC sustained limited cracking and no spalling, while the concrete was moderately damaged.

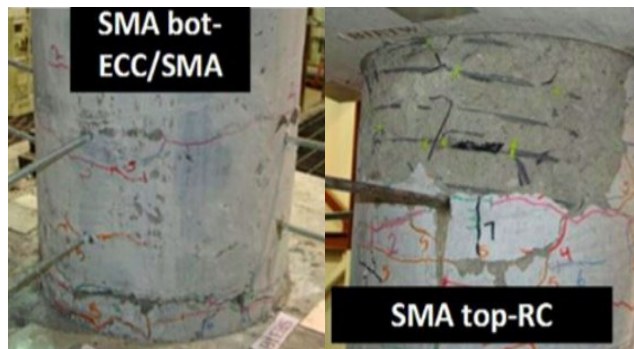


Figure 2.11. Damaged state in a pier of SMA/ECC bent (Cruz Noguez et al. 2012)

ECC has also been used in concrete shear walls. Nagai et al. (2002) and Li et al. (2014) studied the behavior of low-rise ECC reinforced shear walls under lateral cyclic loading. Both studies reported that substituting normal concrete with ECC will enhance the performance of the shear walls in terms of strength, deformability, and damage tolerance.

### **2.2.5 Partially Post-Tensioned Systems**

Post-tensioning is a prestressing technique that consists of stressing tendons that are placed in the ducts left in a concrete member after the concrete has hardened, to increase the stiffness and the cracking resistance of the member. When the member is un-cracked under the service loads, the member is said to be fully prestressed. The post-tensioning can be partial, in the sense that some cracking is accepted under service conditions. According to ACI-ASCE Joint Committee 423 (1999) partial prestressing is ‘an approach in design and construction in which prestressed reinforcement or a combination of prestressed and non-prestressed reinforcement is used such that tension and cracking in concrete due to flexure are allowed under service dead and live loads while serviceability and strength requirements are satisfied.’ If the post-tensioning reinforcement is designed to stay in the elastic range under loading at the ultimate limit state, the reinforcement can be used to provide restoring forces to a structural member.

Sakai and Mahin (2004) performed a study on the application of post-tensioned strands in reducing the residual displacements of circular concrete bridge columns. The study proposed that by replacing some of the longitudinal reinforcement of a bridge column with un-bonded post-tensioned strands, the partially post-tensioned column will show a significant reduction in residual displacements. Then through a series of cyclic tests, the effect of different parameters such as the amount of post-tensioning, mild reinforcement, and post-tensioning stress on the hysteretic response of four bridge columns was studied. For instance, the study shows, when 50% of mild steel in a bridge column is replaced by post-tensioning strands with equal cross-section area and a post-tensioning stress equal to the axial load resulting from dead loads, residual displacements are reduced by 86%.

Cruz Noguez et al. (2012) performed on the seismic behavior of a quarter-scale four-span bridge, which included a two-column bent detailed with post-tensioning rods. The study showed that post-tensioning bridge columns could effectively reduce the residual displacements. Unbonded post-

tensioned rods, as opposed to bonded reinforcement, was used to prevent stress transfer from the reinforcement to the concrete, and thus minimize damage. However, Cruz Noguez et al. (2012) reported that damage to concrete was significant within the plastic zone of the piers. This can be attributed to insufficient non-prestressed reinforcement at the plastic hinge zone, thus allowing the development of large cracks and spalling of concrete. Figure 2.12 illustrates the state of the top and bottom plastic hinges formed in the bent. As shown, the damage to the bottom plastic hinge was severe as the longitudinal reinforcement buckled, and the stirrup ruptured.



Figure 2.12. Damaged state partially post-tensioned bent (Cruz Noguez et al. 2012)

Some researchers also studied pre-stressed shear walls. Kurama et al. (1999) studied the seismic performance of pre-stressed precast shear walls. The study showed that pre-stressed precast walls undergo lateral displacements through gap opening at their horizontal joints and exhibited minimal damage in respect to monolithically built shear walls. Kurama (2000) and Morgen and Kurama (2004) also investigated the response of pre-stressed shear walls with supplemental dampers. They showed that the employment of viscous and frictional damping systems would substantially increase the energy dissipation properties of the pre-stressed precast walls without affecting their desirable characteristics such as high self-centering. Kurama (2002, 2005) also undertook an analytical study on the seismic design of partially pre-stressed shear walls. The study showed that using mild steel along with post-tensioned strands will allow the wall to dissipate energy through the yielding of the mild steel reinforcement while the post-tensioned strands promote the self-centering of the shear wall. It was suggested that for a wide range of post-tensioned precast shear walls, it might be possible to raise the normalized inelastic dissipated energy to 0.5 when at least 50% amount of mild steel of the emulating RC walls corresponding to the post-tensioned wall is provided Kurama (2002).

## **2.3 High-Performance Shear Walls**

In this section, high-performance shear walls, including SMA reinforced concrete shear walls, GFRP reinforced concrete shear walls, post-tensioned shear walls, ECC shear walls, and SFRC shear walls are discussed.

### **2.3.1 SMA Reinforced Concrete Shear Wall**

Abdulridha (2013) conducted a study on the seismic performance of concrete elements reinforced with SMA to reduce residual displacements. Two shear wall specimens – one a conventional steel-reinforced shear wall, and the other an innovative shear wall reinforced with SMA and steel bars – were cyclically tested to failure. The walls were tested in a cantilever fashion, with no external axial loads applied (Fig. 2.13(a)).

The specimens were slender shear walls with aspect ratios (height-to-width) of 2.2. In terms of behavior and failure mode, the walls were designed to resist lateral loads with high ductility and were provided with adequate horizontal reinforcement to eliminate shear modes of failure. In terms of vertical reinforcement, specimens had an identically distributed reinforcement with a ratio of 0.5%, while the concentrated reinforcement of the two specimens was different. The innovative shear wall was detailed with four #4 (12.7 mm) NiTi-SMA bars at each boundary element. The SMA reinforcement bars had a length of 1000 mm, with 50 mm below the foundation and 950 mm above the base crossing the entire length of the plastic hinge. The SMA bars were coupled with 15M (16.0 mm) steel rebars by mechanical sleeves (Zap Scewlok®). In comparison, the RC wall had four 10M (11.3 mm) steel rebars per boundary element. Also, four bonded 10M doweling bars were placed at the interface of each of the two wall panels to increase the strength against sliding failure. Figure 2.13(b) shows the reinforcement detailing of the walls.

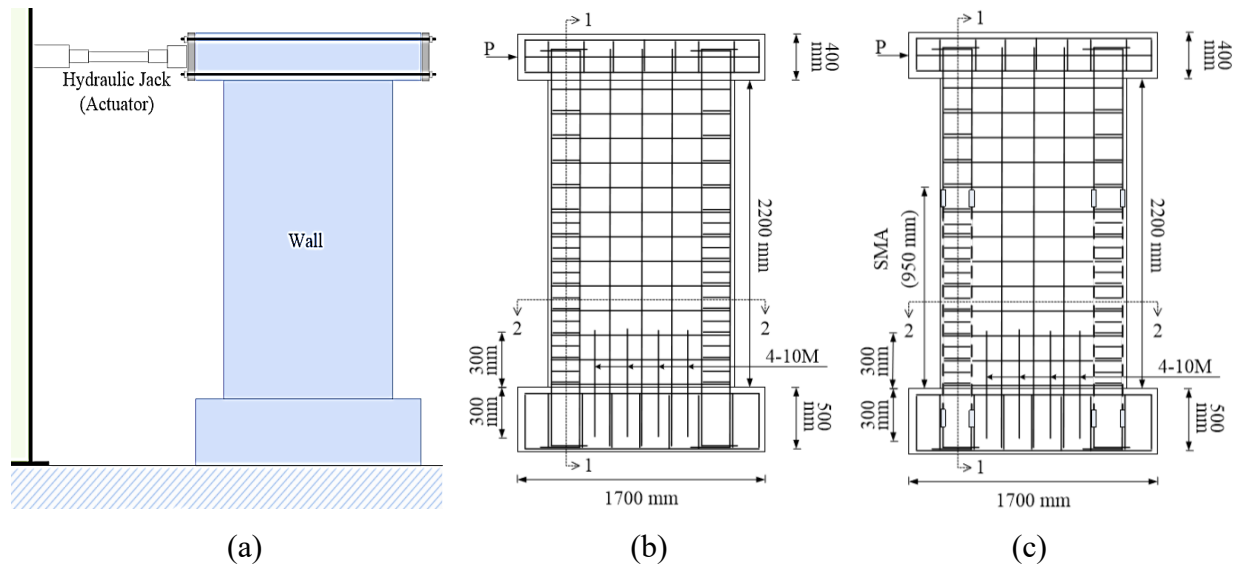


Figure 2.13. Shear wall test performed by Abdulridha (a) test setup, (b) steel reinforced wall, (c) steel-SMA reinforced wall (Abdulridha 2013)

The cyclic responses of the shear walls (Fig. 2.14) indicate that both the walls exhibited comparable amounts of strength, initial stiffness, and displacement capacity. It can be seen that the wall reinforced with steel and SMA bars showed improved self-centering at the end of each cycle. According to the figure, self-centering in the first excursion of each cycle is more pronounced than in the second excursion, which can be attributed to the asymmetric damage sustained at each side of the specimen.

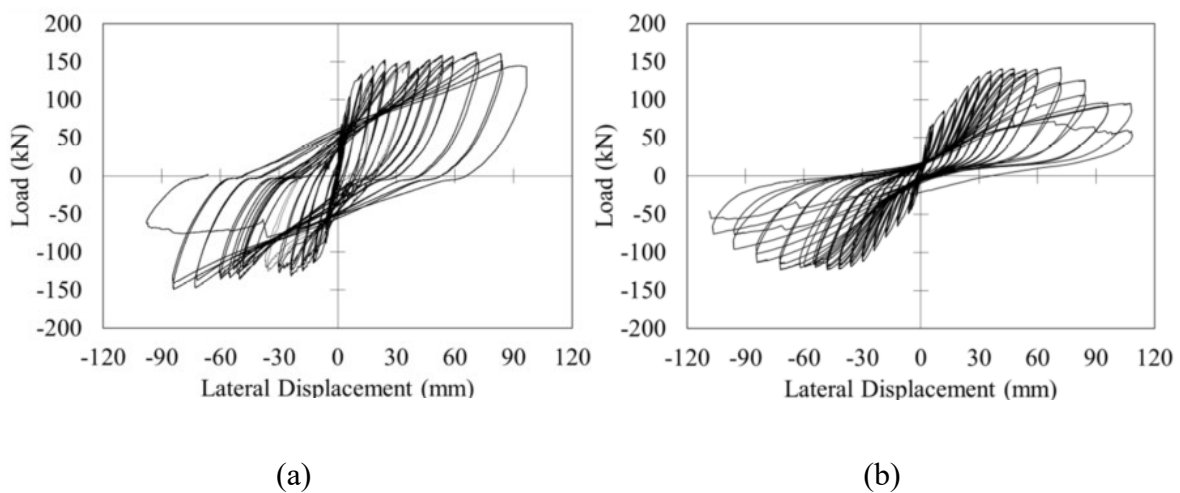


Figure 2.14. Hysteretic response of shear walls: (a) steel-reinforced, (b) steel-SMA reinforced (Abdulridha and Palermo 2014)

Figure 2.15 presents the self-centering performance of the steel-SMA reinforced wall in terms of the recoverable percentage of the ductility ratio versus the ductility ratio. The figure is based on the performance of the wall in the first excursion of each cycle.

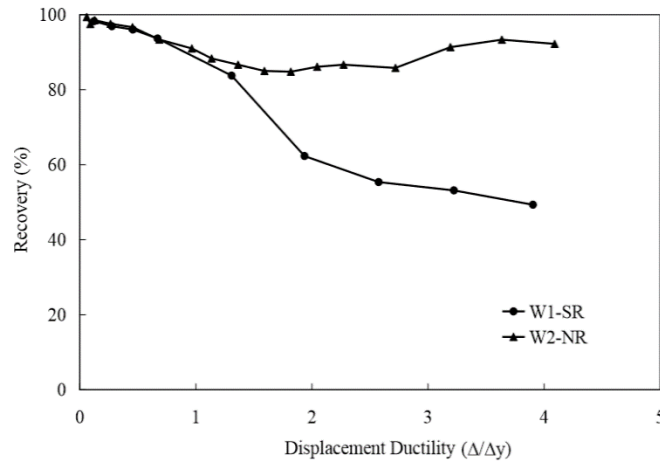


Figure 2.15. Response characteristics of shear wall specimens (Abdulridha 2013)

Figure 2.16 illustrates the effect of loading repetition on the wall strengths, by showing the peak strength of second cycles normalized to that of the first cycles. The figure also shows the failure sequences of the steel-SMA wall, by indicating the order rebar ruptured during the testing. As it is clear from the figure, the rupture of one steel rebar at the ductility level of about 3 triggered the failure, which was followed by the rupture of another rebar and finally an SMA bar.

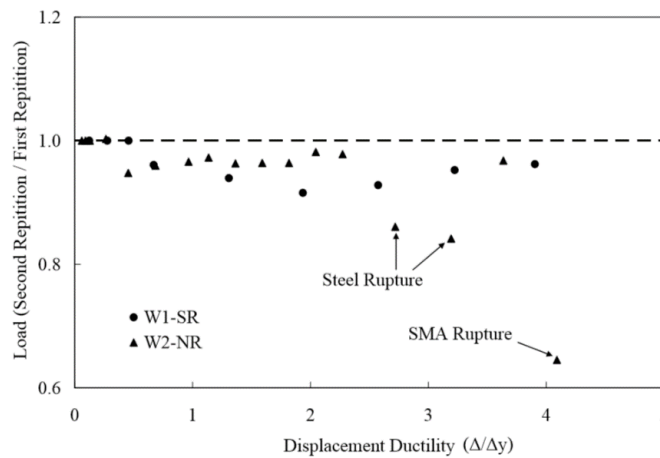


Figure 2.16. Response characteristics of shear wall specimens (Abdulridha 2013)

Damage in the steel-reinforced wall was distributed throughout the wall panel (Fig. 2.17(a)), resulting in less severe damage within the plastic hinge of the specimen. Regarding the steel-SMA reinforced wall, first, a horizontal crack was formed at the elevation of 380 mm (close to the location the dowel bars had ended). The crack then propagated all the way through the wall and changed the behavior of the wall to more of a rigid-body motion as the testing continued. At the left side of the crack (Fig. 2.17(b)), the crushing of concrete and the buckling of SMA bars occurred.

It can be concluded from Fig. 2.14(a) that the SMA bars did not reach their full capacity before the rupture of steel rebars. As the figure shows no evidence of post-yielding over-strength in the response of the steel-SMA reinforced shear wall, which would indicate that the SMA bars did not enter into a strain-hardening range. The early rupture of the steel rebars can also be attributed to the formation of the wide crack that occurred at the height of 380 mm in the wall. The opening of the crack caused increased strain demands on the steel bars crossing the crack.

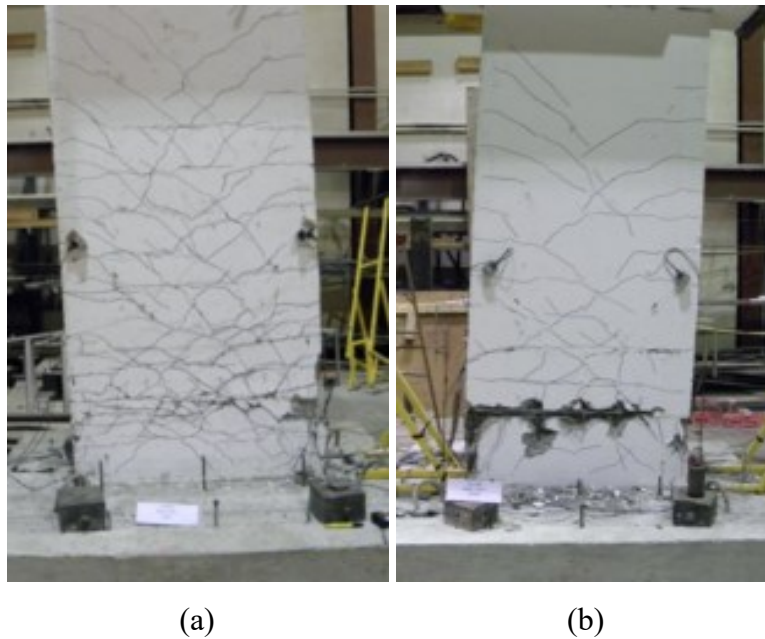


Figure 2.17. Post-test state of conventional (left) and steel-SMA reinforced shear wall (right)  
(Abdulridha 2013)

### 2.3.2 GFRP Reinforced Concrete Shear Walls

In 2013, Mohamed et al. (Mohamed et al. 2014b) undertook a study on slender shear walls reinforced GFRP bars. The main goal of the study was to investigate the adequacy of seismic performance of concrete shear walls reinforced with GFRP bars rather than steel rebars. The experimental program was designed to assess if GFRP reinforced walls were able to achieve required levels of strength and lateral deformation while avoiding brittle failure modes. Also, the energy dissipation capacity of the walls was investigated.

Four shear walls were tested. Three of them were entirely reinforced with GFRP bars, while the last one was a hybrid GFRP/steel specimen. Figure 2.18 illustrates the test setup and the outline of the specimens. The walls were tested under displacement reversals while carrying an axial load ratio (ALR) of 7%, applied through two post-tensioned rods.

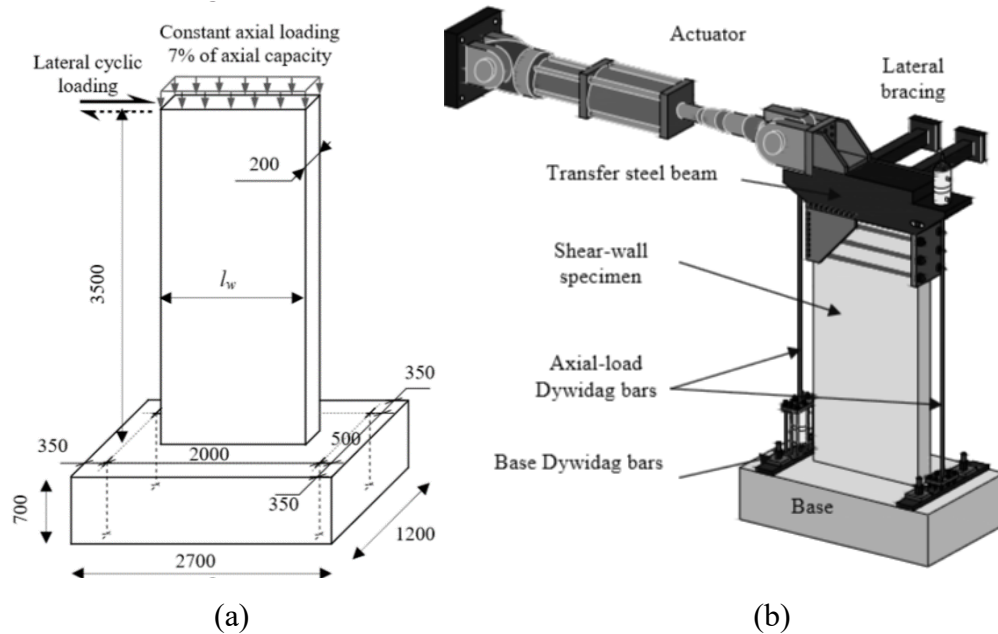


Figure 2.18. Specimens tested by Mohamed (2013) (a) dimensions, (b) test setup

Since the aspect ratio was the parameter of the study, the length  $l_w$  was determined 1500 mm for specimens ST15 and G15, while specimens G12 and G10 had  $l_w$  of 1200 mm and 1000 mm, respectively. The reinforcement layout of the specimens is shown in Fig. 2.19. The specimen ST15 and G15 were designed to have similar axial stiffness (EA), and the other GFRP reinforced walls were designed to have similar reinforcement ratios to the G15 wall.

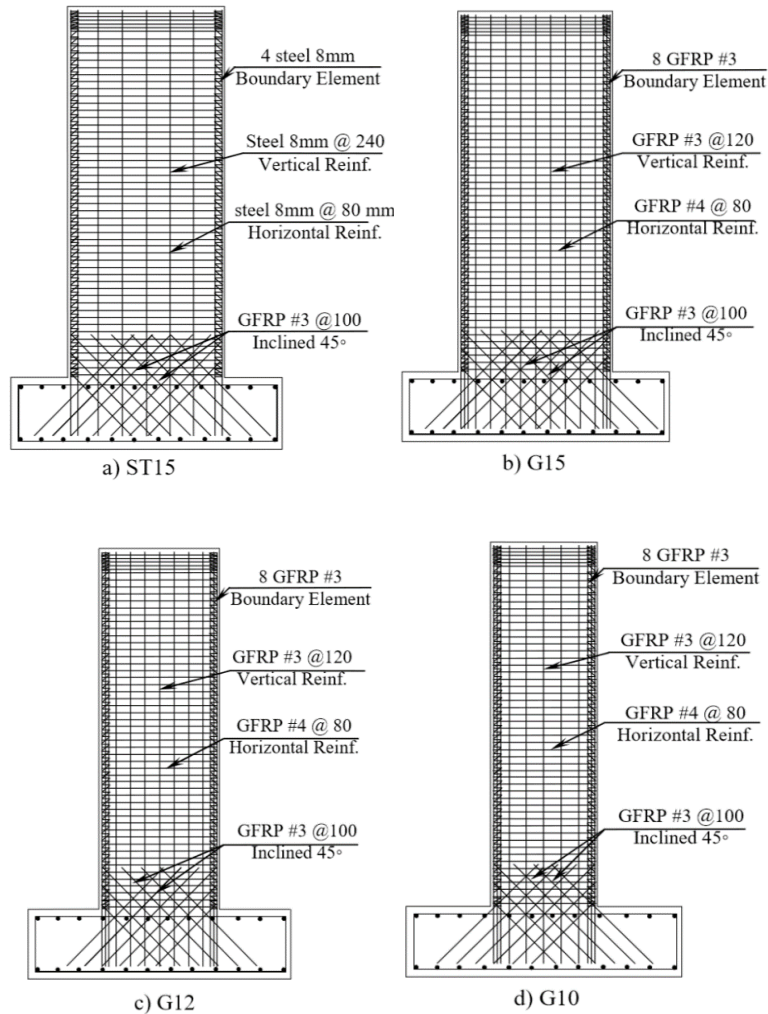


Figure 2.19. Reinforcement layouts of GFRP reinforced specimens (Mohamed 2013)

The top displacement versus base shear response of the specimens is illustrated in Fig. 2.20. All the GFRP walls reached their calculated flexural strength, with no indication of brittle modes of failure such as shear or sliding shear failure. For the steel-reinforced wall (ST15), the progression of the damage consisted of cracking, reinforcement yielding, cover spalling, reinforcement buckling, and finally, concrete crushing at toes. The failure of the GFRP walls was initiated by concrete cracking, cover spalling, and ultimately occurred by crushing of concrete and then rupture of the outermost GFRP bars.

Regarding the energy dissipation capability of the specimens, all the GFRP reinforced walls dissipated relatively low amounts of energy since the response of the walls were dominated by the

quasi-linear behavior of the GFRP bars. Low energy dissipation is not a desirable feature of seismic-resistant structural systems. However, the GFRP walls exhibited a significant self-centering ability, which is attributed to the behavior of GFRP material, and the axial loads, which promote crack closure.

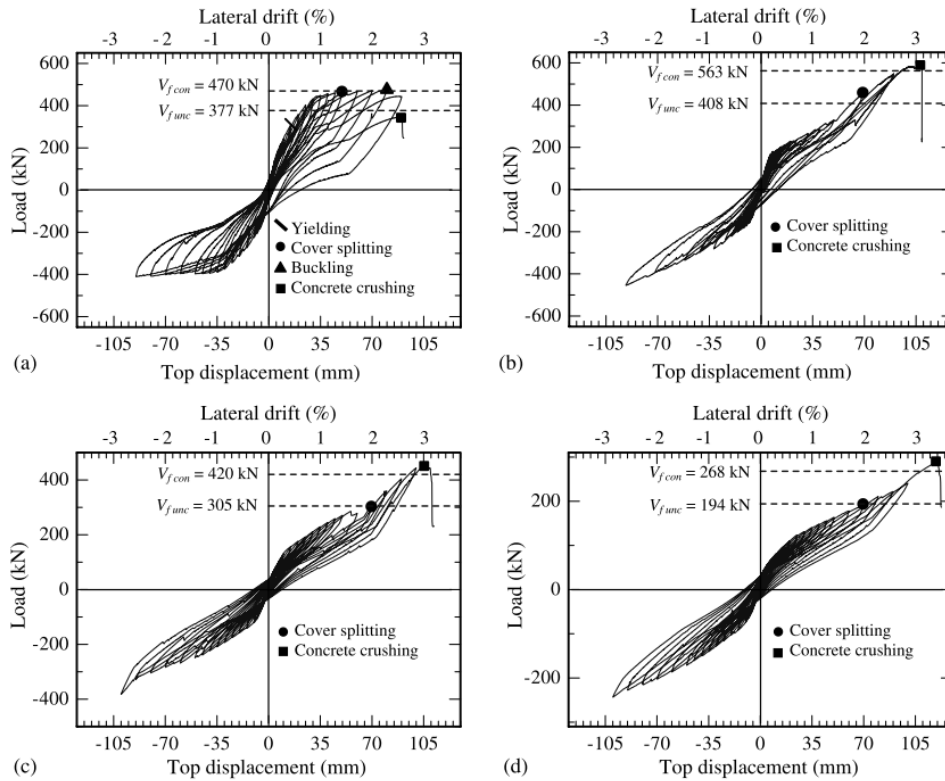


Figure 2.20. Cyclic behavior of specimens (Mohamed et al. 2014b)

The damaged state of the specimens after the completion of the test is illustrated in Fig. 2.21. It is seen that the cracking is distributed through the two thirds the height of the walls, which helps to avoid damage concentration at the lower heights of the walls. The crushing of concrete at the toes of the specimens is also apparent.

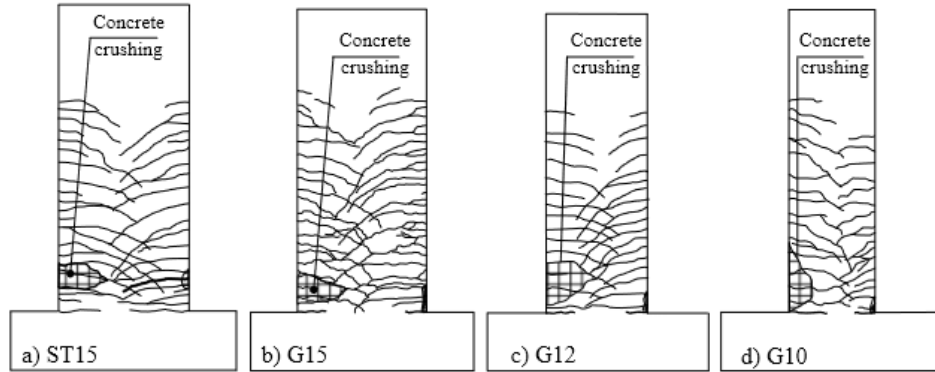


Figure 2.21. State of shear wall after testing (Mohamed 2013)

Ghazizadeh (2017) performed a study on low-rise shear walls detailed with hybrid longitudinal reinforcement and SFRC. The study consisted of testing two shear walls with an aspect ratio of 1.0. The specimen termed control wall was a wall made with conventional reinforced concrete, while the hybrid wall was a steel-reinforced SFRC wall detailed with GFRP bars. Figure 2.22 shows the reinforcement layout of the specimens.

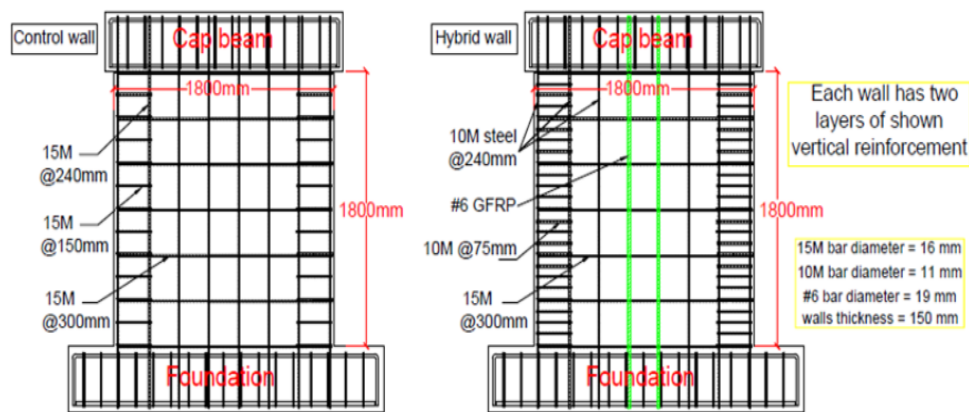


Figure 2.22. Reinforcement layout of specimens (Ghazizadeh 2017)

The specimens were tested under cyclic loading with no axial load applied. Figure 2.23 shows the hysteretic responses of the specimens. As can be seen from the figure, the hybrid wall had comparable strength and energy dissipation capacity to the control wall while illustrating improved self-centering. The ratio of the residual displacement to maximum displacement at the last cycle was 0.5, and 0.63 for the hybrid and control walls, respectively.

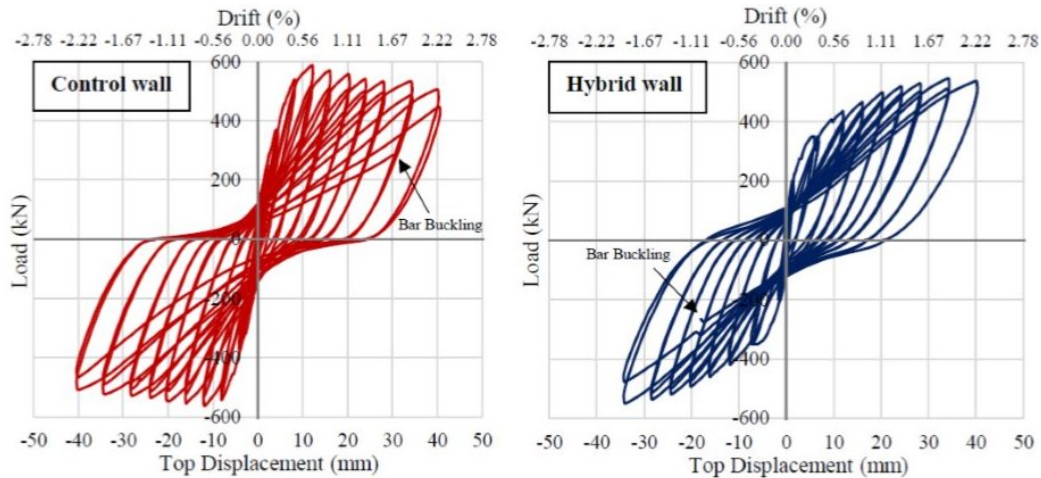


Figure 2.23. Hysteretic response of specimens (Ghazizadeh 2017)

As can be observed from Fig. 2.24 the hybrid wall detailed with SFRC showed enhanced damage mitigation in comparison to the control wall. The hybrid wall had narrower cracks and less spalling.



Figure 2.24. Damaged state of specimens (Ghazizadeh 2017)

### 2.3.3 Post-Tensioned Shear Walls

Cheng and Mander (1997) introduced the concept of damage-avoiding design (DAD). Figure 2.25 explains the concept with three RC shear walls – a conventional monolithic RC wall, a pre-stressed wall (with no continuous mild steel), and a partially pre-stressed wall (with continuous mild steel). After a large load reversal, the monolithic RC shear wall has a considerable amount of residual displacement and cracking, while the pre-stressed and the partially pre-stressed walls have negligible residual displacements, with only a limited or negligible amount of cracking. The strands provide restoring forces that return the wall into its original position, minimizing permanent lateral deformations.

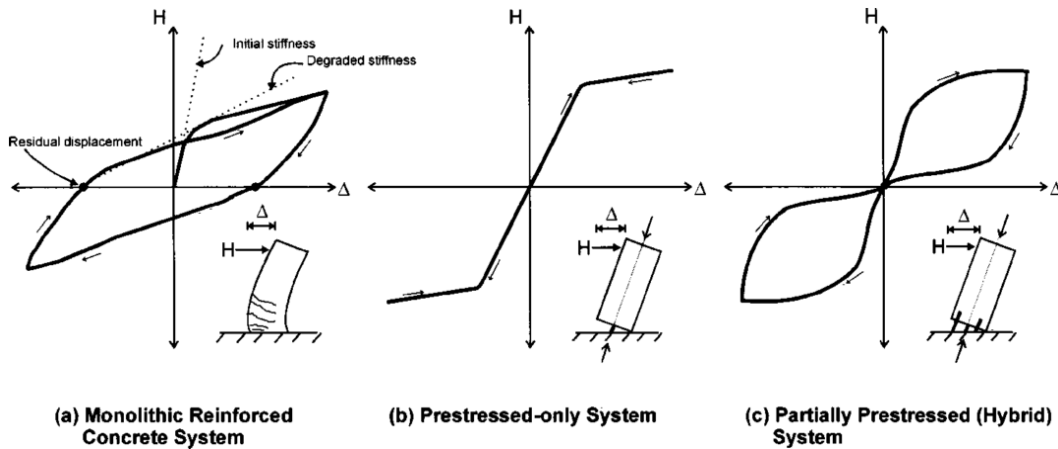


Figure 2.25. Cyclic response of reinforced concrete walls (Holden et al. 2003)

In terms of energy dissipation, the conventional, monolithically built wall showed superior energy dissipation properties, while the pre-stressed wall almost dissipates no energy. The partially pre-stressed wall, on the other hand, shows acceptable levels of energy dissipation with residual displacements and limited cracking altogether.

Schultz et al. (1998) conducted an experimental study on jointed precast shear walls (Fig. 2.26). The study included the testing of a precast post-tensioned shear wall under cyclic lateral load and overturning moment. As explained in the complementary study by Erkmen and Schultz (2009), the shear wall was post-tensioned by six bars with a diameter of 16 mm (#5). The post-tensioning bars had a strength of 1124 MPa and were stressed up to 60% of their strengths (695 MPa). As shown in Fig. 2.27, the hysteretic response of the specimen illustrated insignificant amounts of residual drift ratio upon the un-loading of the specimen. The origin-oriented hysteretic response of the specimen translates into high levels of self-centering and limited dissipating energy capacity of the shear wall. The available energy dissipation capacity of the specimen was sourced from the yielding of the post-tensioning bars.

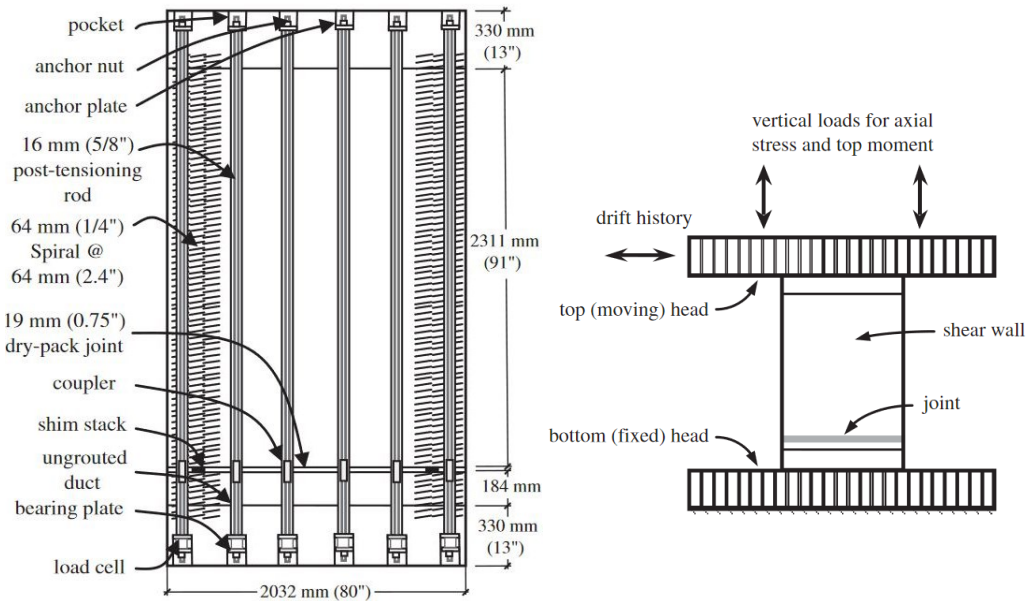


Figure 2.26. Test specimen (Schultz et al. 1998)

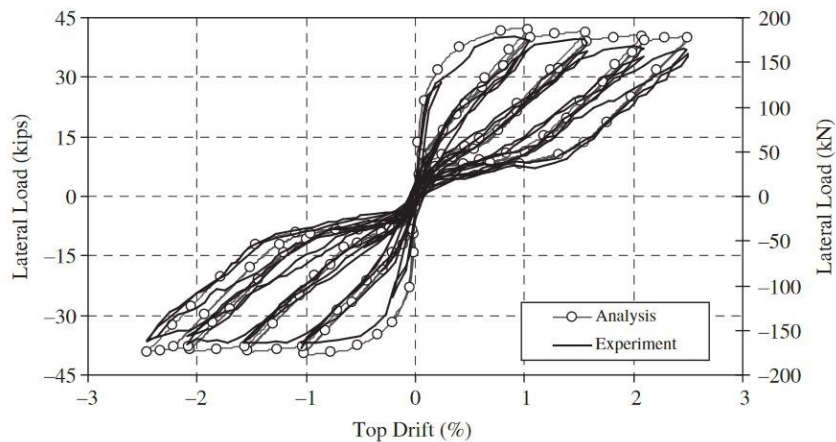


Figure 2.27. Hysteretic result (Schultz et al. 1998)

Holden et al. (Holden et al. 2003) also performed a study on the seismic performance of precast concrete shear walls. The study included testing two shear walls with identical geometries. The control specimen (unit 1) was a precast RC wall restrained rigidly to its foundation to emulate the response of a cast-in-place shear wall. The innovative specimen (unit 2) was a precast post-tensioned shear wall detailed with two CFRP tendons, and two bonded mild steel rebars, which served as energy dissipater. Also, steel fiber reinforced concrete was used instead of conventional concrete for damage mitigation purposes. The CFRP tendons had a peak strength of 2289 MPa

and an elastic modulus of 166 GPa. The energy dissipater rebars were two bonded 20 mm in diameter rebars milled down to a diameter of 16 mm over a length of 165 mm. The precast post-tensioned shear experiment is illustrated in Fig. 2.28.

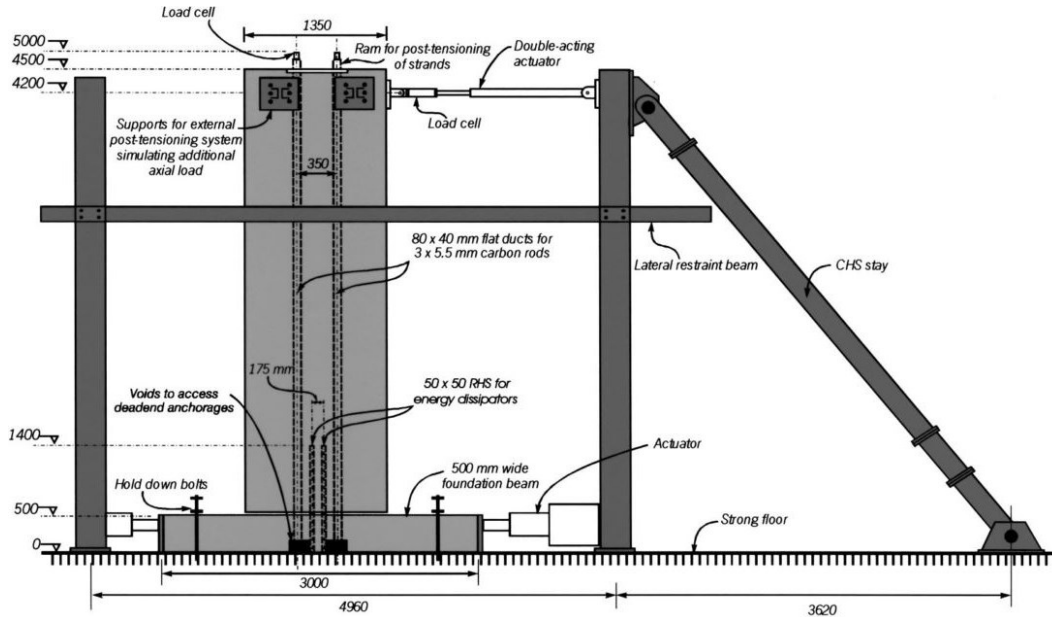


Figure 2.28. Post-tensioned specimen at test setup (Holden et al. 2003)

Figure 2.29 shows the hysteretic responses of the control and the innovative shear walls. As can be observed from the figure, the control specimen had wide cycles resulting in high energy dissipation and considerable residual drift ratios due to the reinforcement yielding. On the other hand, the innovative specimen featured narrow cycles, which translate into limited energy dissipation and small residual drift ratios.

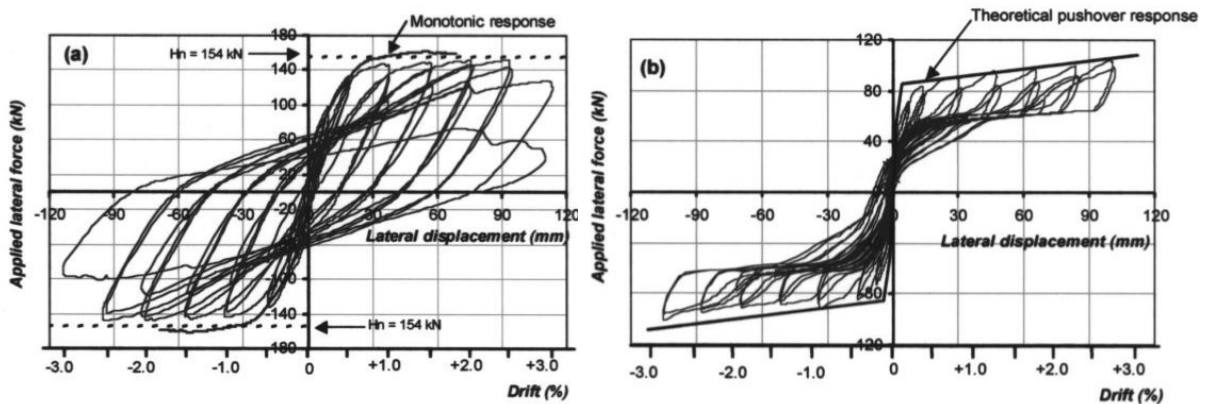


Figure 2.29. Hysteretic response of specimens (Holden et al. 2003)

Figure 2.30 shows the residual drift ratio of each specimen versus the peak drift. As it is seen, the innovative specimen had insignificant residual drift ratios in comparison to the control specimen.

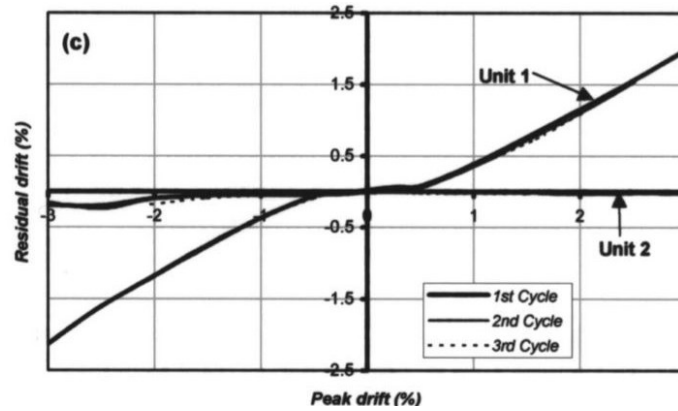


Figure 2.30. Residual drift of specimens (Holden et al. 2003)

Regarding energy dissipation capacity, Fig. 2.31(a) illustrates the equivalent viscous damping of the specimens during the test. As mentioned, the high residual drift ratio and energy dissipations of the control specimen were due to the yielding of vertical reinforcement. For the innovative wall, the only source of dissipating energy was the energy dissipater bonded rebars, which caused a limited amount of energy dissipation.

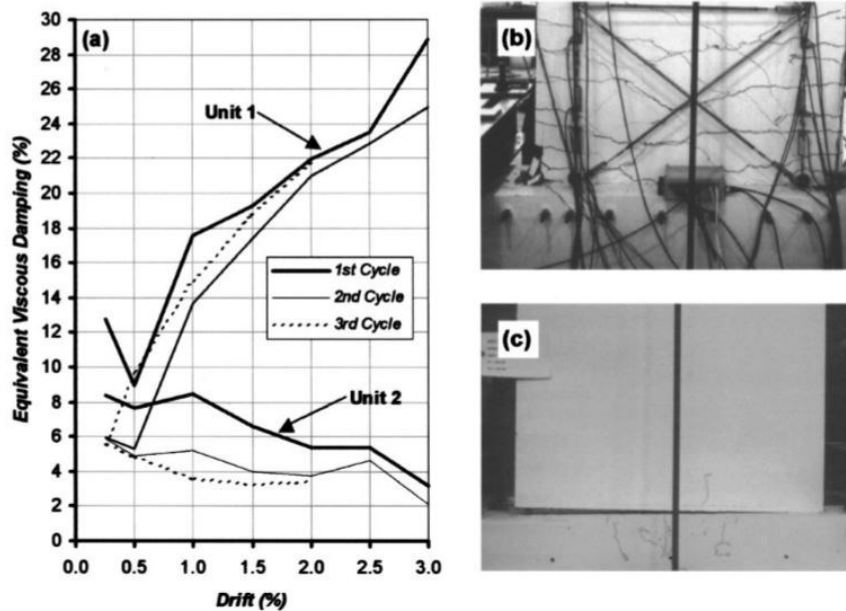


Figure 2.31. (a) Equivalent viscous damping of specimens, (b) cracking of unit 1 at drift ratio of 2.5%, (c) cracking of unit 2 at drift ratio of 3% (Holden et al. 2003)

Figure 2.31(b), (c) shows the damage that the control and the innovative specimens sustained at the drift ratios of 2.5% and 3%, respectively. It is apparent that the control specimen sustained extensive damage, including flexural and shear cracks accompanied by spalling. The innovative specimen, on the other hand, suffered no perceptible damage.

Kurama (2005) performed a study on seismic design of partially post-tensioned precast shear walls. The study numerically simulated the cyclic and seismic behavior of two similar six-story shear walls with bonded vertical reinforcement at the boundaries and unbonded post-tensioned bars in the middle. One of the shear walls termed PP6-BO is illustrated in Fig. 2.32.

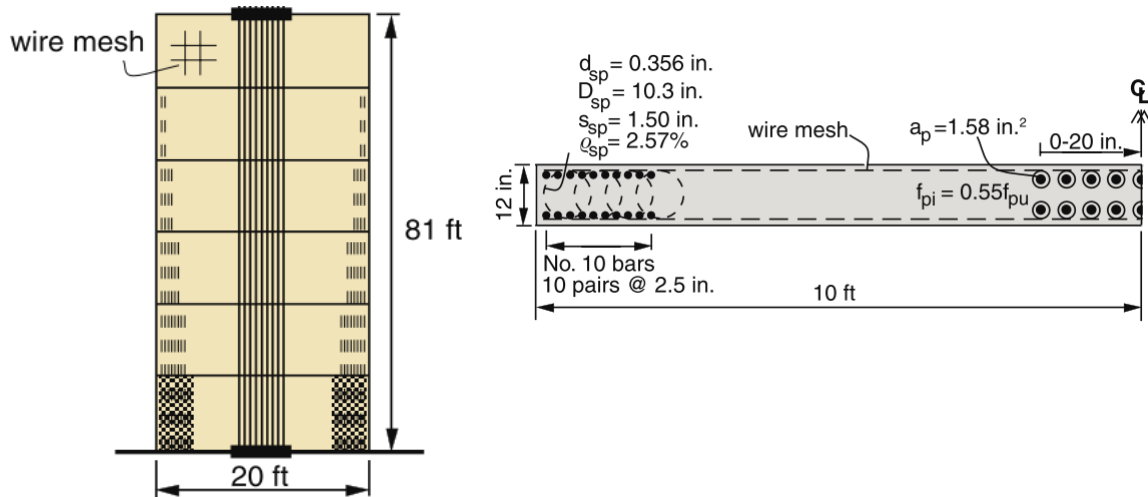


Figure 2.32. Shear wall PP6-BO scheme and cross-section (Kurama 2005)

The cyclic response of the specimens features significant self-centering and desirable energy dissipation levels (Fig. 2.33). Regarding the energy dissipation, as the mild steel bars started to yield (drift ratio of 0.3%), the relative dissipated energy of the shear wall surpassed 0.125%, which according to Ghosh et al. (2004) is the lower-bound for adequate energy dissipation. The energy dissipation capacity increased by up to 30% as the roof drift went on to the ratio of 2%. The study also showed that in comparison to monolithically built walls, partially post-tensioned shear walls require less amount of mild steel since the post-tensioning reinforcement and the post-tensioning forces participate in the stiffness and strength attainment of the walls.

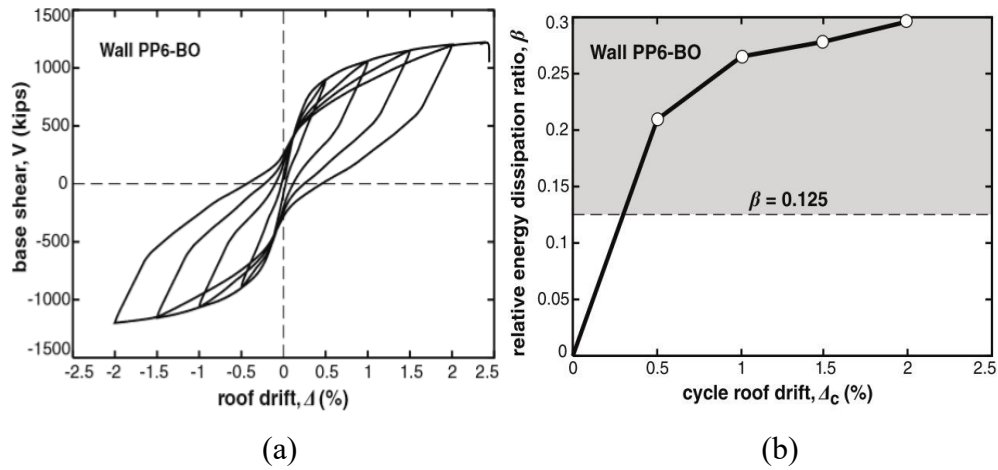


Figure 2.33. PP6-BO wall (a) hysteretic response, (b) relative energy dissipation ratio (Kurama 2005)

### 2.3.4 ECC Shear Walls

To the author's knowledge, the only available ECC shear wall experimental test in the literature is that performed by Nagai et al. (2002), which explored the shear strength of walls cast with ECC. The study included testing three cantilever ECC shear walls under displacement reversals while carrying a gravity load of 900 kN. The specimens were low-rise, with a height-to-width aspect ratio of 0.58, and designed to fail in shear, which is a brittle mode of failure. The wall panels were made of ECC, while the rest of the specimens was cast with normal concrete. The test studies the strength of the shear walls for different wall reinforcement ratios ( $\rho_{WS1}=0.43\%$ ,  $\rho_{WS2}=0.21\%$ ,  $\rho_{WS3}=0.64\%$ ), wall thicknesses ( $t_{WS1}=75$  mm,  $t_{WS2}=75$  mm,  $t_{WS3}=50$  mm) and the anchoring methods of horizontal reinforcing systems.

The shear force drift response of the specimens is shown in 2.34. The shear strengths of the specimen were determined and compared to the shear strengths of identical normal concrete shear walls. The comparison showed that the ECC walls featured 15% to 20% more shear strength than the concrete walls. Also, the ECC panels formed numerous fine cracks indicating the participation of ECC in resisting tensile stresses (Fig. 2.35).

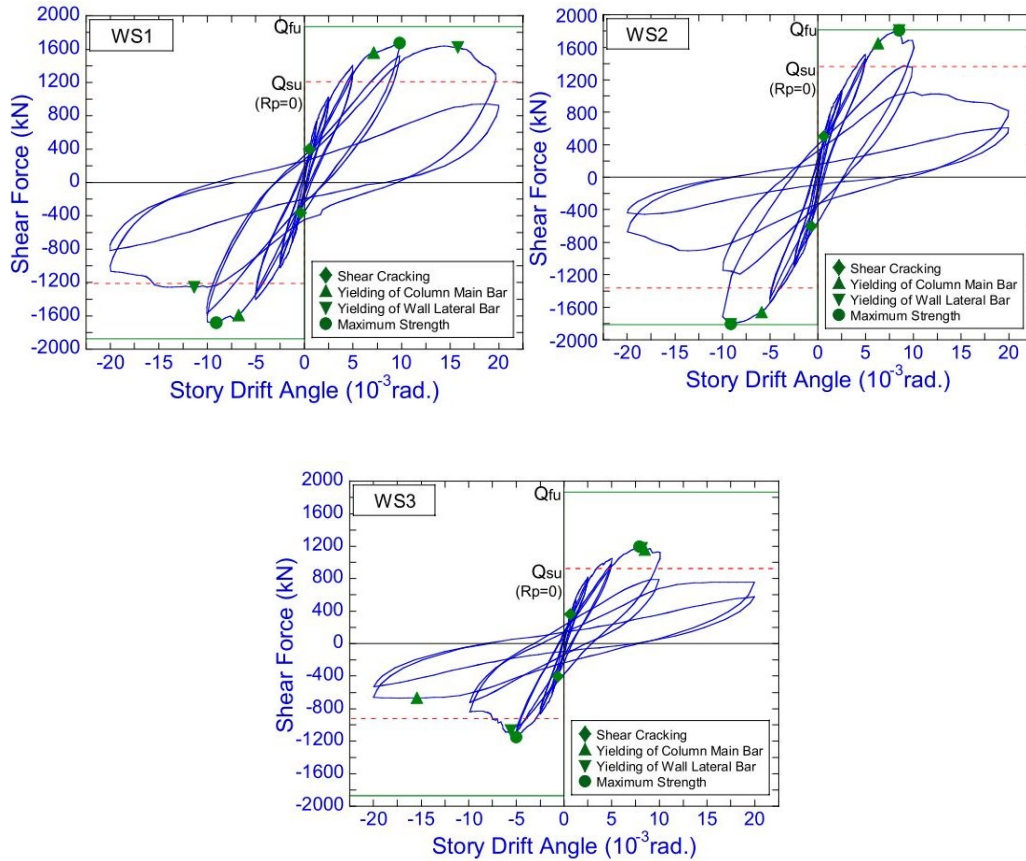


Figure 2.34. Hysteretic response of specimens (Nagai et al. 2002)

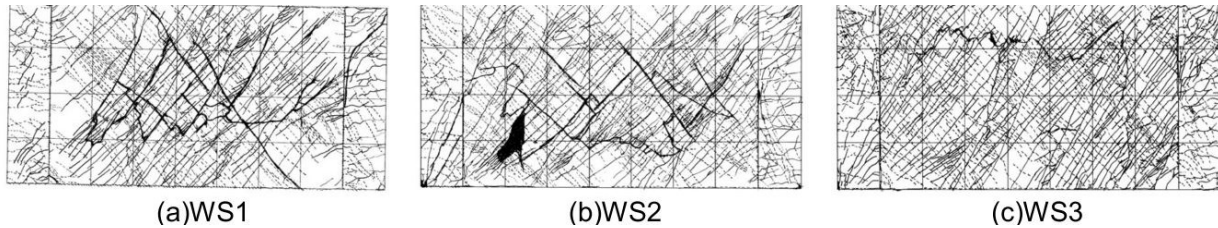


Figure 2.35. Cracking pattern of specimens (Nagai et al. 2002)

Also, Li et al. (2014) conducted an analytical study exploring the behavior of framed ECC shear walls. First, an analytical biaxial material model of ECC was developed in OpenSees. The stress-strain relationship of the material is shown in Fig. 2.36. Then the material model was used to simulated the response of two ECC shear walls identical to SW4 and SW13 reinforced concrete shear walls tests by Gao (1999). Regarding the RC specimens, SW4 had more reinforcement ratio and higher axial load ratio than SW13. The test results showed that SW4 had a brittle response,

while the behavior of specimen SW13 was more ductile (Gao 1999). The response of the RC and ECC walls is shown in Fig. 2.37.

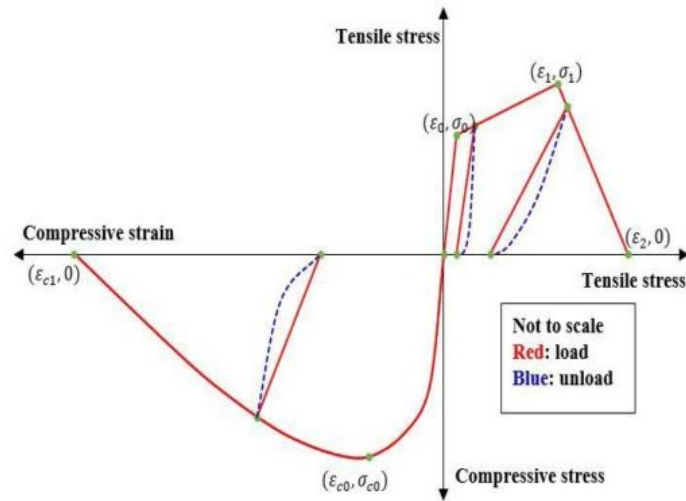


Figure 2.36. Stress-strain relationship for ECC (Li et al. 2014)

As illustrated in Fig. 2.37, using ECC instead of normal concrete increased the ductility of both shear walls. In addition, using ECC notably increased the levels of lateral load resistance and energy dissipation capacity of the walls as the ECC shear walls dissipated four times more energy was in respect to concrete walls.

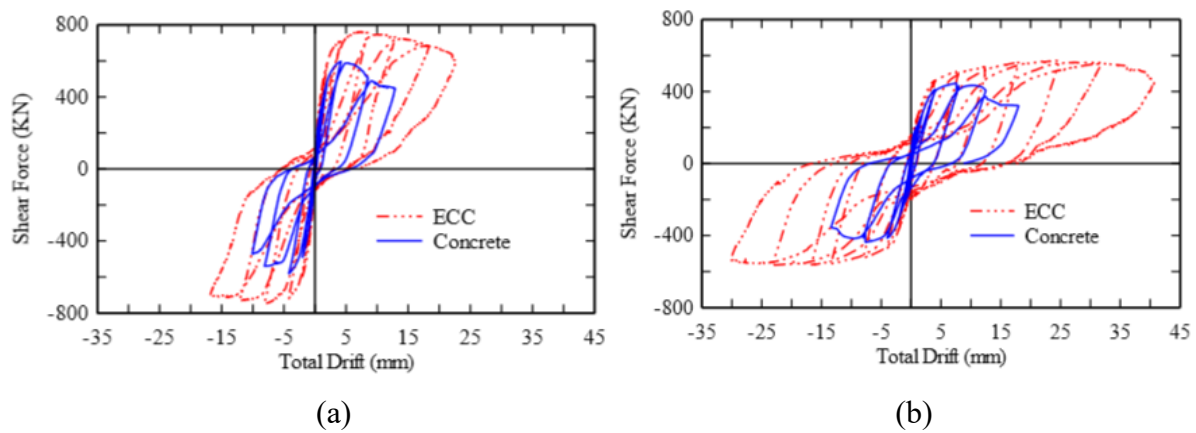


Figure 2.37. Cyclic behavior of (a) SW4 wall detailed with concrete and ECC, (b) SW13 wall detailed with concrete and ECC (Li et al. 2014)

### 2.3.5 SFRC Shear Walls

Athanasopoulou and Parra-montesinos (2014) investigated the seismic behavior of low-rise shear walls detailed with high-performance fiber reinforced concrete (HPFRC). The main objective of the study was to evaluate the performance of low-rise HPFRC shear walls with simplified reinforcement. The study included testing of nine large-scale cantilever reinforced concrete and HPFRC shear walls. The walls were tested under cyclic horizontal loading with zero applied loads axial. In terms of drift capacity, HPFRC walls demonstrated comparable performance than normal concrete walls even with their confining reinforcement being eliminated. In fact, the HPFRC walls with relaxed reinforcement details illustrated drift capacity of 2% to 3% under moderate shear reversals ( $6.5\sqrt{f'_c}$ ), while it was approximately 2.3% for RC walls. In terms of sustained damage, HPFRC also walls formed more cracks with smaller widths and sustained less spalling in comparison to RC specimens. Figure 2.38 shows the reinforcement layout of two specimens – one reinforced concrete and one reinforced SFRC – tested by Athanasopoulou and Parra-montesinos (2014). Figure 2.38(a) shows the reinforcement detailing of the RC specimen. Figure 2.38(b) as well shows the reinforcement detailing of the reinforced SFRC specimen, which is simplified with respect to the RC specimen.

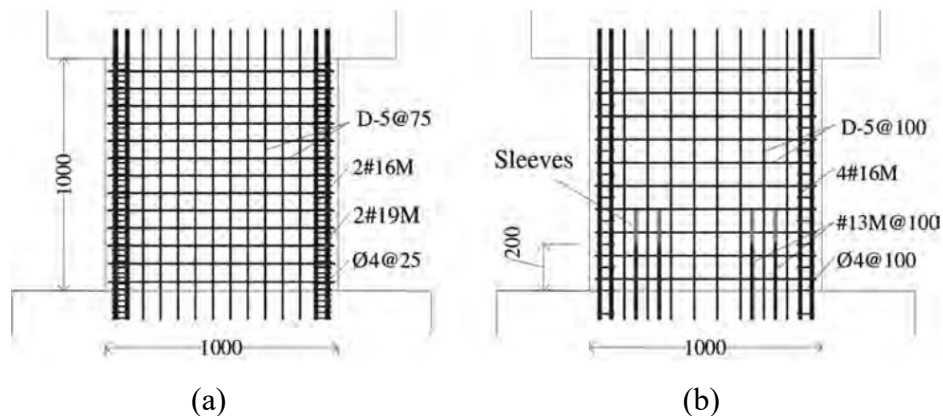


Figure 2.38. Reinforcement layout of specimens (a) detailed with concrete (b) detailed with SFRC (Athanasopoulou and Parra-montesinos 2014)

The hysteresis of the specimens is shown in Fig. 2.39. According to the figure, even though the SFRC wall had simplified reinforcement, both specimens showed comparable responses in terms of strength and drift capacity. The results also showed that the strength degradation in the SFRC

wall was less critical, as the wall sustained mitigated damage during the test. Figure 2.40 shows damage to the specimens at the end of the experiment. As it is clear from the figure, damage included spalling and matrix disintegration to the RC wall was severe, while the reinforced SFRC wall just formed several fine cracks.

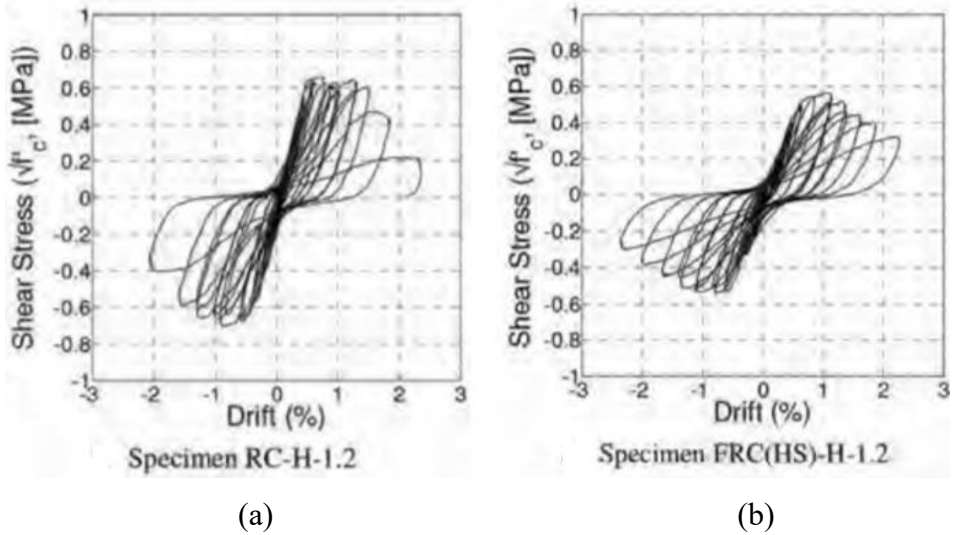


Figure 2.39. Hysteresis of (a) concrete wall, (b) SFRC wall (Athanasopoulou and Parra-montesinos 2014)

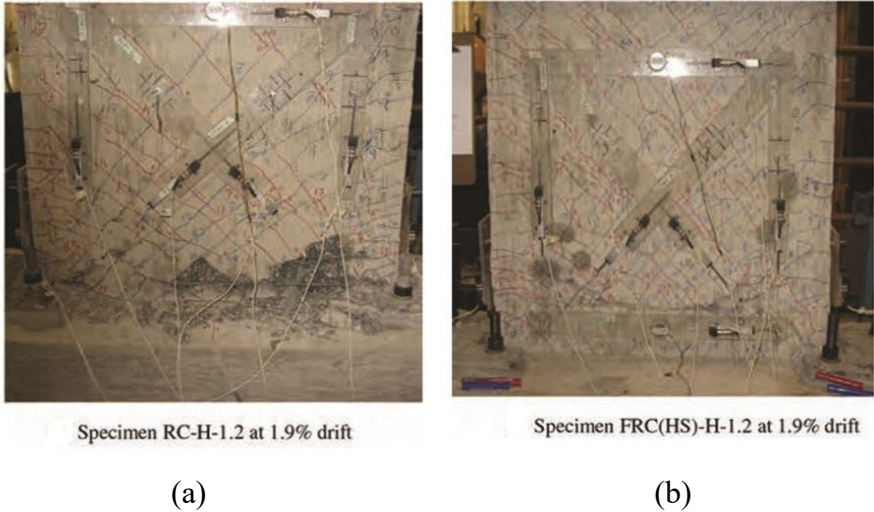


Figure 2.40. Damage to (a) concrete wall, (b) SFRC wall (Athanasopoulou and Parra-montesinos 2014)

## 2.3 Testing Methods

Several types of tests have been developed to investigate the performance of shear wall systems under static and dynamic loads. Since the type of testing influences the applicability of the obtained results and conclusions, it is convenient to review the most common test methods for shear walls briefly.

### 2.3.1 Shaking Table Testing

A shaking table is a computer-controlled system used for simulating earthquakes in laboratory settings. Shaking table systems can have up to six degrees of freedom, on which structural systems can be studied at the component- and system-levels. Testing structures on shaking tables provide the researchers with valuable data, including structure displacements, velocities, and accelerations at selected locations.

Figure 2.41 shows a full-scale, four-story RC structure tested by Nagae et al. (2015). The structure, which was designed to the most current US seismic design provisions, was subjected to North-South, East-West, and vertical components of JMA-Kobe and JR-Takatori records of 1995 Hyogoken-Nanbu earthquake. The input wave of the test was assigned to be a sequence of the JMA-Kobe records with scaling factors of 10, 25, 50, and 100% accompanied by JR-Takatori record scaled to 40 and 60%. During the test, the structure underwent lateral story drift ratios of 4% or higher. However, the structure satisfied the collapse prevention performance level, which is in line with the design objectives of current seismic codes. Figure 2.42 shows the hysteretic response of the structure under JMA-Kobe records with scaling factors of 25%, 50%, and 100%. According to the figure, the structure retained 2% of residual drift after deforming up to the drift ratio of 3%. Figure 2.43 shows the damage in the shear walls of the structure.

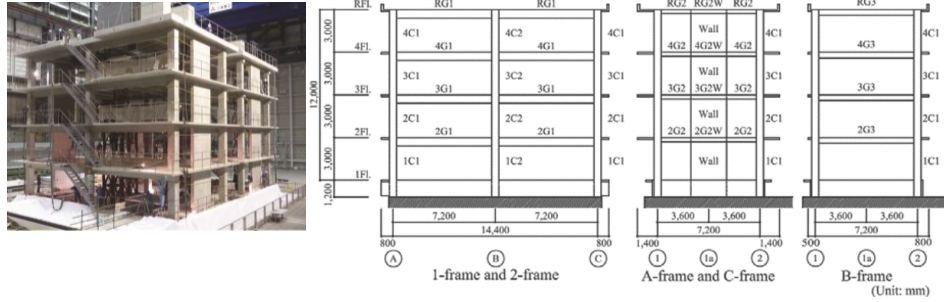


Figure 2.41. Seismic testing of a full-scale 4-story structure on shaking table (Nagae et al. 2015)

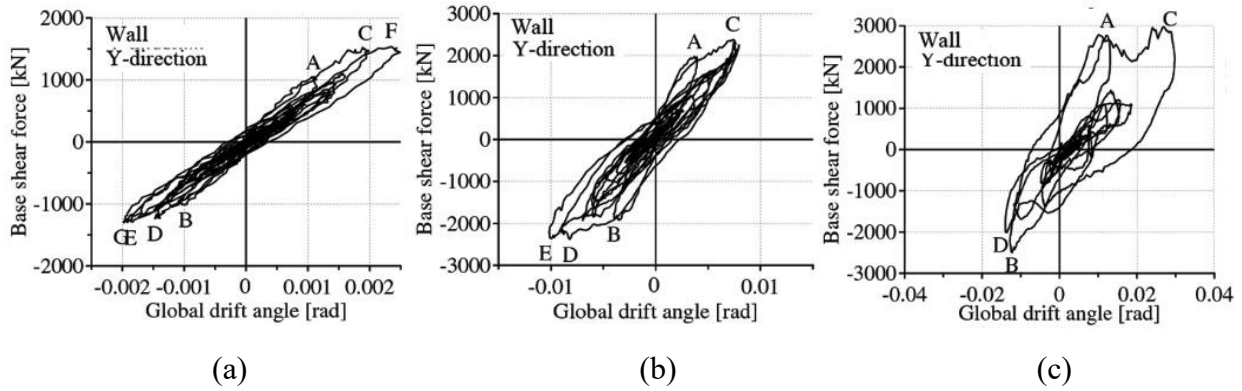


Figure 2.42. Hysteretic response of structure under JMA-Kobe record scaled to (a) 25%, (b) 50%, (c) 100% (Nagae et al. 2015)

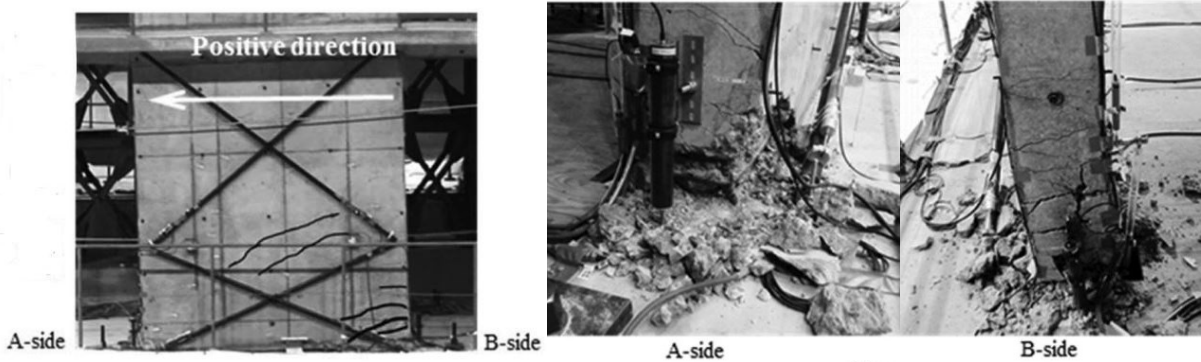


Figure 2.43. Damage in walls of structure (Nagae et al. 2015)

Martinelli and Filippou (2009) studied the performance of a full-scale, seven-story RC structure under a series of four earthquakes with increasing intensity. The test results indicated good agreement between the predicted and measured responses (Fig. 2.44) The structure was modeled in a two-dimensional space using beam-column elements with a fiber cross-section, and with considering the interaction between the axial force and bending moment. Also, the study pointed

out the limitations of fiber cross-section models, since fiber cross-section models were not able to accurately capture bond-slip properties in RC members.

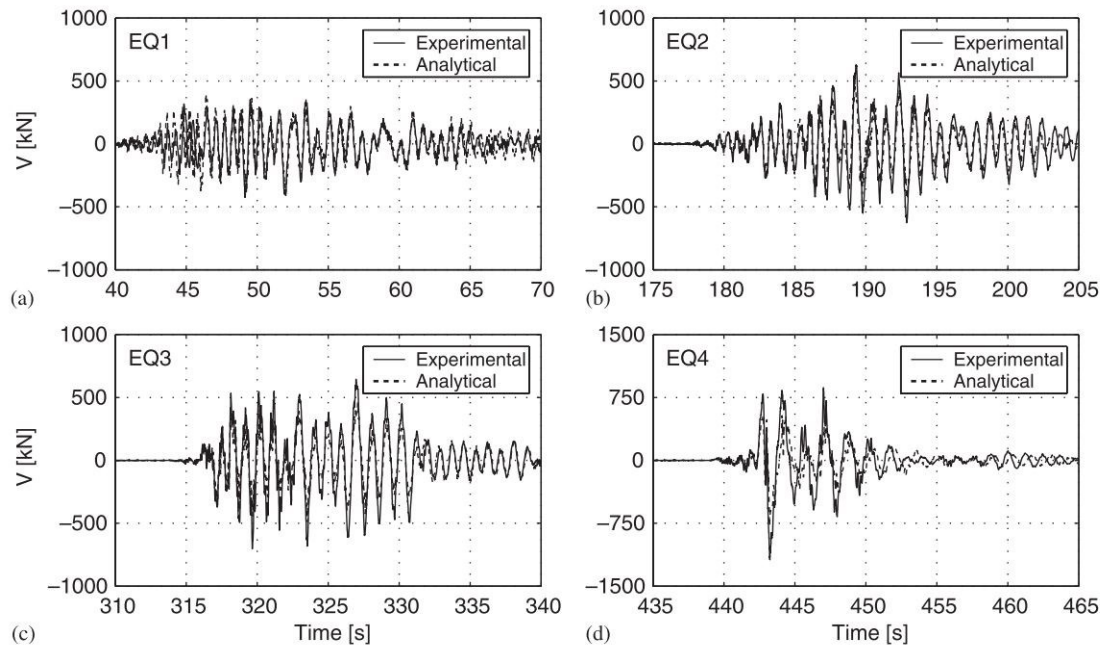


Figure 2.44. Experimental and analytical response history results of seven-story structure (Martinelli and Filippou 2009)

### 2.3.2 Hybrid Testing

Hybrid testing is a technique to test large scale structures under seismic loads in a cost-effective way as using hybrid methods eliminates the need for incorporating large masses into experimental setups. In this method, only structural elements with complex behavior are modeled physically, while the rest of the structure is modeled numerically using computer finite element programs. Figure 2.45 demonstrates the notion of the hybrid testing method in a study performed on a half-scale steel frame substructure to investigate the seismic performance and collapse mechanism of the structure (Del Carpio Ramos et al. 2014). The results were as well used in assessing the accuracy of computer programs in predicting the behavior of the frame as it collapsed.

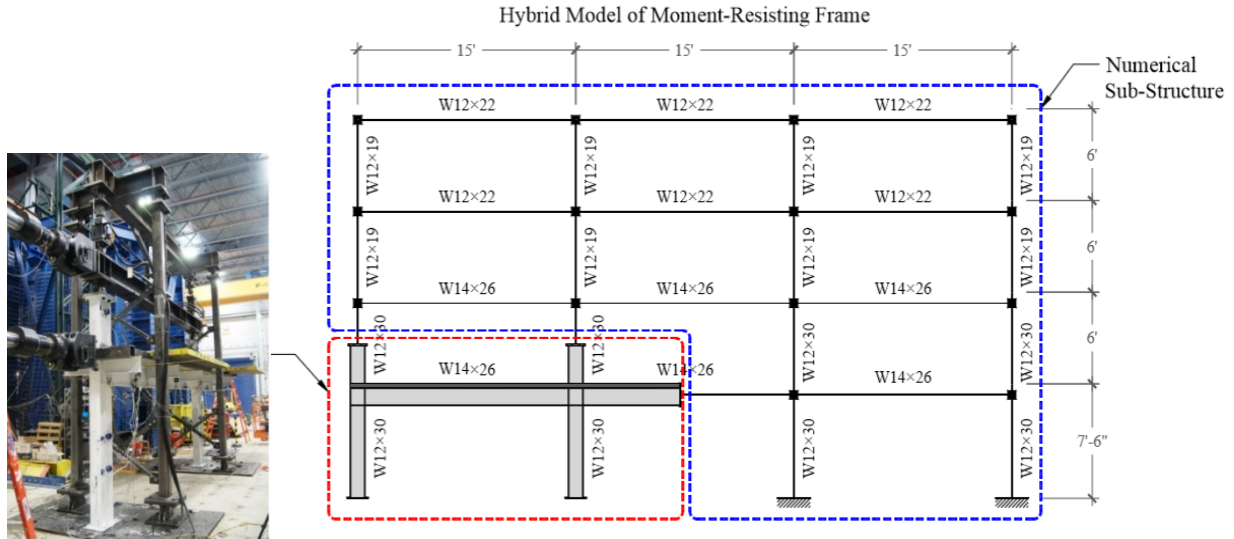


Figure 2.45. Hybrid testing of a frame structure (Del Carpio Ramos et al. 2014)

According to Whyte and Stojadinovic (2012), at each time step, earthquake load is applied to the finite element model of the structure. Then an integration method is used to solve the governing equation of motion of the structure (Eq. 2.1). The equation is solved for a target displacement, to which a set of computer-controlled hydraulic actuators move the desired substructure. Then, the reactions of the physical substructure are recorded and transmitted to the computer system to be used in the calculations for the next time step. Figure 2.46 demonstrates the process schematically.

$$[M][\ddot{U}] + [C][\dot{U}] + F([U]) = [M]r[\ddot{U}_g] \quad (2.1)$$

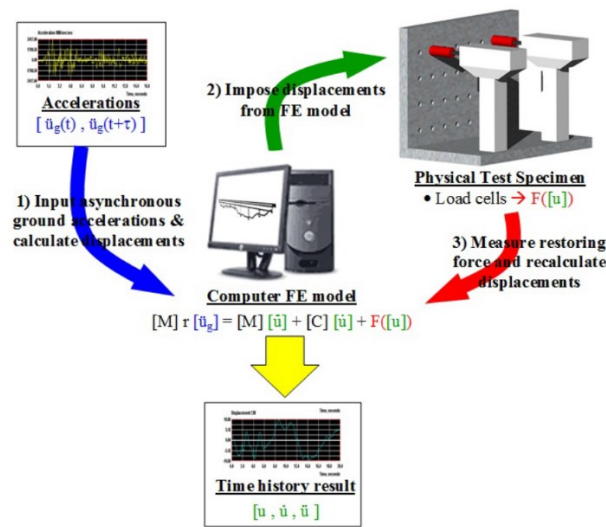


Figure 2.46. Hybrid testing method (Whyte and Stojadinovic 2012)

Regarding shear walls, Whyte and Stojadinovic (2012) simulated two identical thick, squat shear walls (Fig. 2.47). Since the walls were to be used in a sensitive structure, hybrid testing was used to obtain the seismic behavior of the walls under a series of earthquake excitations. The walls were 200 mm thick, 3000 mm long, and 1650 mm high. The reinforcement of the walls was distributed in two curtains with a ratio of 0.67 in both the horizontal and vertical directions. During the hybrid test, wall 1 was subjected to a series of earthquakes with an increasing intensity, which consisted of an operational basis earthquake (OBE), a design basis earthquake (DBE), a beyond design basis earthquake (BDBE), and finally a DBE aftershock. The wall 2 was subjected to an OBE, a BDBE, and two DBE aftershocks consecutively. OBE, DBE, and BDBE accelerograms were assigned as Kocaeli, Turkey earthquake record scaled to 0.05263, 0.1407, 0.4221. The seismic responses of the specimens during DBE and DBED are shown in Fig. 2.48.



Figure 2.47. Hybrid testing of a shear wall specimen (Whyte and Stojadinovic 2012)

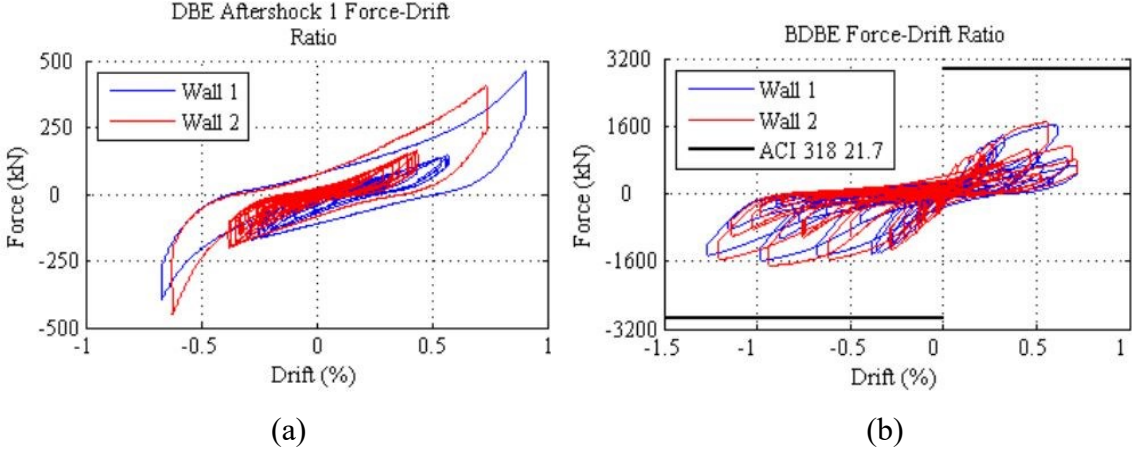


Figure 2.48. Response of specimens under (a) DBE aftershock 1, (b) BDBE records

### **2.3.3 Cyclic Testing**

The cyclic test is an alternative way to identify the characteristics of structural elements as well as to predict their seismic performance and long-term durability. In general, cyclic tests reveal the in-plane response of structural elements with the and out-of-plane displacements being restrained. The in-plane lateral loads are applied in a force-controlled fashion before yielding when the load steps can be chosen more conveniently. After yielding, the tests are usually continued in a displacement-controlled way. Depending on the used protocol, each cycle is repeated two or more times, while the amplitude of the cycles follows an ascending manner. Cyclic tests allow for the identification of properties such as yield displacement, ultimate displacement, stiffness, strength, residual displacements, hysteretic behavior, and energy dissipation capacity of a structural member. Regarding dynamic effects, the influence of the strain rate on the strength and stiffness of both concrete and steel cannot be captured in a quasi-static test; however, those effects can be approximated through empirical relationships available in the literature (Driver et al. 1998).

#### **2.3.3.1 General considerations**

Due to the limitations and constraints of available resources, often, it is not possible to experimentally study the behavior of an entire shear wall building. The alternative is to investigate a single wall or a portion of it, sometimes including the effects of the connections to other structural elements, such as slabs and beams, through suitable boundary conditions. Applied loads such as gravity and lateral loads are simulated with actuators and appropriate fixtures, and base fixity is commonly simulated using foundation blocks bolted to heavily reinforced slabs.

If only a portion of a shear wall structure can be studied, it is convenient to select the segment of the wall that exhibits more clearly the structural behavior under study. For instance, in a cantilevered, slender wall dominated by flexural behavior, the bottom of the wall will be a critical region since the plastic hinge will develop there. Choosing the bottom of the wall as a testing specimen will allow a comprehensive investigation of the nonlinear response of the steel and concrete materials, their damaged state, and associated failure modes. Evidently, the test setup should include the effects of the upper wall segment, such as gravity loads and moments at the top of the specimen.

Most RC shear wall tests such are conducted under fixed-free (single-curvature) boundary conditions, while a very few (Hidalgo et al. 2002) are tested under fixed-fixed conditions (double-curvature), as shown in Fig. 2.49. Single-curvature tests are appropriate to investigate the flexural and flexural-shear responses, while double-curvature setups are suitable for the study of shear-critical structures.

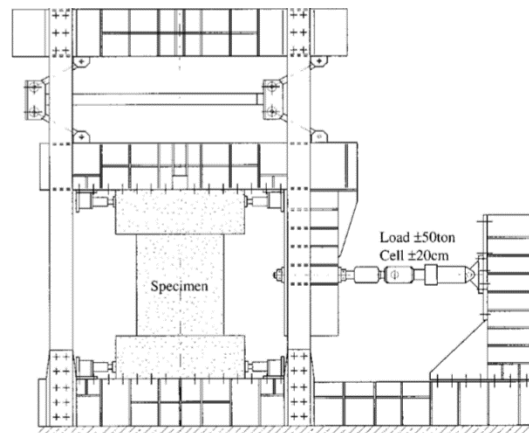


Figure 2.49. Test setup used in (Hidalgo et al. 2002) to study shear failure of shear walls

To determine what type of test is most appropriate for the study of the innovative shear walls investigated in this project, it is convenient to describe the mechanics of RC buildings under lateral loads briefly. Frame structures generally exhibit shear inter-story deformations, characterized by double-curvature bending in the columns between stories. In contrast, buildings that incorporate shear walls as a primary load resisting system develop mostly flexural deformations, with a plastic hinge region forming along the lower stories. This behavior is similar to that of a cantilevered element to a great extent. For this reason, fixed-free boundary conditions are often used to investigate the flexural response of shear walls, which is the scope of this study. It is noted that depending on the distribution of mass and stiffness in the building, and the interaction between shear walls and the companion frame system, it is possible that the behavior of a building with shear walls deviates from that described above.

### 2.3.3.2 Axial Load

Another important aspect of the experimental testing of shear walls is the level of axial load applied to the specimens. A review of the literature shows that the level of axial load used in wall tests falls in one of the following three categories: zero, low (below  $0.2A_gf'_c$ ), or high (ranging between  $0.25-0.5A_gf'_c$ ) (Su and Wong 2007). Axial loads in shear wall tests are often applied through actuators exerting a downward force at the top of the specimen or through post-tensioned bars installed between the loading beam at the top of the wall and the rigid foundation (Fig. 2.50). The issue with post-tensioned bars is that they tend to provide restoring forces that return the specimen to its original position. Using pinned-pinned hydraulic jacks at the top is more appropriate for applying gravity forces since no restoring forces are created.

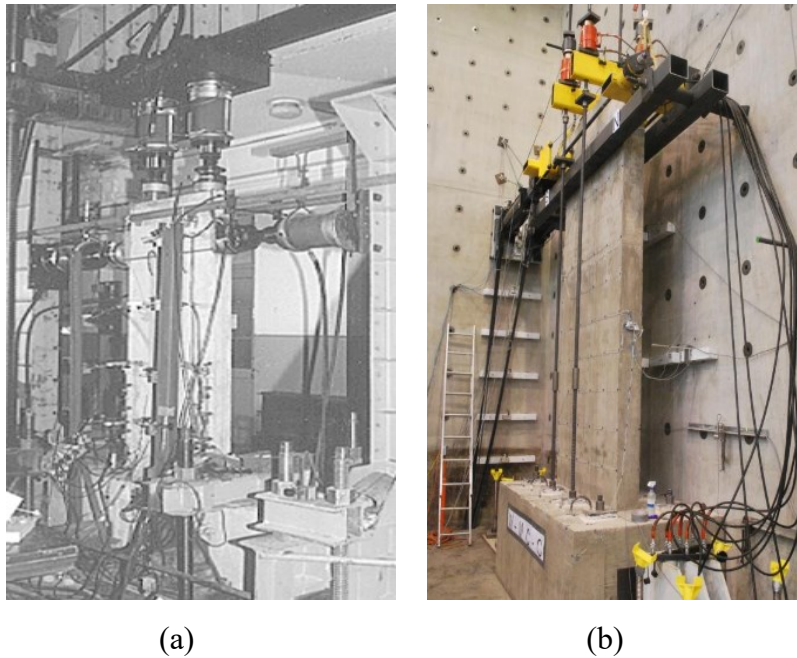


Figure 2.50. Applying axial force with (a) hydraulic actuators (Zhang and Wang 2000), (b) post-tensioning rods (Escolano-Margarit et al. 2012)

Generally, in RC elements, the presence of axial loads increases flexural capacity and stiffness, but it reduces ductility by causing early crushing of the concrete at the compressive region. Second-order effects also are produced by axial loads on laterally deformed structural elements, imposing additional deformations and forces. Depending on its value, the presence of an axial load can increase the shear capacity of concrete elements as they tend to close existing cracks and can

increase the shear forces needed to cause cracks. Crack closure also promotes self-centering of the laterally loaded RC elements upon un-loading. If the axial load is high (i.e., greater than  $0.4A_gf'_c$ ), there will be a reduction in the flexural strength and surely ductility due to the early crushing at the toes of the shear wall, while the longitudinal reinforcement in tension may not yield in tension.

Shear walls carry different levels of axial loads depending on the type of structure, building height, distribution of walls on the plan floor, etc. Gravity loads in the walls of low-rise buildings are usually small, and tests on this type of structure are often conducted with no axial load. However, the axial loads in high-rise buildings located in non-seismic areas can be as high as  $0.6A_gf'_c$  (Zhang and Wang 2000). As explained above, these walls would fail at much lower ductility ratios in contrast to the walls with low or without axial loads. The failure modes of these shear walls are either toe crushing or out-of-plane buckling. Figure 2.51 presents the cyclic response and failure mode of two shear wall specimens with identical dimensions and vertical reinforcement layouts while carrying different axial load ratios (ALR) of 25% and 50%. As the ALR doubled from 25% to 50%, the lateral strength increased marginally, but the ductility was substantially declined. The wall with higher ALR fails in a brittle way without of plane buckling instead of toe crushing.

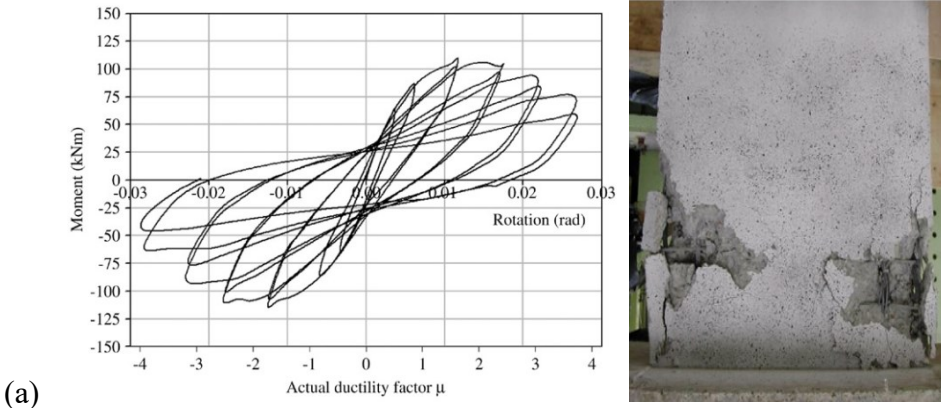


Figure. 2.51. Cyclic response and failure mode of two shear walls with axial load ratios (a) of 25%, (b) 50%. (Su and Wong 2007) continued

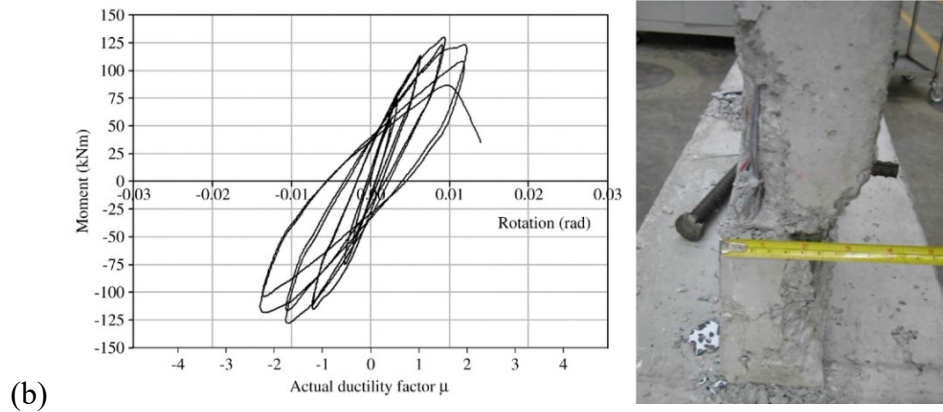


Figure. 2.51. Cyclic response and failure mode of two shear walls with axial load ratios (a) of 25%, (b) 50%. (Su and Wong 2007)

Therefore, tests that do not include the presence of axial loads cannot account for the ductility reduction, second-order effects, or out-of-plane buckling failure modes. On the other hand, the absence of axial loads permits the independent evaluation and assessment of the self-centering capacity provided by the innovative reinforcement schemes investigated in this study. Research has shown that the effects of axial load can be included through analytical means, such as the finite-element analysis (Maciel et al. 2016).

## 2.4 Conclusion

As discussed above, innovative materials are used in different structural elements to mitigate damage in the elements and improve their performance under cyclic and seismic loads. However, it seems that researchers usually focus on improving one damage indicator, such as permanent drift ratio or concrete damage, while overlooking the other. This research project employs both fiber-reinforced cementitious composites and self-centering reinforcement to reduce concrete damage and increase self-centering properties in RC shear walls.

## **CHAPTER 3 REINFORCED CONCRETE SHEAR WALLS DETAILED WITH INNOVATIVE MATERIALS: PERFORMANCE**

### **3.1 Abstract**

This chapter presents the experimental results of a pilot study performed on the seismic performance of three types of damage-resistant, slender reinforced concrete (RC) shear walls. The study explored three innovative schemes for the mitigation of post-earthquake damage, including permanent lateral deformation and concrete damage, in RC shear walls. Each innovative shear wall had an aspect ratio of 2.0 and was reinforced with a hybrid reinforcing system consisting of mild steel and a type of self-centering reinforcement such as shape memory alloy bars, glass fiber reinforced polymer bars, or high-strength steel strands. To mitigate concrete damage, the walls were detailed with fiber-reinforced cementitious composites, either engineered cementitious composite or steel fiber reinforced concrete. The specimens were supported as cantilevers and then were tested up to failure under pseudo-static, cyclic loads. As test results showed, the innovative shear walls had smaller residual drift ratios and mitigated damage compared to a conventional RC shear wall. The innovative walls also showed significant levels of energy dissipation and ductility throughout testing.

### **3.2 Introduction**

According to seismic rehabilitation guidelines for buildings, e.g., FEMA 273 (1997) and FEMA 356 (2000), the performance level of a structural element such as an reinforced concrete (RC) shear wall can be assessed with two indicators: a) the amount of permanent and transient drift ratios of the element, b) the extent of damage, such as crack width, concrete crushing, and reinforcement buckling sustained by the element. To enhance the seismic performance of RC structures, these damage indicators must be reduced. One option is to overcome the limitations of current RC structures by using innovative details and materials, which offer higher performances and damage resilience properties.

Recent studies undertaken by Saiidi and Wang (2006), Saiidi et al. (2009), and Cruz Noguez et al. (2012) demonstrated that detailing the plastic hinge region of a bridge pier with shape-memory

alloy (SMA) bars and engineered cementitious composite (ECC) will enhance the seismic performance of the structural element by reducing permanent deformations and mitigating concrete damage. Partially post-tensioning of bridge piers was also another innovative scheme studied by Sakai and Mahin (2004), and Cruz Noguez et al. (2012). The studies illustrated the superior efficiency of the scheme in reducing permanent deformations through comparison with piers with no post-tensioning. However, it was shown by the latter study that post-tensioned piers can sustain substantial damage within their plastic hinge zones.

In regard to building structures, Alam et al. (2009, 2012) explored the seismic performance of RC frame structures detailed with SMA bars within their plastic hinge locations. The studies showed that innovative frames reinforced with SMA could effectively recover their lateral drift ratios. Abdulridha and Palermo (2014) studied the cyclic response of a slender steel RC shear wall detailed with SMA bars within its plastic hinge region. Test results showed that despite suffering serious damage along its plastic hinge region, the steel-SMA reinforced shear wall had a substantial self-centering characteristic.

Mohamed et al. (2014) studied the seismic behavior of three concrete shear walls reinforced with glass fiber reinforced polymer (GFRP) bars. The walls were similar in the reinforcement ratio but different in length and aspect ratio. As test results showed, the GFRP reinforced walls reached satisfactory levels of deformability, substantial self-centering, and improved resilience in terms of cover spalling while avoiding brittle modes of failure. On the other hand, the fully GFRP reinforced walls had insignificant levels of energy dissipation in comparison to a control RC shear wall due to the linear elastic behavior of their GFRP bars.

Holden et al. (2003) studied the seismic performance of a precast steel fiber reinforced concrete (SFRC) shear wall detailed with two post-tensioned tendons and two energy dissipater bars. The precast wall showed significant self-centering and damage resilience due to its rocking motion. Nevertheless, the specimen had insignificant levels of energy dissipation due to the absence of continuously bonded rebars across the joint of the shear wall.

This chapter illustrates the results of an exploratory investigation with the general objective of improving the seismic performance of slender RC shear walls. Given the fact that each of the

mentioned studies was focused on one part of the solution, this study was aimed to improve the overall performance of RC shear walls by reducing permanent drift ratio and concrete damage in RC shear walls while providing the walls with significant levels of ductility and energy dissipation.

In this chapter, the responses of three innovative shear walls with identical geometries, boundary conditions, and loading protocols, but different innovative materials and details, are investigated. Then, the improvement in the seismic performance of each innovative wall over a conventional RC shear wall is discussed in terms of a decrease in the amount of two key damage indicators: concrete damage and residual drift ratios. The innovative shear walls were reinforced with mild steel rebars and self-centering reinforcements such as SMA bars, GFRP bars, and high-strength steel strands. The shear walls were also detailed with a type of fiber-reinforced cementitious composite (FRCC) for being more damage resilient. In the following sections, the obtained test results are discussed in terms of hysteretic response, ductility, damage propagation, self-centering, and energy dissipation in the innovative shear walls and a control RC shear wall.

### **3.3 Experimental Program**

#### **3.3.1 Material Properties**

The materials used in this study can be classified into two categories – reinforcing materials and cementitious materials. 10M mild steel bars, #5 GFRP bars, #4 NiTi bars (SMA bars), and high-strength seven-wire steel strands with a diameter of 13 mm were the various types of reinforcement used in the construction of shear walls. The tensile stress-strain relationship of each type of reinforcement is illustrated in Fig. 3.1. The stress calculations of the reinforcements were performed using the nominal diameter and cross-sectional area of each type of reinforcement, which is summarized in Table 3.1.

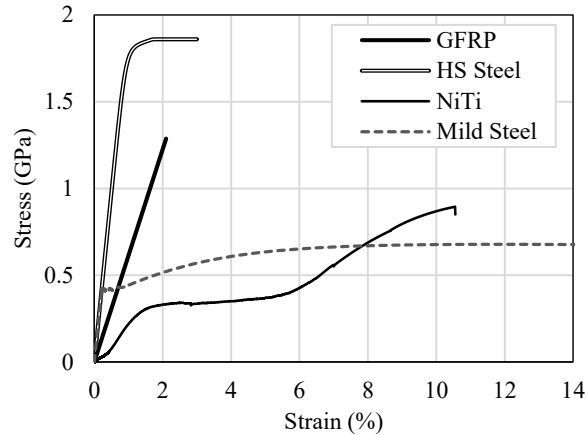


Figure 3.1. Tensile stress-strain relationships of various types of concrete reinforcement

Table 3.1. Mechanical properties of self-centering reinforcements

Self-centering Reinforcement	Size	Elastic Modulus (GPa)	Nominal Diameter (mm)	Nominal Area (mm <sup>2</sup> )	Yield Strength (MPa)	Ultimate Strength (MPa)
GFRP	#5	62.6	15.9 <sup>a</sup>	199 <sup>a</sup>	N.A.	1150
HS steel	13 mm	195	12.7	98.7	1670	1860
NiTi	#4	27.4	12.7	127	330	890

<sup>a</sup> Effective diameter and cross-sectional area (including coating) are 17.3 mm and 235 mm<sup>2</sup>

(according to the manufacturer)

In addition, the effective diameter and cross-sectional area (including coating) of #5 GFRP bars are shown in Table 3.1. As can be seen, the effective diameter and area of #5 GFRP bars were larger than the nominal diameter and area of the bars due to the fact that the GFRP bars were sand coated. For this reason, the stress resistance properties of #5 GFRP bars were associated with their nominal area rather than their effective area as the coating of the bars does not effectively participate in the resistance of tensile stresses. According to the manufacturer, #5 GFRP bars had an elastic behavior with an ultimate strain of 2.1%, and ultimate stress of 1150 MPa and a stiffness value of 62.6 GPa.

In the case of #4 NiTi bars, mechanical properties of a 500 mm long #4 NiTi coupon specimen were determined in accordance with ASTM F2516-14 (2014). The NiTi bar had an elastic behavior up to about a strain of 1.0%, which was corresponding to an elastic modulus of 27.4 GPa. Then, the bar exhibited a stress plateau up to a strain of 6% with an upper plateau strength (UPS) of 330 MPa, and a lower plateau strength (LPS) of 120 MPa (Fig. 3.2). For strain values of 6% or smaller, the NiTi bar recovered its elongations upon unloading (super-elasticity). However, beyond a 6% strain, the bar showed strain hardening and started to retain residual strains after unloading. The tensile strain capacity of the NiTi bar was 10.5%, which was corresponding to a stress capacity of 890 MPa.

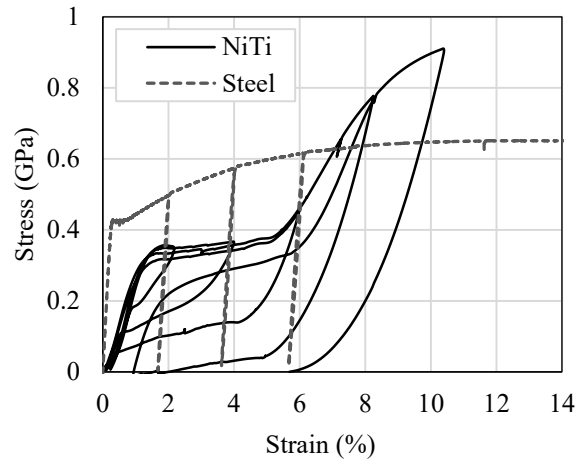


Figure 3.2. Cyclic stress-strain relationship of a #4 NiTi bar and a 10M steel bar

The used high-strength steel strands had yield and ultimate stress values of 1670 MPa and 1860 MPa, and a stiffness value of 195 GPa, according to the manufacturer. In the case of mild steel bars, Table 3.2 shows the average properties of the 10M and 15M steel rebars used in the construction of each specimen – CW (control wall), GFRP-ECC, PPT-SFRC, and SMA-SFRC. The properties of the mild steel rebars were determined through the testing of three 500 mm long coupon specimens for each group of reinforcement, according to annex A9 of ASTM A370-14 (2014).

Table 3.2. Mechanical properties of mild steel reinforcement

Specimen	Size	Elastic	Yield	Ultimate
		Modulus (GPa)	Strength (MPa)	Strength (MPa)
CW	10M <sup>a</sup>	184	421	634
GFRP-ECC	10M	173	415	626
PPT-SFRC	10M	173	415	626
SMA-SFRC	10M	184	421	634
SMA-SFRC	15M <sup>b</sup>	191	439	617

<sup>a</sup> Nominal diameter and cross-sectional area are 11.3 mm and 100 mm<sup>2</sup>

<sup>b</sup> Nominal diameter and cross-sectional area are 16.0 mm and 200 mm<sup>2</sup>

The cementitious materials consisted of conventional concrete, ECC, and SFRC. The fiber volume fractions of the materials were 0%, 2%, and 0.75%, respectively. The fibers used in ECC are made of PVA (polyvinyl alcohol) with a length of 12 mm, a minimum aspect ratio of 300, and a minimum tensile strength of 1000 MPa (Choi and Lee 2015). According to the manufacturer, the steel fibers used in the SFRC material were hooked-end with a length of 50 mm, an aspect ratio of 55, and a tensile strength of 1200 MPa.

The compressive strengths of the cementitious materials were determined based on ASTM C39-15a (2015). The average compressive strengths of the concrete, ECC, and two SFRC mixes used in the construction of CW, GFRP-ECC, PPT-SFRC, and SMA-SFRC shear walls were 48 MPa, 38 MPa, 62 MPa, and 51 MPa respectively. In terms of post-peak response, fiber-reinforced materials exhibited improved compressive strain capacities, as can be seen in Fig. 3.3.

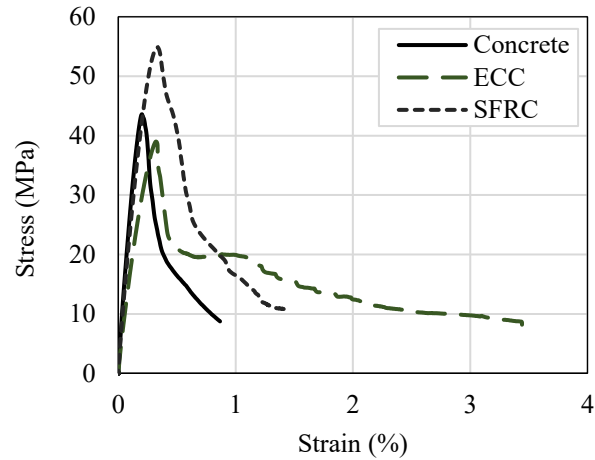


Figure 3.3. Compressive stress-strain relationships of cementitious materials

The tensile properties of FRCC materials were determined through direct tension tests in case of ECC and four-point loading tests for SFRC materials. Figure 3.4 shows the tensile stress-strain relationships of three ECC prism specimens. Each specimen had a linear tensile stress-strain response followed by a plateau, and then a descending segment. The average tensile stress and strain capacities of the specimens were 3.11 MPa and 0.95%, respectively. In contrast, the stress-strain relationship of plain concrete only consists of a linear segment since the material rapidly loses its tensile stress resistance with the formation and propagation of cracks.

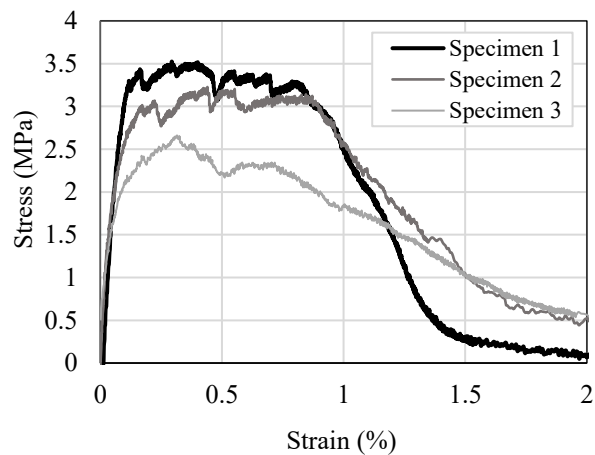


Figure 3.4. Tensile stress-strain relationships of three ECC prism specimens corresponding to GFRP-ECC wall

To identify the tensile properties of SFRC, fib (2013) recommends the testing of SFRC notched beams under four-point loading tests. The method of testing implies that tensile behavior in SFRC

is more influenced by crack opening rather than uniform cracking as it is in ECC. A four-point loading test identifies the relationship between tensile stress and crack mouth opening displacement (CMOD) in an SFRC beam. Figure 3.5 illustrates the relationship between tensile stress and CMOD in three SFRC beams corresponding to the PPT-SFRC wall. At first, the tensile stress of each specimen increased linearly by the increase in the amount of CMOD. However, the relationship became nonlinear with the propagation of a crack formed at the notch location of each specimen. Finally, the strength of beam specimens started to decrease with the further propagation of cracks. In contrast to SFRC, tensile stresses in a conventional concrete specimen sharply decrease after the linear rise of tensile stress with CMOD when the formed cracks open (fib 2013).

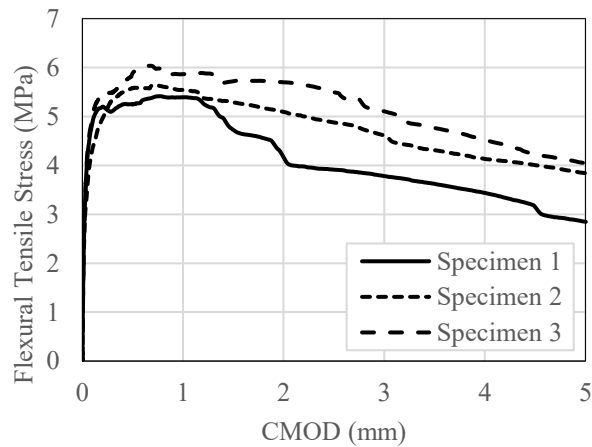


Figure 3.5. Flexural tensile stress-CMOD relationships of three SFRC notched beam specimens corresponding to PPT-SFRC wall

According to fib (2013), the post cracking behavior of SFRC can be assessed through the flexural tensile stress of notched beams at CMODs of 0.5 mm and 2.5 mm. The average flexural tensile stress of SFRC beams associated with the PPT-SFRC wall was calculated as 5.55 MPa at a CMOD of 0.5 mm and 4.75 MPa at 2.5 mm CMOD, while the forgoing stresses were 3.50 MPa and 3.88 MPa respectively regarding SMA-SFRC wall.

### 3.3.2 Test Specimens

Four RC shear walls consisting of one conventional wall and three innovative walls were constructed and tested under cyclic displacement reversals up to failure. Each specimen consisted of three segments, a foundation, a wall panel, and a cap-beam, which were cast monolithically.

The walls were slender with an aspect ratio, shear span to length, of 2.0 (Fig. 3.6). The baseline specimen of this study was a conventional steel-reinforced concrete shear wall, which was termed the control wall (CW). The control wall and the innovative walls were designed to satisfy the seismic provisions for reinforced concrete structures in North America, CSA A23.3-14 (2014), and ACI 318-14 (2014). Since these standards do not fully cover the application of innovative materials in reinforced concrete structures, appropriate codes of practice, including CSA S806-12 (2012) and CPCI (2007), were used accordingly.

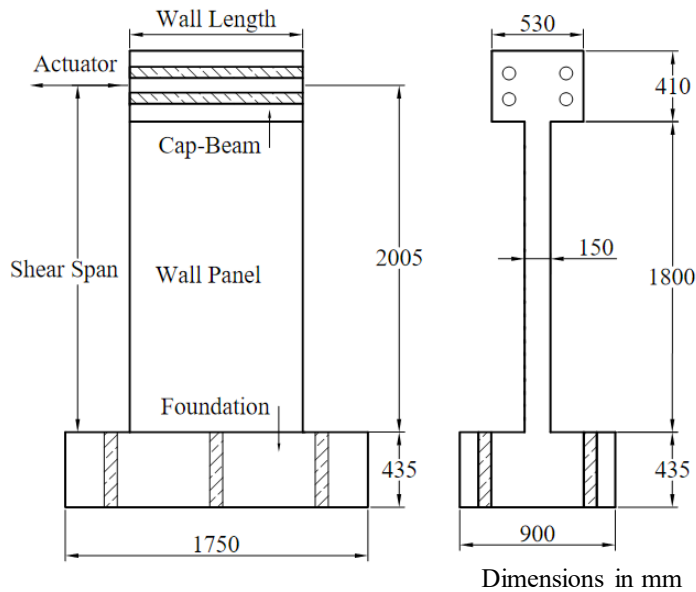


Figure 3.6. Geometry of shear wall specimens

The reinforcement layout of the control wall was selected in a way to be comparable to those of shear walls tested by Abdulridha and Palermo (2014). However, the required modifications were made in the reinforcement layout of the wall according to the design specification of the innovative specimens of this study. The control wall had a reinforcement ratio of 1.8% in each boundary element, while it had a reinforcement ratio of 0.4% for distributed reinforcement. To prevent a brittle shear failure, the transverse reinforcement ratio of the wall was selected as 1.0%. The stirrups confining boundary elements were designed to meet buckling prevention requirements of CSA A23.3-14 (2014) and special boundary element specifications, according to ACI 318-14 (2014). Figure 3.7 shows the reinforcement layout of the control wall.

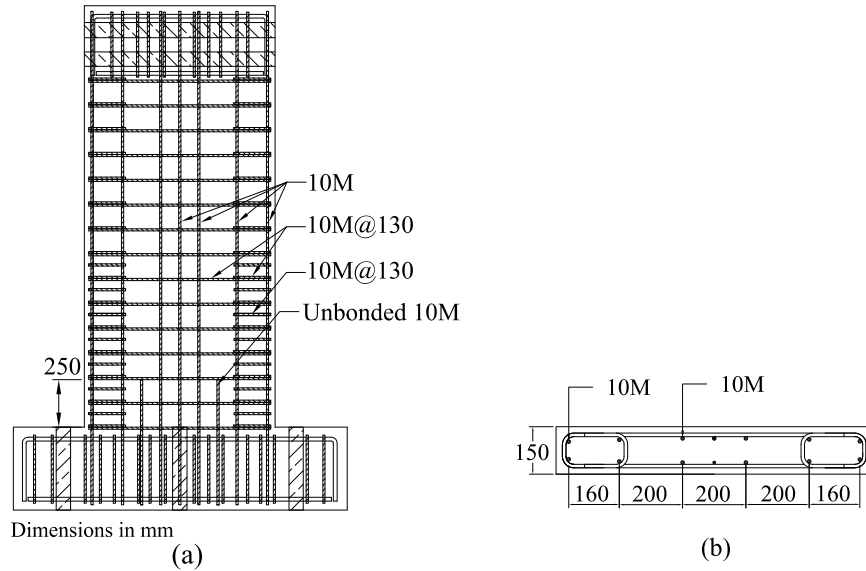


Figure 3.7. Reinforcement details of control wall (a) CW elevation, (b) CW cross-section

In terms of lateral force resistance, the control wall was expected to have a flexural strength of 173 kN based on the measured material properties, the CSA A23.3-14 provisions for reinforced-concrete walls, and unit strength reduction factors. The wall had a diagonal tension strength of 452 kN, and a web crushing strength of 976 kN as well. Also, the sliding shear resistance of the control was increased to 682 kN by detailing the base of the wall with four un-bonded 10M rebars.

The idea behind the design of innovative shear walls was to increase the self-centering of the control wall using three types of self-centering reinforcement while the reinforcement layout of the specimen is preserved as much as possible. It was also taken to account to provide significant amounts of ductility and energy dissipation to the innovative shear walls. As shown in Fig. 3.8, each innovative shear wall was detailed with a hybrid reinforcing system consisting of mild steel for energy dissipation and ductility purposes, and a type of self-centering reinforcement (SMA, GFRP, or high-strength steel) for reducing permanent displacements. Each specimen was also detailed with FRCC for damage mitigation as well.

SMA-SFRC wall was an SFRC shear wall reinforced with 10M mild steel and #4 NiTi bars. Since the NiTi bars had a significant ultimate tensile strain capacity, the bars were placed along the boundaries of the SMA-SFRC wall to provide the specimen with increased self-centering without compromising its deformability. However, due to cost constraints, only a limited height of the wall

was detailed with SMA. In fact, each boundary element of the SMA-SFRC wall was detailed with four #4 NiTi bars up to a height of 550 mm, while the sections above and below the SMA reinforced regions were reinforced with four 15M steel bars in order to restrict nonlinear rebar elongations of boundaries to NiTi bars. Figures 3.8(a) and 3.8(d) show the reinforcement layout of the SMA-SFRC specimen.

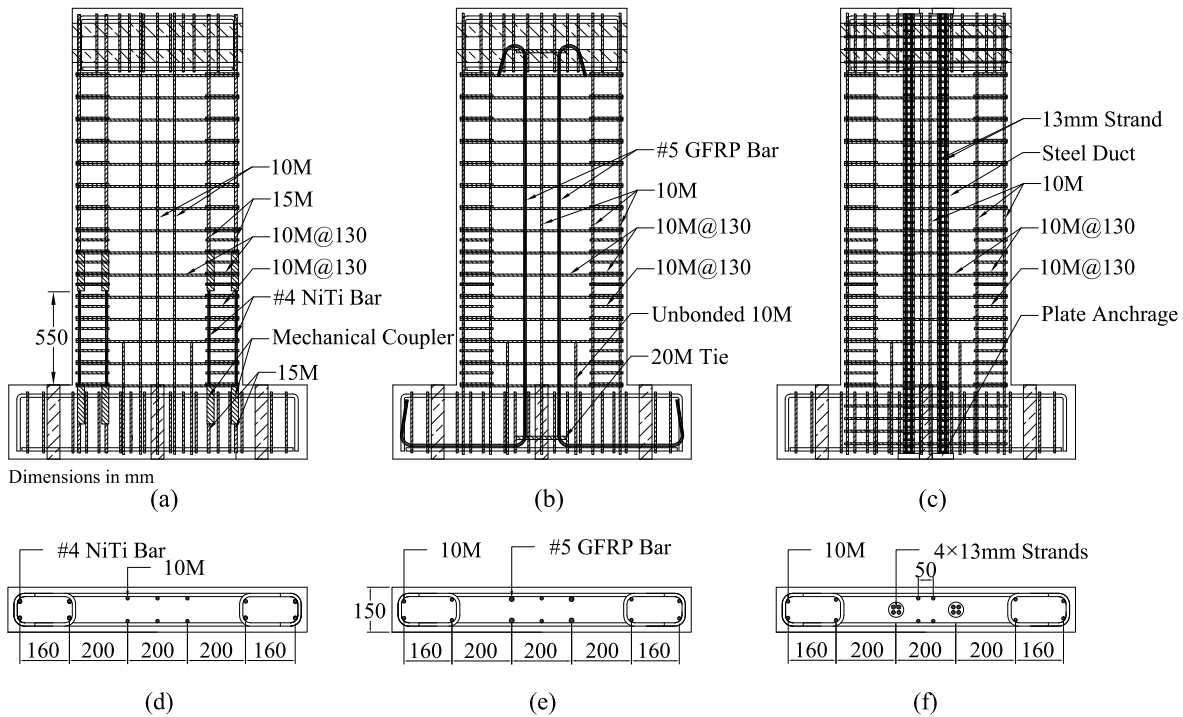


Figure 3.8. Reinforcement details of innovative shear walls (a) SMA-SFRC elevation, (b) GFRP-ECC elevation, (c) PPT-SFRC elevation, (d) SMA-SFRC cross-section, (e) GFRP-ECC cross-section, (f) PPT-SFRC cross-section

The diameter of the NiTi bars was selected based on the fact that #4 NiTi bars and 10M steel bars require almost the same amounts of tensile force to reach yielding. Thus, it was possible to increase the self-centering of the control wall while maintaining the lateral force-resisting strengths of the specimens at a comparable level. Each of the SMA bars was gripped by two special screw-lock mechanical couplers, each of which had been welded to a 15M rebar previously. In the case of distributed reinforcement, the outer rows of the reinforcement were placed closer to the centerline of the wall than the boundary elements. This measure was implemented to protect the outer rows

of distributed reinforcement from the excessive straining and early failure of those bars observed in Abdulridha and Palermo (2014).

The GFRP-ECC wall was an ECC shear wall reinforced with 10M mild steel and #5 GFRP bars. Since the GFRP bars had a brittle response with respect to mild steel rebars, the bars were placed in the web of the specimen. Also, to protect the GFRP bars from high tensile and compressive strains, the bars were placed closer to the centerline of the wall. In order to preserve the generality of the distributed reinforcement layout, only the outer rows of the web reinforcement were detailed with GFRP, and one row of steel reinforcement was maintained in the web of the shear wall. Figures 3.8(b) and 3.8(e) show the reinforcement layout of the GFRP-ECC specimen.

Since GFRP is almost twice as strong as mild steel, a steel-GFRP reinforced wall with the same lateral load strength as that of the control wall was bound to have an inadequate ratio of GFRP reinforcement to exhibit a meaningful self-centering characteristic. For this reason, having a comparable reinforcement layout to the control wall with maximum self-centering was considered as the design objective of the GFRP-ECC wall. As a result, #5 GFRP bars, which had the maximum diameter, which satisfied The testing spacing between GFRP bars in accordance with CSA S806-12 (2012), were selected to be used.

The PPT-SFRC wall was an SFRC reinforced wall detailed with mild steel and post-tensioned high-strength steel strands. The specimen had a similar reinforcement layout to that of the control wall. However, in order to protect the strands from yielding and preserve the energy dissipation and ductility properties of the specimen, the outer rows of the distributed reinforcement in the web of the wall were substituted with two post-tensioned tendons. Also, to satisfy the minimum allowable ratio of distributed reinforcement, an additional row of mild steel was placed in the web of the specimen. Figures 3.8(c) and 3.8(f) show the reinforcement layout of the PPT-SFRC specimen.

Since post-tensioning normally increases the strength of shear walls, the post-tensioned specimen would have had insufficient amounts post-tensioning to exhibit an increase in self-centering had it been designed to have similar strength to that of the control wall. For this reason, the PPT-SFRC wall was designed to have maximum self-centering while maintaining a comparable reinforcement

layout and ductility level to those of the control wall. As a result, each tendon was decided to consist of four (13 mm in diameter) high-strength steel strands. In addition, each strand was stressed to 43% of its yield strength. This was due to the relative shortness of the specimen, which caused large anchorage seating losses and limited the post-tensioning stress level.

### 3.3.3 Testing procedure and loading protocol

Specimens were tested under lateral in-plane displacement reversals, according to ATC 24 (1992). The specimens were supported as cantilevers, and no axial load was applied to the specimens externally since it was desired to study the effect of innovative materials on the self-centering of shear walls independently. The displacement reversals were applied to the mid-height of the cap-beam of each specimen while the out-of-plane displacement at the top point of the specimen was restrained (Fig. 3.9).

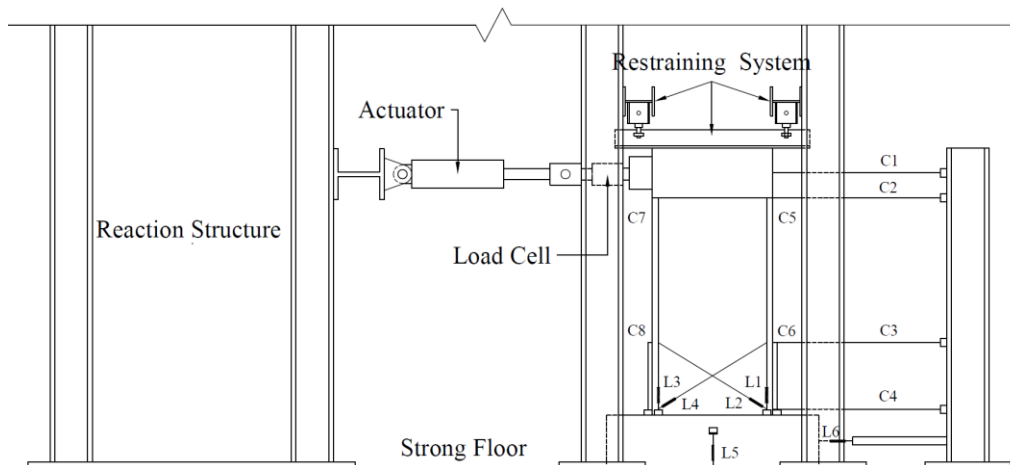


Figure 3.9. Test setup

As shown in Fig. 3.9, the eastern face of each specimen was instrumented with six LVDTs ( $L_1$  to  $L_6$ ) and eight cable transducers ( $C_1$  to  $C_8$ ). The instrumentation was used to measure the lateral and vertical deformations of each specimen at different heights, as well as diagonal elongations between heights of 50 mm to 550 mm. In addition, the response of each shear wall was captured using a digital image correlation system (DIC) facing the western side of specimens.

## 3.4 Experimental Results

### 3.4.1 Load-displacement hysteretic response

Figure 3.10 shows the hysteretic response of each specimen in terms of base shear versus the drift ratio. Figure 3.10 also presents the average values for the effective stiffness, peak strength, and failure drift ratio of each specimen. The base shear of each shear wall was equal to the lateral load applied to the specimen and was measured with a load cell placed between the specimen and the loading unit (Fig. 3.9). The drift ratio of each shear wall was the ratio of the lateral deformation of the specimen at the loading point over the shear span of the wall (Fig. 3.9). Each experiment was started in a force control manner up to the first rebar yielding. Then, the experiments were continued up to a drift ratio of 4% except for SMA-SFRC wall, which was able to resist higher drift ratios without a significant loss in its lateral force resistance.

The hysteretic response of each specimen was stable, symmetric, and with no brittle shear failure. The force-displacement cycles of innovative walls were more pinched due to the higher self-centering characteristics of the walls in comparison to the control wall. The innovative walls also had wide hysteresis loops and dissipated significant amounts of energy. In terms of peak strength, CW and SMA-SFRC walls had comparable strengths of 174.5 kN and 171.8 kN, respectively. Also, GFRP-ECC and PPT-SFRC walls reached greater strengths as anticipated –249.8 kN and 341.8 kN, respectively. This was due to the fact that the specimens were detailed with high-strength reinforcements and were designed to show notable levels of self-centering rather than comparable strength with respect to the control wall.

The backbone curve of the hysteretic response of each specimen was idealized to a bi-linear relationship using the equivalent elastoplastic yielding with reduced stiffness model by Park (1988). In this model, the elastic part of each idealized response and its corresponding backbone curve share a point at a strength of  $0.75H_u$ , with  $H_u$  being the peak strength of the shear wall. Afterward, the elastic line changes into a plateau with a strength of  $H_u$  and continues to the point at which lateral resistance of the wall decreases to  $0.8H_u$ . The idealized backbone curve of each specimen is shown in Fig. 3.10. Based on the idealized responses, the effective stiffness of each of CW, GFRP-ECC, and SMA-SFRC walls was determined as 11.1 kN/mm, 10.6 kN/mm, and

10.5 kN/mm, respectively. The effective stiffness of PPT-SFRC was 23.9 kN/mm as the wall was prestressed and had a 42% more longitudinal reinforcement ratio than CW.

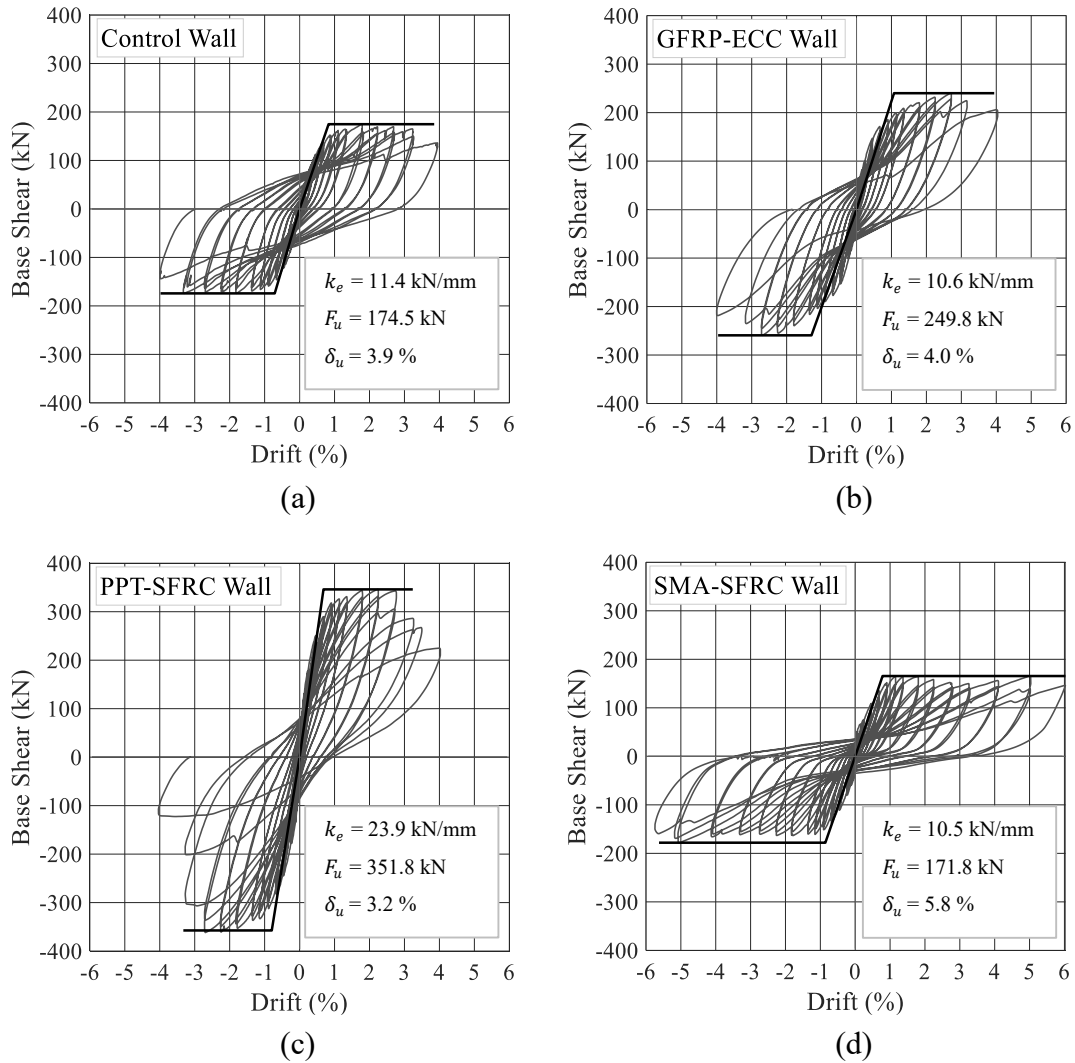


Figure 3.10. Hysteretic response and idealized bilinear behavior of each shear wall (a) control wall, (b) GFRP-ECC, (c) PPT-SFRC, (d) SMA-SFRC

The ductility of each specimen was determined as the ratio of the ultimate drift to the yield drift of the idealized backbone curve of the specimen. The ductility of each specimen was investigated for both positive and negative drift ratios (Fig. 3.11). The minimum ductility value of CW was 4.6, corresponding to a yield drift ratio of 0.83% and an ultimate drift ratio of 3.85%. GFRP-ECC wall had a minimum ductility of 3.1, corresponding to yield and ultimate drift ratios of  $-1.29\%$  and  $-3.96\%$ , respectively. The minimum ductility of the PPT-SFRC wall was 4.0, as the wall had a

yield drift ratio of  $-0.80\%$  and an ultimate drift ratio of  $-3.16\%$ . The SMA-SFRC wall had a minimum ductility of 6.6, the highest among the specimens. The minimum ductility of the SMA-SFRC wall was corresponding to yield and ultimate drift ratios being  $-0.85\%$  and  $-5.63\%$ , respectively.

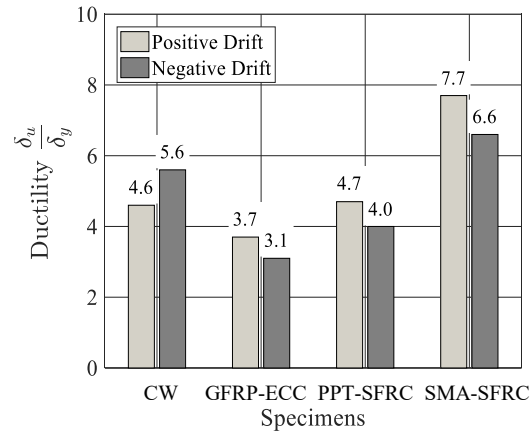


Figure 3.11. Ductility indices of shear walls

### 3.4.2 Damage Propagation and Failure Modes

Figure 3.12 shows the key damage resilience milestones of specimens. The first type of damage sustained by the specimens was cracking. At drift ratios of  $0.05\%$ ,  $0.10\%$ , and  $0.15\%$ , a hairline crack was detected on each of SMA-SFRC, CW, and GFRP-ECC, respectively. The first crack on PPT-SFRC was identified at a larger drift ratio ( $0.25\%$ ) since the specimen was under compressive stresses due to post-tensioning.

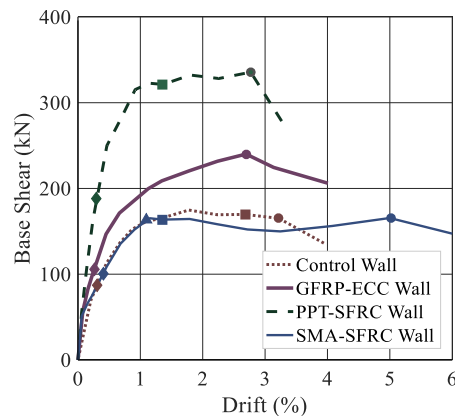


Figure 3.12. Backbone curves and damage resilience milestones of shear walls

Yielding of longitudinal reinforcement was the next type of damage shear walls underwent. At drift ratios of 0.26%, 0.30%, and 0.31%, the outmost reinforcement of GFRP-ECC, PPT-SFRC, and CW yielded respectively. In the case of the SMA-SFRC wall, the first row of the longitudinal steel reinforcement in the web of the specimen first yielded at a drift ratio of 0.41%, while the outmost SMA reinforcement yielded at 1.1% drift. Cover spalling occurred for all the specimens except for the GFRP-ECC wall. The cover of SMA-SFRC and PPT-SFRC spalled at a drift ratio of 1.35%, while it was at 2.70% drift for CW.

The most critical type of damage that specimens sustained was the tensile failure of longitudinal steel rebar, which was followed by the strength degradation and, ultimately, the failure of the shear walls. The failure of the outmost steel rebar first occurred at 2.72% and 2.75% drift ratios for GFRP-ECC and PPT-SFRC walls, while it was at a 3.25% drift ratio for CW. SMA-SFRC featured the highest drift capacity among the specimens as the first rebar failure of the wall occurred at a drift ratio of 5.0%. It is interesting to mention that the ruptured rebars on each side of the SMA-SFRC wall were located in the outmost rows of the distributed reinforcement of the wall while the outmost NiTi bars had not failed yet.

### **3.4.3 Damage Propagation**

Apart from the initial imperfections of specimens, different types of concrete damage, including cracking and cover spalling, were identified and marked on the eastern surface of each shear wall during testing. Also, the non-contact deformation measurements performed on the western surface of each wall were used to determine the maximum and residual values of the crack opening of the specimens. 3.13-3.15 illustrates the progression of damage on the eastern surface each wall at drift ratios of 0.45%, 1.35%, 3.25%. These drift ratios, which are coincident with the major damage resilience milestones of the walls, are associated with different levels of seismic performance. According to FEMA 273 (1997), maximum transient drift ratio of an RC shear wall corresponds to the seismic performance levels of immediate occupancy (IO), life safety (LS) and collapse prevention (CP) when it is smaller than drifts of 0.5%, 1.0%, and 2.0% respectively.

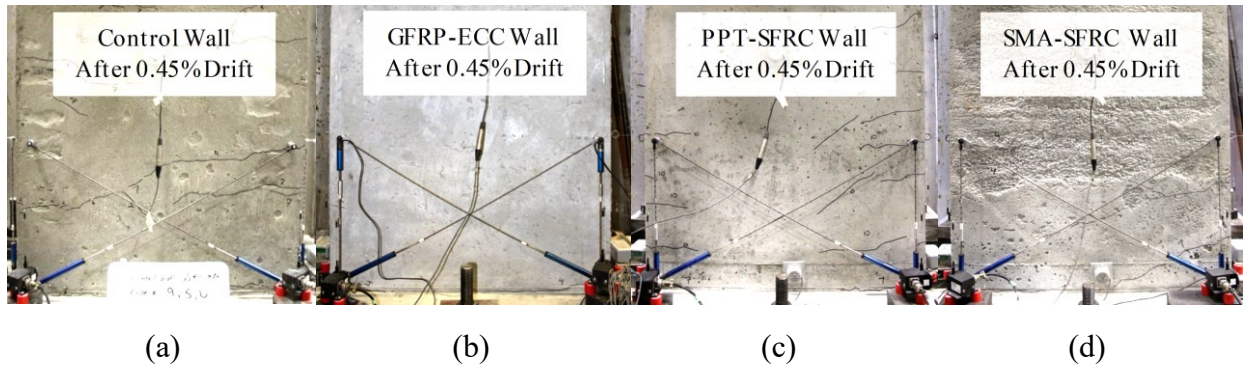


Figure 3.13. Damaged walls after  $\delta=0.45\%$  (a) CW(b) GFRP-ECC, (c) PPT-SFRC, (d) SMA-SFRC

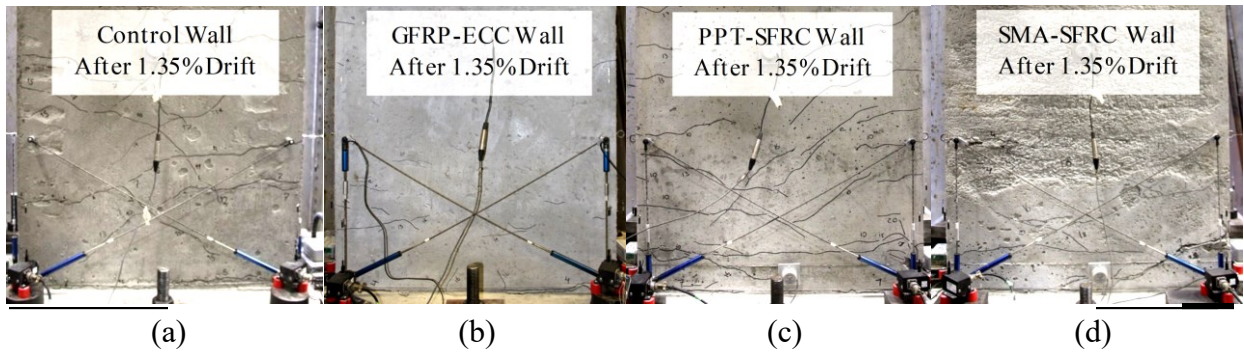


Figure 3.14. Damaged walls after  $\delta=1.35\%$  (a) CW(b) GFRP-ECC, (c) PPT-SFRC, (d) SMA-SFRC

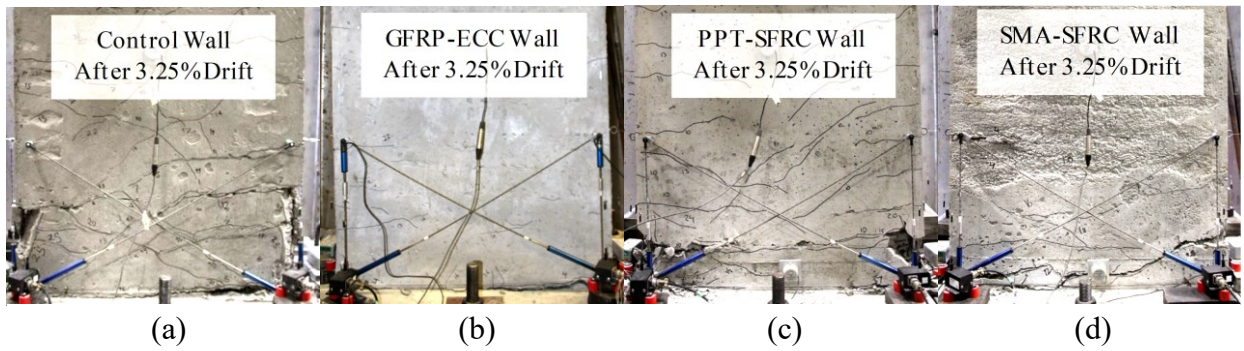


Figure 3.15. Damaged walls after  $\delta=3.25\%$  (a) CW(b) GFRP-ECC, (c) PPT-SFRC, (d) SMA-SFRC

At 0.25% drift, all the specimens had hairline cracks. At 0.45% drift, the specimens had undergone yielding and were cracked with CW and PPT-SFRC walls sustaining more cracks than others (Fig. 3.13). The maximum crack width in PPT-SFRC was 2.5 mm, while it was 1.6 mm, 1.2 mm,

and 1.0 mm in SMA-SFRC, CW, and GFRP-ECC walls. After unloading, residual crack opening in all the specimens was about 0.5 mm.

After 1.35% drift, the existing cracks had propagated within the webs of specimens. At this stage, PPT-SFRC and SMA-SFRC had sustained cover spalling despite other specimens (Fig. 3.14). PPT-SFRC wall had a maximum crack opening of 9.5 mm, the highest in comparison to other specimens. The maximum crack opening in SMA-SFRC, GFRP-ECC, and CW was 8.0 mm, 6.5 mm, and 5.0 mm, respectively. On the other hand, the PPT-SFRC wall had a residual crack opening of 2.5 mm, while GFRP-ECC, SMA-SFRC, and CW had residual crack openings of 4.0 mm, 3.5 mm, and 3.0 mm respectively. The smaller residual crack opening of the PPT-SFRC wall was because of the compressive stresses, which were generated in the shear wall due to post-tensioning.

At a drift ratio of 3.25%, the base shear of the PPT-SFRC wall had decreased by 20%, causing the failure of the specimen. In contrast, the rest of the specimens continued to resist lateral forces effectively, although CW and GFRP-ECC had already undergone rebar rupture. At this stage, CW and PPT-SFRC walls had sustained serious cover spalling, while it was less serious for SMA-SFRC, and no spalling for GFRP-ECC (Fig. 3.15). The crack opening in SMA-SFRC, PPT-SFRC, GFRP-ECC, and CW walls was 26 mm, 24 mm, 18 mm, and 14 mm at loading; then, those values decreased to 16 mm, 6.5 mm, 10 mm, and 12 mm after unloading.

After a drift ratio of 4%, CW and GFRP-ECC specimens had failed. The maximum crack opening in CW, GFRP-ECC, and SMA-SFRC walls was 18 mm, 22 mm, and 33 mm, respectively. Thereafter, the residual crack widths of the walls decreased to 15 mm, 11 mm, and 22 mm with the release of applied lateral loads.

At a 5% drift, the SMA-SFRC wall was the only specimen that was able to deform without experiencing a significant decrease in lateral resistance. At this stage, rebar buckling and rebar rupture had occurred in the outmost row of web reinforcement on the south side of the wall. The maximum and residual crack opening of the SMA-SFRC shear wall after 5% drift were 41 mm and 30 mm, respectively.

### 3.4.4 Self-Centering

Figure 3.16 compares the residual drift ratios of each innovative shear wall and the control wall. The residual drift ratio of a shear wall at each displacement demand was defined as the amount permanent drift ratio of the wall after the first displacement reversal with that displacement demand. As illustrated in Fig. 3.16, the innovative shear walls had generally smaller residual drift ratios and higher self-centering in comparison to the control wall. The reduction in the amounts of residual drift ratio in each innovative wall in comparison to the control wall is shown in Fig. 3.17(a). In addition, the ratio of residual drift ratio of each innovative shear wall to that of the control wall at all drift ratio demands is displayed in Fig. 3.17(b).

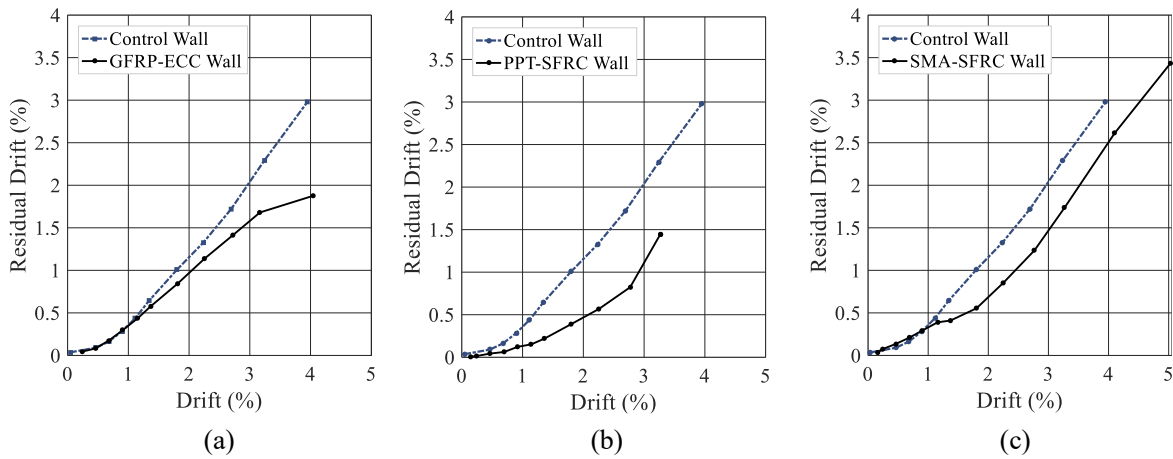


Figure 3.16. Residual drift ratio of each innovative wall vs. control wall (a) GFRP-ECC, (b) PPT-SFRC, (c) SMA-SFRC

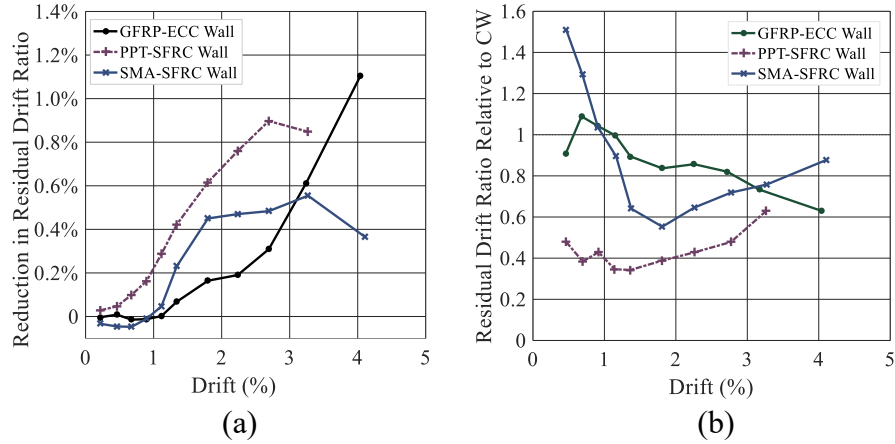


Figure 3.17. (a) Reduction in residual drift ratio in each innovative wall with respect to control wall, (b) ratio of residual drift ratio of each innovative wall to that of control wall

Residual drift ratios started from zero and then increased, as higher displacement demands were applied to specimens. For the control wall, permanent drifts increased almost linearly with applied demands for drift ratios of 1% and higher, leading to a permanent drift of 3% after unloading from a 4% drift. In the case of the GFRP-ECC wall, the reduction in residual drift ratios became appreciable after a drift ratio of 1% when enough restoring forces were developed in the GFRP bars of the wall. Then after 2.7% of drift, the self-centering of the wall increased even more, with the rupturing of one of the outmost steel rebars of the wall. At 3.25% drift, the reduction in the amount of residual drift in GFRP-ECC was 0.6% with respect to CW, corresponding to a 27% reduction. At a drift ratio of 4%, the reduction was 1.1%, which was corresponding to a decrease of 37%.

PPT-SFRC wall illustrated largely reduced residual drift ratios in comparison to CW. For drift ratios between 0.25% and 2.70%, the wall showed a decrease of more than 50% in residual drift. At 3.25% drift, the permanent drift of PPT-SFRC was smaller than that of CW by an amount of 0.85%, corresponding to a decrease of 37%.

SMA-SFRC wall showed marginally higher residual drifts than CW at drift ratios smaller than 1%. However, the specimen started to have smaller permanent drift ratios from 1% drift to 2% drift as the outmost SMA bars of the wall started to yield. Then, for drift ratios of 2% or larger, the specimen continued to have reduced permanent drifts with almost a constant value compared to the control wall. At 3.25% drift, the reduction in the residual drift ratio of the SMA-SFRC wall

with respect to that of CW was 0.55%, corresponding to a 24% decrease. After a drift of 4%, the reduction was 0.36%, corresponding to a decrease of 12%.

### 3.4.5 Energy Dissipation

To compare the energy dissipation capacity of specimens, the normalized energy dissipation concept by Hidalgo et al. (2002), was used. The normalized dissipated energy in a hysteresis loop is the area covered by the force-displacement loop over the area of the rectangle surrounding the loop. Figure 3.18 shows the normalized dissipated energy of each innovative shear wall in comparison to that of the control wall. In addition, the ratio of the normalized dissipated energy of each innovative shear wall to that of the control wall at different drift ratio demands is displayed in Fig. 3.19.

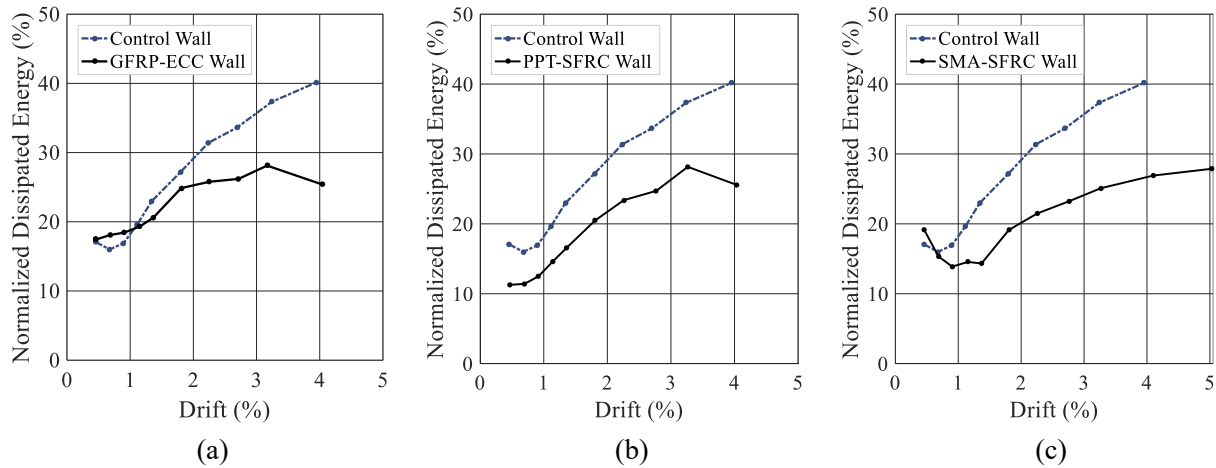


Figure 3.18. Normalized dissipated energy of each innovative wall vs. control wall (a) GFRP-ECC, (b) PPT-SFRC, (c) SMA-SFRC

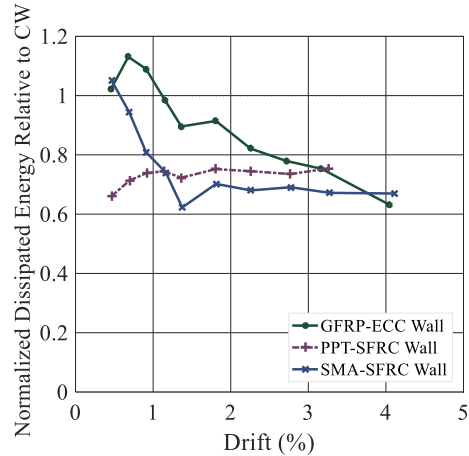


Figure 3.19. Ratio of normalized dissipated energy of each innovative wall to that of control wall

According to Fig. 3.18, the energy dissipation capacity of the GFRP-ECC wall was higher than that of CW before a 1% drift. However, after a 1% drift, the specimen started to have increased self-centering and consequently decreased energy dissipation characteristics in comparison to CW. Then, the normalized dissipated energy of the GFRP-ECC wall decreased to 62% of that of CW at a 4% drift. In the case of the PPT-SFRC wall, the normalized dissipated energy of the wall to that of CW was about 73%, from a drift of 1% to 3.25%. For SMA-SFRC, normalized dissipated energy was slightly higher than that of CW at 0.5% drift. However, it decreased to 62% of CW normalized dissipated energy at 1.8% drift and then plateaued about 67% up to 4% drift.

### 3.5 Performance Assessment

The damage specimens sustained during testing was reported in terms of crack width, cover spalling, and rebar fracture. In terms of cracking, all the innovative shear walls formed fewer but deeper cracks than the control wall. After unloading, all the specimens exhibited crack closure to some extent. Among them, crack closure was the highest in PPT-SFRC and the lowest in CW for most of the drift ratios. In terms of cover spalling, the GFRP-ECC wall had the best performance among other specimens due to the superior post-cracking behavior of ECC. Ultimately, all the specimens experienced steel rebar rupture, although the SMA-SFRC wall was the only specimen that did not undergo rebar failure in its boundary regions, which resulted in having the highest ultimate drift ratio among the specimens.

Also, the specimens can be compared based on their residual drift ratios. According to FEMA 273 (1997) and FEMA 356 (2000), the permanent drift ratio of a concrete shear wall should be negligible in IO performance level, lower than 0.5% in LS level, and it can have a maximum residual drift ratio of 2.0% in case of CP level. FEMA also limits the transient maximum drift ratios corresponding to IO, LS, and CP performance levels to 0.5%, 1%, and 2%, respectively.

In order to compare the shear walls of this study at the IO performance level, 0.125% was chosen as the permanent drift ratio limit for the IO performance level. This residual drift ratio was associated with a maximum transient drift ratio of 0.57% in the control wall, corresponding to early stages of yielding in the wall – the first yielding in CW occurred at a drift ratio of 0.31%. It is also worthwhile to mention that permanent drift ratio limits for IO performance level regarding reinforced and unreinforced masonry walls are 0.2 % and 0.3%, respectively, according to FEMA.

Table 3.3 discusses the seismic performance of test specimens based on their permanent drift ratios. The table reports the drift ratio, after which each shear wall exceeded the permanent drift ratio limit associated with each of IO, LS, and CP performance levels.

Table 3.3. Seismic performance of specimens in terms of permanent drift ratio

Comparison Criteria	IO (Negligible Permanent Drift)				LS (Permanent Drift Ratio of 0.5%)				CP (Permanent Drift Ratio of 2.0%)			
	CW	GFRP -ECC	SMA- SFRC	PPT- SFRC	CW	GFRP -ECC	SMA- SFRC	PPT- SFRC	CW	GFRP -ECC	SMA- SFRC	PPT- SFRC
Levels of Drift ratio associated with permanent drift ratio limits	0.57	0.55	0.42	0.94	1.18	1.25	1.64	2.08	2.96	4.0 <sup>a</sup>	3.52	3.25 <sup>a</sup>
Improvement over CW	–	–4%	–26%	65%	–	6%	39%	76%	–	35%	19%	10%

<sup>a</sup> Ultimate drift ratio of the wall

For the IO performance level, GFRP-ECC and SMA-SFRC walls exceeded 0.125% residual drift before CW as each of GFRP and SMA has a lower elastic modulus than steel. On the other hand, the drift ratio, after which the PPT-SFRC wall exceeded a permanent drift of 0.125%, was 65% larger than that of CW. The reason behind this can be attributed to the high performance of post-tensioning in crack closure and residual drift ratio reduction.

In the case of LS performance level, all the innovative shear walls showed improvement in comparison to CW. GFRP-ECC wall exceeded the residual drift ratio of 0.5% after experiencing a 1.25% drift, which was 6% larger in comparison to that of CW. SMA-SFRC and PPT-SFRC walls exceeded 0.5% permanent drift ratio after undergoing drift ratios of 1.64% and 2.08%, respectively, corresponding to 39% and 76% increase to that of CW.

Regarding the CP performance level, the SMA-SFRC wall exceeded 2% of permanent drift ratio after experiencing a drift ratio of 3.52%, which was 19% higher in comparison to that of CW. At this performance level, GFRP-ECC and PPT-SFRC walls failed before reaching a permanent drift ratio of 2%; therefore, the ultimate drift ratios of these specimens, 4.0%, and 3.25% respectively, were reported as their collapse drift ratios in Table 3.3. As discussed, the GFRP-ECC wall showed the highest performance in comparison to other specimens in regard to the CP performance level. This can be explained by the increase in the self-centering of the specimen after the failure of its outmost rebars.

### **3.6 Conclusions**

The following conclusions were drawn from this experimental study.

- The shear walls reinforced with steel rebars and self-centering reinforcement showed reduced permanent deformations while maintaining comparable levels of energy dissipation and ductility to those of the control wall, which was a conventional RC shear wall. This means that an innovative wall is more likely to have a lower permanent displacement after a strong earthquake with respect to a comparable conventional RC wall. As a result, the innovative wall will require less retrofitting to be safe to reside.
- The shear walls detailed with fiber-reinforced cementitious composite showed increased resilience in terms of cracking and spalling with respect to the control wall. However, as the fiber-reinforced shear walls formed fewer cracks, they experienced wider cracks in comparison to the control wall. More damage resistance will lead to lower strength and stiffness degradation, higher rebar protection, and lower retrofitting costs in shear walls.
- The shear walls detailed with GFRP and SMA showed improved self-centering after a drift ratio

of 1%, which is appropriate for improving the LS and CP seismic performance levels of shear walls. The post-tensioned specimen exhibited self-centering from the beginning of testing, suitable for improving the performance of shear walls, especially their IO and LS performance levels.

- The shear wall detailed with SMA along its boundaries was the only specimen whose outmost rebars did not rupture, which led to a notable increase in the ductility of the wall. As a result, the innovative walls will be able to deform larger deformations without showing strength degradation, which can be a substantial advantage of the steel-SMA reinforced walls over conventional RC shear walls in strong seismic events.

# CHAPTER 4 SEISMIC DESIGN OF THREE DAMAGE-RESISTANT CONCRETE SHEAR WALLS DETAILED WITH SELF-CENTERING REINFORCEMENT

## 4.1 Abstract

Recent studies have shown that the innovative shear walls detailed with a type of self-centering reinforcement and fiber reinforced concrete are effective in reducing the permanent displacement and concrete damage compared to conventional concrete (RC) shear walls. However, more investigation is required into the seismic design parameters, such as the inelastic rotational capacity and plastic hinge length of innovative shear walls. This chapter investigates the response of three innovative walls cast with fiber-reinforced composites and reinforced with steel rebars and a type of self-centering reinforcement consisting of shape memory alloy (SMA) bars, glass fiber reinforced polymer (GFRP) bars, or high-strength steel strands. The response of each innovative wall is compared to that of a conventional RC shear wall called the control wall. Then, the inelastic rotational capacity, plastic hinge length, and self-centering of the innovative walls are discussed within the framework of the seismic design codes of North America.

It is shown that innovative walls can undergo significant inelastic rotational deformations due to the use of ductile reinforcements, such as steel or SMA bars, at their boundaries, while the reinforcement with lower tensile strain capacities, such as PT strands and GFRP bars, were placed away from the boundaries. It is also shown that the crack opening at the base of each innovative wall was greater in comparison to that of the control wall. This was due to the use of fiber-reinforced composites and self-centering reinforcements with low bonding stresses in the walls, which increased the rocking in the response of the innovative walls. It is shown that the plastic hinge in the steel-GFRP reinforced and post-tensioned walls was shorter than in the control wall since plastic strains were more concentrated in steel rebars adjacent to the bases of the walls. In the steel-SMA reinforced wall, the plastic hinge length was longer than in the control wall due to the low bonding properties of the SMA bars compared to the control wall. The self-centering capacity of the innovative walls at different seismic performance levels is also discussed, and three improved self-centering objectives for the design of innovative walls are introduced.

## 4.2 Introduction

In the traditional design philosophy of structures, seismic loads are reduced in accordance with the ductility level of the lateral load resisting system used in a structure (ACI 318-14 2014; CSA A23.3-14 2014). In the performance-based seismic design (PBSD) of building structures, the structural and non-structural elements of buildings are required to satisfy targeted building performance levels for given levels of seismic hazard, according to FEMA 356 (2000). For instance, for a given earthquake with a specific return period, a building structure is required to satisfy certain levels of performance, such as immediate occupancy (IO), life safety (LS), and collapse prevention (CP). Traditionally, targeted building performance levels for a building structure are based on the damage levels that the structural and non-structural members of the building have sustained. In addition, the PBSD allows the owners of structures to define further performance objectives, such as self-centering, to lower the probability of future rehabilitation or reconstruction.

The permanent drift ratio and the damage to the structural elements of a building can be used to evaluate the post-earthquake state of the building, according to FEMA 356 and FEMA 273 (1997). Ramirez and Miranda (2012) showed that in contrast to the non-ductile buildings, economic losses in ductile buildings are mainly due to the permanent inter-story drift. In fact, the current economic loss estimates which do not account for permanent inter-story drift ratios can dramatically underestimate the sustained losses. For instance, in some cases, economic loss estimates which account for forced demolitions caused by the permanent inter-story drift ratio were 45% more than the current estimates which neglect permanent drifts. It can be concluded that the seismic performance of ductile buildings can be effectively improved by reducing their permanent drift ratios. The permanent drift ratio in a building can be decreased in many ways, e.g., by the use of dampers, seismic isolators, or self-centering reinforcements.

The permanent drift ratio in reinforced concrete (RC) members is caused by the plastic strain that the steel reinforcement of the member sustains. In recent studies performed by Saiidi and Wang (2006), Saiidi et al. (2009), and Cruz Noguez et al. (2012), it was shown that bridge piers detailed with shape-memory alloy (SMA) bars and engineered cementitious composite (ECC) in the plastic hinge region had enhanced seismic performance due to their mitigated damage and reduced

permanent deformations. Another innovative type of pier, studied by Cruz Noguez et al. (2012) and Sakai and Mahin (2004), was the partially post-tensioned bridge pier. The studies showed that the post-tensioning of bridge piers was highly effective in reducing the permanent deformations of bridge piers despite the substantial damage they underwent along their plastic hinge zones.

Tolou Kian and Cruz-Noguez (2018) investigated three types of innovative shear walls with improved self-centering and damage resistance. The study included the testing of four shear walls consisting of a conventional RC wall and three innovative walls under cyclic loads. The innovative walls were cast with a type of fiber-reinforced cementitious composite (FRCC). The types of FRCC composites used in the study consisted of ECC, which has synthetic fibers, and steel fiber reinforced concrete (SFRC). The walls were reinforced with steel rebars along with a type of self-centering reinforcement such as SMA bars, glass fiber reinforced polymer (GFRP) bars, or high-strength steel strands. The study showed that the innovative walls had improved self-centering properties and mitigated concrete damage in terms of cracking and cover spalling compared to the conventional control wall of the study.

Abdulridha and Palermo (2014) investigated the cyclic response of a slender concrete wall reinforced with steel and SMA bars. It was shown that the steel-SMA reinforced wall had a significantly improved self-centering property in comparison to a conventional control wall, although sustaining more damage during testing.

Mohamed et al. (2014) explored the cyclic response of three concrete shear walls that were reinforced with GFRP bars. According to the study, the GFRP reinforced walls avoided brittle modes of failure while illustrating adequate deformability and substantial self-centering properties. However, due to the elastic behavior of its GFRP bars, the walls dissipated lower amounts of energy in comparison to a comparable control RC wall.

Tolou Kian et al. (2018) investigated the response of two steel-GFRP reinforced walls through experimental testing. According to the study, the walls with the hybrid reinforcement had a moderate improvement in the self-centering while maintaining a significant energy dissipation property in comparison to the comparable control RC shear walls of the study. Holden et al. (2003) studied the cyclic response of a precast post-tensioned shear wall. According to the study, the wall

illustrated a significant improvement in self-centering due to the absence of continuous steel rebars along the boundaries of the wall. However, the energy dissipation capacity of the wall was insignificant. In addition, since the wall was adequately reinforced and cast with SFRC, it sustained minimal damage. It has also been shown through several studies, such as by Parra-Montesinos (2014), that casting structural members with SFRC improves the damage mitigation in shear walls in comparison to conventional walls cast with normal concrete.

As summarized above, a limited number of experimental studies are available on the behavior of innovative shear walls. The number of studies focusing on the design parameters of the innovative shear walls is even more limited. One of the few studies performed in this regard was by Mohamed et al. (2013). The study proposed a force modification factor ( $R$ ) for purely GFRP-reinforced shear walls based on the experimental study carried out by Mohamed et al. (2014).

Since there is a gap in the literature on the underlying response characteristics and design parameters of the innovative shear walls, the present study aims to provide further insight into the design of such elements. The flexural and shear responses of three innovative walls are investigated and compared with those of an RC shear wall, which had a comparable reinforcement layout. Then, the key response parameters, such as inelastic rotational capacity and plastic hinge length, which are used in the seismic design of shear walls, are investigated.

### **4.3 Experimental Program**

#### **4.3.1 Test Specimens**

The experimental program of this study consisted of testing four slender shear walls under cyclic displacements. The specimens were identical in geometry with a shear span of 2005 mm, a length of 1000 mm, and a thickness of 150 mm. However, the walls had different longitudinal reinforcement. The control wall (CW) of the experiment was a conventional steel-reinforced wall, while the others were reinforced with steel and a type of self-centering reinforcement. Each self-centering wall had a similar reinforcement layout to the control wall with the substitution of some of the steel rebars in the CW with GFRP bars, SMA bars, or high-strength steel strands. The specimens were also detailed with FRCC to have mitigated concrete damage. In this regard, the GFRP reinforced wall was cast with ECC; however, due to some difficulties in providing the

required amount of ECC, the SMA-reinforced and the post-tensioned walls were cast with ready-mix SFRC. Four 10M starter bars, each of which wrapped in a plastic cover, were placed at the base of each shear wall to increase the resistance of the shear walls against sliding shear without the bars participating in the flexural resistance of the walls.

The reinforcement layouts of the innovative shear walls were comparable to that of the control wall (Fig. 4.1(a)). In the case of the GFRP-reinforced and post-tensioned walls, self-centering reinforcement was placed in the webs of the shear walls, as shown in Fig. 4.1 (b) and (c). This measure was adopted to protect the self-centering reinforcement from excessive straining and allowing the specimens to reach their maximum ultimate drift ratios. In the case of the SMA-reinforced wall, up to a height of 550 mm of each boundary element of the wall was reinforced with NiTi (SMA) reinforcement, while the sections above the SMA reinforced regions were reinforced with 15M steel bars (Fig. 4.1(d)). Further information on the design of the specimens is available in Tolou Kian and Cruz-Noguez (2018).

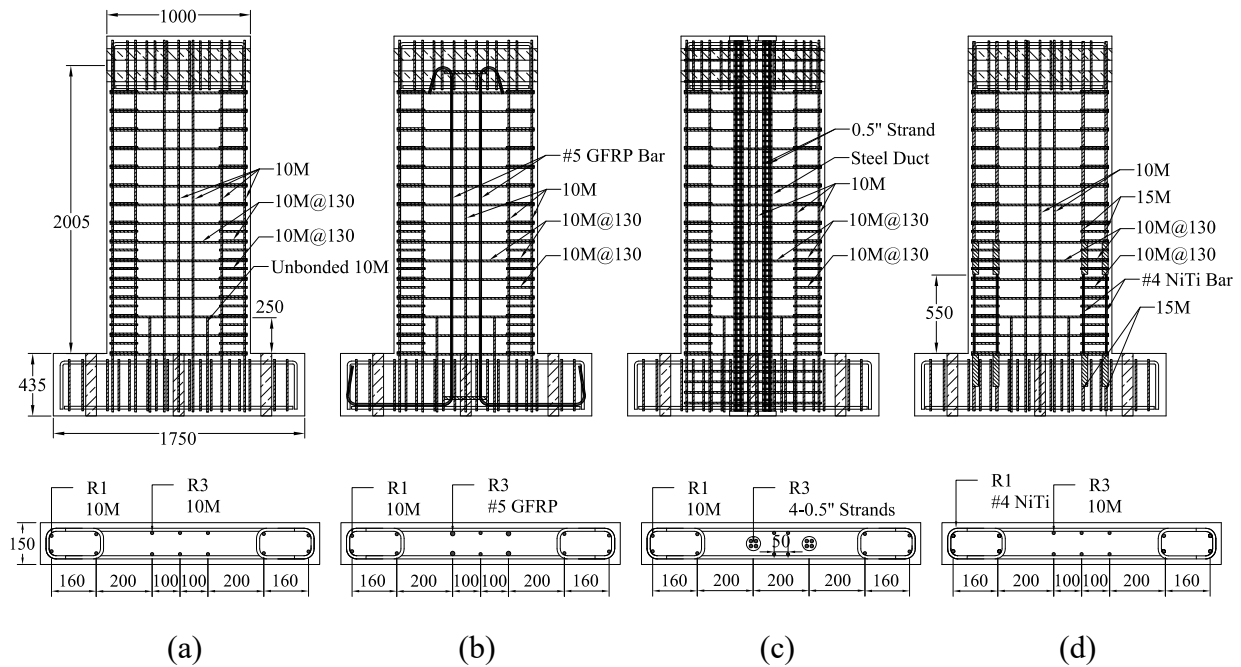


Figure 4.1. Reinforcement detailing of (a) CW, (b) GFRP-ECC, (c) PT-SFRC, (d) SMA-SFRC

As shown in Table 4.1, the GFRP bars and high-strength steel stands had higher elastic limits than the conventional mild steel bars used in the construction of the walls. For this reason, designing the GFRP-reinforced and post-tensioned specimens with the same lateral load resistance to that of

the control wall would result in inadequate ratios of self-centering reinforcement and insignificant improvements in the self-centering of the walls. Therefore, the specimens were designed to have comparable reinforcement layouts to the control wall with maximum self-centering and significant ductility despite reaching higher peak strengths in comparison to the control wall. On the other hand, by using #4 NiTi bars, it was possible to increase the self-centering of the control while maintaining a comparable level of lateral load resistance to the wall. This was because the self-centering in the NiTi bars stems from super-elasticity rather than elasticity, which was the case for the GFRP and high-strength steel reinforcement.

### 4.3.2 Material Properties

The fiber content and compressive strength of each cementitious composite used in the construction of the specimens are summarized in Table 4.1.

Table 4.1. Properties of different types of cementitious material

Cementitious material	Fiber Content (%)	Compressive Strength (MPa)
Concrete	0.00	47.6
ECC	2.00	38.2
SFRC <sup>a</sup>	0.75	51.3
SFRC <sup>b</sup>	0.75	62.2

<sup>a</sup> Used in the SMA-SFRC Wall

<sup>b</sup> Used in the PT-SFRC Wall

The tensile properties of the SFRC mixes were identified through four-point load testing of notched SFRC beams associated with the SMA-SFRC and PT-SFRC walls. At crack mouth opening displacements of 0.5 and 2.5 mm, the average flexural stress was 5.55 and 4.75 MPa in the SFRC beams corresponding to the SMA-SFRC wall, while it was 3.50 MPa and 3.88 MPa in the case of the PPT-SFRC wall. The tensile properties of the ECC mix used in the GFRP-ECC wall were determined through the direct tension test. The average tensile stress and strain capacities of the ECC were determined as 3.11 MPa and 0.95%, respectively.

The properties of the reinforcing materials used in the construction of the specimens are summarized in Table 4.2.

Table 4.2. Mechanical properties of different types of reinforcement

Reinforcement	Elastic Modulus (GPa)	Nominal Area (mm <sup>2</sup> )	Yield Strength (MPa)	Ultimate Strength (MPa)
#5 GFRP	62.6	199	N.A.	1150
0.5" HS-steel	195	98.7	1670	1860
#4 NiTi (SMA)	27.4	127	330	890
10M steel <sup>a</sup>	184	100	421	634
10M steel <sup>b</sup>	173	100	415	626
15M steel	191	200	439	617

<sup>a</sup> Used in the CW and SMA-SFRC Walls

<sup>b</sup> Used in the GFRP-ECC and PT-SFRC Walls

### 4.3.3 Testing

The specimens were tested in single curvature bending while displacement reversals were applied to the cap-beam, and out-of-plane displacements at the top of the cap-beam were restrained (Fig. 4.2). According to Tolou Kian and Cruz-Noguez (2018), the first rebar yielding in the CW, GFRP-ECC, PT-SFRC, and SMA-SFRC walls occurred at drift ratios of 0.31%, 0.26%, 0.30%, and 0.41%, respectively. The CW, GFRP-ECC, and PT-SFRC walls were tested up to a drift ratio of 4.0%, which corresponds to 12.9, 15.4, and 13.3 times the first yielding drift ratios of the walls respectively. The SMA-SFRC wall was tested up to a drift ratio of 6.0%, corresponding to 14.6 times the first yielding drift ratio of the wall.

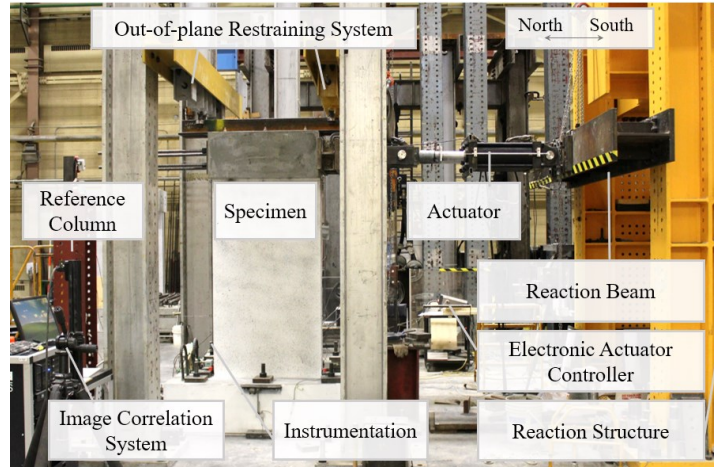


Figure 4.2. Test setup

A digital image correlation system (DIC) was used to capture the displacements of each shear wall, besides conventional linear variable differential transducers (LVDTs) and cable transducers. The DIC system was able to accurately measure the deformations of the specimens, as can be seen in Fig. 4.3. Figure 4.3 shows the drift ratios measured at the top of the control wall using the DIC system and a cable transducer. The two measurements were well in agreement, and their relative error was less than 3.0% for drift ratios of greater or equal to 1.0%. In other words, the difference between the DIC and LVDT measurements can be deemed as insignificant after 1.0% drift.

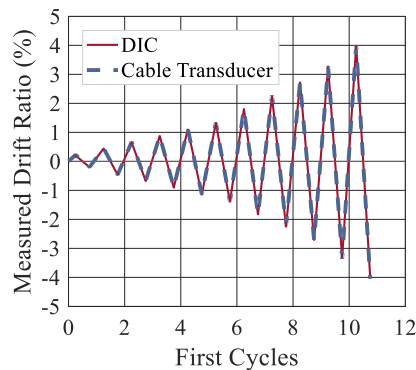


Figure 4.3. Drift ratio at top point of control wall panel measured with cable transducer and DIC system.

Each wall panel was divided into eight stripes with similar heights, along which the average longitudinal strain, shear strain, and curvature were calculated using the DIC measurements (Fig. 4.4(a)). The reinforcing system of each shear wall was instrumented with post-yielding strain

gauges. The strain gauges were mounted adjacent to the base of each shear wall, where plastic deformations were expected. Figure 4.4(b) shows the strain gauge layout used for the control wall. The strain gauge layouts of the innovative walls were similar to that of the CW; however, additional strain gauges were used to capture the response of each wall outside the plastic hinge region. Regarding the GFRP-ECC and PT-SFRC walls, two rows of strain gauges were mounted on the boundary steel rebars of the walls at heights of 0.90 and 1.25 m from the foundation. In the case of the SMA-SFRC wall, a row of strain gauges was mounted right above the mechanical couplers of the outmost SMA bars at 0.75 m above the foundation.

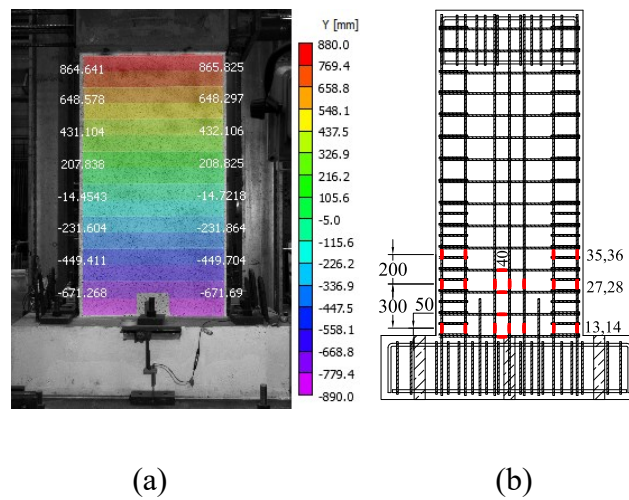


Figure 4.4. Response measurement tools (a) DIC system, elevation measurement for CW, (b) strain gauge layout of CW

## 4.4 Response Parameters

### 4.4.1 Post-Testing State and Cracking

The state of each specimen at the end of testing, when the lateral load resistance of the specimen was decreased by 20%, is shown in Fig. 4.5. The CW wall had sustained flexural and shear cracks as well as cover spalling and rebar rupturing on both sides at 4.0% drift (Fig. 4.5(a)). The GFRP-ECC wall had suffered a distinctive flexural crack along its base together with rebar rupturing on both sides at 4.0% drift (Fig. 4.5(b)). At 3.3% drift, the PT-SFRC wall had formed some minor flexural cracks along with a crack spreading along the length of the wall. The wall had also suffered notable cover spalling on both sides and rebar rupturing on its northern side (Fig. 4.5(c)). After the resistance degradation of the PT-SFRC wall, the test was continued up to 4.0% drift, at which a

global buckling was observed close to the base of the wall. At 6.0% drift, the SMA-SFRC wall had formed few flexural cracks with a crack spreading along the base of the wall (Fig. 4.5(d)). The specimen had also suffered some spalling on its boundaries and its web. The cover-spalling in the web of the wall which was caused by the buckling of the longitudinal web rebars of the wall.

All of the shear walls sustained a major crack adjacent to their bases, which accommodated most of the flexural deformations of the walls. However, the crack was intensified in the innovative walls because of the use of smooth reinforcement, unbonded reinforcement, and fiber-reinforced composite in the construction of innovative specimens. It is also worth mentioning that no reinforcement slipped out of the foundation. Also, no cracking accumulation was observed where the starter bars ended. This was because the starter bars were unbonded and did not provide flexural resistance to the shear walls.

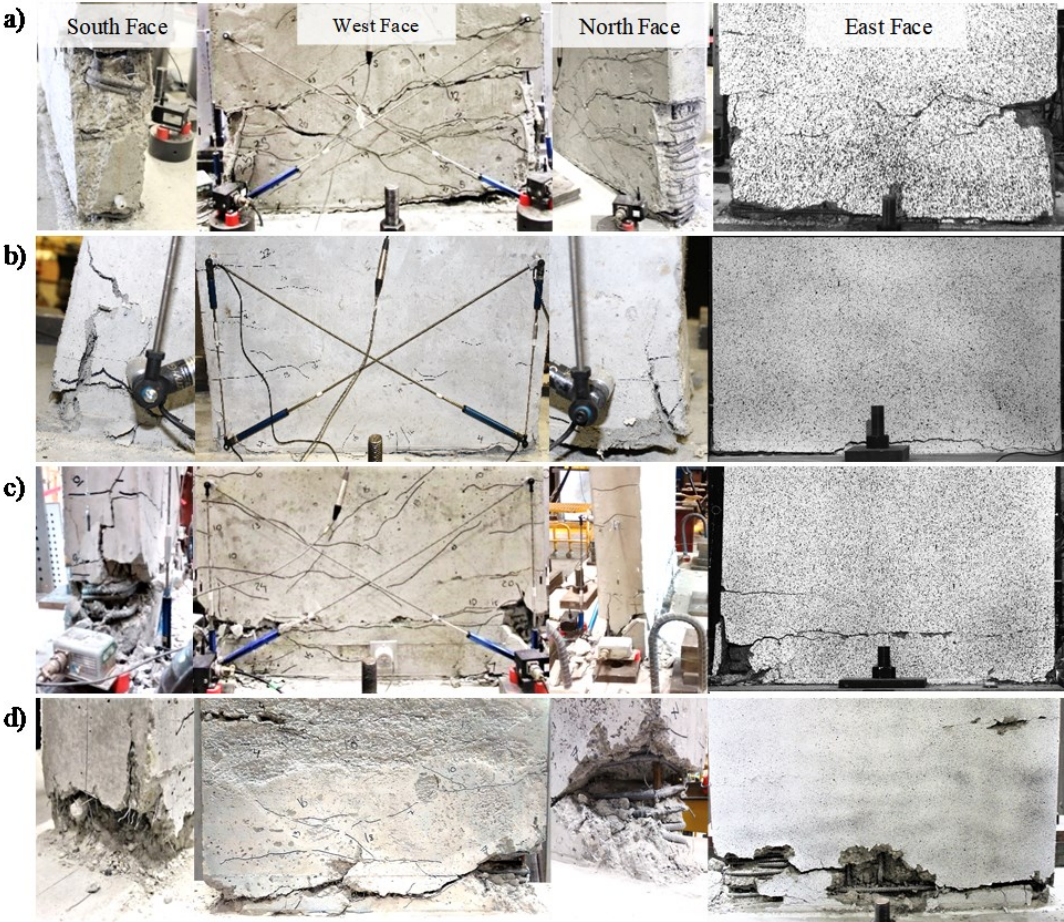


Figure 4.5. Sustained concrete damage in (a) CW at  $\delta=4.0\%$ , (b) GFRP-ECC at  $\delta=4.0\%$ , (c) PT-SFRC at  $\delta=3.3\%$ , (d) SMA-SFRC at  $\delta=6.0\%$

The crack width of the major crack formed at the base of each specimen was measured using the DIC system at different drift ratios (Fig. 4.6). The control wall experienced a lower crack width in comparison to other specimens during testing. This was because the wall formed multiple cracks compared to other specimens. The GFRP-ECC wall had a comparable crack width to the CW wall, while it was higher in the SMA-SFRC and PT-SFRC walls during testing.

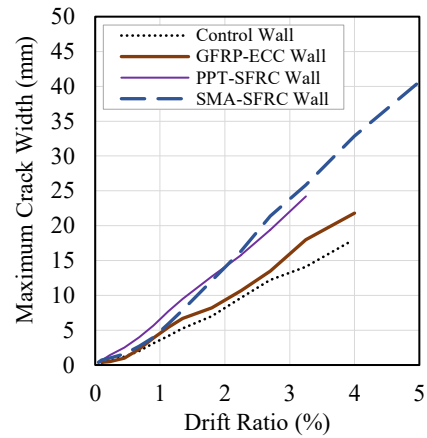


Figure 4.6. Crack width measured at loading

#### 4.4.2 Hysteretic Response

The hysteretic response of each shear wall is shown in Fig. 4.7. As can be seen, the hysteretic responses were symmetric and showed significant amounts of ductility and energy dissipation. The hysteretic responses of the self-centering specimens were more pinched in comparison to that of the control wall. This was because the walls had lower permanent drift ratios than the control wall.

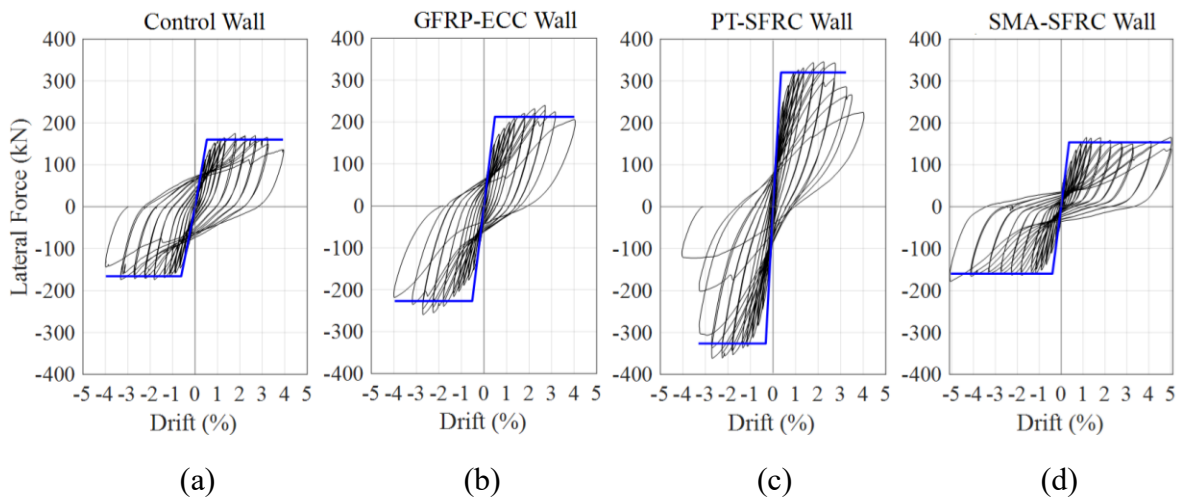


Figure 4.7. Hysteretic response of (a) CW, (b) GFRP-ECC, (c) PT-SFRC, (d) SMA-SFRC

In general, the innovative walls sustained lower permanent drift ratios compared to the control wall. To put this into perspective, the drift ratio recovery that is the ratio of the recovered drift ratio to the total drift ratio was calculated for each specimen (Fig. 4.8). In general, the drift ratio recovery of the specimens decreased as the testing progressed. The PT-SFRC wall was effective in recovering drift ratios from the beginning of testing, while it took higher drift ratios to activate the self-centering properties of the SMA-SFRC and GFRP-ECC walls. After unloading from 2.7% drift and the before any shear wall undergoes rebar rupturing, the drift ratio recovery in the CW, GFRP-ECC, SMA-SFRC, and PT-SFRC walls was 0.36, 0.48, 0.65, and 0.69, respectively.

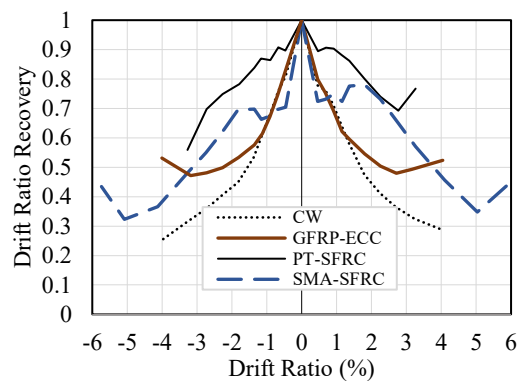


Figure 4.8. Recovery of drift ratios after unloading

#### 4.4.3 Curvature Distribution

Average curvatures between the horizontal lines shown in Fig. 4.4(a) were determined by fitting the best line to the distribution of average vertical strains along the length of the wall. According to Fig. 4.9(a), the distributions of average curvatures in the control wall were almost linear below a height of 600 mm. In the case of the GFRP-ECC, PT-SFRC and SMA-SFRC walls, high curvature values were developed adjacent to the base of each shear wall, where each specimen formed a crack along its base, which accommodated most of the flexural deformations of the wall (Fig. 4.9 (b) and (d)). This was because the self-centering reinforcement had lower bond properties than deformed steel bars, and the fiber-reinforced composites used in the construction of the walls had a higher cracking tolerance than concrete. Also, each of the GFRP-ECC and SMA-SFRC walls formed a crack on the south boundary about a height of 600 mm, which is reflected in the curvature distributions of the walls. The curvature distribution of the PT-SFRC wall was asymmetric adjacent to its base as the specimen formed more cracks on its north side (Fig. 4.9(c)).

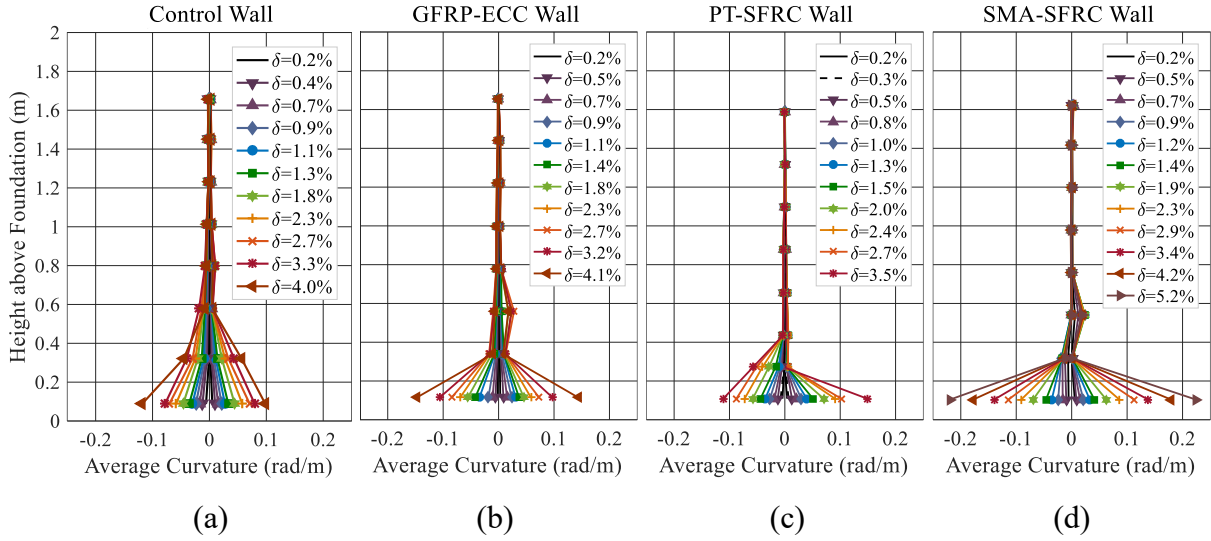


Figure 4.9. Distribution of average curvature for (a) CW, (b) GFRP-ECC, (c) PT-SFRC, (d) SMA-SFRC walls

#### 4.4.4 Shear Strain Distribution

As shown in Fig. 4.4(a), the height of each shear wall was divided into eight stripes. The average shear strain along the height of each stripe was determined based on the change in the length of two diagonals of each stripe, according to Eq. 4.1, which was proposed by Oesterle et al. (1976).

$$U_s = \frac{(d'_1 - d_1)d_1 - (d'_2 - d_2)d_2}{2HL} \quad (4.1)$$

In Eq. 4.1,  $L$  is the horizontal distance between the diagonals at the base of each stripe,  $d_1$  and  $d_2$  are the original lengths of the diagonals at the beginning of testing, and the parameters  $d'_1$  and  $d'_2$  are the lengths of the diagonal at different stages of testing.

The shear strain was at its maximum at the base of each shear wall and decreased with the height of the wall. The shear strain was higher at the base of the control wall in comparison to other specimens (Fig. 4.10) since CW formed multiple shear cracks adjacent to its base. In the case of the innovative specimens, shear strains decreased more rapidly with the height of the wall as the innovative walls formed fewer cracks in comparison to the control wall. This was because the innovative shear walls had a rocking response above their base crack, which resulted in the relatively small deformations of their upperparts since the self-centering reinforcements were either unbonded or had lower bond strengths than deformed steel bars.

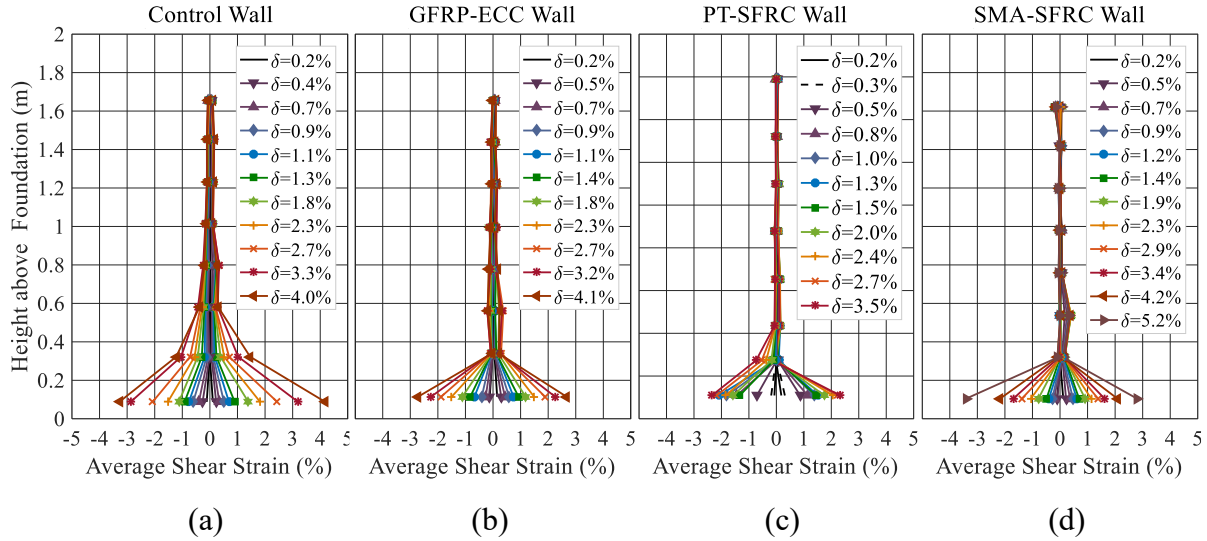


Figure 4.10. Distribution of average shear strains for (a) CW, (b) GFRP-ECC, (c) PT-SFRC, (d) SMA-SFRC

The average shear strain at the base of each shear wall versus the drift ratio applied to the wall is shown in Fig. 4.11. Shear strains in the SMA-SFRC wall were minimum in comparison to other specimens. This was because of the rocking behavior of the wall caused by the lower bond strength, stiffness, and yield strength of NiTi bars in comparison to 10M steel rebars. As a result, the wall had relatively greater flexural and smaller shear deformations with respect to other specimens.

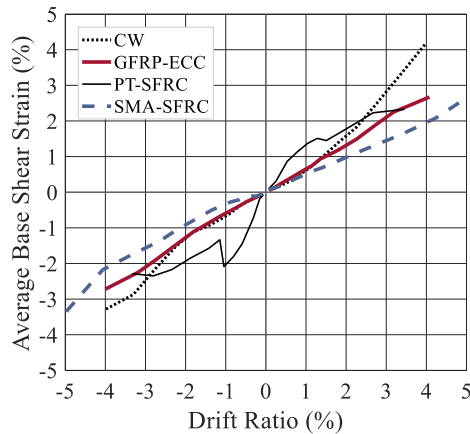


Figure 4.11. Average shear strain at base of walls

The PT-SFRC wall experienced the greatest shear strains for drift ratios between  $-2.5\%$  and  $2.5\%$ . This can be attributed to the presence of post-tensioning compressive stresses in the wall, which

increased the stiffness of the wall. Therefore, the wall underwent greater shear and less flexural deformations with respect to other specimens. However, with the propagation of a flexural crack across the length of the wall, shear strains decreased. This was because more lateral displacements were accommodated by flexural deformations afterward. For the control and GFRP-ECC walls, shear strains were comparable for drift ratios less than or equal to 1% on each side. Then, the control wall underwent higher shear strains as the wall formed more shear cracks.

#### 4.4.5 Wall Deformation Decoupling

As discussed earlier, the vertical and horizontal displacement measurements obtained from the DIC system were used in the calculation of the flexural and shear response of each specimen during the loading and unloading stages of testing. The contribution of the flexural and shear displacements into the total drift ratio of each shear wall is shown in Fig. 4.12. According to the figure, between 80% and 90% of the drift ratio of the control wall was accommodated by flexure. This was between 85% and 95% for the GFRP-ECC and SMA-SFRC walls, and between 68% and 90% for the PT-SFRC wall. At the beginning of testing, the PT-SFRC wall experienced more shear displacements in comparison to other specimens. However, after the wall formed flexural cracks, shear displacements in the PT-SFRC wall became comparable to those of other specimens.

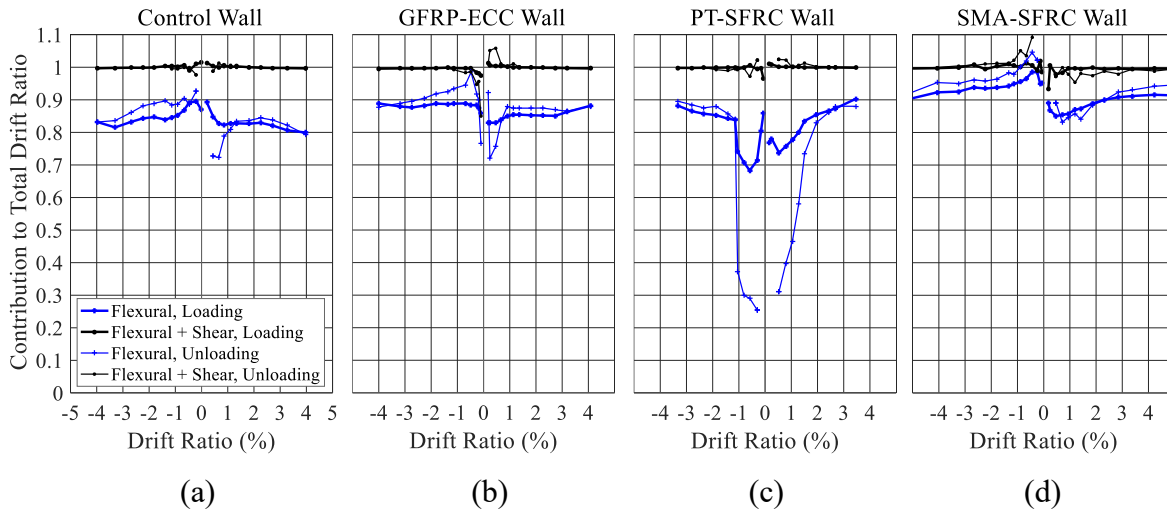


Figure 4.12. Decomposition of flexural and shear drift ratios for (a) CW, (b) GFRP-ECC, (c) PT-SFRC, (d) SMA-SFRC

It is worth mentioning that the foundation of each shear wall was restrained against horizontal displacements with metal wedges. Each foundation was also bolted to the strong floor of the lab with six post-tensioned rods to prevent the foundations from rocking. In addition, the DIC system eliminated horizontal rigid body displacements of the specimens. Thus, only flexural and shear displacements are shown in Fig. 4.12.

Similar calculations were made to decouple the permanent flexural and shear deformations of each specimen after unloading. As Fig. 4.12 shows, permanent drift ratios mainly consisted of permanent flexural drifts. For example, more than 70% of the permanent drift ratio in the control wall and GFRP-ECC wall, and 85% of the permanent drift ratio in the SMA-SFRC wall were comprised of permanent flexural drift ratios. However, in the case of the PT-SFRC wall, permanent shear deformations were more significant at the beginning of testing. For example, permanent flexural drifts made up less than 30% of the permanent drift ratios of the PT-SFRC wall for drift ratios between  $-0.4$  and  $0.4$ . This was because the un-cracked wall was able to recover most of its flexural displacements but not the shear displacements upon unloading. After the wall cracked, the permanent flexural displacement in the PT-SFRC wall increased and made up more than 85% of the permanent drift ratios of the wall at the end of testing (3.3% drift).

Figure 4.13 shows the ratios of shear to flexural displacements in the shear walls at different drift ratios. The ratio of shear to flexural displacements in the control wall increased from 0.14 to 0.2, plateaued between drift ratios of 0.7% to 2.7%, and then reached 0.25 at 4.0% drift. The increase in the shear to flexural displacements ratio of the CW can be attributed to the fact that the wall formed more shear cracks, as the experiment progressed, facilitating more shear deformation. On the other hand, the ratio of shear to flexural displacements in the innovative specimens was generally descending as the walls formed flexural cracks rather than shear cracks. The ratio of shear to flexural displacements in the GFRP-ECC wall decreased from 0.21 to 0.18, plateaued between 1.0% and 2.8% drifts, and then decreased to 0.13 at 4.1% drift. For the SMA-SFRC wall, shear to flexural ratio was about 0.16 up to a drift ratio of 1.0%. Then, it decreased and plateaued about 0.10 between drift ratios of 2.3% and 5.0%. For the post-tensioned wall, the ratio of shear to flexural deformations dropped to 0.11 at 3.3% drift, after experiencing a slight increase to 0.37 at 0.5% drift.

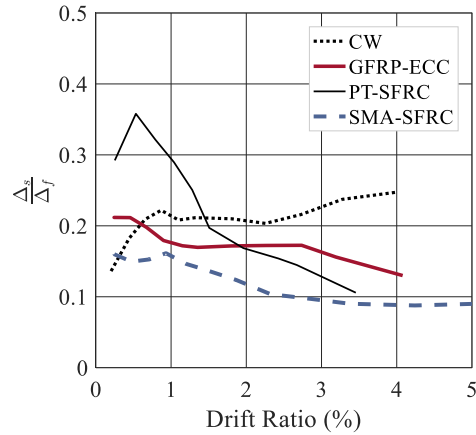


Figure 4.13. Ratio of shear to flexural displacements

As can be seen in Fig. 4.13, the ratio of shear to flexural displacements in each of the CW, GFRP-ECC, and SMA-SFRC were constant at parts of their lateral displacement range. Therefore, shear deformations of these walls can be estimated by a factor of their flexural deformations. On the other hand, the shear to flexural displacements ratio of the PT-SFRC wall, which descended from a drift ratio of 0.5% to 3.3%.

## 4.5 Design Parameters

### 4.5.1 Stiffness

The peak-to-peak stiffness of each specimen is shown in Figure 4.14(a). The control wall, which was cast with concrete, showed a lower initial stiffness in comparison to other specimens cast with FRCC. At a drift ratio of 0.15%, the stiffness of the control wall was 18.6 kN/mm, while it was 26.1, 29.6, and 48.8 kN/mm for the SMA-SFRC, GFRP-ECC, and PT-SFRC walls. The stiffness of each specimen decreased as higher drift ratios were applied to the walls. The decrease in the stiffness of the innovative walls was more steeply as the fiber reinforcement of the walls was pulled out due to cracking.

Figure 4.14(b) illustrates the relative stiffness of the innovative walls to that of the control wall. In the case of the SMA-SFRC wall, relative stiffness varied from 2.1 to 0.9. For the GFRP-ECC wall, relative stiffness changed between 2.2 and 1.4, and it was between 2.4 and 1.7 for the PT-SFRC wall. It is also worthwhile to mention that casting the steel-SMA and steel-GFRP reinforced walls with FRCC, provided the walls with an adequate initial stiffness with respect to the control wall.

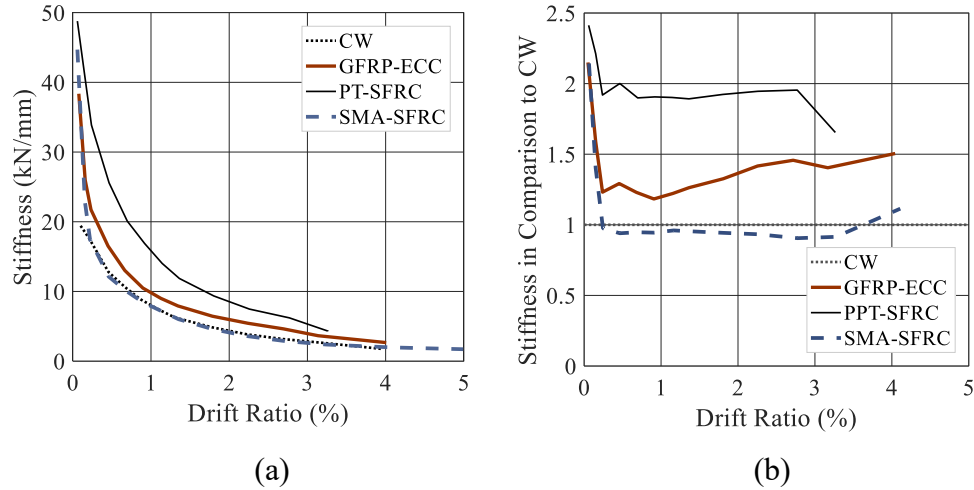


Figure 4.14. Peak-to-peak stiffness (a) calculated, (b) relative to CW

#### 4.5.2 Inelastic Rotational Capacity

Rotational deformation at the top of each specimen was calculated based on the vertical elongations measured with the DIC system on the north and south sides of the specimens ( $V_S$  and  $V_N$ ) and the distance between the two measurements,  $l$ , as shown in Eq. 4.2.

$$\theta = \frac{V_S - V_N}{l} \quad (4.2)$$

At the beginning of testing (drift ratio of 0.1%), rotation distributions were linear along the heights of the specimens as no major cracking or excessive straining had occurred. As the testing continued, most of the rotational deformations occurred near the base of each wall, where most of the nonlinear deformations took place. In the calculation of the inelastic rotational capacity of each specimen, the first rebar yielding of the specimen was considered as the onset of inelastic rotation. The yield rotation for each of the CW, GFRP-ECC, PT-SFRC, and SMA-SFRC walls was 0.008, 0.007, 0.002, and 0.005 rad, respectively.

The SMA-SFRC wall had an inelastic rotational capacity of 0.058 rad, which was the highest among the shear walls, while the minimum capacity was for the PPT-SFRC wall with an inelastic rotational capacity of 0.033 rad. In the case of the control and the GFRP-ECC walls, the inelastic rotational capacity was 0.04 rad, as shown in Fig. 4.15.

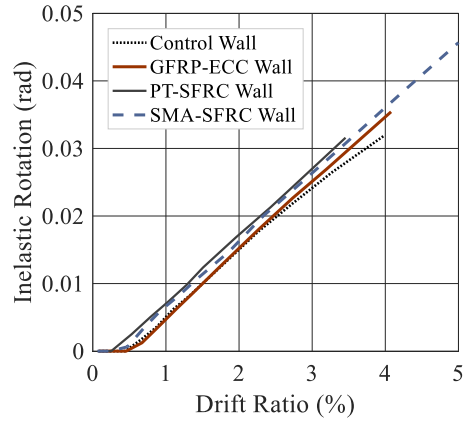


Figure 4.15. Inelastic rotational deformations at top points of walls

### 4.5.3 Plastic Hinge Length

Seismic analysis requires the calculation of the elastic and plastic deformation capacities of the force-resisting elements of a structure to assess the adequacy of the elements against displacement demands. In order to conduct this ductility check, an accurate determination of the plastic hinge length is important.

To perform a ductility check for a cantilever shear wall, the curvature distribution of the wall is idealized, assuming that the nonlinear rotation takes place along a certain length in the lower part of the wall, known as the plastic hinge. Figure 4.16 shows an idealized cantilever wall, the actual (“true”) curvature distribution of the wall measured during an experiment, and the idealized curvature distribution of the wall. The difference between the two is due to cracking, localized yielding, and rigid body rotation that occurs in a real structure.

The flexural displacement at the top of the wall,  $\Delta_f$ , is considered as the sum of the yield and plastic flexural displacements of the wall, termed  $\Delta_{fy}$  and  $\Delta_{fp}$ , respectively. The curvature at the base of the wall,  $\phi_{base}$  is considered as the sum of the yield and plastic curvatures of the wall, termed  $\phi_y$  and  $\phi_p$ , respectively. In Figure 4.16, the plastic hinge length of the wall is termed  $L_p$ .

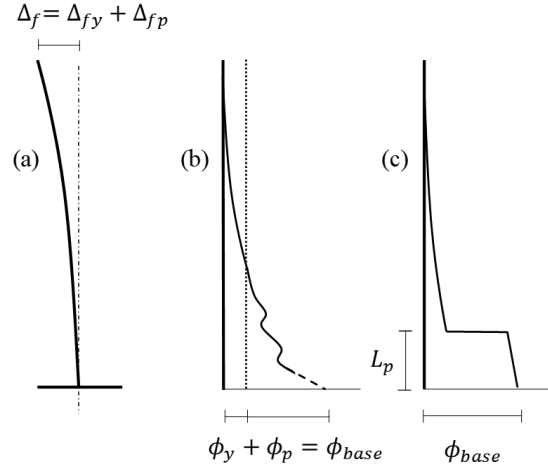


Figure 4.16. Plastic hinge analysis (a) idealized cantilever wall (b) true curvature distribution, (c) idealized curvature distribution

The curvature is the gradient of longitudinal strains along the length of a shear wall. To calculate the longitudinal strain along the height of each specimen, two methods were used. One method consisted of using the longitudinal elongations measured on the surface of each wall measured with the DIC system. The other method was to use the rebar strains of the walls, which were measured with strain gauges.

Rebar strains were selected to be used in the calculation of the curvature along the walls. This was because to accurately detect the plastic strain occurred along the rebars of the specimens since the bond between the self-centering reinforcement and their surrounding cement-based composites was not as strong as the bond of the deformed steel rebars and concrete used in conventional RC walls is. For this reason, the self-centering reinforcement could slip through their surrounding material, which increased the rocking response of the innovative walls compared to the control wall.

Figure. 4.17 shows the distribution of longitudinal strains along the rebar R1 of each shear wall, which is specified in Fig. 4.1. As can be seen in the figure, tensile strains increased significantly at the bases of the shear walls due to rebar yielding. Plastic deformations occurred over a longer segment of the control wall with respect to the GFRP-ECC and PT-SFRC walls. This can be attributed to the fact that the control wall formed more cracks in comparison to the forgoing walls. In the case of the SMA-SFRC wall, the SMA bars experienced relatively uniform strain

distributions due to the lack of strong bonding between the SMA bars and their surrounding SFRC matrix and the low modulus of elasticity of the SMA bars compared to the steel rebars.

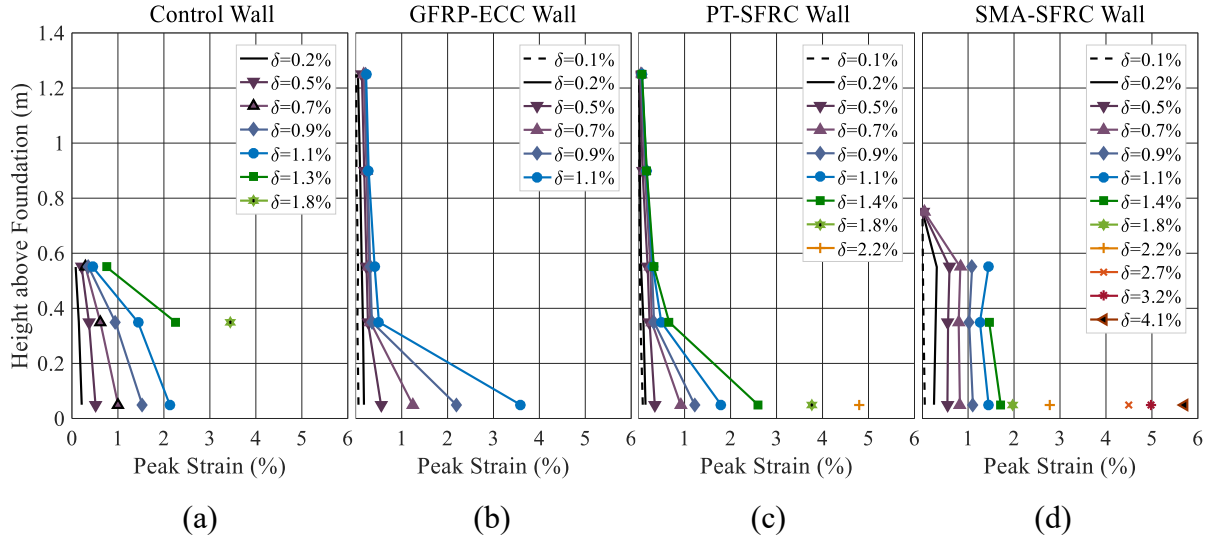


Figure 4.17. Longitudinal strain along outmost boundary reinforcement (R1) in (a) CW, (b) GFRP-ECC, (c) PT-SFRC, (d) SMA-SFRC

The curvature distribution along the height of each shear wall was obtained as the gradient of boundary rebar strains over the length of the wall using Eq. 4.3. The calculated curvatures are shown in Fig. 4.18. In Eq. 4.3,  $\varepsilon_{b1}$  and  $\varepsilon_{b2}$  are the boundary rebar strains of each shear wall. The yield curvature of each wall corresponded to the yielding of the outmost steel rebars of the wall. In the case of the SMA-SFRC wall, the yield curvature corresponded to the yielding of the outmost web reinforcement of the wall. This was because the outmost rebars in the web of the SMA-SFRC wall reached the yielding before the SMA bars reached their stress plateau. The yield curvature in the CW, GFRP-ECC, PT-SFRC, and SMA-SFRC walls was 3.0, 2.8, 3.1, and 5.8 rad/km, respectively.

$$\phi = \frac{\varepsilon_{b1} - \varepsilon_{b2}}{l_w} \quad (4.3)$$

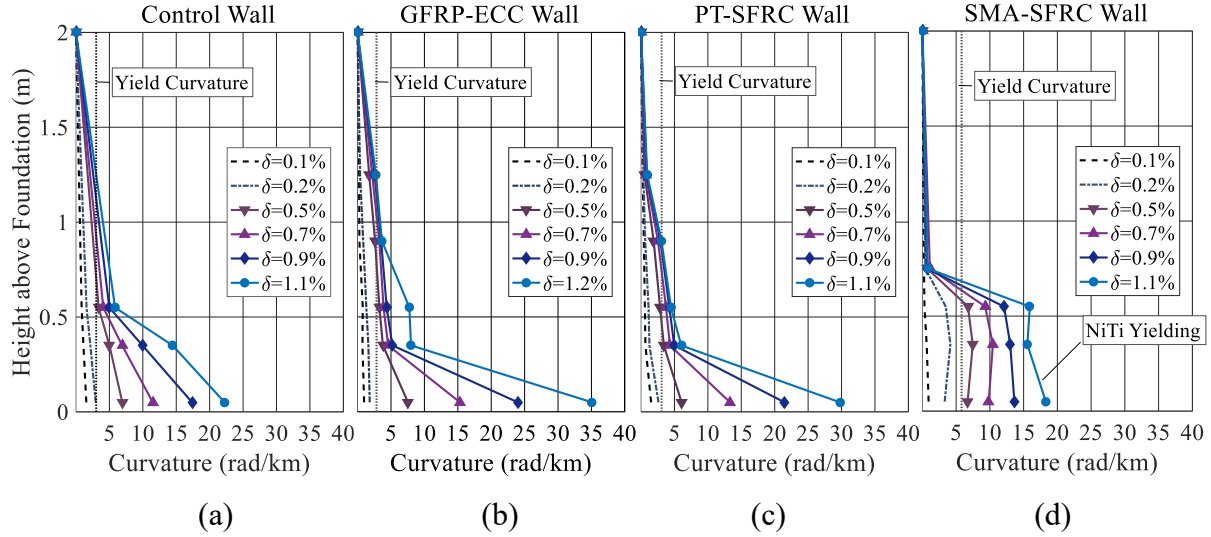


Figure 4.18. Curvature distribution along (a) CW, (b) GFRP-ECC, (c) PT-SFRC, (d) SMA-SFRC

The plastic hinge length of each wall was calculated in terms of the plastic flexural displacement, the plastic base curvature, and the height,  $H$ , of each shear wall, as shown in Eq. 4.4.

$$\Delta_{fp} = \phi_p L_p \left( H - \frac{L_p}{2} \right) \quad (4.4)$$

The plastic hinge length of the control wall changed between 500 mm and 380 mm between drift ratios of 0.46% and 1.13% (Fig. 4.19). For the GFRP-ECC wall, the plastic hinge length varied between 280 mm and 230 mm, and for the PT-SFRC wall, the plastic hinge length was from 430 mm to 250 mm. The plastic hinge was shorter in the GFRP-ECC and PT-SFRC walls compared to the CW wall. This was because the base curvatures of the GFRP-ECC and PT-SFRC walls were higher compared to the control wall. For the SMA-SFRC wall, plastic hinge length changed between 460 mm and 600 mm, which is approximately the length of the SMA reinforced region of the wall. As shown in Fig. 4.18, tensile strains along the SMA bars were almost constant, which was because of the low bond stress of the bars. As a result, uniform curvature distributions, which were already similar to the idealized curvature distributions, were obtained along the SMA reinforced part of the wall (0.5 m). The plastic hinge length of the wall was about 0.5 m, as shown in Fig. 4.19.

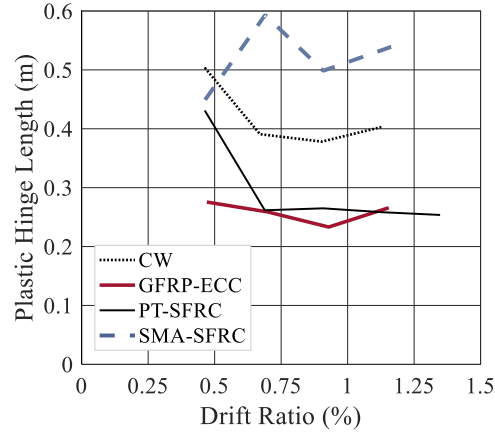


Figure 4.19. Plastic hinge length

Compared to  $0.5l_w$ , the plastic hinge length proposed by Park and Paulay (1975) for RC shear walls, the plastic hinge of the CW wall was between 76% and 100% when the drift ratio of the wall was between 0.46% and 1.13%. The ratio of the plastic hinge length to  $0.5l_w$  was between 46% and 56% for the GFRP-ECC wall, between 46% and 56% for the PT-SFRC wall, and between 92% and 120% for the SMA-SFRC wall.

#### 4.5.4 Self-Centering Moment

The restoring moment generated by the self-centering reinforcement and axial loads in RC shear walls is termed the self-centering moment. The self-centering moment is a parameter that explains the reason behind the ability of the innovative shear walls to recover the drift ratios they were subjected to. To calculate the self-centering moment of each innovative wall, first, the force in the self-centering reinforcement of the wall was calculated based on the longitudinal strains and the stress-strain relationship of the self-centering reinforcement at the base of the wall. Then, the distance between each self-centering reinforcement and the resultant compressive force in the concrete of the wall was calculated.

To calculate the distance between the force of each self-centering reinforcement and the resultant compressive force in each shear wall, first, the neutral axis and the distance,  $c$ , of the neutral axis from the extreme compression fiber at the base of the wall were determined (Fig. 4.20). The neutral axis is found by determining the point at which the strain is zero. The point with a zero strain was determined using the rebar strain at the boundaries of the walls. Then, the distance  $l_c$ , the distance

between the neutral axis and the resultant concrete compressive force at the base of each innovative wall was approximated by  $\frac{2}{3}c$ .

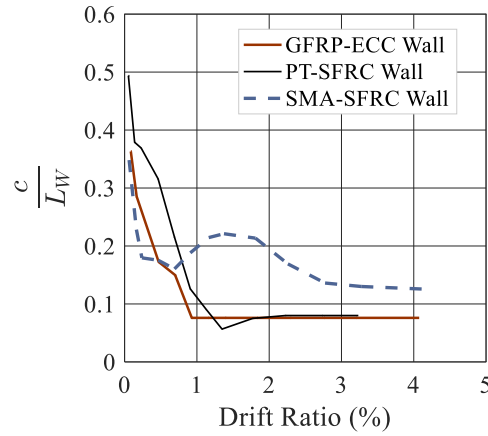


Figure 4.20. Distance of neutral axis from extreme compression fiber at bases of walls normalized to lengths of walls

It is important to have a close estimation of the distance  $l_c$  since it is in the calculation of the self-centering moment in shear walls. When the compressive stresses distribution of concrete at the toe of a shear wall is linear,  $l_c$  is equal to  $0.67c$ . Then, with the response of the concrete becoming nonlinear, the resultant compressive force of the distribution moves towards the neutral axis of the section, which reduces the distance  $l_c$ . A lower bound to  $l_c$  is  $0.50c$ , which corresponds to the case of the uniform compressive stress distribution.

As discussed earlier, the self-centering reinforcement moment of each innovative shear wall was calculated, assuming  $l_c$  is equal to  $0.67c$  since a reliable measurement for the compressive stress at the toes of the shear walls was not available. This assumption is valid since, at the beginning of testing, the distribution of compressive stresses in the shear walls was linear, the upper and lower bounds to the distance  $l_c$  are close, and the distance  $c$  decreases as the response of concrete becomes nonlinear.

As the experiments went on, greater drift ratios were applied to the walls, which caused the walls to undergo greater lateral deformations and, consequently, greater base curvatures. This resulted in the neutral axes of the shear walls shifting from their mid-sections toward their boundaries, which increased the self-centering moment of the walls. However, during unloading, the neutral

axes of the shear walls moved back toward their mid-sections as the demand for high lateral deformations and curvatures decreased on the shear walls. This also decreased the self-centering moment in the walls.

With the release of lateral loads, the self-centering moments caused a recovery in the plastic strain of the steel reinforcement in the innovative shear walls, which resulted in a reduction in the permanent drift ratios of the walls. Despite other specimens, the PT-SFRC wall had the highest self-centering moment, even at the very beginning of testing, which was because of the presence of tensile stresses in the post-tensioned strands of the wall. The self-centering moments of the PT-SFRC and GFRP-ECC walls increased with the lateral displacement demands of the walls reaching 430 and 281 kN.m respectively at a 3.2% drift, which comprised over 70% and 60% of the resisting moments of the walls, respectively. In the SMA-SFRC wall, the self-centering moment was almost constant at drift ratios greater than or equal to 1%. The self-centering moment reached 144 kN.m at a 3.2% drift, comprising about 50% of the resisting moment of the wall. Figure 4.21 shows the self-centering moments of the innovative walls during testing.

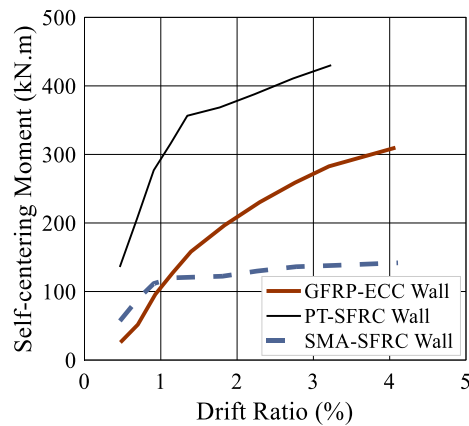


Figure 4.21. Self-centering moment

Adequate amounts of self-centering reinforcement should be incorporated into an innovative shear wall for reaching desired levels of drift ratio recovery. For this reason, appropriate amounts of the self-centering moment should be developed in the shear wall to recover the plastic strains suffered by the steel reinforcement of the wall. To study the underlying reason for the improved self-centering of the innovative walls, the ratio of drift ratio recovery in the innovative walls over that of the control wall was calculated for different self-centering moments of the innovative walls (Fig

4.22). In Fig. 4.22, the self-centering moment in each innovative wall is shown relative to the resisting moments of the wall, calculated as the lateral force of the wall multiplied by the height of the wall. In Fig. 4.22, a zero ratio of self-centering to resisting moments corresponds to a conventional RC wall, while it means all of the longitudinal reinforcements in a shear wall are self-centering when the ratio of self-centering to resisting moments is equal to unity.

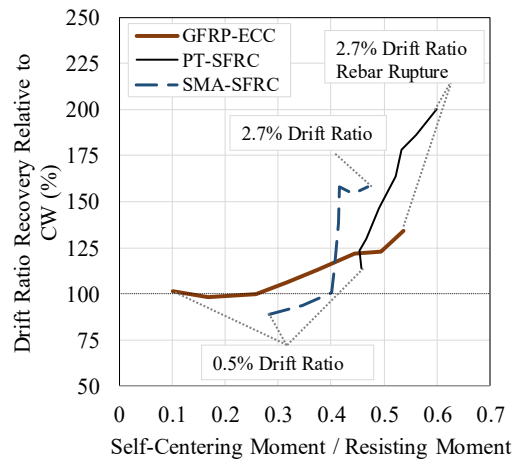


Figure 4.22. Ratio of self-centering over resisting moments for specimens

The self-centering moment comprised 0.1 to 0.53 of the resisting moment of the GFRP-ECC wall when the drift ratio changed from 0.5% to 2.7%. The wall had a reduced permanent drift ratio with respect to the control wall when, at 0.9% drift, more than 0.26 of its resisting moment was self-centering. The GFRP-ECC wall showed a -2% to 34% improvement in the drift ratio recovery with respect to the control wall. This means the self-centering reinforcement incorporated in the GFRP-ECC wall was not enough to generate 0.26 of the resisting moment of the wall from the beginning of testing.

The self-centering moment in the PT-SFRC wall comprised from 0.48 to 0.60 of the resisting moment of the wall as the drift ratio of the wall increased from 0.5% to 2.7%. The wall had an improved drift ratio recovery from the beginning of testing and showed a 14% to 100% improvement in the drift ratio recovery compared to the control wall. This means the self-centering reinforcement used in the PT-SFRC wall was adequate to enhance the drift ratio recovery of the wall from the beginning of testing.

The self-centering moment comprised from 0.29 to 0.47 of the resisting moment of the SMA-

SFRC walls as the drift ratio of the wall increased from 0.5% to 2.7%. The wall had a lower drift ratio recovery than the control wall until more than 40% of the resisting moment of the wall, at 0.9% drift, was made up of the self-centering moment. The SMA-SFRC wall had a -11% to 58% improvement in the drift ratio recovery compared to the control wall. This means the self-centering reinforcement incorporated in the SMA-SFRC wall was not enough to trigger further drift ratio recovery compared to the control wall from the beginning of testing.

## 4.6 Implications for Design

### 4.6.1 Reinforcement Layout

It is important to use appropriate reinforcement layouts in the design of innovative shear walls. This is because the self-centering reinforcement has different mechanical properties, such as stiffness, ultimate strain, and ultimate strength, in comparison to conventional steel rebars. The innovative shear walls of this study were designed in order to have comparable deformation capacities and increased self-centering in comparison to the control wall.

Since excessive localized rebar straining led to the resistance degradation and failure in the shear walls, the strain envelopes of the outmost boundary and web reinforcement (R1 and R3 as defined in Fig. 4.1) of the shear walls were studied. The strain in the forgoing rebars at 50 mm above the foundation is shown in Fig. 4.23(a) and (b), respectively. The strain curves of Fig. 4.23 have different lengths, as different strain gauges went out of order at different stages of testing.

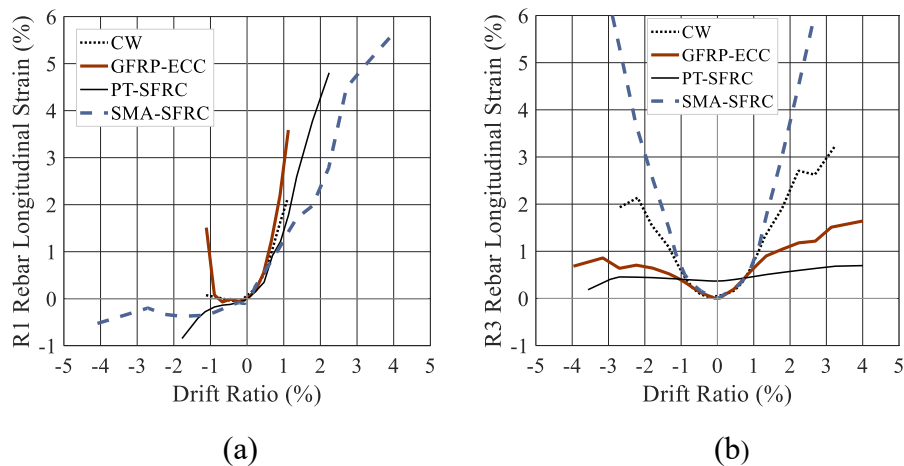


Figure 4.23. Longitudinal strain at 50 mm above foundation in (a) R1, (b) R3

At 1.1% drift, the tensile strain in the R1 rebar of the GFRP-ECC wall was 3.6% and was higher than the tensile strain in the R1 rebars of other shear walls. This was because at the early stages of testing, the GFRP bars of the specimen, which had a lower stiffness in comparison to 10M steel rebars, were not effectively participating in resisting tensile stresses. For this reason, it is recommended to place adequate steel reinforcement in the web of a steel-GFRP reinforced shear wall to prevent excessive demand on the boundary steel bars. The steel reinforcement in the web of the wall helps to control crack opening in the steel-GFRP reinforced shear wall.

At 1.1% drift, the outmost SMA bars of the SMA-SFRC wall experienced a tensile strain of 1.4%, which was lower than the tensile strain in the R1 rebars of other specimens. This can be attributed to the smooth surface of the NiTi bars, which caused a weaker mechanical bond for the SMA bars in comparison to 10M steel rebars. Also, at 4.0% drift, the tensile strain in the SMA bars was less than 6.0%, the limit after which the self-centering of the bars declines. This shows that the length of the SMA bars was adequate for the SMA-SFRC wall. The shorter length of SMA would result in higher strain demands on the SMA bars.

The outmost steel rebars in the PT-SFRC wall experienced a peak strain of 1.8%, at 1.1% drift. The demand on the R1 bars of the PT-SFRC wall was comparable to that of the control wall, which was 2.1% at 1.1% drift. The similarity between the demand on the R1 bar in the PT-SFRC and CW walls can be attributed to the comparable bonded reinforcement ratio in the walls.

At 3.2% drift, the R3 rebars in the control wall experienced a strain demand of 3.2%. In the GFRP-ECC wall, the R3 bars were made of GFRP, which experienced a tensile strain of 1.5% at 3.2% drift. The lower strain demand on the GFRP bars can be attributed to the linear stress-strain relationship of the bars and their lower bond strength in comparison to deformed the steel bars. As a result, the GFRP bars did not reach their ultimate strain of 2.1% before a boundary steel rebar rupturing. This shows that the location of the GFRP bars in the middle segment of the web of the GFRP-ECC wall was appropriately chosen to protect the bars from high tensile strains.

At 3.2% drift, the R3 rebar in the SMA-SFRC wall reached a tensile strain of 7.8%, which was the highest in comparison to the tensile strains of other R3 rebars. This can be attributed to the lower stiffness and bond stress of SMA bars in comparison to 10M steel rebars, which caused more

demands being undertaken by their adjacent R3 steel rebars. For this reason, the R3 rebar in the SMA-SFRC wall ruptured at a drift ratio of 5.0%, which was beyond the ultimate drift ratio of the control wall. The reason that the R3 rebars in the SMA-SFRC wall did not fracture at the early stages of testing was that the bars were placed 200 mm away from their adjacent SMA bars. The 200 mm distance between the SMA and steel bars protected the steel bars from the high tensile strains caused by the rocking nature presented in the response of the wall. For this reason, it is recommended that when affordable, the outmost rows of steel reinforcement in the web of a steel-SMA reinforced wall have a minimum distance of 200 mm from their adjacent SMA bars.

The R3 reinforcement in the PT-SFRC wall consisted of four post-tensioned high-strength strands. Since the strands were unbonded, they only reached a strain of 0.7% at 3.2% drift. This is particularly important since the tendons should not reach the yielding (1.0% strain) to maintain their self-centering properties. Thus, it can be concluded that the post-tensioned tendons of the wall were appropriately post-tensioned to about 40% of their yield strength and placed at one-third and two-thirds of the web of the PT-SFRC wall.

#### **4.6.2 Rotational Capacity**

CSA A23.3-14 and ACI 318-14 have similar provisions that provide shear walls with adequate boundary elements. These provisions ensure that shear walls avoid early failure. Provided the boundary elements of a shear wall are adequate, the inelastic rotational capacity of the wall is controlled by a limiting tensile strain for the rebars of the wall.

The ultimate curvature at the base of an RC shear wall can be estimated as  $\phi_u = (\epsilon_s + \epsilon_c)/l_w$  where  $\epsilon_s$  is a limiting tensile strain for steel bars,  $\epsilon_c$  is the maximum compressive strain of concrete and  $l_w$  is the wall length. As a result, the inelastic rotational capacity of the wall equals  $0.5(\epsilon_s + \epsilon_c) - 0.002$  assuming the plastic hinge length of the wall is  $0.5l_w$  based on Park and Paulay (1975). Then, by specifying a 5% limit to the tensile strain of steel bars and a concrete maximum compressive strain of 0.0035, an upper limit of 0.025 rad is obtained to the inelastic rotational capacity of slender RC shear walls, which is required by CSA A23.3-14.

To calculate the inelastic rotational capacity of SMA-SFRC walls, two limiting tensile strains should be used – a strain limit of 6% corresponding to the strain recovery limit in SMA bars and

a strain limit of 5% regarding the fracture of steel rebars located adjacent to the SMA bars. A uniform strain of 6% in the outmost SMA bars of an SMA-SFRC wall corresponds to a greater than 5% strain in the adjacent steel bars of the SMA bars. For this reason, a limiting tensile strain of 5% was used for the first row of steel reinforcement in the web of the wall.

As shown in Fig. 4.24(a), a uniform strain of 4.6% to 3.5% is developed in the outmost SMA bars of 1 m to 10 m long shear walls assuming each boundary element of the wall has a length of  $0.15l_w$  and the first row of steel rebars is placed 200 mm away from their adjacent SMA bars. It was also assumed that longitudinal strains were distributed linearly along the web of the shear walls, a strain of 0.02% was at  $0.5L_w$  above the foundation of the first row of steel bars (Fig. 4.25(b)), and a strain of 5% at the base of the bars (Fig. 4.25(c)). Also, the inelastic rotational capacity in SMA-SFRC walls with lengths of 1m to 10 m was calculated to be from 0.035 to 0.029 rad, as shown in Fig. 4.24(c). The inelastic rotational capacity calculations were based on the assumption that the length of SMA reinforcement in the wall is equal to  $0.5l_w$ , and the plastic hinge length of the wall is  $0.5l_w$ . As shown in Fig. 4.19, the assumptions are in line with the calculated plastic hinge length of the SMA-SFRC wall for drift ratios between 0.46% and 1.16%.

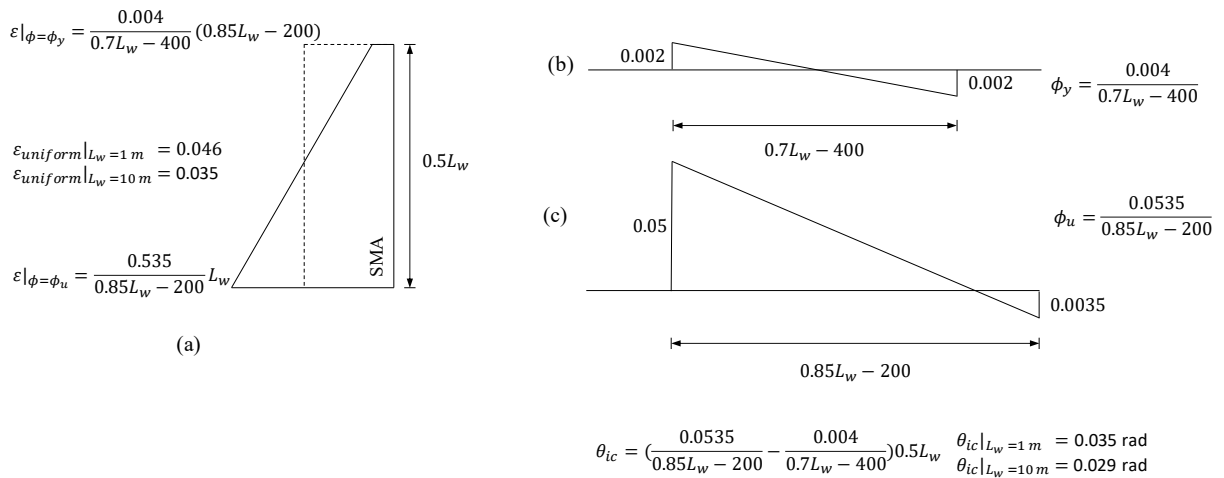


Figure 4.24. Refined calculations for (a) strain along SMA bars, (b) yield curvature (c) ultimate curvature and inelastic rotational capacity

In the GFRP-ECC and PT-SFRC walls, the plastic hinge length was shorter than in the control wall, which means that it can be unconservative to design the walls with a plastic hinge length of  $0.5l_w$ . According to Fig. 4.19, the plastic hinge length in the GFRP-ECC and PT-SFRC walls was

56% of  $0.5l_w$  at a 1.1% drift. Assuming the ratio of plastic hinge length in the GFRP-ECC and PT-SFRC walls over that of CW remains constant, an upper-limit for the inelastic rotational capacity of 0.014 rad ( $0.56 \times 0.025$  rad) can be calculated for the tested walls. The results discussed above are limited to the tested walls, which included one wall for each type of innovative wall studied. The walls also had zero axial loads.

### 4.6.3 Drift Ratio Recovery

In the performance-based design of structures, the performance level of shear walls can be assessed using the maximum transient drift ratios the walls have experienced. FEMA 273 and FEMA 356 limit the maximum transient drift ratios of shear walls to be 0.5%, 1%, and 2% in the IO, LS, and CP levels of performance, respectively. According to FEMA, the permanent drift ratio of a concrete shear wall should be negligible in the IO performance level, lower than 0.5% in the LS level, and it can have a maximum permanent drift ratio of 2.0% in the CP performance level. Assuming a permanent drift ratio of a 0.125% for a concrete shear wall in the IO performance level according to Tolou Kian and Cruz-Noguez (2018), the minimum levels of drift ratio recovery a wall requires to comply with FEMA are 0.75, 0.5 and zero in the IO, LS, and CP performance levels.

Enhanced drift ratio recovery goals should be aimed for innovative shear walls with improved self-centering. Three enhanced self-centering design objectives, which improve upon the self-centering goals introduced by FEMA 273. The self-centering design objectives define the minimum drift ratio recovery an innovative shear wall should have in order to satisfy the IO, LS, and CP seismic performance levels. The first enhanced self-centering design objective (objective I) requires the permanent drift ratio criteria of FEMA 273 for the IO and LS performance levels. However, the objective requires the LS permanent drift ratio limit of FEMA, 0.5% permanent drift ratio, for the CP level. The drift ratio recovery of the shear wall must be above curve ABCDEH, shown in Fig. 4.25, to satisfy this objective. The require drift ratio recovery to satisfy a permanent drift ratio of 0.5% (the LS permanent drift ratio limit) at 2% is  $\frac{3}{4}$  or 0.75 (point H).

The enhanced self-centering design objective II requires FEMA limits for the IO performance level. However, the objective requires the IO and LS permanent drift ratio limits of FEMA, 0.125%, and 0.5% permanent drift ratio for LS and CP performance levels, respectively. The drift

ratio recovery of a shear wall must be above curve ABCIEH, shown in Fig. 4.25, to satisfy this objective. The required drift ratio recovery to satisfy a permanent drift ratio of 0.125% (the IO permanent drift ratio limit) at 1% drift is  $\frac{7}{8}$  or 0.875 (point I).

The enhanced self-centering design objective III requires the IO self-centering limit of FEMA at all drift ratios. The drift ratio recovery of a shear wall must be above curve ABCIJ, shown in Fig. 4.25, to satisfy this objective. The required drift ratio recovery to satisfy a permanent drift ratio of 0.125% (the IO permanent drift ratio limit) at 2% drift is  $\frac{15}{16}$  or 0.9375 (point J).

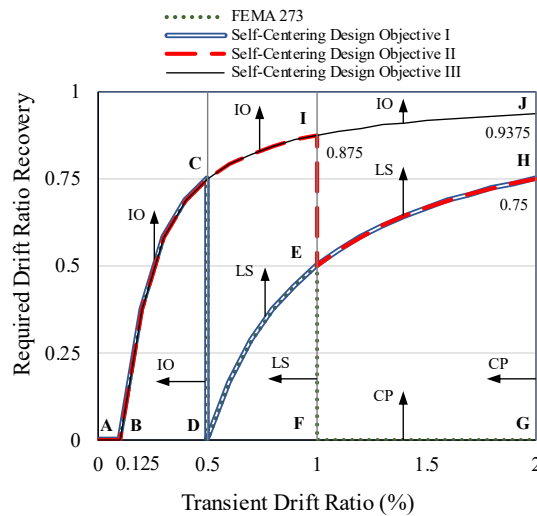


Figure 4.25. Required drift ratio recovery for different self-centering objectives

Figure 4.26 shows the drift ratio recovery obtained by each shear wall. The self-centering properties of the PT-SFRC wall were in accordance with the enhanced self-centering design objective II. The SMA-SFRC wall satisfied the enhanced self-centering design objective I, except for a slight shortcoming just before 0.5% drift. The CW and GFRP-ECC walls followed FEMA self-centering goals recommended for conventional RC shear walls.

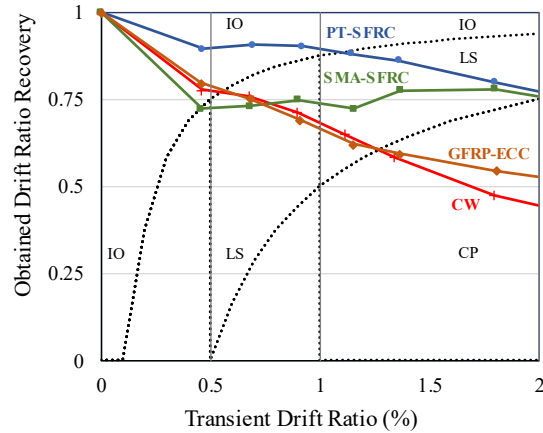


Figure 4.26. Drift ratio recovery of shear walls

## 4.7 Conclusions

The following conclusions were drawn from the study performed on the seismic and design parameters of three types of innovative shear walls with improved self-centering and damage mitigation properties.

- The innovative shear walls had lower permanent drift ratios than the control wall. For this reason, three self-centering objectives were introduced for designing innovative walls. The new objectives improved upon FEMA self-centering limits recommended for RC shear walls at different performance levels. In this regard, the PT-SFRC and SMA-SFRC walls met the self-centering objective II and I, respectively, while it was the FEMA self-centering objectives for the GFRP-ECC and control walls.
- The ratio of the self-centering moment over the resisting moment was 48%, 29%, and 10% in the case of PT-SFRC, SMA-SFRC, and GFRP-ECC walls at 0.5% drift. This was the reason that the PT-SFRC wall had improved self-centering from the beginning of testing. The self-centering in the GFRP-ECC and SMA-SFC walls was improved compared to the control wall when the ratio of the self-centering moment over the resisting moment in the walls went over 26% and 40%, respectively.
- The innovative walls tended to demonstrate rocking behavior. This was because the walls were cast with FRCC and reinforced with smooth or unbonded self-centering reinforcement. As a result, the walls formed fewer flexural cracks above their bases, and the cracks had a greater opening in

comparison to the cracks formed in the control wall.

- The reinforcement layout in the innovative shear walls was designed in a way that the failure of the wall was not triggered by the failure of the self-centering reinforcement of the wall. For this reason, self-centering reinforcements with desirable elastic behavior, such as GFRP bars and high strength steel strands, were placed in the middle thirds of the webs of GRP-ECC and PT-SFRC walls. The SMA bars had a ductile super-elastic behavior and were placed in the boundaries of the SMA-SFRC wall. In the SMA-SFRC wall, the first rows of steel reinforcement were placed with a 200 mm distance from the boundary elements of the wall to be protected from high levels of localized tensile strain.
- The SMA-SFRC walls had an inelastic rotational capacity of 0.058 rad, which was the greatest in comparison to 0.04 and 0.03 rad, the inelastic rotational capacity of the GFRP-ECC and PT-SFRC walls. This was because the SMA-SFRC wall did not undergo rebar rupturing in the boundary elements despite the other shear walls.
- Between drift ratios of 0.5% and 1.1%, plastic hinge length in the GFRP-ECC and PT-SFRC walls was shorter in comparison to the control wall. This was due to the rocking response of the walls. In the SMA-SFRC wall, the plastic hinge was up to the top of the SMA reinforced region of the wall when the drift ratio was between 0.5% 1.1%. This was because the SMA bars had lower stiffness and bond stress values than steel.
- Shear deformations were more significant in the control wall than in the innovative walls, except for the PT-SFRC wall at the beginning of testing. The ratio of shear to flexural displacements was ascending for the control wall, while it was descending for the innovative walls. This can be attributed to the cracking pattern and the rocking response of the innovative walls.
- The innovative shear walls, which were cast with FRCC, showed higher initial stiffness than the control wall. This was more notable in the case of the steel-SMA and steel-GFRP reinforced walls, which are prone to having low stiffness due to the lower elastic modulus of SMA and GFRP in comparison to steel.

## CHAPTER 5 ANALYSIS MODEL FOR INNOVATIVE SHEAR WALLS

### 5.1 Abstract

Recent studies have shown that innovative reinforced concrete (RC) shear walls that have improved self-centering can effectively reduce the permanent drift ratios of building structures while providing them adequate levels of stiffness, strength, and energy dissipation. However, the available experimental data on the innovative walls is limited due to experimental constraints and limited project scopes that consist of testing only a few specimens in each experimental campaign. One solution is to develop reliable finite-element analysis models for conventional and innovative shear walls. Performing numerical studies using analysis models that are validated with experimental results allows for the study of various parameters of the innovative walls under different loading schemes.

This chapter presents the results of a study performed on the improvement of self-centering in reinforced concrete (RC) shear walls. In this study, the finite element models of one conventional and three innovative shear walls were developed. The innovative walls were cast with fiber-reinforced concrete and detailed with 10M steel bars and a type of self-centering reinforcement consisting of shape memory alloy bars, glass fiber reinforced polymer bars, and post-tensioned high strength steel strands. It is shown that the FE models of the walls were able to closely predict the overall response of each shear wall specimen in terms of lateral force-displacement. The models were also able to provide a close prediction of the local behavior of the walls, such as cracking patterns, rebar strain, and curvature.

### 5.2 Introduction

Conventional bridge and building structures designed with traditional seismic philosophies can effectively resist strong earthquakes. However, this usually occurs at the cost of the structures sustaining significant nonlinear deformations, which can result in the structures suffering extensive damage and residual deformation. For this reason, innovative structural elements with improved self-centering properties and damage-resistant cementitious composites represent a cost-effective alternative to conventional construction, since modern structural engineering is shifting from

adequacy to sustainability.

Since bridges are generally considered as more critical than typical residential buildings, innovative materials were used in bridge structures first. Saiidi et al. (2007, 2009) and Saiidi and Wang (2006) showed a notable reduction in the residual deformations and damage of innovative bridge piers whose plastic hinge regions were detailed with engineered cementitious composites (ECC) and shape-memory alloy (SMA) bars. Cruz Noguez et al. (2012) conducted a shake table experiment on a four-span bridge specimen. The study showed the benefits of using self-centering reinforcement, such as SMA bars and post-tensioning tendons, along with ECC and elastomers in the improvement of the self-centering and damage mitigation of bridge piers. Partially post-tensioning of bridge piers was studied by Cruz Noguez et al. (2012) and Sakai and Mahin (2004). It was shown that partially post-tensioned bridge piers had significantly reduced permanent drift ratios in comparison to conventional piers in spite of substantial damage the piers sustained in the plastic hinge regions.

For building structures, a limited number of experimental studies performed on shear wall specimens are available in the literature. Holden et al. (2003) studied the cyclic response of a precast shear wall detailed with un-bonded tendons and energy dissipating bars. The study showed that the innovative wall had superior self-centering and damage mitigation with a limited energy dissipation capacity. Tolou Kian and Cruz-Noguez (2018) studied the cyclic response a monolithic post-tensioned reinforced concrete (RC) shear walls and showed that the wall had up to 66% less permanent drift ratio and energy dissipation capacity in comparison to a comparable control RC shear wall.

Abdulridha and Palermo (2014) studied the cyclic response of a steel-SMA reinforced shear wall. The study concluded that the innovative wall had substantial self-centering properties with sufficient levels of stiffness, strength, and energy dissipation. Tolou Kian and Cruz-Noguez (2018) also tested a steel-SMA reinforced shear wall with similar geometrical properties, but cast with steel fiber reinforced concrete (SFRC). The wall had a higher damage resistance; however, lower self-centering properties with respect to the former study. The steel-SMA reinforced wall tested by Tolou Kian and Cruz-Noguez (2018) had up to 58% less permanent drift ratio than the control wall of the study.

Mohamed et al. (2014) studied the cyclic response of three GFRP-reinforced concrete shear walls under an axial load ratio of 7%. The study showed that GFRP-reinforced walls had substantial self-centering and comparable levels of deformability with respect to a conventional control RC shear wall. Each of the GFRP-reinforced walls showed a lower energy dissipation capacity in comparison to the control wall of the study due to the lack of energy dissipating reinforcement in the specimens. Tolou Kian and Cruz-Noguez (2018) and Ghazizadeh and Cruz-Noguez (2018) studied a slender and a squat steel-GFRP shear wall. According to the studies, the slender and squat steel-GFRP shear walls had up to 37% and 26% less drift ratio than their corresponding RC control walls, respectively. On the other hand, energy dissipation capacity in the slender and squat steel-GFRP shear walls went as low as 62% and 85% of that their corresponding control walls.

Bohl and Adebar (2012) used VecTor2 to develop a finite element model for the shear wall specimen tested by Adebar et al. (2007). The developed model was able to calculate the curvature distribution of the wall correctly. The model was used in a parametric study on the plastic hinge length of RC shear walls. The study concluded in deriving a more accurate equation for the plastic hinge length in steel-reinforced concrete shear walls.

A simplified DRAIN-2DX (Prakash et al. 1993) model in which wall panels were modeled as fiber beam-column elements was successfully used by Kurama (2000). The model was used to study post-tensioned precast concrete walls with external systems providing additional passive energy dissipation to the walls. Kurama then proposed a design method for such systems. (Kurama et al. 1999; Kurama 2005) studied the response of six-story post-tensioned precast concrete walls with different reinforcement layouts through fiber element modeling and proposed a design method for these walls to resist code specific design basis earthquakes.

Alam et al. (2009, 2012) used the fiber modeling approach in SeismoStruct (Seismosoft 2010) to study the seismic performance of RC frames detailed with steel-SMA reinforcement in the plastic hinge. The study showed that innovative frames could effectively recover their lateral drift ratios, although experiencing higher displacement demands. Abdulridha (2013) proposed an analytical model for SMA behavior, which was incorporated into VecTor2 software founded by Vecchio (1989). Then, VecTor2 was used by (Abdulridha 2013; Abdulridha et al. 2013) to perform refined FE analyses on a one-story steel-SMA reinforced shear wall and a beam element and a beam-

column joint, in which the concrete matrix and reinforcement of the structural members were modeled with quadrilateral plane-stress and truss elements respectively. Maciel et al. (2016) covered the effects of axial loads on the cyclic response of steel and steel-SMA reinforced concrete shear walls.

Mohamed et al. (2014) simulated three GFRP RC shear walls in VecTor2. The study showed that GFRP- reinforced walls can control and reduce shear distortion in RC shear walls. Ghazizadeh et al. (2018) also used VecTor2 to perform a post-test FE analysis and a parametric study on a one-story shear wall. The study investigated the most appropriate reinforcement layout for the squat steel-GFRP reinforced wall.

### **5.3 Analysis Model**

The response of each shear wall under quasi-static cyclic loads and earthquake acceleration records was calculated using VecTor2, which is a finite element (FE) program specializing in the analysis of reinforced concrete and masonry members. VecTor2 was founded by Vecchio (1989) and has been continuously improved. This state-of-the-art FE analysis program uses the modified compression field theory by Vecchio and Collins (1986), and the distributed stress field model by Vecchio (2001) to model concrete. Cracked concrete in VecTor2 is modeled as an orthotropic material with a smeared rotating cracking pattern, according to Wong and Vecchio (2002).

VecTor2 includes various behavioral models for different properties of the cementitious materials and the reinforcement used in reinforced concrete members. These models can be calibrated to experimental data. After calibration, concrete models are assigned to first-order plane-stress elements. For the reinforcement of concrete, it is possible to either model the reinforcement with the first-order truss element or define it as the smeared reinforcement in the concrete material. Different bond-slip relationships can also be incorporated into the model using zero-length two-node link elements. To determine the hysteretic response of a shear wall, the FE model of the wall is analyzed under lateral displacement reversals applied to the top of the wall. The analysis is performed using a static nonlinear mode of analysis and the default convergence criteria mode of weighted average displacements (Wong and Vecchio 2002).

To validate the accuracy of the developed FE models in capturing the overall response of

conventional and innovative shear walls, the results of FE models and experimental tests regarding seven shear walls were compared. Four of the walls were tested by the authors (Tolou Kian and Cruz-Noguez 2018). Three of the shear walls, which were tested by Ghazizadeh and Cruz-Noguez (2018), Abdulridha and Palermo (2014) and Holden et al. (2003), were selected from the literature.

### 5.3.1 Modified Compression Field Theory (MCFT)

The MCFT is an analytical method developed by Vecchio and Collins (Vecchio and Collins 1986) in 1986 to predict the behavior (load-deformation) of reinforced concrete elements subjected to in-plane normal and shear stresses. In the MCFT, new formulations based on average stress and strain are used to describe the response of cracked concrete. According to (Vecchio 1989), cracked concrete is modeled as a solid continuum with orthotropic properties and smeared cracking in the MCFT. The orientation of cracks is not fixed and remains coaxial to the principal compressive stress field of concrete.

The theory predicts the stress and strain values develop along the formed cracks and within the concrete between them. The theory shows that tensile stresses may exist in the concrete between cracks due to the presence of reinforcement in reinforced concrete. Also, due to the presence of tensile stresses, the compressive strength of concrete between the cracks is decreased. Figures 5.1 and 5.2 demonstrate a block of cracked concrete, and the stresses exist between crack and with concrete struts between them.

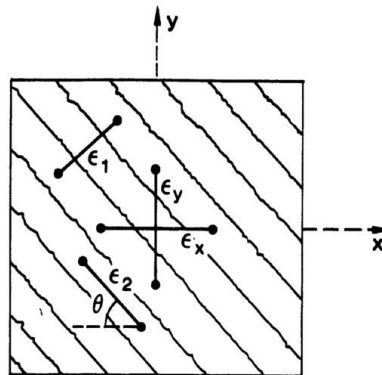


Figure 5.1. Average strains in cracked element (Vecchio and Collins 1986)

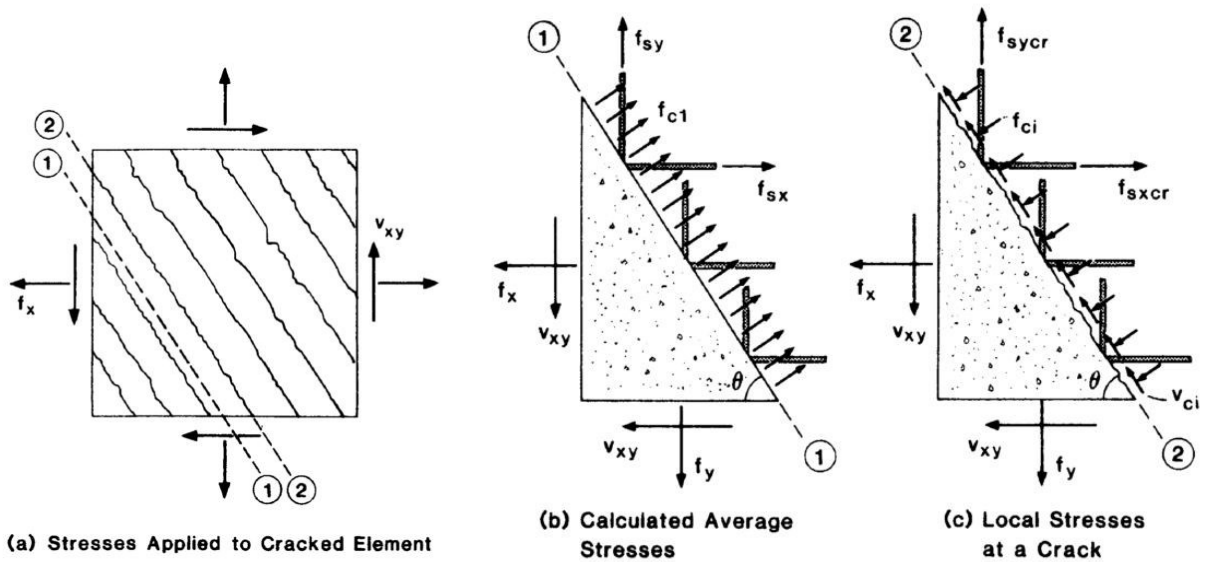


Figure 5.2. Modified compression field theory: (a) stresses applied to cracked elements, (b) calculated average stresses, (c) Local stresses at a crack (Vecchio and Collins 1986)

The reduction of compression strength due to the presence of tensile stresses is also shown schematically in Fig. 5.3. The tensile and compressive stresses of concrete based on its existing strains are shown in Eqs. 5.1 to 5.3.

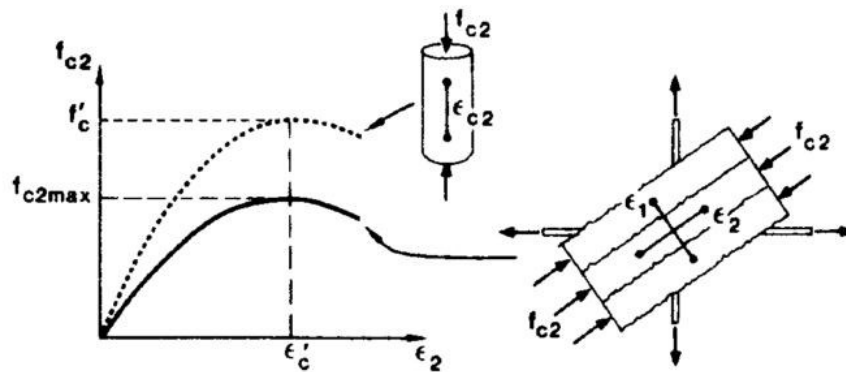


Figure 5.3. Stress-strain relationship of cracked concrete (Vecchio and Collins 1986)

$$f_{c1} = \frac{f'_t}{1 + \sqrt{200\epsilon_{c1}}} \tag{5.1}$$

$$f_{c2} = f_{c2max} \left( 2 \left( \frac{\epsilon_2}{\epsilon'_c} \right) - \left( \frac{\epsilon_2}{\epsilon'_c} \right)^2 \right) \tag{5.2}$$

$$f_{c2max} = f'_c \frac{1}{0.8+0.34\epsilon_1/\epsilon'_c} \leq 1 \quad (5.3)$$

As shown in Fig. 5.4, cracks are formed within the cement-based binder in normal concrete materials. The shear stress developing at crack locations were described based on the empirical equations (Eqs. 5.4 to 5.7) proposed by Walraven (Walraven 1981). The equations calculated the interlock shear stresses ( $v_{ci}$ ), based on the existing normal stresses ( $f_{ci}$ ), the crack width ( $w$ ), and the maximum aggregate dimension ( $a$ ).

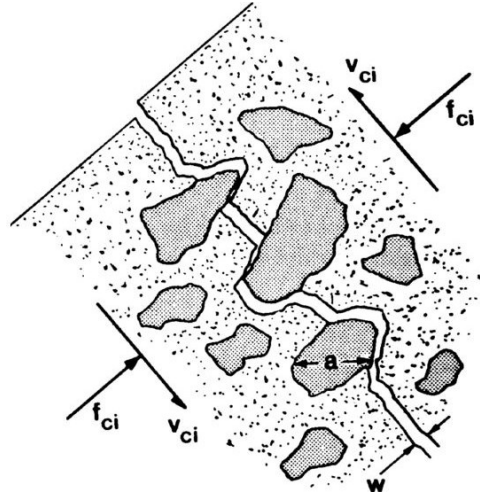


Figure 5.4. Aggregate interlock and transmission of shear stresses (Vecchio and Collins 1986)

$$v_{ci} = 0.18 v_{cimax} + 1.64 f_{ci} - 0.82 \frac{f_{ci}^2}{v_{cimax}} \quad (5.4)$$

$$v_{cimax} = \frac{\sqrt{-f'_c}}{0.31+24w/(a+16)} \quad (5.5)$$

$$w = \epsilon_1 S_\theta \quad (5.6)$$

$$S_\theta = \frac{1}{\frac{\sin\theta}{m_x} + \frac{\cos\theta}{m_y}} \quad (5.7)$$

Along with stress-strain relationships, the theory uses equilibrium and compatibility equations for concrete and reinforcement average strains to describe the behavior of cracked reinforced concrete material.

### 5.3.2 Innovative Walls

Tolou Kian and Cruz-Noguez (2018) performed an experimental test on one conventional RC wall

and three innovative shear walls. Each innovative shear wall was cast with high-performance concrete and reinforced with a type of self-centering reinforcement, including SMA bars, GFRP bars, and post-tensioned high-strength steel strands. The innovative walls were called GFRP-ECC, SMA-SFRC, and PT-SFRC based on the type of innovative reinforcement and cementitious mixes, with which the walls were detailed (Fig. 5.5). The conventional RC shear wall of the study was termed the control wall (CW).

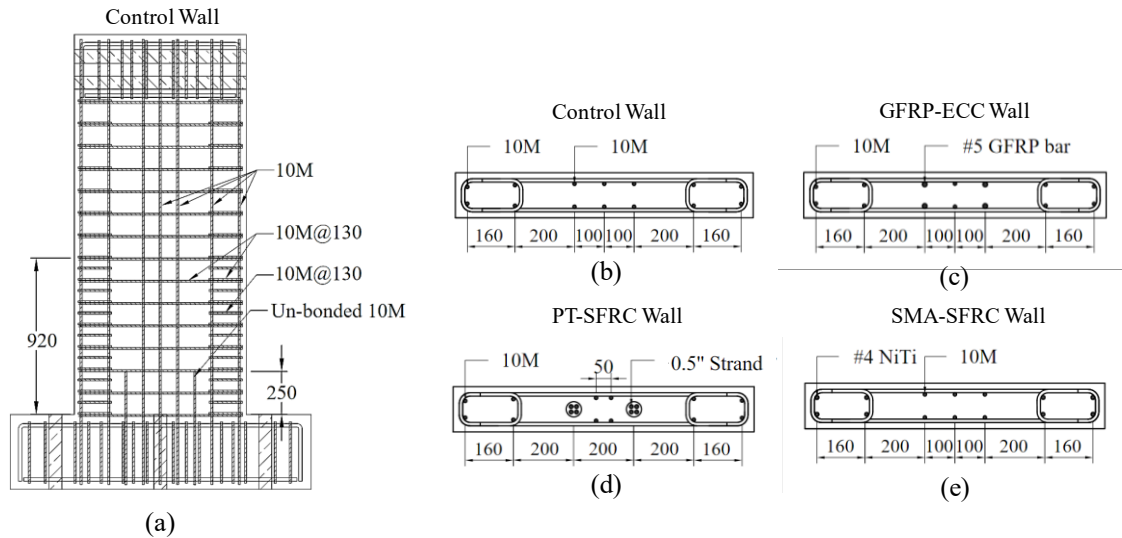


Figure 5.5. Reinforcement layouts: (a) CW vertical layout, and cross-sections for (b) CW, (c) GFRP-ECC, (d) PT-SFRC, (e) SMA-SFRC (Tolou Kian and Cruz-Noguez, 2018)

### 5.3.2.1 Behavioral Materials Models

VecTor2 basic material models were used in the FE modeling of walls. The following advanced behavioral models were also incorporated to precisely tailor the characteristics of models according to material tests. The compressive stress-strain relationships of concrete, ECC, and SFRC mixes were determined based on ASTM C39 (2015). Then, appropriate compressive stress-strain relationships were chosen to replicate the actual behavior of the cement-based materials (Fig. 5.6(a)). For normal concrete, the models developed by Popovics (1973) and Lee et al. (2015) were used to represent the pre-peak and post-peak behavior of concrete. The pre-peak constitutive relationship of ECC was modeled as a parabola, while its post-peak response was based on the model proposed by Park et al. (1982). The compressive pre-peak and post-peak response of each SFRC mix were modeled according to Lee et al. (2015). Figure 5.6(b) shows the cyclic stress-

strain behavior of the cementitious materials used in the FE models of the shear walls.

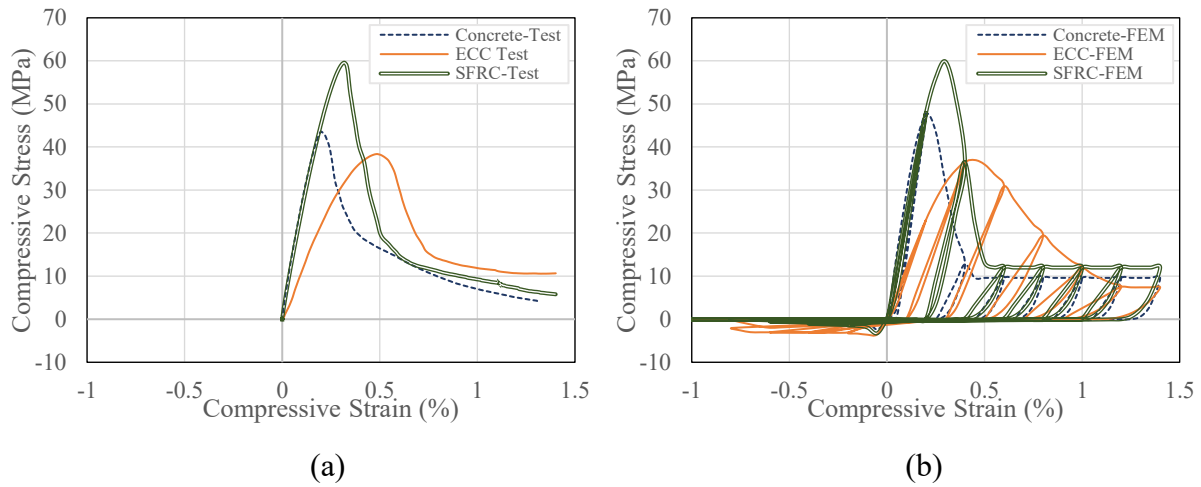


Figure 5.6. Stress-strain response of cementitious materials: (a) measured, (b) calculated

The tensile response of cementitious materials is controlled by their post-cracking behavior. For normal concrete, the tensile stresses rapidly decrease to zero after cracking. However, materials with fiber reinforcement can resist tensile stresses at greater strain values.

The post-cracking response of the concrete material was modeled based on the model suggested by Yamamoto (1999), which consists of a non-linear curve from the cracking point to a characteristic point, and a linear relationship from the characteristic point to zero stress. The post-cracking response of the SFRC materials was modeled according to the predefined *fib* model (2013) of VT2, which is based on the residual flexural stresses,  $f_{R1}$  and  $f_{R3}$ , of a notched SFRC beam at crack mouth opening displacements of 0.5 and 2.5 mm. For the ECC material, the tensile stress-strain relationship was determined according to the direct tension test and was introduced to the software as a trilinear curve shown in Fig. 5.7.

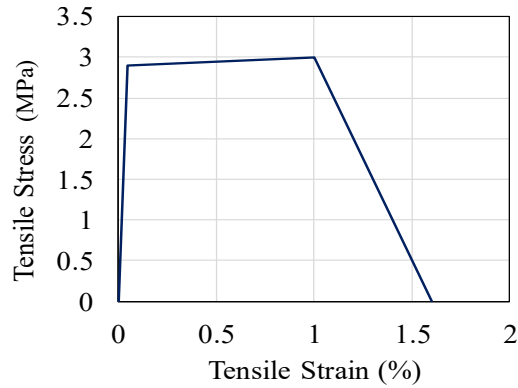


Figure 5.7. Tensile stress-strain relationship of ECC

The tensile stress-strain relationships of the steel and SMA bars were obtained according to ASTM A370-14 (2014) and ASTM F2516-14 (2014), as shown in Fig. 5.8. The ductile steel and SMA2 models of Vector2, which are based on Akkaya et al. (2019) and Abdulridha et al. (2013), were calibrated based on the tensile responses of the steel and SMA bars. For the GFRP bars, the steel behavioral model of VT2 was adjusted to represent a linear stress-strain relationship. For the post-tensioning strands, the predefined tension-only steel material of VT2 was used, as shown in Fig. 5.9. The buckling characteristics of the reinforcing materials were calculated based on Akkaya et al. (2019).

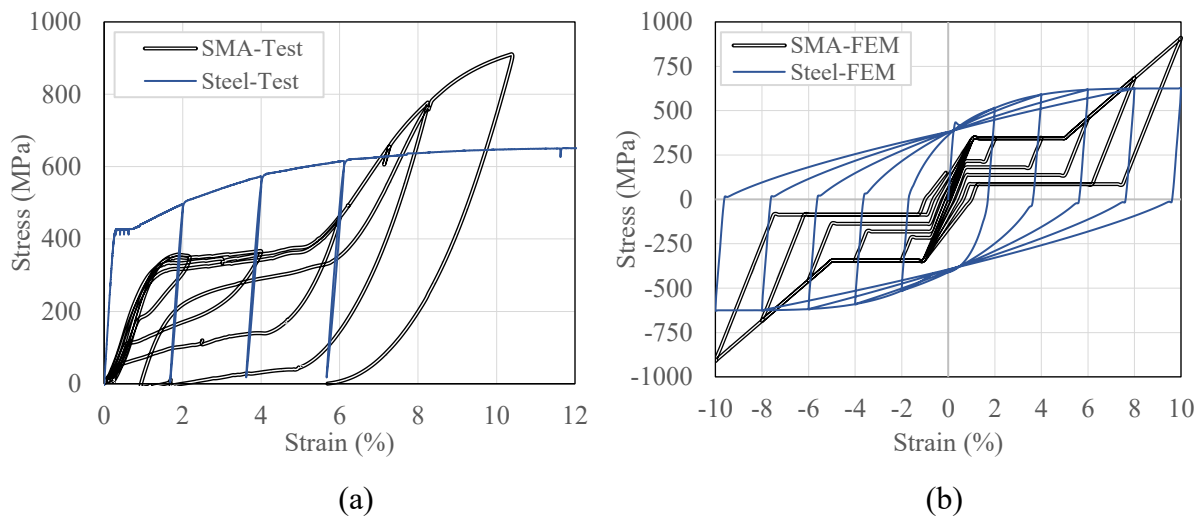


Figure 5.8. Stress-strain relationships of steel and SMA bars: (a) measured, (b) calculated

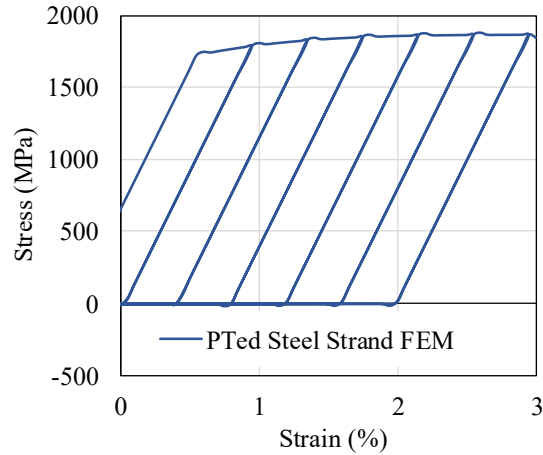


Figure 5.9. Stress-strain relationship of post-tensioned high-strength steel strands

For the steel, GFRP, and SMA bars, bond properties were specified according to Gan (2000), Baena et al. (2009), and Muntasir-Billah and Alam (2016), respectively. The post-tensioned strands and the starter bars, which were placed in the base of each shear wall, were modeled to be un-bonded in the longitudinal direction. Figure 5.10 shows the bond-slip relationships of 10M steel, #5 GFRP, and #4 SMA bars, which were used in the construction of the shear walls.

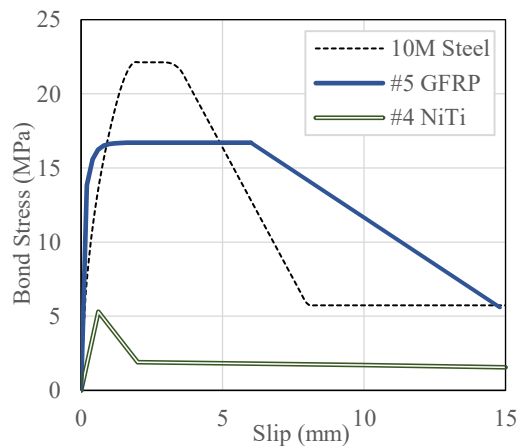


Figure 5.10. Bond-slip relationship for different types of reinforcement

### 5.3.2.2 Finite Element Modeling

Three FE models of the control wall with relatively coarse, moderate, and fine discretizations of the CW wall panel were used to study the sensitivity of results to the mesh-size of the FE models of the wall. Mesh M1 was considered a relatively coarse mesh for the size of the wall. The mesh

had a maximum size of 100 mm in the horizontal and a maximum size of 83 mm in the vertical directions of the CW wall panel. Mesh M2 had a relatively moderate mesh-size compared to the dimensions of the wall. The mesh had a maximum size of 50 mm in the horizontal and the vertical directions of the wall panel. Finally, mesh M3, which was the finest mesh of the analysis, had a maximum size of 27 mm in the horizontal direction and a maximum size of 31 mm in the vertical direction of the wall panel. Figure 5.11 shows the FE models of the control wall using M1, M2, and M3 meshes.

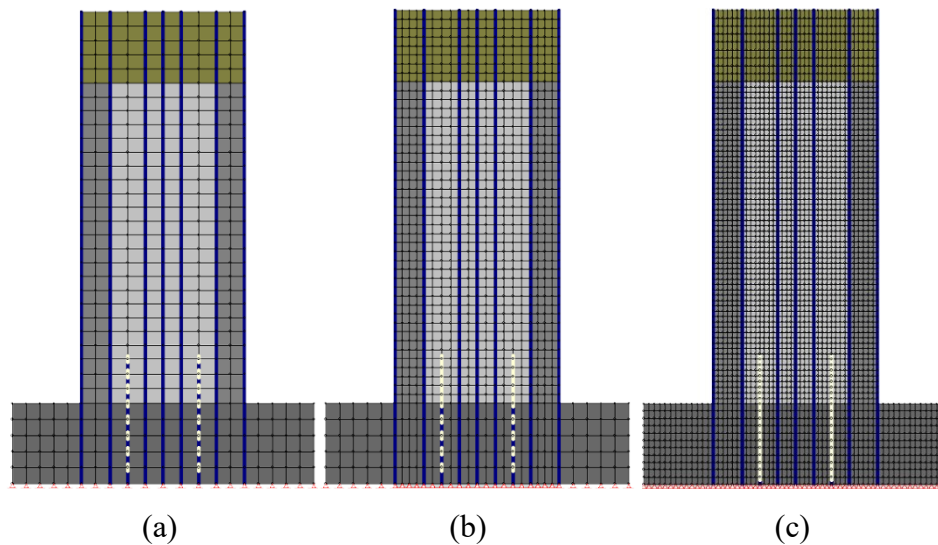


Figure 5.11. FE models of control wall using (a) M1, (b) M2, and, (c) M3

Figure 5.12 shows the calculated lateral force-drift ratio response for the FE models of the control wall under a monotonic lateral load. The M1 mesh resulted in a slightly stronger and more deformable response than other meshes. The strength and ultimate drift ratios of the FE models built based on the M2 and M3 meshes were almost the same. For this reason, since the analysis time of the FE model developed based on M2 mesh was significantly lower than the model that was based on M3 mesh, M2 mesh was used to discretize the shear wall specimens. In addition, the number of four-node elements along the shortest dimension of the FE model of the CW wall panel using M2 mesh was 20. For this reason, the M2 mesh corresponds to a relatively fine mesh according to (Palermo and Vecchio 2007).

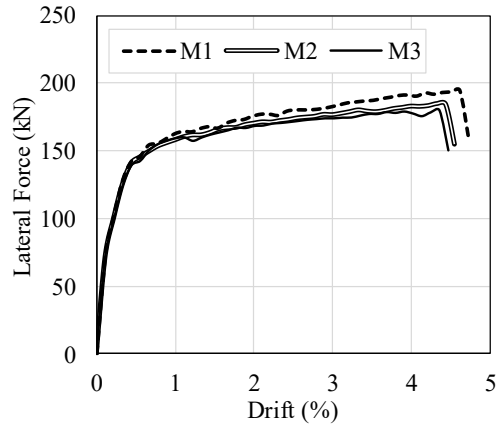


Figure 5.12. Lateral load-displacement response of FE models of control wall with mesh (a) M1, (b) M2, (c) M3

Plane stress rectangular elements, truss elements, and zero-length elements were used to model concrete, reinforcement, and bond properties of the reinforcement in the FE models of the walls, as shown in Fig 5.13. Each FE model was analyzed as lateral displacement reversals were applied to the mid-height of the cap-beam of the wall while no axial load was applied to the wall. The bottom edge of the foundation in each FE model was restrained against horizontal and vertical displacements.

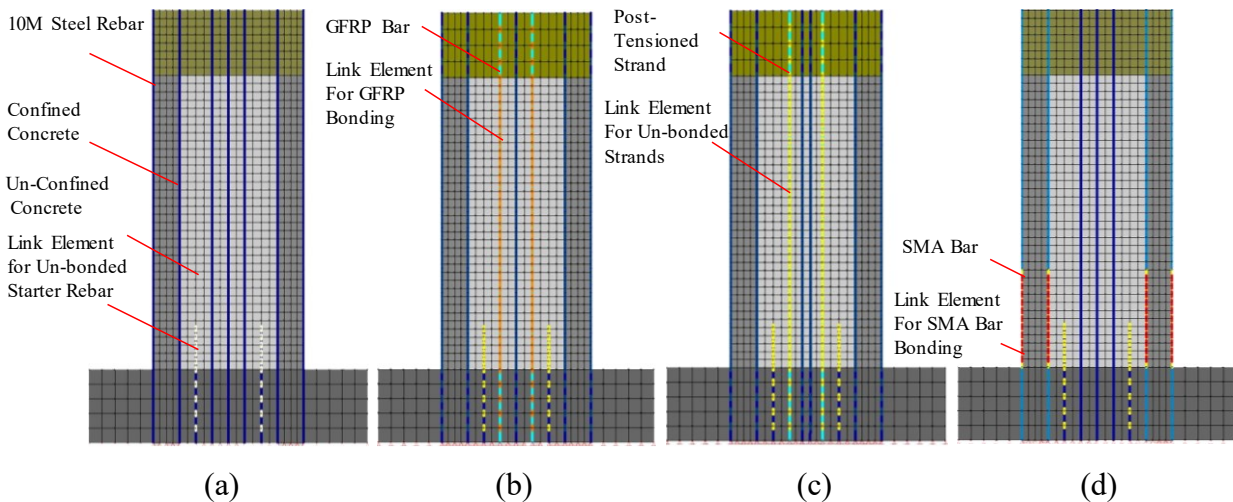


Figure 5.13. FE models of shear walls: (a) CW, (b) GFRP-ECC, (c) PT-SFRC, (d) SMA-SFRC

### 5.3.2.3 Global Performance: Force-Displacement Response

The measured and calculated hysteretic responses of the walls are shown in Fig. 5.14. As can be

seen, the numerical models were able to predict the response of each wall closely. The models predicted the initial stiffness, peak strength, failure mode, ultimate drift ratio, and residual drift ratio of each shear wall closely. The residual drift ratio in a shear wall is the drift ratio that corresponds to zero lateral.

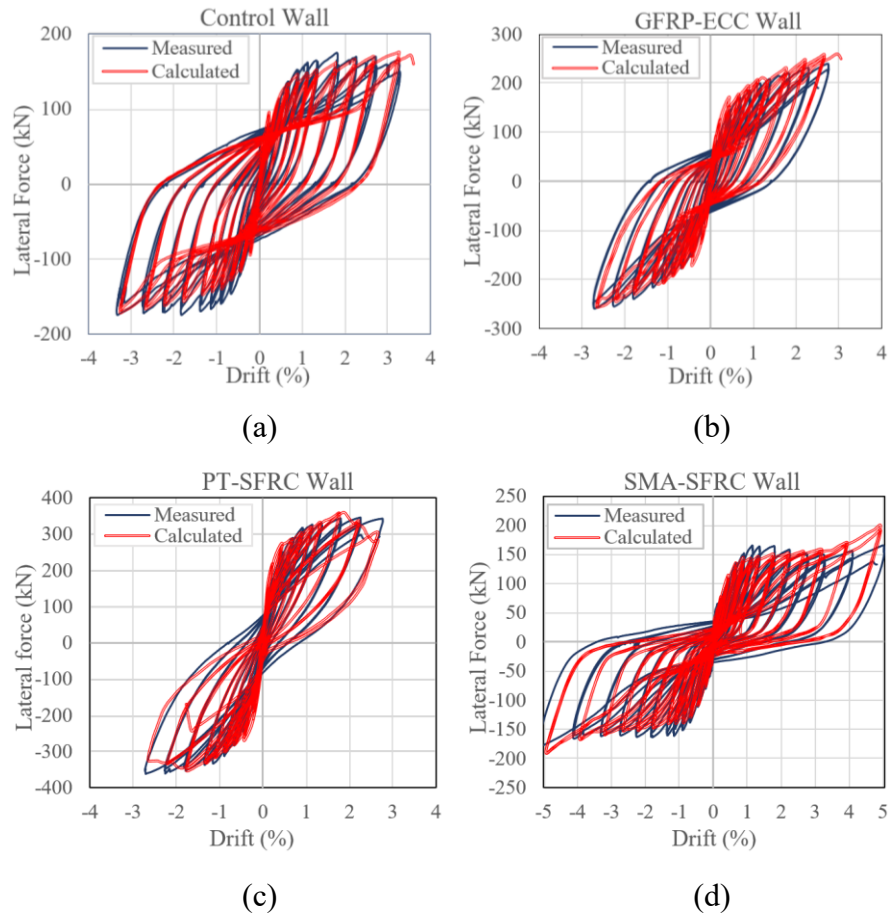


Figure 5.14. Calculated and measured hysteretic responses of shear walls (a) CW, (b) GFRP-ECC, (c) PT-SFRC, (d) SMA-SFRC

In addition to the overall force-displacement response of the specimens, local response parameters of the shear walls, such as cracking patterns, strain distributions, and curvature distributions of the specimens, were calculated.

#### 5.3.2.4 Local Performance: Cracks

The FE models of the specimens could correctly predict the locations of deep cracks of each wall with respect to the experimental results. Figures 5.15 and 5.16 show the cacking patterns obtained

from the FE analysis and experimental testing of the shear walls at a drift ratio of 2.7%. In Fig. 5.15, cracks with a width of 2 mm or greater are shown with thick red lines on the FE models of the specimens. Figure 5.16 was generated using a digital image correlation system (DIC) and originally shows the vertical strain developed on the surface of each wall specimen at a 2.7% drift. As can be seen in Fig. 5.16, a crack can be easily identified in the color map of vertical strains on the surface of the walls. This is because the vertical strains are higher at the crack locations with respect to the un-cracked locations of the walls.

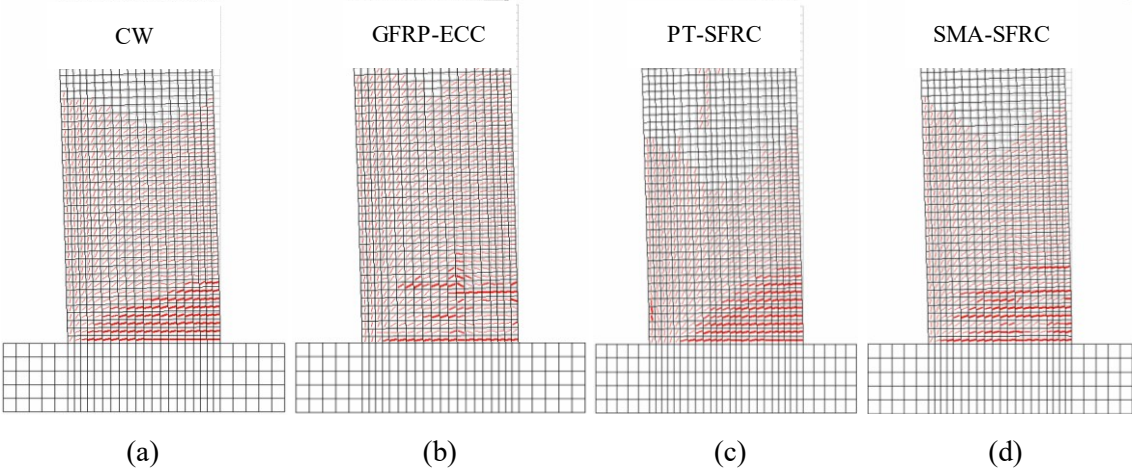


Figure 5.15. Calculated cracking patterns of specimens at 2.7% drift (a) CW, (b) GFRP-ECC, (c) PT-SFRC, (d) SMA-SFRC

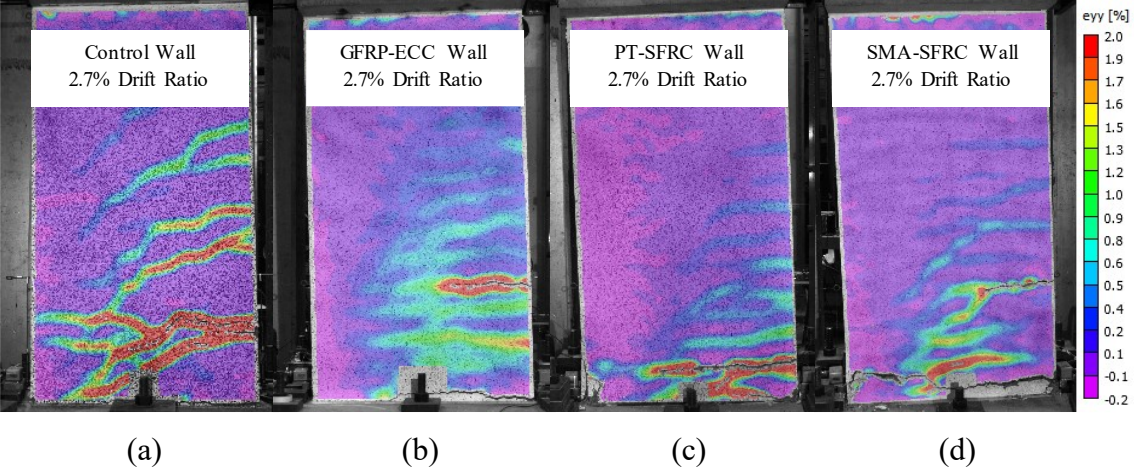


Figure 5.16. Recorded cracking patterns of specimens at a drift of 2.7% (a) CW, (b) GFRP-ECC, (c) PT-SFRC, (d) SMA-SFRC

### 5.3.2.5 Local performance: Longitudinal Strain Distribution

The vertical displacements on the surface of each specimen were captured using the DIC system (Fig. 5.17). Then, the average vertical strain along the height of each wall was determined as the difference between every two adjacent displacements divided by the distance between the locations of the displacements. The same calculations were also performed on the displacements obtained from the FE models of the shear walls to obtain the average strains along the heights of the FE models.

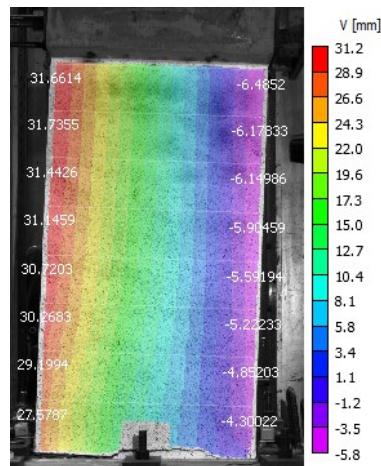


Figure 5.17. Vertical displacements measured with DIC system

Figure 5.18 shows the average strain distributions obtained from the experimental testing and numerical modeling of the shear wall at three peak drift ratios. The strain distributions obtained from the experimental data are displayed with dotted lines and E letters in the legends of the graphs. In contrast, solid lines and N letters used to show the strain distributions obtained from the experimental results. Fig. 5.18 shows that the FE models were able to closely capture the strain developed on the surface of each shear wall.

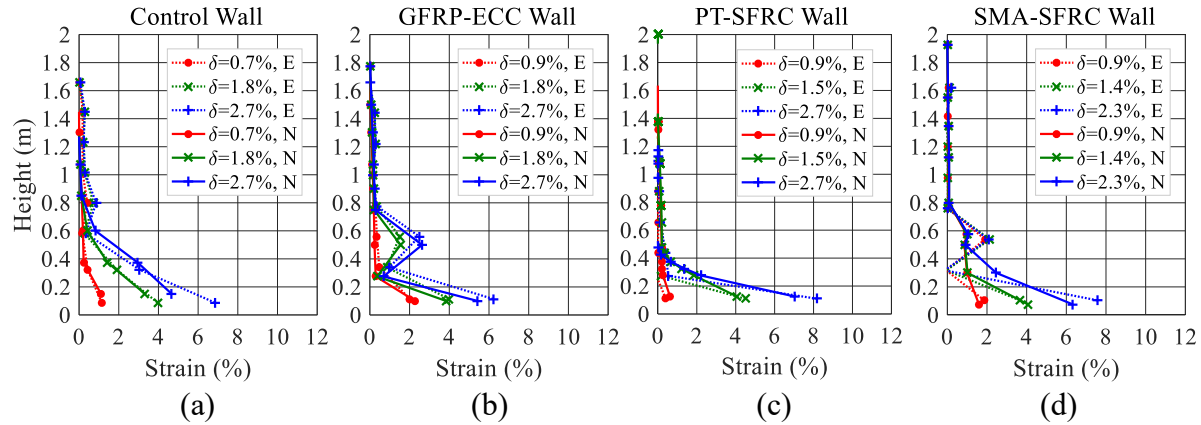


Figure 5.18. Strain distributions of shear wall specimens and FE models for (a) CW, (b) GFRP-ECC, (c) PT-SFRC, (d) SMA-SFRC

The strain measured with strain gauges at different locations of the reinforcing bars of the walls is compared against the strain calculated with the FE models of the walls, as shown in Fig. 5.19. The experimental results are shown by dotted lines and a letter E, while it is solid lines and a letter N for the numerical results. The experimental and analytical strain values in the reinforcement showed good correspondence in terms of the trend and peak values.

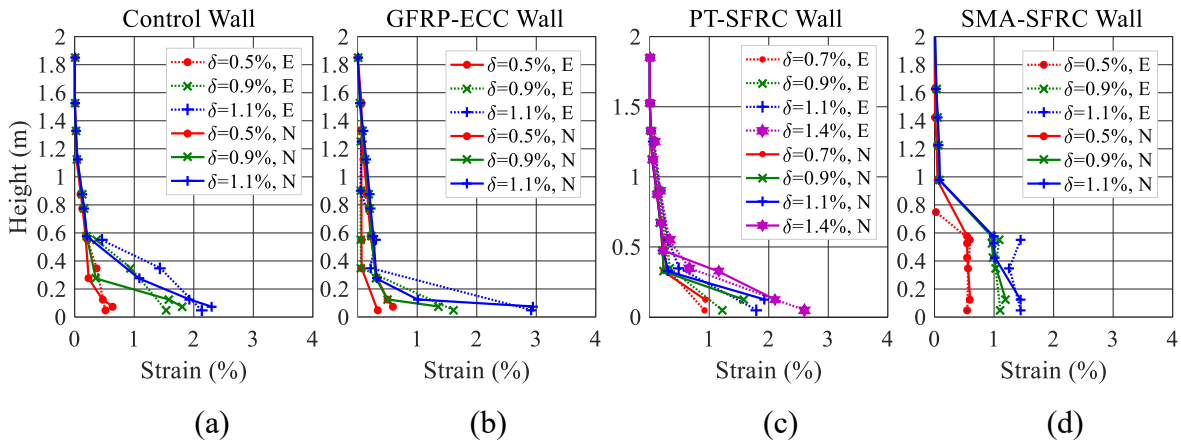


Figure 5.19. Strain distribution of shear wall specimens and FE models for (a) CW, (b) GFRP-ECC, (c) PT-SFRC, (d) SMA-SFRC

### 5.3.2.6 Local performance: Curvature Distribution

The vertical strain distributions were used to calculate the average curvature values of the walls (Fig. 5.20). As explained in 5.3.2.5, the longitudinal strain distributions obtained from the experimental and numerical studies had a close agreement. Thus, the experimental and numerical

curvature distributions of the walls will have a close agreement. In Fig. 5.20, the curvature distributions are shown with dotted lines and E letters in the case of the experimental results and solid lines and N letters in the case of the numerical results. According to the figure, the FE models of the walls were able to closely simulate the curvature distributions of the walls, which can be used in the flexural analysis of the walls.

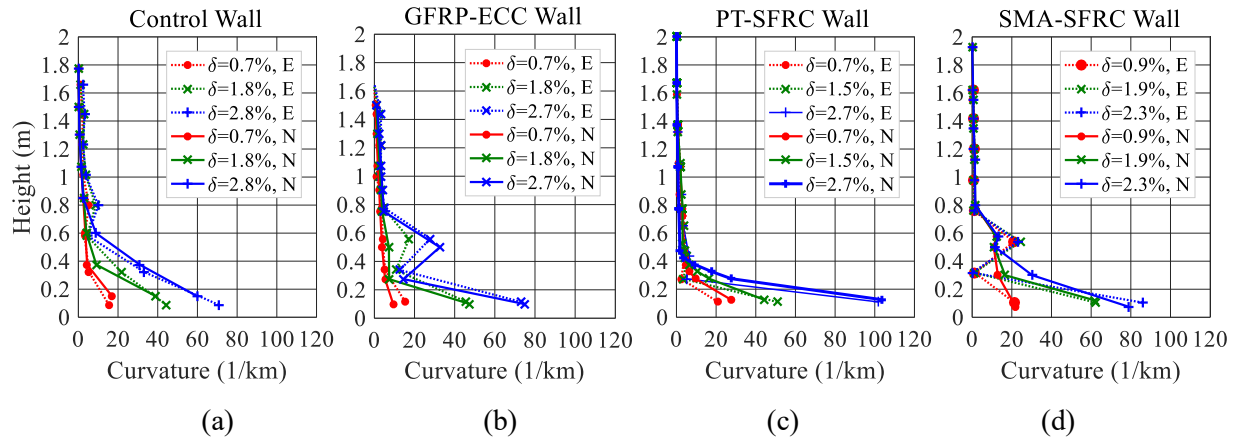


Figure 5.20. Curvature distribution of shear wall specimens and FE models of (a) CW, (b) GFRP-ECC, (c) PT-SFRC, (d) SMA-SFRC

### 5.3.3 Additional Validation

As discussed earlier, the tested shear walls had a length of 1 m, a height of 2 m, and were carrying no axial loads. To include innovative wall specimens with more geometrical varieties into the study, three shear wall specimens from the literature were validated as well. Also, it was desired to validate more than one specimen regarding each type of innovative shear. The validated innovative shear walls from the literature consisted of a squat steel-GFRP reinforced SFRC wall tested by Ghazizadeh and Cruz-Noguez (2018), a steel-SMA reinforced concrete shear wall tested by Abdulridha and Palermo (2014) and a post-tension precast SFRC wall by Holden et al. (2003).

#### 5.3.3.1 Steel-GFRP Reinforced Wall

Ghazizadeh and Cruz-Noguez (2018) tested a squat shear wall, which had an aspect ratio of 1.1. The wall was cast with SFRC and reinforced with a longitudinal reinforcing system made of 10M steel and #6 GFRP bars (Fig. 5.21(a)). The wall was tested under lateral displacement reversals and no axial loads. The wall showed reduced permanent drift ratios and mitigated damage in comparison to a comparable conventional RC shear wall.

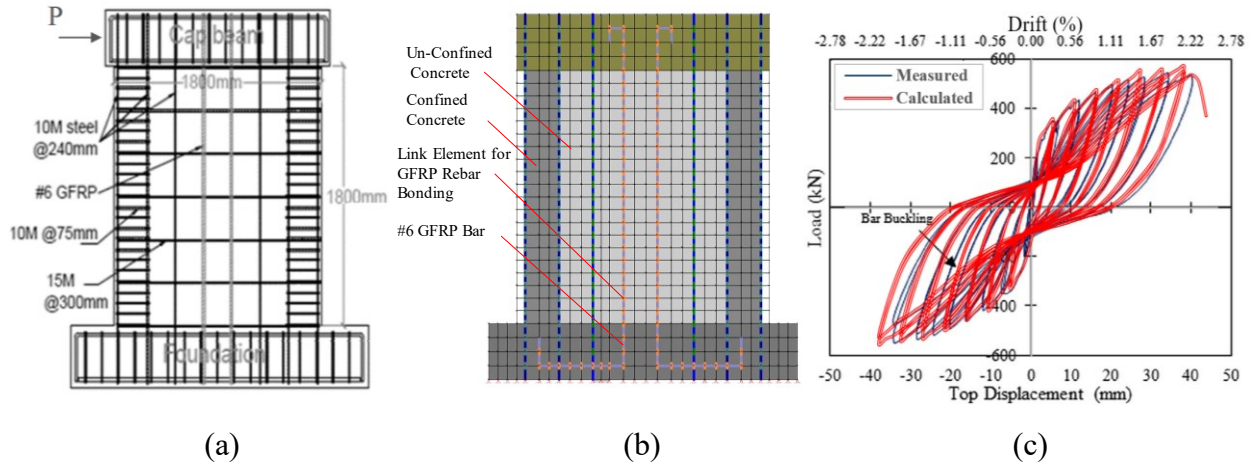


Figure 5.21. Innovative shear wall tested by Ghazizadeh and Cruz-Noguez (2018)  
 (a) reinforcement layout, (b) FE model, (c) experimental and numerical results

The FE model of the wall was developed using similar techniques to those outlined in the previous section (Fig. 5.21(b)). The material models used in the modeling of the shear wall are as follows. The compressive pre-peak and post-peak behavior of the SFRC material of the wall were defined in accordance with Lee et al. (2015). The tensile post-cracking behavior of the material was specified in accordance with the nonlinear behavior proposed by Yamamoto (1999).

The hysteretic and buckling properties of the steel rebars of the wall were modeled using Akkaya et al. (2019). GFRP bars were defined by calibrating steel models to have a linear stress-strain response. The bond-slip relationships of the steel and GFRP bars were defined according to Gan (2000) and Baena et al. (2009), respectively. The measured and calculated hysteretic responses of the wall are shown in Fig. 5.21(c). As can be seen, both experimental and numerical responses were in agreement in terms of initial stiffness, peak strength, ultimate drift ratio, and self-centering.

### 5.3.3.2 Steel-SMA Reinforced Wall

Abdulridha and Palermo (2014) studied the performance of a shear wall reinforced with 10M steel and #4 NiTi bars (Fig. 5.22(a)). The wall was slender with an aspect ratio of 2.2. The wall was tested under lateral displacement reversals and with no axial loads. The hysteretic response of the shear wall illustrated a substantial improvement in the self-centering of the wall over a conventional RC shear wall with comparable geometry and lateral resistance.

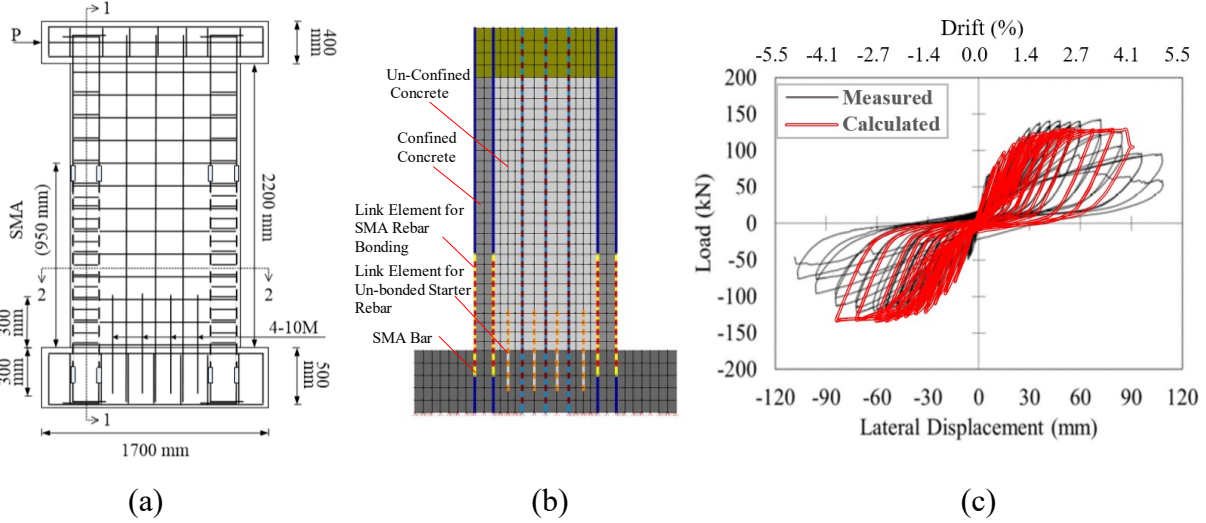


Figure 5.22 Innovative shear wall tested by Abdulridha (2013) (a) reinforcement layout, (b) FE model, (c) experimental and numerical results

The FE model of the wall was developed and analyzed (Fig. 5.22(b)). The pre-peak and post-peak compressive stress-strain relationships of concrete were defined based on a parabolic curve and Saenz (1973), respectively. Also, The post-cracking stress-strain response of concrete in tension was specified according to Yamamoto (1999).

Steel properties were defined as explained earlier. The NiTi bars were defined using the SMA2 constitutive model by Abdulridha et al. (2013). The bond-slip relationship of the bars was specified according to Muntasir Billah and Alam (2016) and introduced to the software. The measured and calculated hysteretic responses of the wall are shown in Fig. 5.22(c). As can be seen in the figure, the FE model of the wall was able to well predict the overall behavior of the shear wall in case of initial stiffness, lateral resistance, residual, and ultimate drift ratios.

### 5.3.3.3 Post-Tensioned Wall

Holden et al. (2003) studied the performance of a precast shear wall post-tensioned with two unbonded carbon fiber reinforced polymer (CFRP) tendons, each of which made of three rods with a diameter of 5.5 mm. The wall was cast with SFRC and was detailed with two bonded steel rebars with a diameter of 16 mm for energy dissipation purposes. The wall was slender with an aspect ratio of the was 3.1 (Fig. 5.23(a)).

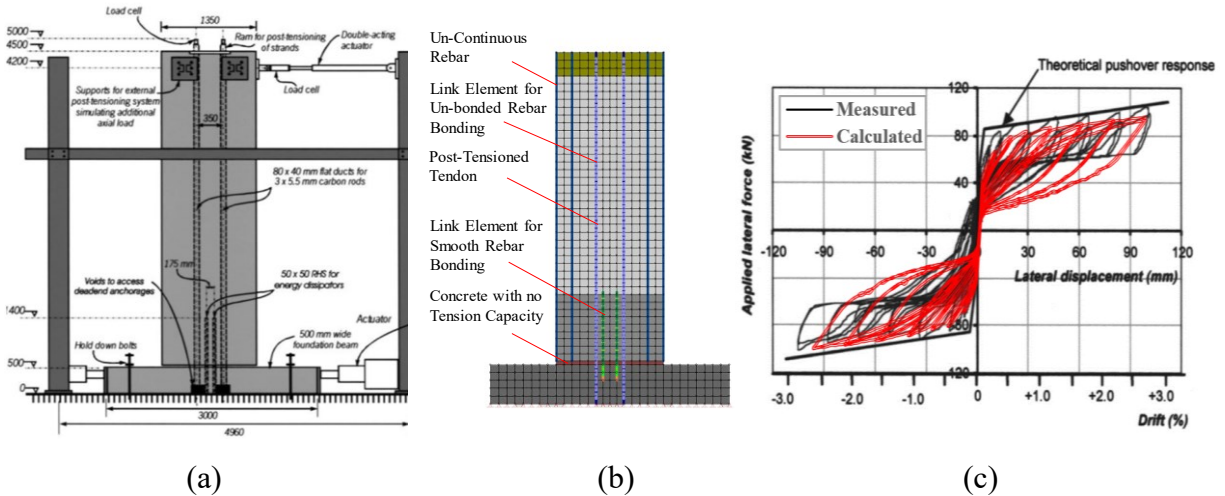


Figure 5.23 Shear wall tested by Holden et al. (2003) (a) reinforcement layout, (b) FE model (c) experimental and numerical results.

The compressive response of the SFRC material of the wall was modeled according to Lee et al. (2015), and the tensile response of the material was specified based on Lee et al. (2014). For CFRP bars, pre-defined models of tension-only steel and un-bonded bars were used to define the stress-strain and bond-slip relationship of the bars. The FE model of the wall was developed and analyzed (Fig. 5.23(b)). The measured and calculated hysteretic responses of the wall are shown in Fig. 5.23(c). As can be seen in Fig. 5.23(c), the model was able to follow the response of the shear wall closely.

## 5.4 Conclusions

The following conclusions were drawn from studying the numerical analysis of innovative shear walls with improved self-centering and damage mitigation properties.

- Off-the-shelf element and material formulations of VecTor2 were able to capture the behavior of the innovative materials even though there was no pre-defined material model for some of the innovative materials such as ECC.
- The bond materials and elements of VecTor2 were able to successfully simulate the bond properties of the SMA bars, the GFRP bars, and the unbonded bars and strands.
- The FE models of the shear walls were able to accurately calculate the strength, stiffness, ultimate

drift ratio, and residual drift ratio of the tested innovative shear walls and the innovative walls from the literature.

- The FE models of the shear walls were able to accurately calculate the average concrete strain distribution, the rebar strain distribution, and the curvature distribution in regard to the tested shear walls.

## CHAPTER 6 PARAMETRIC STUDY

### 6.1 Abstract

In recent years, new generations of reinforced concrete (RC) shear walls with improved self-centering properties have been introduced to structural engineers. Each generation of RC shear walls is reinforced with conventional steel plus a type of self-centering reinforcement, which can be shape memory alloy (SMA) bars, glass fiber reinforced polymer (GFRP) bars, or high-strength steel strands. It has been shown through experimental studies that these shear walls suffer lower permanent drift ratios compared to conventional RC walls after being subjected to cyclic loads. However, since the subject is relatively new, the studies were mainly performed on one-story shear walls with limited lengths, heights, and reinforcement ratios. Besides, design parameters, such as inelastic rotational capacity and plastic hinge length, were usually overlooked in the experiments. The present chapter overcomes these limitations by analyzing the innovative shear walls numerically by using verified finite element analysis models.

This chapter presents a parametric study performed on the design parameters of multistory innovative shear walls, which had different aspect ratios, axial load ratios, and reinforcement ratios. The walls were designed to have comparable levels of lateral resistance while incorporating different types of self-centering reinforcement. The study showed that the innovative walls, especially steel-SMA reinforced walls, had improved self-centering with lower energy dissipation properties in comparison to conventional walls. The study also showed that the properties of the innovative walls depended on the self-centering reinforcement used in the walls. The effective stiffness in the innovative walls, e.g., steel-SMA and steel-GFRP reinforced walls, was lower than in conventional walls as SMA and GFRP had lower modulus elastic than steel. The partially post-tensioned walls showed a comparable level of stiffness to the conventional RC walls.

The study showed when the innovative reinforcement was provided only at the base (steel-SMA reinforced walls), plastic deformations concentrated in a narrow region. When it was provided along the length (steel-GFRP reinforced walls), nonlinear deformations in the concrete were distributed uniformly. When partial post-tensioning was used, these walls tend to exhibit higher

rigid body rotations, which corresponds to a smaller plastic hinge length in the walls. As a result, plastic hinge length was greater in the steel-GFRP wall and shorter in the steel-SMA reinforced and post-tensioned walls compared to the conventional wall. Also, the inelastic rotational capacity was higher in the steel-GFRP reinforced walls compared to conventional walls. The inelastic rotational capacity in the steel-SMA reinforced walls was comparable to that of conventional walls, while it was lower in the post-tensioned walls.

## **6.2 Introduction**

The traditional seismic design philosophy provides conventional structures with adequate strength and deformation capacities. In this way, the structures satisfy life safety and collapse prevention performance levels in the design basis and maximum considered earthquakes of their sites. However, this occurs at the cost of the structure undergoing significant nonlinear deformations and often considerable amounts of permanent drift ratios in its post-earthquake state, which is not accounted for in the traditional seismic design philosophy.

According to Ramirez and Miranda (2012), permanent inter-story drift ratio is a vital damage indicator in reinforced concrete (RC) structures, and overlooking it in economic loss estimations can lead to dramatic underestimations. Ramirez and Miranda (2012) showed that accounting for forced demolition of RC structures due to permanent inter-story drift ratios can increase economic loss estimates by 45% in comparison to the current ones that overlook permanent drifts. For this reason, innovative structural elements that incorporate self-centering materials can increase the adequacy and sustainability of structures, as shown in the following studies.

Saiidi et al. (2007, 2009), Saiidi and Wang (2006), and Cruz Noguez et al. (2012) studied the response of bridge piers detailed with engineered cementitious composites (ECC) and shape-memory alloy (SMA) bars. The studies showed that the innovative bridge piers had significantly lower residual deformations and damage compared to conventional RC piers under cyclic and seismic loads. Cruz Noguez et al. (2012) and Sakai and Mahin (2004) showed that post-tensioning RC bridge piers could also significantly reduce the permanent drift ratios of bridge piers in comparison to the conventional piers. The former study discussed that the post-tensioned piers could suffer more damage in the plastic hinge region compared to traditional RC piers.

Tolou Kian and Cruz-Noguez (2018) studied the cyclic response of three innovative shear walls that had identical geometries and comparable reinforcement layouts. Each of the innovative walls was monolithically cast with fiber reinforced concrete and was detailed with steel rebars and self-centering reinforcement consisting of glass fiber reinforced polymer (GFRP) bars, SMA bars, or high-strength strands post-tensioned to 40% of their yield strength. The study showed that the innovative shear walls suffered less extensive cracking and cover spalling compared to a control RC shear wall. The steel-GFRP, steel-SMA, and partially post-tensioned walls of the study had up to 37%, 58%, and 66% less permanent drift ratios in comparison to the control shear wall of the study.

Mohamed et al. (2014) studied the cyclic response of three GFRP-reinforced concrete shear walls carrying an axial load ratio (ALR) of 7%. The GFRP-reinforced walls showed improved self-centering, comparable deformability levels, and lower energy dissipation properties with respect to a comparable control RC shear wall. Abdulridha and Palermo (2014) studied the response of a steel-SMA reinforced shear wall under displacement reversals. The innovative wall showed substantial self-centering properties with sufficient stiffness, strength, and energy dissipation properties, although suffering more damage compared to a comparable RC control wall. Holden et al. (2003) studied the cyclic response of a post-tensioned precast shear wall incorporating energy dissipating bars. The wall showed a rocking response and returned to its original position after unloading. The innovative wall also sustained minor damage and dissipated limited energy in comparison to a comparable monolithically built RC shear wall.

Aside from the improved performance of innovative shear walls, there are few studies on the design of the walls. Kurama et al. (1999) and Kurama (2005) studied the response of six-story post-tensioned precast concrete walls with different reinforcement layouts and proposed a design method for these walls to resist code specific design basis earthquakes assuming the plastic hinge length of the walls is equal to  $0.2l_w$  when  $l_w$  is the wall length. Mohamed (2013) studied the response of GFRP reinforced walls and suggested a design method, in which plastic hinge length in GFRP-reinforced walls was assumed to be equal to  $0.5l_w$ , as it is usually used for conventional RC walls.

The literature review presented above shows that, in general, the development and the study of damage-resistant RC wall systems have been conducted with a few research groups focusing on certain types of walls, while a comprehensive investigation of the various types and structural options has been scarce. This study aims to present a systematic investigation of several types of advanced walls, assessing their advantages and limitations relative to each other and conventional RC construction, for standard structural parameters. The improvement in the seismic performance of each innovative wall is discussed in terms of two key damage indicators: the concrete damage and residual drift ratio.

The present parametric study is focused on multi-story shear walls, consisting of 54 innovative steel-SMA, steel-GFRP, partially post-tensioned concrete walls, and 18 conventional RC shear walls. The study compares design parameters, such as the ductility, inelastic rotational capacity, and plastic hinge length in the innovative and conventional RC shear walls with different aspect ratios, axial load ratios, and self-centering reinforcement layouts.

### **6.3 Parametric Analysis**

To study the behavior of large-scale innovative RC walls, a parametric study was undertaken on 72 shear walls. The parametric study was performed on five-story shear walls with a height of 14 m since five-story mid-rise buildings are one of the most common structures around the world. The analyses were performed according to the analysis techniques discussed in Chapter 5. The parameters of this study are classified as fixed, independent, and dependent, which are described as follows.

#### **6.3.1 Fixed parameters**

The fixed parameters were not changed in the study and were constant for all the shear walls. The height, thickness, mild steel properties, concrete properties, boundary conditions, and displacement steps in the shear walls were the fixed parameters of the study. In addition, the lateral resistance in shear walls with the same length, axial load ratio, and reinforcement layouts, but different types of self-centering reinforcement was the same.

### 6.3.2 Independent parameters

The independent parameters were varied to investigate their effects on the dependent parameters. The study had four independent parameters consisting of the type of self-centering reinforcement, the length, the axial load ratio, and the reinforcement layout for the walls.

The types of self-centering reinforcement were comprised of GFRP bars, SMA bars, and post-tensioned high-strength steel strands in the longitudinal direction. The walls could also have no self-centering reinforcement (control walls). Three reinforcement layouts (*S*) of S1, S2, and S3 were defined for each type of shear walls. In the innovative shear walls with a specific type of self-centering reinforcement, the S3 layout had the highest, and the S1 layout had the lowest self-centering reinforcement ratios while the steel reinforcement in the layouts stayed the same. In the control walls, the S3 layout had the highest, and the S1 layout had the lowest steel reinforcement ratios along their lengths.

The length (*L*) in the shear walls was 2.6, 4.5, or 6.7 m, which translates into aspect ratios of 4.8, 3.1 and 2.1, respectively, as the height of the shear walls was 14 m. The last independent parameter was the axial load (*A*). The cyclic response in the shear walls was determined under two axial load cases. In load case I, no axial load was applied to the walls, while in load case II, a uniform axial load with an ALR of 1% was applied to each story level of the walls. The load case II resulted in an ALR of 5% in the first story of the walls.

### 6.3.3 Dependent parameters

The dependent parameters of the study consisted of the strength, stiffness, energy dissipation, ductility, inelastic rotational capacity, plastic hinge length, and self-centering moment. Each dependent parameter was studied under different values of the independent parameters.

### 6.3.4 Shear walls

The geometry, loading, and boundary conditions of the shear walls are shown in Fig. 6.1(a). Figure 6.1(b) shows the regions (*R*), in which the reinforcement of the shear wall could change. In Fig. 6.1(b),  $L_b$  is the length of the boundary element, and  $L_w$  is the length of the web in a typical shear wall.

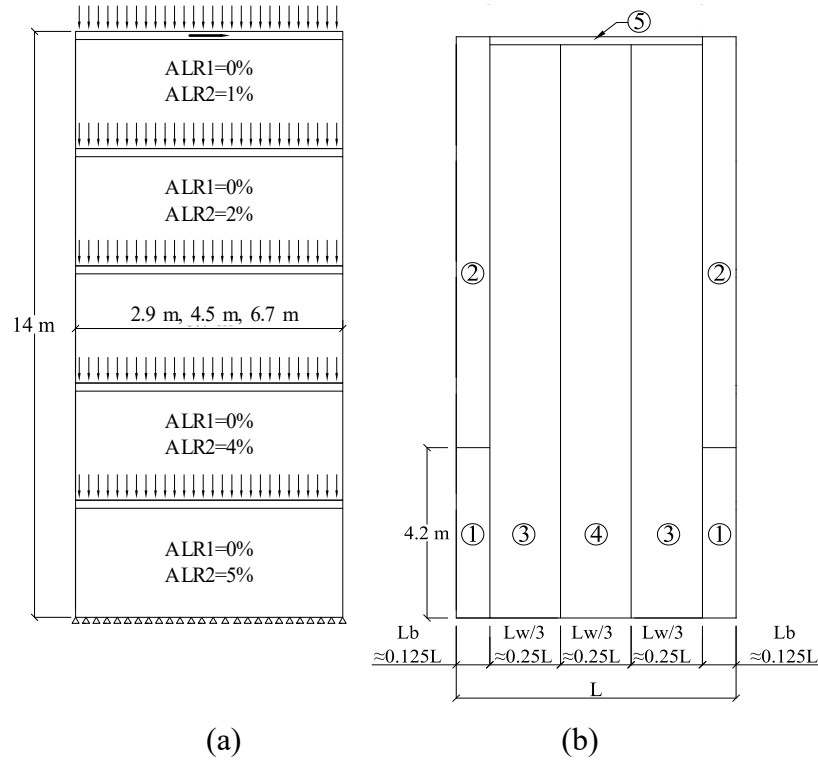


Figure 6.1. Shear walls (a) schematics (b) regions with different reinforcement

Each shear wall was given a specific name with a special format (“TWALS”), according to the independent parameters of the study – self-centering reinforcement type, axial load ratio, length, and reinforcement layout of shear walls.

The term TW in the name of the walls stands for the type of shear walls. When the walls are reinforced with steel bars, steel-GFRP bars, steel-SMA bars, or steel bars along with post-tensioned high-strength steel strands, the term TW is replaced with CW, GW, SW, or PW, respectively. The term A stands for the axial load. The term is replaced with A1 and A2 in the case of 0% and 5% ALRs at the base of each wall.

The term L stands for the length of shear walls. The term is replaced with L1, L2, and L3 for shear walls with lengths of 2.6, 4.5, or 6.7 m. Finally, the term S corresponds to the reinforcement layout and, consequently, the reinforcement ratio of the shear walls. The term is replaced with S1, S2, or S3 as the reinforcement ratio in a wall with a defined geometry and axial load ratio increases. The self-centering reinforcement ratios were selected in a way that walls with different self-centering reinforcement types but the same axial load ratio, length, and reinforcement layout have a

comparable lateral resistance. Table 6.1 displays the axial load ratio, aspect ratio, and length of the walls, as well as the reinforcement ratio in the different regions (R) of the walls defined in Fig. 6.1(b).

Table 6.1. Nomenclature of the walls

No	General Wall Name	Load ALR	Geometry L (m) H/L		Vertical Reinforcement				Horizontal Reinforcement		
					Boundary			Web R4	Boundary		Web
					R1	R2	R3		0°	90°	
1	CWAIL1S1	0%	2.9	4.8%	Steel Bars 1.5%	Steel Bars 1.5%	0.6%	Steel Bars 0.6%	1.3%	2.5%	1.3%
2	CWAIL1S2	0%	2.9	4.8%	Steel Bars 1.9%	Steel Bars 1.9%	0.6%	Steel Bars 0.6%	1.3%	2.5%	1.3%
3	CWAIL1S3	0%	2.9	4.8%	Steel Bars 2.1%	Steel Bars 2.1%	0.6%	Steel Bars 0.6%	1.3%	2.5%	1.3%
4	GWAIL1S1	0%	2.9	4.8%	Steel Bars 1.5%	Steel Bars 1.5%	0.6%	GFRP Bars 0.9%	1.3%	2.5%	1.3%
5	GWAIL1S2	0%	2.9	4.8%	Steel Bars 1.5%	Steel Bars 1.5%	0.6%	GFRP Bars 1.3%	1.3%	2.5%	1.3%
6	GWAIL1S3	0%	2.9	4.8%	Steel Bars 1.5%	Steel Bars 1.5%	0.6%	GFRP Bars 1.8%	1.3%	2.5%	1.3%
7	SWAIL1S1	0%	2.9	4.8%	SMA Bars 2.3%	HS Steel Bars 2.3%	0.6%	Steel Bars 0.6%	1.3%	2.5%	1.3%
8	SWAIL1S2	0%	2.9	4.8%	SMA Bars 3%	HS Steel Bars 3%	0.6%	Steel Bars 0.6%	1.3%	2.5%	1.3%
9	SWAIL1S3	0%	2.9	4.8%	SMA Bars 3.8%	HS Steel Bars 3.8%	0.6%	Steel Bars 0.6%	1.3%	2.5%	1.3%
10	PWAIL1S1	0%	2.9	4.8%	Steel Bars 1.5%	Steel Bars 1.5%	0.6%	PT Strands 0.2%	1.3%	2.5%	1.3%
11	PWAIL1S2	0%	2.9	4.8%	Steel Bars 1.5%	Steel Bars 1.5%	0.6%	PT Strands 0.3%	1.3%	2.5%	1.3%
12	PWAIL1S3	0%	2.9	4.8%	Steel Bars 1.5%	Steel Bars 1.5%	0.6%	PT Strands 0.4%	1.3%	2.5%	1.3%
13	CWAIL2S1	0%	4.5	3.1%	Steel Bars 1.3%	Steel Bars 1.3%	0.6%	Steel Bars 0.6%	1.3%	2.0%	1.3%
14	CWAIL2S2	0%	4.5	3.1%	Steel Bars 1.7%	Steel Bars 1.7%	0.6%	Steel Bars 0.6%	1.3%	2.0%	1.3%
15	CWAIL2S3	0%	4.5	3.1%	Steel Bars 1.9%	Steel Bars 1.9%	0.6%	Steel Bars 0.6%	1.3%	2.0%	1.3%
16	GWAIL2S1	0%	4.5	3.1%	Steel Bars 1.3%	Steel Bars 1.3%	0.6%	GFRP Bars 0.9%	1.3%	2.0%	1.3%
17	GWAIL2S2	0%	4.5	3.1%	Steel Bars 1.3%	Steel Bars 1.3%	0.6%	GFRP Bars 1.4%	1.3%	2.0%	1.3%
18	GWAIL2S3	0%	4.5	3.1%	Steel Bars 1.3%	Steel Bars 1.3%	0.6%	GFRP Bars 1.9%	1.3%	2.0%	1.3%
19	SWAIL2S1	0%	4.5	3.1%	SMA Bars 2%	HS Steel Bars 2%	0.6%	Steel Bars 0.6%	1.3%	2.0%	1.3%
20	SWAIL2S2	0%	4.5	3.1%	SMA Bars 2.7%	HS Steel Bars 2.7%	0.6%	Steel Bars 0.6%	1.3%	2.0%	1.3%
21	SWAIL2S3	0%	4.5	3.1%	SMA Bars 3.3%	HS Steel Bars 3.3%	0.6%	Steel Bars 0.6%	1.3%	2.0%	1.3%
22	PWAIL2S1	0%	4.5	3.1%	Steel Bars 1.3%	Steel Bars 1.3%	0.6%	PT Strands 0.2%	1.3%	2.0%	1.3%
23	PWAIL2S2	0%	4.5	3.1%	Steel Bars 1.3%	Steel Bars 1.3%	0.6%	PT Strands 0.3%	1.3%	2.0%	1.3%
24	PWAIL2S3	0%	4.5	3.1%	Steel Bars 1.3%	Steel Bars 1.3%	0.6%	PT Strands 0.4%	1.3%	2.0%	1.3%
25	CWAIL3S1	0%	6.7	2.1%	Steel Bars 1.3%	Steel Bars 1.3%	0.6%	Steel Bars 0.6%	1.3%	1.8%	1.3%
26	CWAIL3S2	0%	6.7	2.1%	Steel Bars 1.6%	Steel Bars 1.6%	0.6%	Steel Bars 0.6%	1.3%	1.8%	1.3%
27	CWAIL3S3	0%	6.7	2.1%	Steel Bars 1.8%	Steel Bars 1.8%	0.6%	Steel Bars 0.6%	1.3%	1.8%	1.3%
28	GWAIL3S1	0%	6.7	2.1%	Steel Bars 1.3%	Steel Bars 1.3%	0.6%	GFRP Bars 1%	1.3%	1.8%	1.3%
29	GWAIL3S2	0%	6.7	2.1%	Steel Bars 1.3%	Steel Bars 1.3%	0.6%	GFRP Bars 1.4%	1.3%	1.8%	1.3%
30	GWAIL3S3	0%	6.7	2.1%	Steel Bars 1.3%	Steel Bars 1.3%	0.6%	GFRP Bars 1.9%	1.3%	1.8%	1.3%
31	SWAIL3S1	0%	6.7	2.1%	SMA Bars 1.9%	HS Steel Bars 1.9%	0.6%	Steel Bars 0.6%	1.3%	1.8%	1.3%
32	SWAIL3S2	0%	6.7	2.1%	SMA Bars 2.5%	HS Steel Bars 2.5%	0.6%	Steel Bars 0.6%	1.3%	1.8%	1.3%
33	SWAIL3S3	0%	6.7	2.1%	SMA Bars 3.1%	HS Steel Bars 3.1%	0.6%	Steel Bars 0.6%	1.3%	1.8%	1.3%

General		Load	Geometry		Vertical Reinforcement				Horizontal Reinforcement		
No	Wall Name	ALR	L (m)	H/L	Boundary			Web	Boundary		Web
					R1	R2	R3	R4	0°	90°	0°
34	PWA1L3S1	0%	6.7	2.1%	Steel Bars 1.3%	Steel Bars 1.3%	0.6%	PT Strands 0.2%	1.3%	1.8%	1.3%
35	PWA1L3S2	0%	6.7	2.1%	Steel Bars 1.3%	Steel Bars 1.3%	0.6%	PT Strands 0.3%	1.3%	1.8%	1.3%
36	PWA1L3S3	0%	6.7	2.1%	Steel Bars 1.3%	Steel Bars 1.3%	0.6%	PT Strands 0.4%	1.3%	1.8%	1.3%
37	CWA2L1S1	5%	2.9	4.8%	Steel Bars 1.5%	Steel Bars 1.5%	0.6%	Steel Bars 0.6%	1.3%	2.5%	1.3%
38	CWA2L1S2	5%	2.9	4.8%	Steel Bars 1.9%	Steel Bars 1.9%	0.6%	Steel Bars 0.6%	1.3%	2.5%	1.3%
39	CWA2L1S3	5%	2.9	4.8%	Steel Bars 2.1%	Steel Bars 2.1%	0.6%	Steel Bars 0.6%	1.3%	2.5%	1.3%
40	GWA2L1S1	5%	2.9	4.8%	Steel Bars 1.5%	Steel Bars 1.5%	0.6%	GFRP Bars 0.9%	1.3%	2.5%	1.3%
41	GWA2L1S2	5%	2.9	4.8%	Steel Bars 1.5%	Steel Bars 1.5%	0.6%	GFRP Bars 1.3%	1.3%	2.5%	1.3%
42	GWA2L1S3	5%	2.9	4.8%	Steel Bars 1.5%	Steel Bars 1.5%	0.6%	GFRP Bars 1.8%	1.3%	2.5%	1.3%
43	SWA2L1S1	5%	2.9	4.8%	SMA Bars 2.3%	HS Steel Bars 2.3%	0.6%	Steel Bars 0.6%	1.3%	2.5%	1.3%
44	SWA2L1S2	5%	2.9	4.8%	SMA Bars 3%	HS Steel Bars 3%	0.6%	Steel Bars 0.6%	1.3%	2.5%	1.3%
45	SWA2L1S3	5%	2.9	4.8%	SMA Bars 3.8%	HS Steel Bars 3.8%	0.6%	Steel Bars 0.6%	1.3%	2.5%	1.3%
46	PWA2L1S1	5%	2.9	4.8%	Steel Bars 1.5%	Steel Bars 1.5%	0.6%	PT Strands 0.2%	1.3%	2.5%	1.3%
47	PWA2L1S2	5%	2.9	4.8%	Steel Bars 1.5%	Steel Bars 1.5%	0.6%	PT Strands 0.3%	1.3%	2.5%	1.3%
48	PWA2L1S3	5%	2.9	4.8%	Steel Bars 1.5%	Steel Bars 1.5%	0.6%	PT Strands 0.4%	1.3%	2.5%	1.3%
49	CWA2L2S1	5%	4.5	3.1%	Steel Bars 1.3%	Steel Bars 1.3%	0.6%	Steel Bars 0.6%	1.3%	2.0%	1.3%
50	CWA2L2S2	5%	4.5	3.1%	Steel Bars 1.7%	Steel Bars 1.7%	0.6%	Steel Bars 0.6%	1.3%	2.0%	1.3%
51	CWA2L2S3	5%	4.5	3.1%	Steel Bars 1.9%	Steel Bars 1.9%	0.6%	Steel Bars 0.6%	1.3%	2.0%	1.3%
52	GWA2L2S1	5%	4.5	3.1%	Steel Bars 1.3%	Steel Bars 1.3%	0.6%	GFRP Bars 0.9%	1.3%	2.0%	1.3%
53	GWA2L2S2	5%	4.5	3.1%	Steel Bars 1.3%	Steel Bars 1.3%	0.6%	GFRP Bars 1.4%	1.3%	2.0%	1.3%
54	GWA2L2S3	5%	4.5	3.1%	Steel Bars 1.3%	Steel Bars 1.3%	0.6%	GFRP Bars 1.9%	1.3%	2.0%	1.3%
55	SWA2L2S1	5%	4.5	3.1%	SMA Bars 2%	HS Steel Bars 2%	0.6%	Steel Bars 0.6%	1.3%	2.0%	1.3%
56	SWA2L2S2	5%	4.5	3.1%	SMA Bars 2.7%	HS Steel Bars 2.7%	0.6%	Steel Bars 0.6%	1.3%	2.0%	1.3%
57	SWA2L2S3	5%	4.5	3.1%	SMA Bars 3.3%	HS Steel Bars 3.3%	0.6%	Steel Bars 0.6%	1.3%	2.0%	1.3%
58	PWA2L2S1	5%	4.5	3.1%	Steel Bars 1.3%	Steel Bars 1.3%	0.6%	PT Strands 0.2%	1.3%	2.0%	1.3%
59	PWA2L2S2	5%	4.5	3.1%	Steel Bars 1.3%	Steel Bars 1.3%	0.6%	PT Strands 0.3%	1.3%	2.0%	1.3%
60	PWA2L2S3	5%	4.5	3.1%	Steel Bars 1.3%	Steel Bars 1.3%	0.6%	PT Strands 0.4%	1.3%	2.0%	1.3%
61	CWA2L3S1	5%	6.7	2.1%	Steel Bars 1.3%	Steel Bars 1.3%	0.6%	Steel Bars 0.6%	1.3%	1.8%	1.3%
62	CWA2L3S2	5%	6.7	2.1%	Steel Bars 1.6%	Steel Bars 1.6%	0.6%	Steel Bars 0.6%	1.3%	1.8%	1.3%
63	CWA2L3S3	5%	6.7	2.1%	Steel Bars 1.8%	Steel Bars 1.8%	0.6%	Steel Bars 0.6%	1.3%	1.8%	1.3%
64	GWA2L3S1	5%	6.7	2.1%	Steel Bars 1.3%	Steel Bars 1.3%	0.6%	GFRP Bars 1%	1.3%	1.8%	1.3%
65	GWA2L3S2	5%	6.7	2.1%	Steel Bars 1.3%	Steel Bars 1.3%	0.6%	GFRP Bars 1.4%	1.3%	1.8%	1.3%
66	GWA2L3S3	5%	6.7	2.1%	Steel Bars 1.3%	Steel Bars 1.3%	0.6%	GFRP Bars 1.9%	1.3%	1.8%	1.3%
67	SWA2L3S1	5%	6.7	2.1%	SMA Bars 1.9%	HS Steel Bars 1.9%	0.6%	Steel Bars 0.6%	1.3%	1.8%	1.3%
68	SWA2L3S2	5%	6.7	2.1%	SMA Bars 2.5%	HS Steel Bars 2.5%	0.6%	Steel Bars 0.6%	1.3%	1.8%	1.3%
69	SWA2L3S3	5%	6.7	2.1%	SMA Bars 3.1%	HS Steel Bars 3.1%	0.6%	Steel Bars 0.6%	1.3%	1.8%	1.3%
70	PWA2L3S1	5%	6.7	2.1%	Steel Bars 1.3%	Steel Bars 1.3%	0.6%	PT Strands 0.2%	1.3%	1.8%	1.3%
71	PWA2L3S2	5%	6.7	2.1%	Steel Bars 1.3%	Steel Bars 1.3%	0.6%	PT Strands 0.3%	1.3%	1.8%	1.3%
72	PWA2L3S3	5%	6.7	2.1%	Steel Bars 1.3%	Steel Bars 1.3%	0.6%	PT Strands 0.4%	1.3%	1.8%	1.3%

### 6.3.4.1 Reinforcement layout of Control Walls

The reinforcement layouts of three control walls with a reinforcement layout of S1 and different lengths are shown in Fig. 6.2. Each of the walls was reinforced with longitudinal 20M bars in the boundary element and with longitudinal 15M bars in the web of the wall placed at every 200 mm. The control walls with reinforcement layouts of S2 and S3 had 25% and 42% more reinforcement ratios with respect to the control wall with an S1 reinforcement layout.

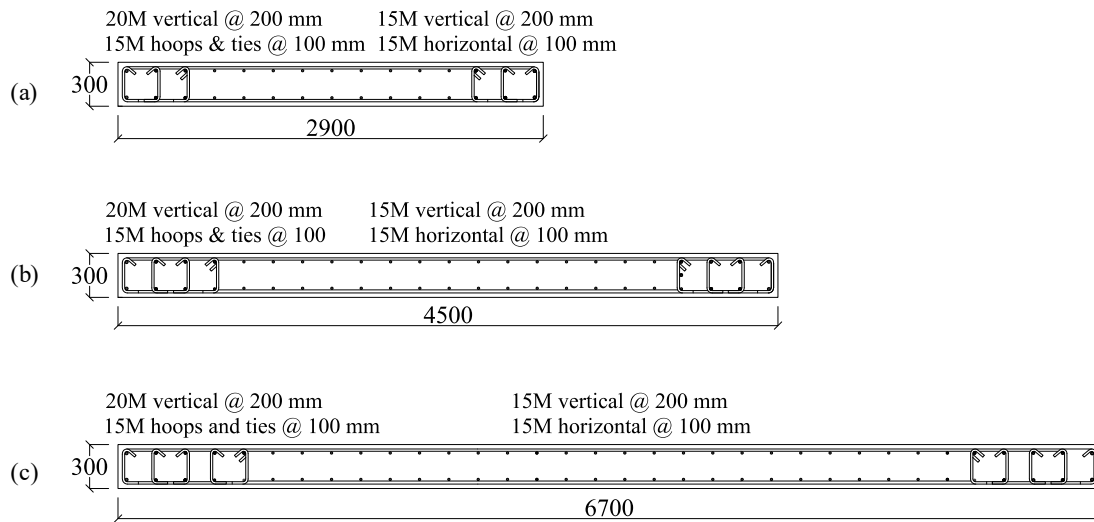


Figure 6.2. Reinforcement layout of (a) CWA1L1S1, (b) CWA1L2S1, (c) CWA1L3S1

### 6.3.4.2 Reinforcement layout of Innovative Walls

The reinforcement layouts of the innovative walls were designed based upon the reinforcement layouts of the control walls shown in Fig. 6.2. The following modifications were applied to the reinforcement layouts of the control walls. Region-4 (Fig. 6.1(b)) in each steel-GFRP reinforced wall (GW) was reinforced with either two, three, or four rows of 20M GFRP corresponding to S1, S2, or S3 reinforcement layouts. Region-4 in each partially post-tensioned wall (PW) was reinforced with a row of post-tensioned tendons and two rows of #3 steel rebars. The tendons were post-tensioned to 835 MPa (0.5F<sub>y</sub>). The tendons had areas of either 130, 200, or 268 mm<sup>2</sup> in the case of S1, S2, or S3 reinforcement layouts. Figure 6.3(a) and (b) show the reinforcement layouts of the GWA1L1S1 and PWA1L1S1 walls.

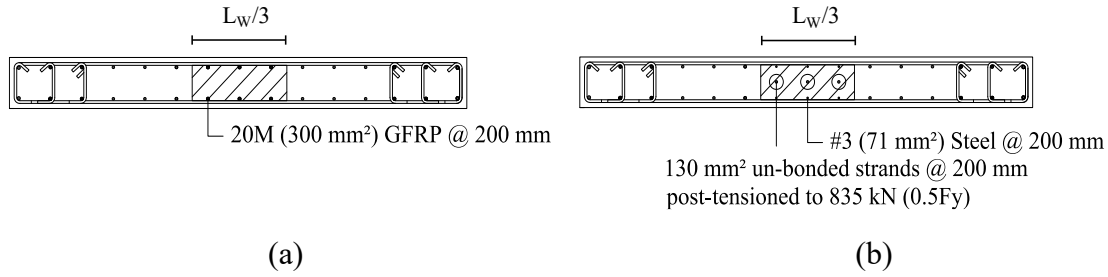


Figure 6.3. Reinforcement layout of (a) GWA1L1S1, (b) PWA1L1S1 walls

The region-1 in each SW wall was reinforced with either three, four, or five rows of 20M SMA bars regarding S1, S2, or S3 self-centering reinforcement layouts. The region-2 of each SW wall was reinforced with 20M high strength steel rebars that had a yield strength of 520 MPa and the same layout as described for region-1 of the wall. The distance between every two adjacent reinforcements in the control and the innovative shear walls of this study was 200 mm. Figures 6.4 shows the reinforcement layout of the SWA1L1S1 walls.

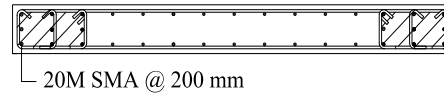


Figure 6.4. Reinforcement layout of SWA1L1S1 wall

Table 6.2 summarizes the self-centering reinforcement used in the innovative walls with S1, S2, and S3 reinforcement layouts. The cross-sectional area of the self-centering reinforcement in the S2 and S3 layouts can also be determined by multiplying the cross-sectional area of self-centering reinforcement in S1 layouts to the coefficients displayed in Table 6.3.

Table 6.2. Self-centering reinforcement layouts

	GW Region 4	SW Region 1	PW Region 4
S1	2-20M GFRP Bar @ 200mm	3-20M SMA Bar @ 200mm	H.S. Steel Strand 130 mm <sup>2</sup> @ 200mm
S2	3-20M GFRP Bar @ 200mm	4-20M SMA Bar @ 200mm	H.S. Steel Strand 200 mm <sup>2</sup> @ 200mm
S3	4-20M GFRP Bar @ 200mm	5-20M SMA Bar @ 200mm	H.S. Steel Strand 268 mm <sup>2</sup> @ 200mm

Table 6.3. Self-centering reinforcement ratio in S2 and S3 relative to S1

Shear Wall	$\alpha_2$	$\alpha_3$
Steel-GFRP	1.50	2.00
Post-tensioned	1.54	2.00
Steel-SMA	1.33	1.67

### 6.3.5 FE Modeling

#### 6.3.5.1 Mesh-Size Sensitivity Analysis

The FE model of each shear wall was developed based on a mesh with rectangular elements. In the horizontal direction, the element size was 100 mm in the boundary elements and 200 mm in the web of each wall. In the vertical direction, the element size was 150 mm along the first two stories, 200 mm along the third and fourth stories, and 300 mm along the fifth story of each wall.

The element sizes were selected as the results of a sensitivity analysis showed the adequacy of the mesh used in the discretization of the walls. A sensitivity analysis was performed on the mesh described above, mesh M1, and mesh M2 that had half the mesh-size of mesh M1 in the horizontal direction and the same mesh-size in the vertical direction. Figure 6.5 shows the CWA1L2S1 wall discretized with mesh M1 and mesh M2. The horizontal and vertical degrees of freedom at the base of the models were restrained, and a monotonically increasing displacement was applied to the top middle point of the FE models of the wall.

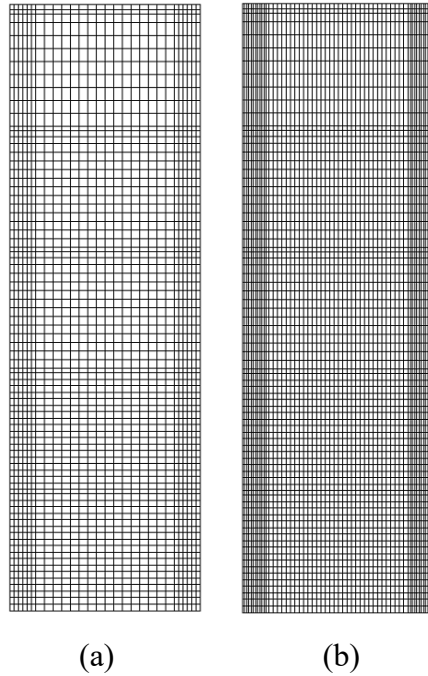


Figure 6.5. CWA1L2S1 wall discretized with (a) mesh M1, (b) mesh M2

Figure 6.6 shows the pushover lateral force-displacement responses of the FE models developed using mesh M1 and mesh M2. As can be seen in the figure, the lateral force-displacement responses of the wall were almost identical. For this reason, the FE models of the shear walls were generated based on mesh M1, which offered a substantially lower computational cost in comparison to the models created based on mesh M2. Furthermore, the finite element models of the walls with a length of L1, and a mesh of M1, had 18 four-node elements along the horizontal direction. These models correspond to a relatively fine mesh based on (Palermo and Vecchio 2007).

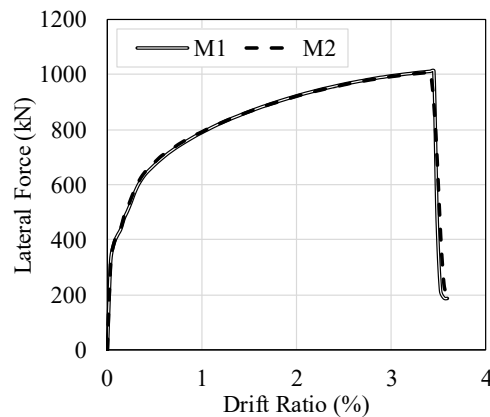


Figure 6.6. Lateral load-displacement response of FE model of CWA1L2S1 wall discretized with mesh (a) M1, (b) M2

### 6.3.5.2 FE Models

The properties of the concrete material used in the boundaries of each shear wall were specified by VecTor2 based on the Montoya (2000) confinement model, according to the confining steel hoops of the boundary elements. The longitudinal reinforcement in each shear wall was modeled with truss elements to precisely model the location of each longitudinal reinforcement and incorporate the bond properties of the self-centering reinforcement into the FE modes of the walls (Fig. 6.7).

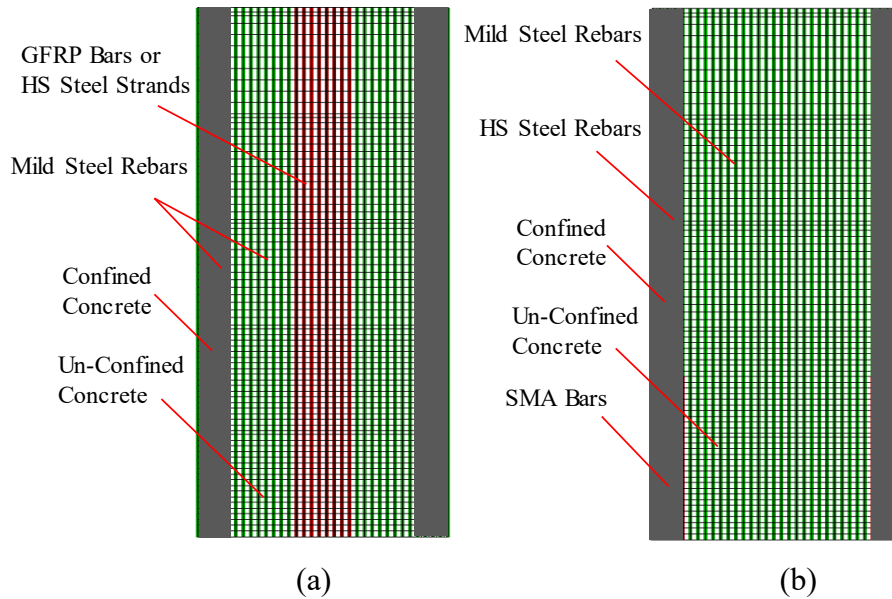


Figure 6.7. FE models (a) steel-GFRP reinforced and partially post-tensioned walls, (b) steel-SMA reinforced walls

The reinforcement was defined using the same behavioral models described in Chapter 5. Cyclic lateral displacements were applied to the middle top points of the walls while the horizontal and vertical degrees of freedom at the base of the walls were restrained. The mechanical properties of the reinforcement used in the analysis of the walls are summarized in Table 6.4.

Table 6.4. Mechanical properties of different types of reinforcement

Reinforcement	Elastic Modulus (GPa)	Yield Strength (MPa)	Ultimate Strength (MPa)
Steel bars	200	420	620
GFRP bars	62.6	N.A.	1150
HS Steel strands	195	1670	1860
NiTi bars	27.4	330	890

### 6.3.6 Cyclic Response

The shear walls described in the previous section were subjected to cyclic displacement reversals with a cycle increment of 140 mm (1% drift ratio) and a displacement step of 5 mm (0.036% drift ratio). The displacement reversals, shown in Figure 6.8, were applied to the top middle node in the FE model of each wall.

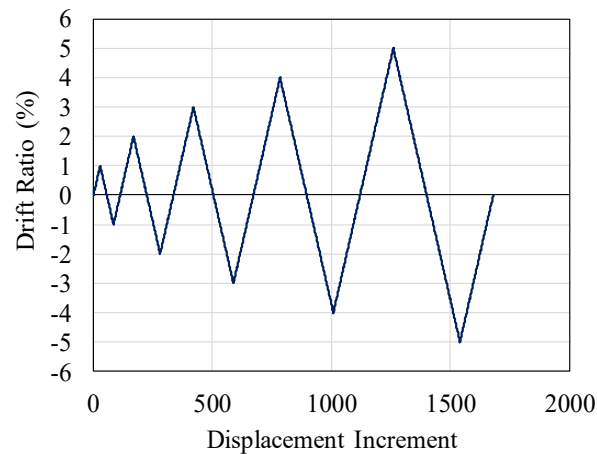


Figure 6.8. Loading protocol

The most slender shear walls, which had an aspect ratio of 4.8, had the highest ultimate drift ratio, which varied between 4.0% and 6.2%. On the other hand, the least slender shear walls with an aspect ratio of 2.1 had the lowest ultimate drift ratios, which ranged from 2.6% to 3.3%. The hysteretic response of the innovative walls was more pinched in comparison to their corresponding CW shear walls due to the lower permanent drift ratios of the innovative walls.

The hysteretic responses of the innovative shear walls with a reinforcement layout of S3 and ALRs of 0% and 5% are shown in Figs. 6.9 and 6.10, respectively. As can be seen in the figures, the hysteretic responses of the innovative shear walls are displayed in contrast to the response of their corresponding control walls. The innovative walls had comparable lateral resistance to the control walls while showing some levels of energy dissipation and deformability. The walls also showed higher levels of self-centering compared to the control walls.

The innovative shear walls with reinforcement layout of S1 and S2 had similar hysteretic responses to those shown in Figs. 6.9 and 6.10. However, the lateral resistance in the innovative walls was lower than the lateral resistance of the walls with a layout of S3.

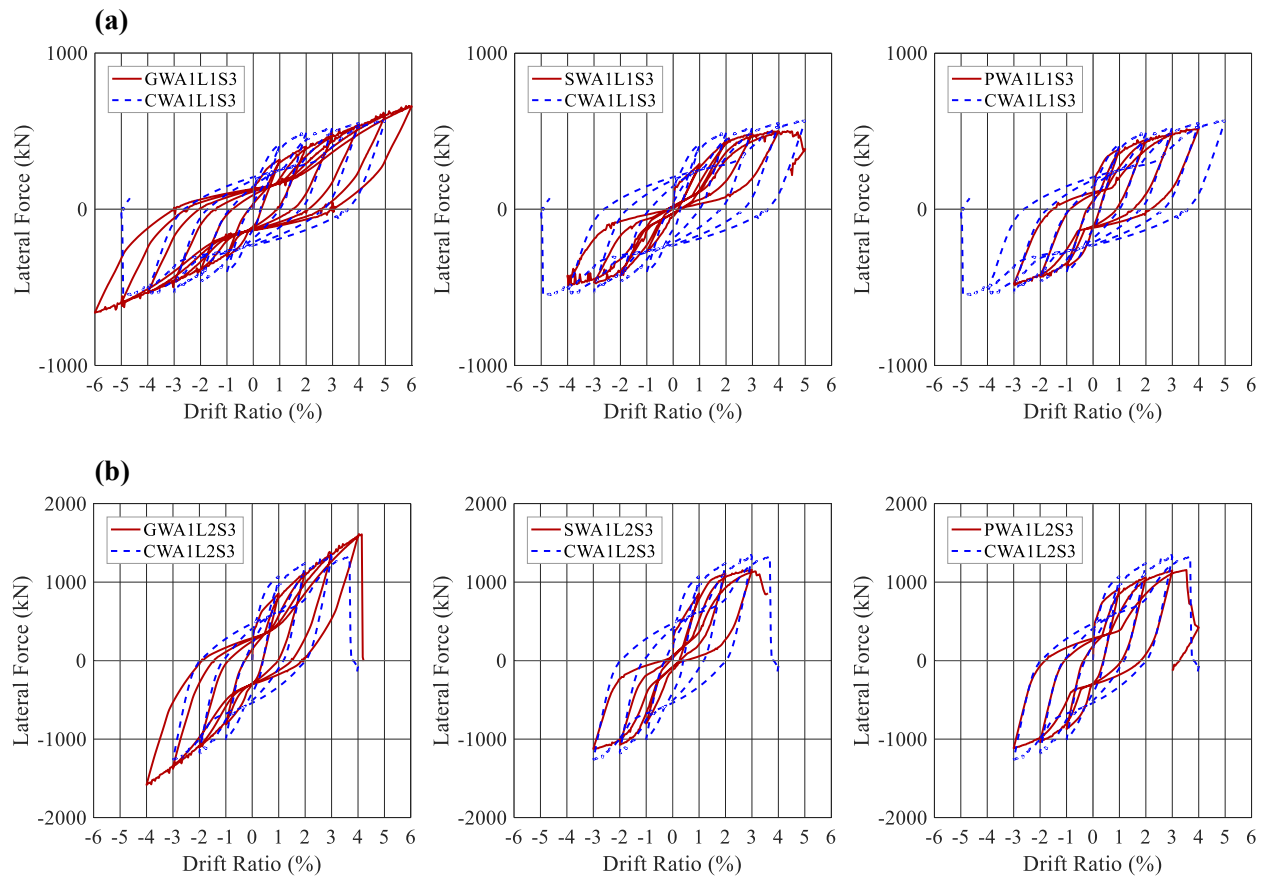


Figure 6.9. Hysteretic response of innovative walls (a) GWA1L1S3, SWA1L1S3, PWA1L1S3, (b) GWA1L2S3, SWA1L2S3, PWA1L2S3, (c) GWA1L3S3, SWA1L3S3, PWA1L3S3

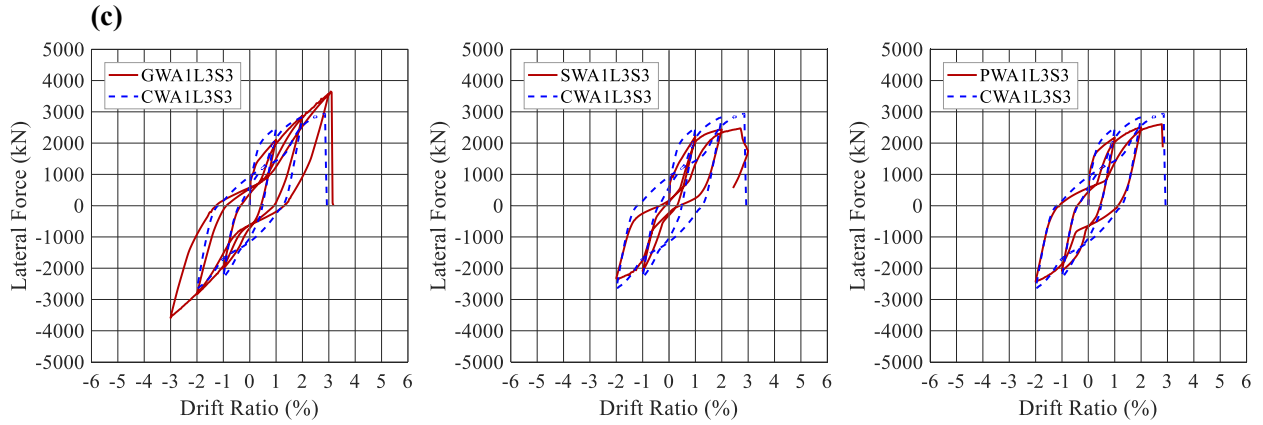


Figure 6.9. Continued

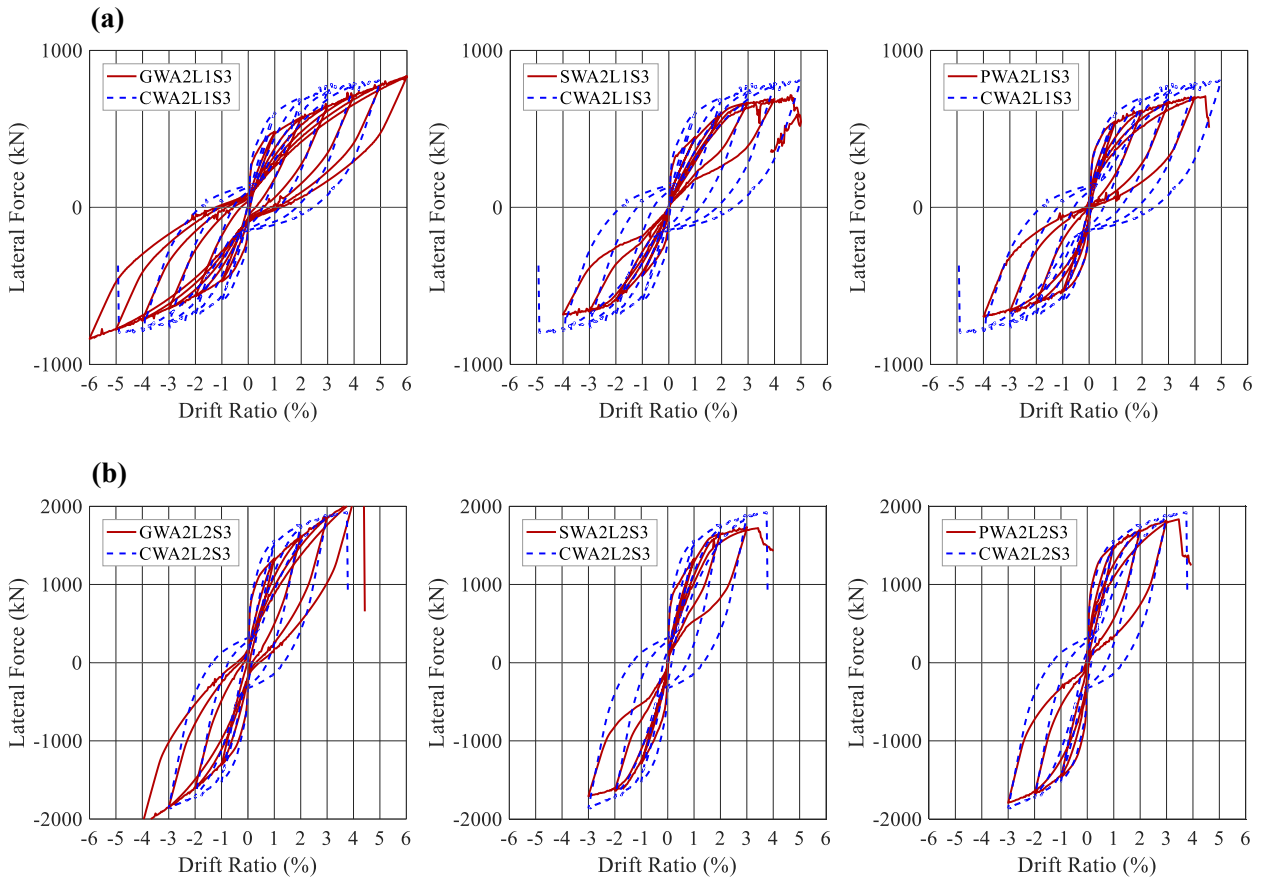


Figure 6.10. Hysteretic response of innovative walls (a) GWA2L1S3, SWA2L1S3, PWA2L1S3, (b) GWA2L2S3, SWA2L2S3, PWA2L2S3, (c) GWA2L3S3, SWA2L3S3, PWA2L3S3

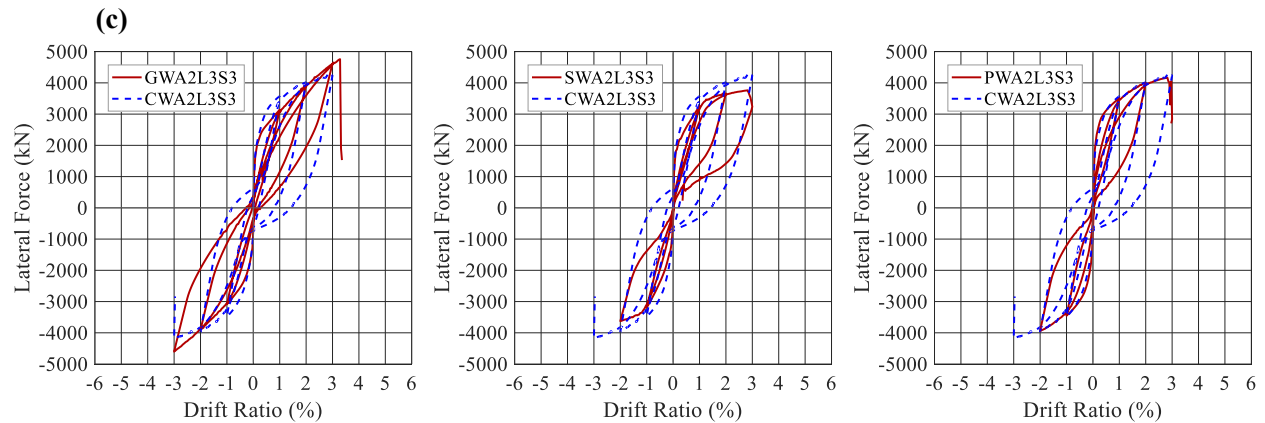


Figure 6.10. Continued

The self-centering in the shear walls was more significant in the presence of axial loads in comparison to the no-axial-load case. This is consistent with research performed by Maciel et al. (2016). The walls with axial loads also had higher lateral stiffness and resistance in comparison to their corresponding control and innovative walls with no axial loads. This was because axial loads increase crack closure, which results in the participation of cracked concrete in resisting stresses.

## 6.4 Cyclic Response Parameters

In this section, different properties of the cyclic response of the walls are studied. Different cyclic response properties of the shear walls were displayed in bar graphs to make a comparison between the shear walls easier. Each bar graph shows the response properties of the CW, GW, SW, and PW walls that have the same ALR, respectively.

### 6.4.1 Lateral Resistance

The lateral resistance in the shear walls significantly increased with the increase of the length in the walls. This is because shear walls with longer cross-sections have higher resisting moments, which correspond to higher lateral resisting forces. Also, the increase in the reinforcement ratio of the walls caused an increase in the lateral resistance of the walls. This is also due to the increase in the resisting moments of the walls.

The increase in the ALR of the walls increased the resistance of the walls. The reason for this is that the axial loads increase crack closure, which resulted in the participation of cracked concrete

in resisting stresses. Figures 6.11(a) and (b) show the lateral resistance of the shear walls when the axial load ratio is 0% and 5%, respectively.

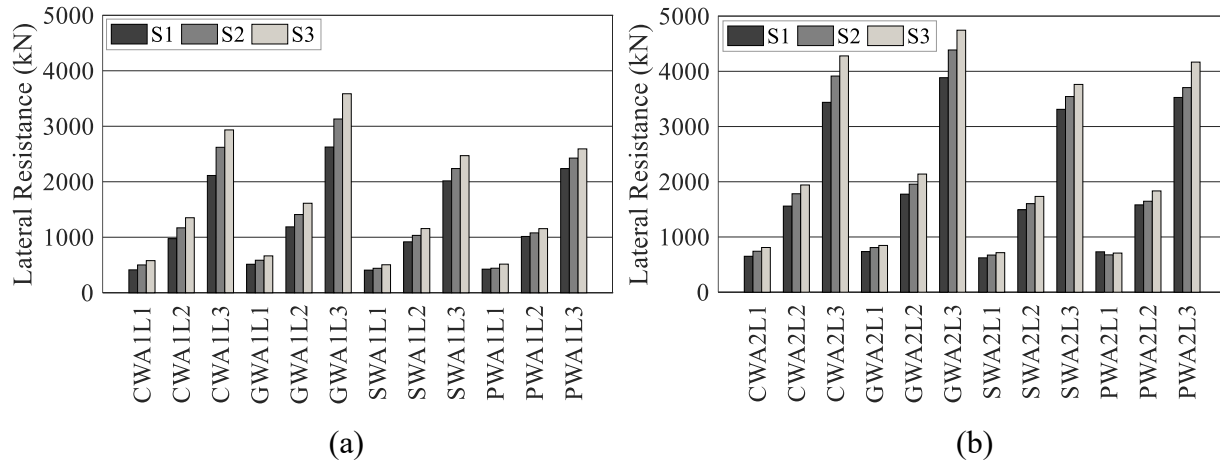


Figure 6.11 Lateral Resistance in shear walls with ALRs of (a) 0%, (b) 5%

The control and innovative walls with the same length, ALR, and reinforcement layouts were designed to have comparable lateral resistance. Under no axial loads, the resistance in the innovative walls relative to the resistance of their corresponding CW walls was between 1.15 to 1.24% for the GW walls, from 0.84 to 0.99 for the SW walls, and from 0.85 to 1.06 for the PW walls (Fig. 6.12(a)). Under an ALR of 5%, the relative resistance was between 1.05 to 1.13% for the GW walls, from 0.88 to 0.96 for the SW walls and from 0.88 to 1.12 for the PW walls (Fig. 6.12(a)).

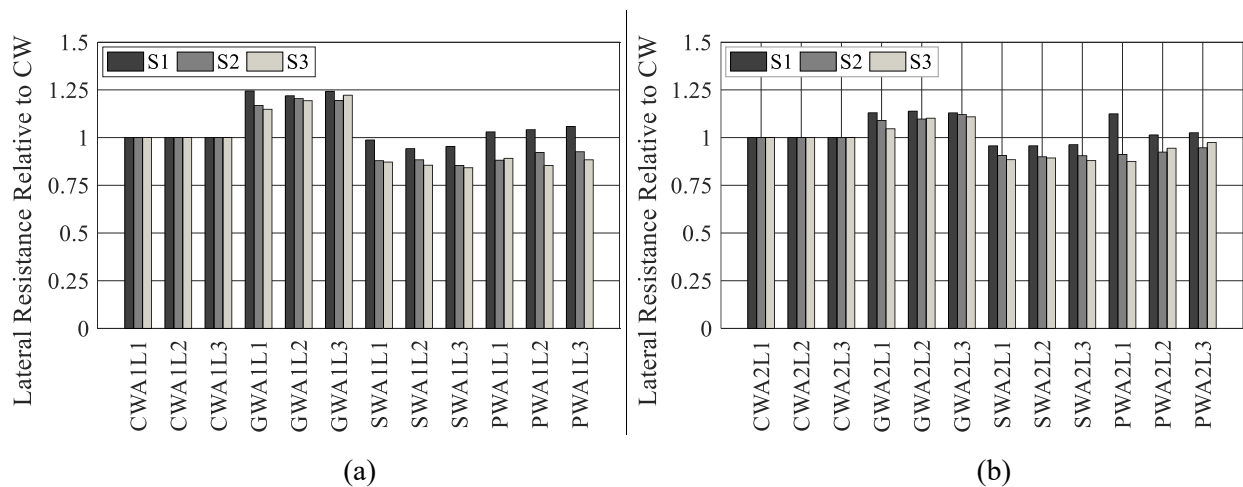


Figure 6.12. Relative lateral resistance to CW in shear walls with ALRs of (a) 0%, (b) 5%

### 6.4.2 Effective Stiffness

The stiffness is an essential parameter in the design of shear walls since it controls the serviceability limit states of shear walls. The hysteretic response of each wall was idealized using reduced stiffness equivalent elasto-plastic yield model by Park (1988) to study the stiffness of the innovative shear walls.

The stiffness in the shear walls significantly increased with the increase in the length of the walls. This was because of the higher moments of inertia of the longer shear walls. On the other hand, the increase of reinforcement ratios did not have a significant impact on the stiffness of the walls.

The stiffness in the shear walls increased with the increase of the axial load ratio. This is because the axial loads increased the resistance of the shear walls to form flexural cracks at the early stages of analysis, leading to an increase in the stiffness of the walls. Figures 6.13(a) and (b) show the effective stiffness of the shear walls when the axial load ratio is 0% and 5%, respectively.

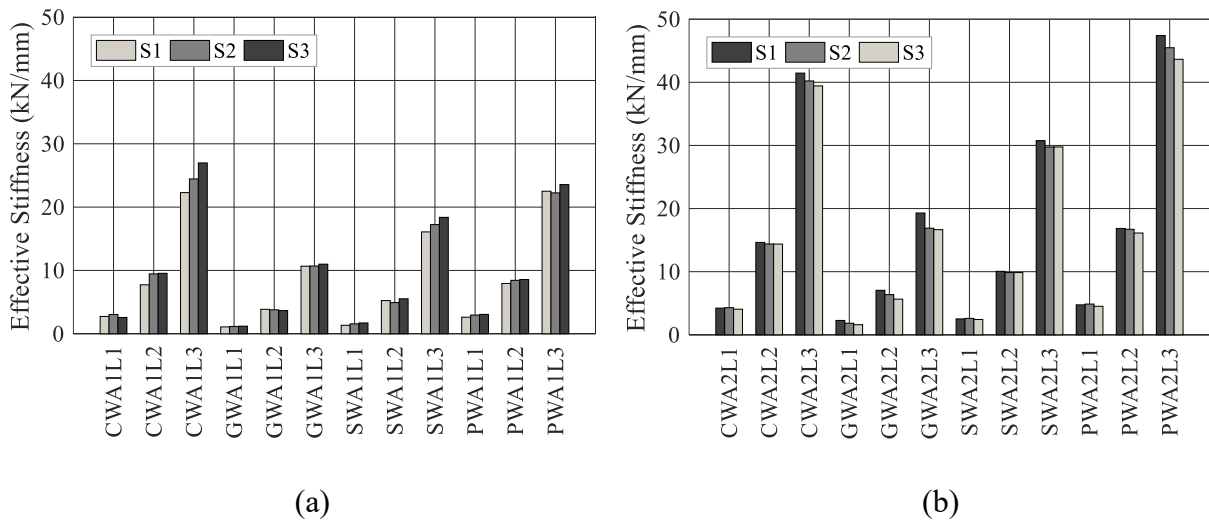


Figure 6.13 In-plane effective stiffness in shear walls with ALRs of (a) 0%, (b) 5%

In the case of the self-centering reinforcement, the effective stiffness in the SW and GW walls was lower than in their corresponding CW walls due to the lower modulus of elasticity of SMA and GFRP in comparison to steel. The effective stiffness of the PW walls was slightly lower than that of their corresponding CW wall when the walls carried no axial loads. This was since the PW walls had less bonded reinforcement.

On the other hand, the PW walls showed higher stiffness values compared to the CW walls when carrying an ALR of 5%. This was because the compressive stresses developed due to the post-tensioning and axial loads controlled the cracking of the walls, which resulted in a higher moment of inertia and stiffness for the walls.

In the absence of axial loads, the stiffness in the innovative walls relative to the stiffness of their corresponding CW walls varied from 0.38 to 0.50 for the GW walls, from 0.49 to 0.72 for the SW walls, and from 0.87 to 1.19 for the PW walls (Fig. 6.14(a)). With 5% ALR, the relative stiffness varied from 0.39 to 0.54 for the GW walls, from 0.60 to 0.76 for the SW walls, and from 1.12 to 1.16 for the PW walls (Fig. 6.14(b)).

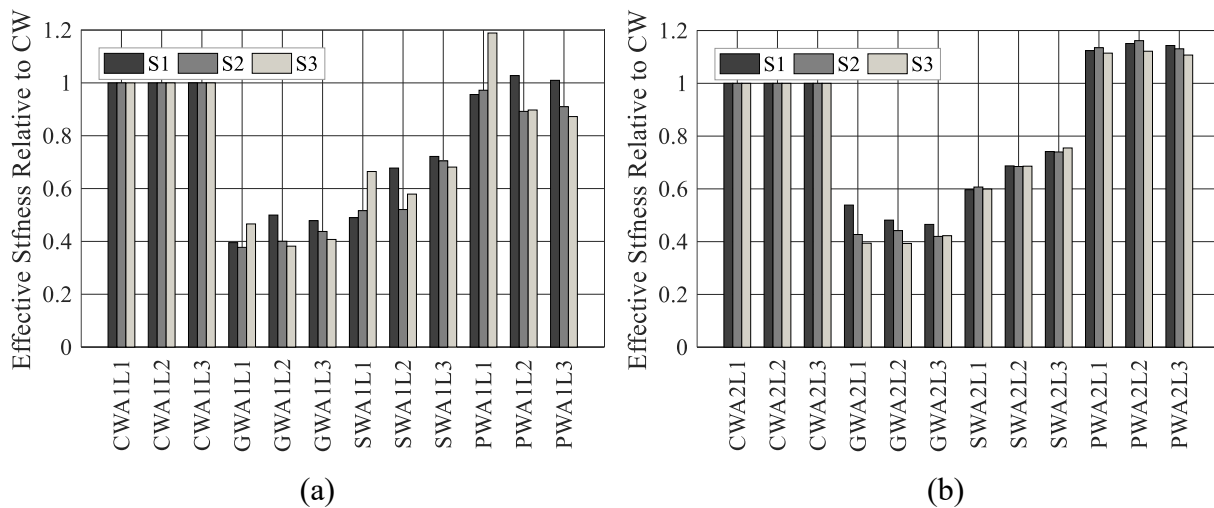


Figure 6.14. Relative effective stiffness to CW for shear walls with ALRs of (a) 0%, (b) 5%

### 6.4.3 Ultimate Drift Ratio

The ultimate drift ratio in the shear walls notably decreased as the lengths of the walls increased, and the shear walls became less slender. The ultimate drift ratio in the shear walls did not notably change with the increase of the axial load ratio. However, in most cases, the drift ratio capacity in the shear walls that carried no axial loads was slightly lower than in the shear wall with an ALR of 5%. This was because the failure mode in the shear walls was rebar rupturing rather than concrete crushing. Also, an ALR of 5% was not great enough to trigger concrete crushing, as the boundaries of the walls were adequately confined. For this reason, compressive strains caused a slight improvement in the ultimate drift ratios of the walls. The drift capacity of the walls decreased

as the lengths of the walls increased, and the walls became less slender. Figures 6.15(a) and (b) show the ultimate drift ratio of the shear walls.

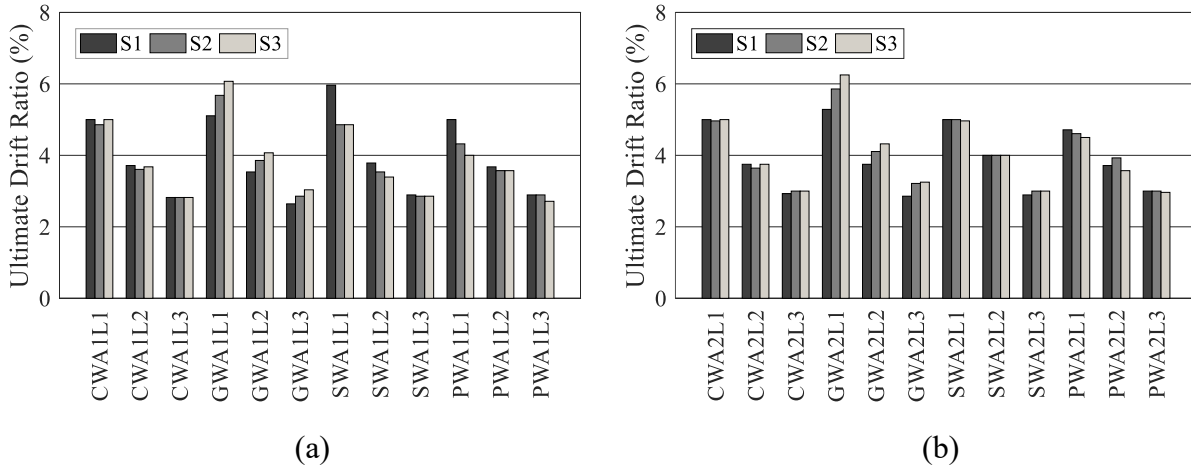


Figure 6.15. Ultimate drift ratio in shear walls with ALRs of (a) 0%, (b) 5%

The ultimate drift ratio in the GW walls experienced an increase as the reinforcement ratio in the walls increased. On the other hand, the ultimate drift ratios were not significantly affected by the increase in the reinforcement ratios of other types of shear walls. This can be explained by the fact that the curvature was more evenly distributed in the GW walls compared to the CW, PW, and SW walls (section 6.5.3.1). For this reason, more GFRP reinforcement resulted in more evenly curvature distributions and lower tensile strain demands on the rebars at the bases of the walls, which increased the deformability of the walls in comparison to other types of shear walls.

In the case of the self-centering reinforcement, the GW walls reached higher drift ratio capacities compared to their corresponding CW walls, as discussed above. The SW and PW walls generally had comparable ultimate drift ratios to their CW walls. In the absence of axial loads, the drift ratio capacity in the innovative walls relative to the drift ratio capacity of their corresponding CW walls varied from 0.94 to 1.21 for the GW walls, from 0.92 to 1.19 for the SW walls, and from 0.80 to 1.03 for the PW walls (Fig. 6.16(a)). In the case of 5% ALR, the relative drift ratio capacity changed from 0.98 to 1.25 for the GW walls, from 0.99 to 1.10 for the SW walls and from 0.90 to 1.08 for the PW walls (Fig. 6.16(b)).

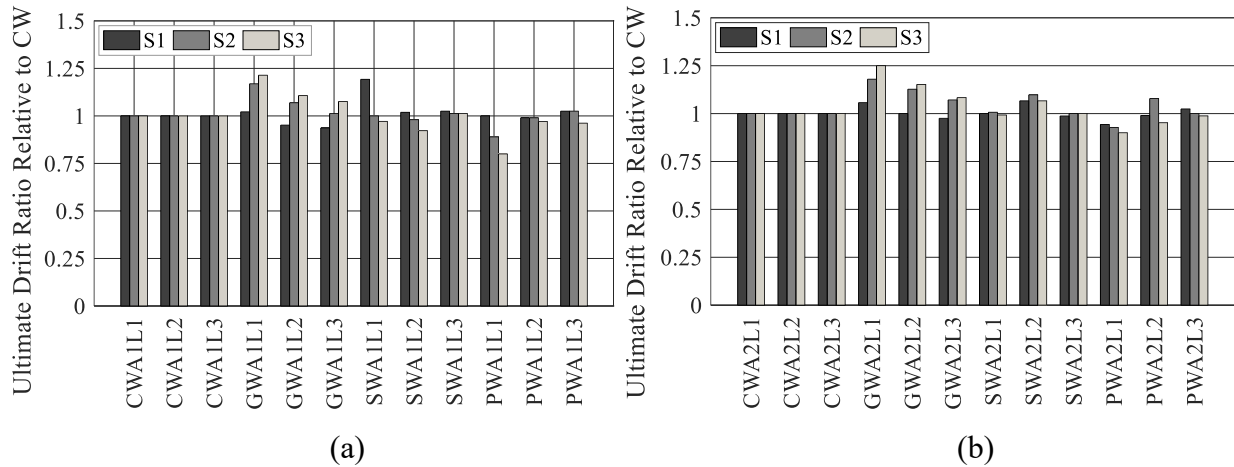


Figure 6.16. Relative ultimate drift ratio to CW for shear walls with ALRs of (a) 0%, (b) 5%

### 6.4.4 Energy Dissipation

The energy dissipation capacity in the shear walls increased by the length of the walls, as more reinforcement was available in longer walls. On the other hand, more self-centering reinforcement led to higher self-centering and lowered the normalized energy dissipation of the walls. The axial load also increased the self-centering of shear walls and caused a decrease in the energy dissipation capacity. Axial loads also decreased the energy dissipation capacity in the shear walls. This decrease was because the hysteretic response of the walls showed higher self-centering properties and was more pinched in the presence of the axial loads. The normalized dissipated energy of the shear walls in the second cycle of their hysteretic response, which reached drift ratios of +2% and -2%, is shown in Fig. 6.17.

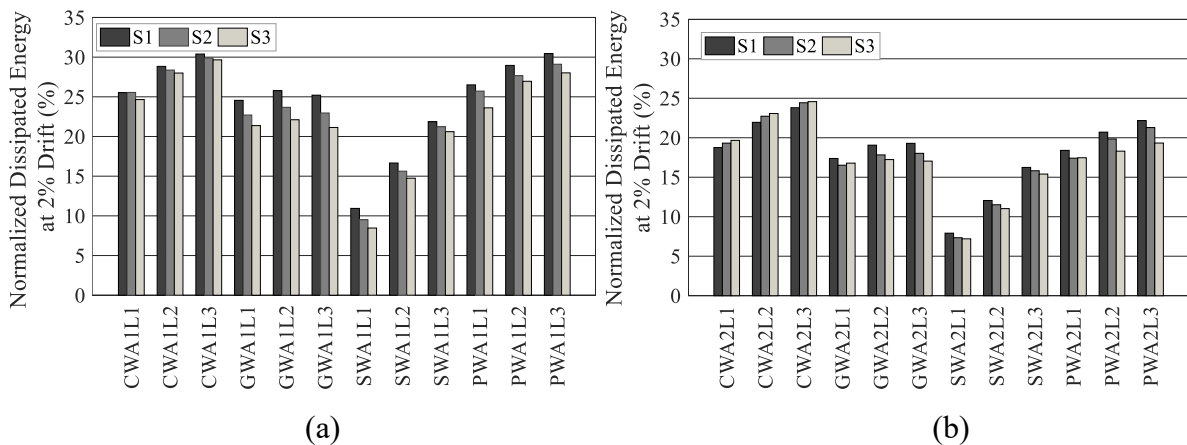


Figure 6.17. Normalized dissipated energy in shear walls with ALRs of (a) 0%, (b) 5%

In general, the innovative shear walls had lower values of normalized energy dissipation in comparison to their corresponding CW walls. This disadvantage was because the more pinched hysteretic behavior of the innovative walls in contrast to the CW walls, as the walls had higher self-centering properties. In the absence of axial loads, the energy dissipation capacity in the innovative walls relative to the energy dissipation capacity of their corresponding CW walls varied from 0.69 to 0.93 for the GW walls, from 0.34 to 0.72 for the SW walls, and from 0.95 to 1.04 for the PW walls (Fig. 6.18(a)). With 5% ALR, the relative energy dissipation capacity varied from 0.71 to 0.96 for the GW walls, from 0.37 to 0.68 for the SW walls, and from 0.79 to 0.98 for the PW walls (Fig. 6.18(b)).

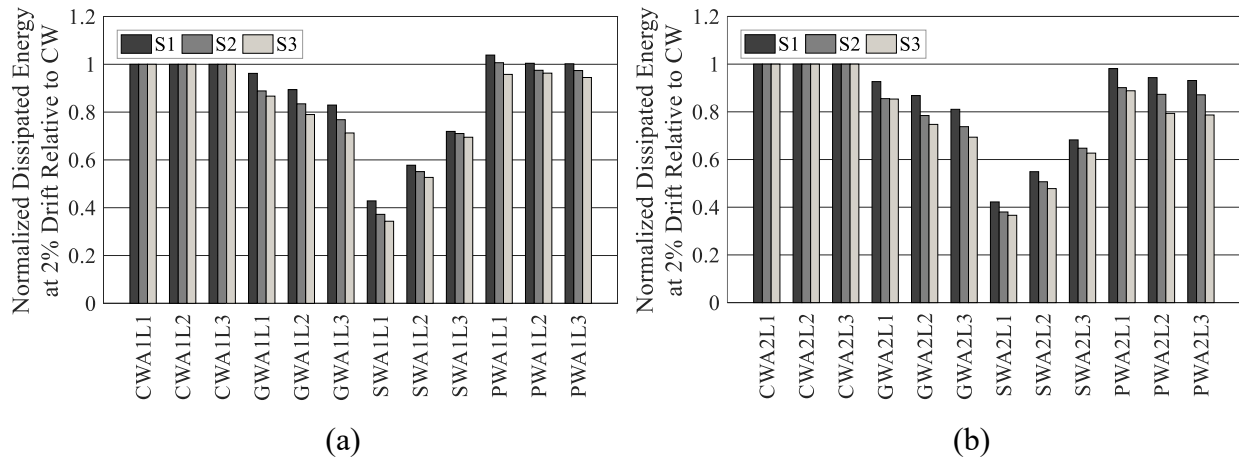


Figure 6.18. Normalized dissipated energy in the second cycle of hysteretic response of shear walls relative to CW walls when ALR is (a) 0%, (b) 5%

## 6.4.5 Effects of Independent Parameters on Cyclic Response Parameters

### 6.4.5.1 Effects of Axial Loads

As discussed above, axial loads increased the lateral resistance of the shear walls. The reason for this is that the effect of axial loads on the concrete crack closure in the shear walls, resulting in the cracked concrete resisting compressive stresses. Also, axial loads increased the effective stiffness of the shear walls for the same reason. The effect of axial loads was not notable on the ultimate drift ratios of the walls. This was because the boundaries of the walls were adequately confined, and the axial loads were not high enough to initiate concrete crushing at the toes of the shear walls. Axial loads had a decreasing impact on the energy dissipation of the shear walls. This was because

axial loads increased the self-centering of shear walls, which increased the pinching in the cyclic response of the shear walls.

#### **6.4.5.2 Effects of Wall Lengths**

The increase in the length of the shear walls increased the lateral resistance of the walls. This was because shear walls that had longer cross-sections illustrated higher resisting moments and, consequently, higher lateral resisting forces. The increase in the length of the shear walls improved the effective stiffness of the walls. This was because it increased the moments of inertia of the shear walls. The increase in the length of the shear walls increased the energy dissipation of the walls. This was because there was more reinforcement in the longer walls to dissipate energy. The increase in the length of the shear walls decreased the ultimate drift ratio in the shear walls. This was because higher strain values were associated with the curvature in the less slender shear walls compared to the more slender walls.

#### **6.4.5.3 Effects of Reinforcement Ratio**

The rise in the reinforcement ratio increased the lateral resistance of the walls since higher reinforcement ratios correspond to higher resisting moments and lateral resisting forces. The increase in the reinforcement ratio of the shear walls had an insignificant effect on the stiffness. This is because the stiffness in the shear walls is a function of wall dimensions rather than the reinforcement ratio. The increase in the reinforcement ratio of the shear walls decreased the energy dissipation of the walls. This was because more self-centering reinforcement resulted in higher self-centering properties and more pinching in the hysteretic response of the walls. The reinforcement ratio had a small decreasing impact on the ultimate drift ratios of the shear walls except for the GW walls. This was because higher GFRP reinforcement improved the uniformity of the curvature distribution in the GW walls while it was the opposite for the other types of walls.

#### **6.4.5.4 Effects of Self-Centering Reinforcements**

The type of self-centering reinforcement also affected the response of the shear walls. The steel-GFRP reinforced walls had lower stiffness and energy dissipation levels compared to the control walls. This was because of the linear elastic response of the GFRP bars of the shear walls. The GW walls had higher ultimate drift ratios in comparison to the control walls, as a result of the more

evenly distributed curvature in the GW walls. The steel-SMA reinforced walls had lower stiffness compared to the CW walls due to the lower modulus of elasticity of the SMA bars than steel. The SW walls had lower energy dissipation levels compared to the CW walls. This was because of the low bond properties of the SMA bars in the shear walls. The SW walls had comparable ultimate drift ratios in contrast to the control walls.

The partially post-tensioned walls showed a higher stiffness level compared to the control walls. This was due to the post-tensioning compressive stresses of the walls, which improved crack closure in the shear walls. The PW walls had slightly lower ultimate drift ratios than the CW walls since the curvature distribution was more concentrated at the base of the walls. The walls also had lower energy dissipation capacity compared to the CW walls as the self-centering was higher and in the PW walls, and their hysteretic responses were more pinched.

## 6.5 Design Parameters

### 6.5.1 Ductility

#### 6.5.1.1 Idealized Force-Displacement Response

The hysteretic response of each shear wall was idealized with the reduced stiffness equivalent elasto-plastic yield model by Park (1988) to evaluate the yield drift ratio and the ductility in the shear walls. The idealized back-bone curve of each wall shared three points with the hysteretic response of the wall at lateral loads of zero,  $0.75H_u$ , and  $H_u$ , with  $H_u$  being the peak lateral load of the wall. The idealized backbone curves of the walls are shown in Fig. 6.19 and 6.20.

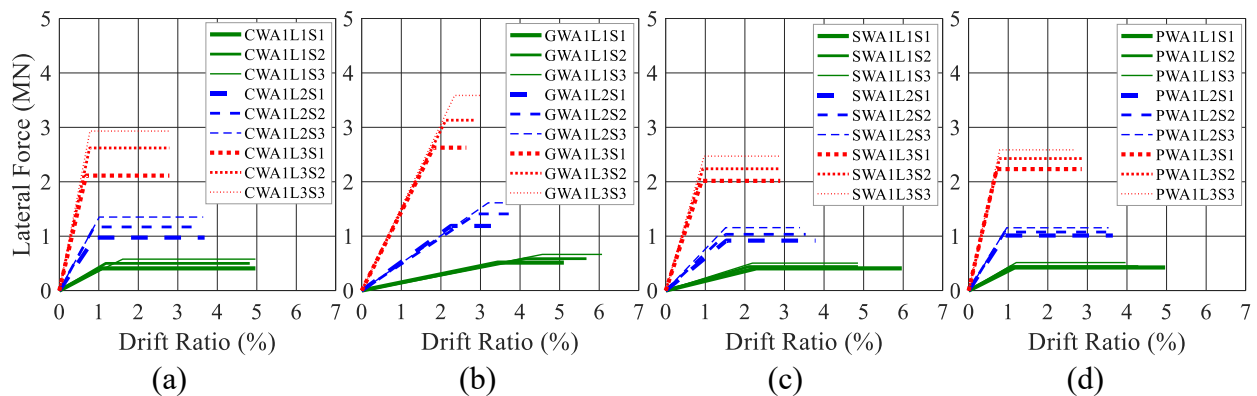


Figure 6.19. Idealized back-bone curves using reduced stiffness equivalent elasto-plastic model for shear walls with an ALR of 0% (a) CW, (b) GW, (c) SW, (d) PW

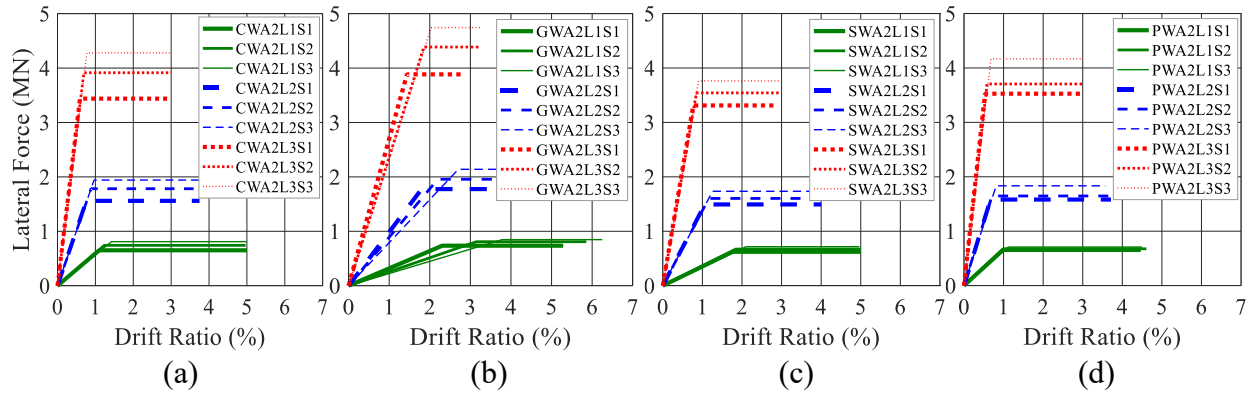


Figure 6.20. Idealized back-bone curves using reduced stiffness equivalent elasto-plastic model for shear walls with an ALR of 5% (a) CW, (b) GW, (c) SW, (d) PW

### 6.5.1.2 Yield Drift Ratio

The yield drift ratio slightly decreased as the length of the shear walls increased. This can be attributed to the lower curvature and lateral displacement of shear walls with longer cross-sections at a given tensile strain. On the other hand, the yield drift ratio in the shear walls increased as the reinforcement ratio of the walls increased. This observation can be attributed to the increase in the lateral resistance in the shear walls while the stiffness of the walls remained relatively constant. The yield drift ratio in the shear walls slightly decreased with the increase in the axial load ratios of the walls. This is because axial loads enhanced the stiffness of the shear walls. Figure 6.21 shows the yield drift ratios of the shear walls with respect to their ultimate drift ratios.

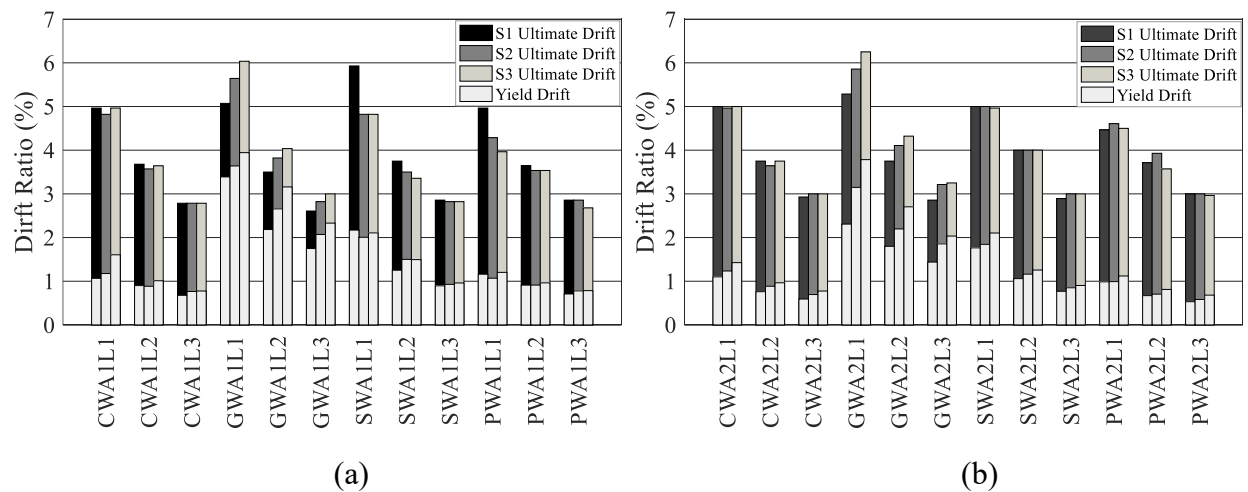


Figure 6.21. Yield and ultimate drift ratios in shear walls with ALRs of (a) 0%, (b) 5%

In the case of the self-centering reinforcement, the yield drift ratio in the SW and GW walls was higher than in their corresponding CW walls. This was because of the lower modulus of elasticity of SMA and GFRP in comparison to steel, which led to the lower stiffness in the walls. On the other hand, the yield drift ratio in the PW walls was lower than that of their corresponding CW, as the PW walls had higher stiffness as a result of post-tensioning. The yield drift ratio in the innovative walls with ALRs of 0% and 5% relative to the yield drift ratio of their corresponding CW walls was between 2.1 and 3.2 for the GW walls, between 1.2 and 2.0 for the SW walls and between 0.7 and 1.1 for the PW walls.

### 6.5.1.3 Displacement Ductility

The ductility levels of the shear walls slightly increased, as an ALR of 5% was applied to the walls. This was since the yield drift ratios were lower in the walls with an ALR of 5% compared to the no axial load case. The ductility of the walls did not notably change with the increase in the length of the shear walls. This was because the yield and ultimate drift ratios of the slender walls changed almost proportionate to each other. The ductility of the walls decreased with the increase in the reinforcement ratio of the walls. This was because the increase in the reinforcement ratio in the walls increased the yield drift ratio of the shear walls while it did not have a significant effect on the ultimate drift ratios of the walls. Figures 6.22 shows the displacement ductility of the walls.

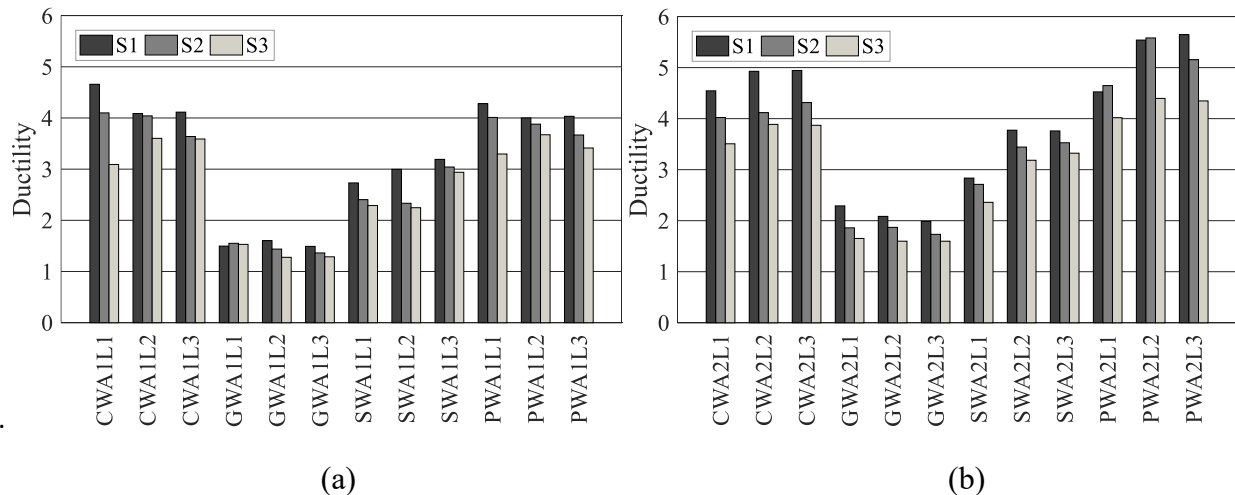


Figure 6.22. Displacement ductility in shear walls with ALRs of (a) 0%, (b) 5%

The displacement ductility was lower in the GW and SW walls compared to the ductility of their corresponding CW walls. This was due to the higher yield drift ratios of the walls compared to the CW walls. On the other hand, the PW walls had lower yield drift ratios than their corresponding CW walls resulting in the higher ductility of the walls. This was because the ultimate drifts were comparable in the comparable innovative and control walls.

The displacement ductility in the innovative walls with ALRs of 0% and 5% relative to the ductility in their corresponding CW walls was between 0.32 and 0.5 for the GW walls, between 0.58 and 0.86 for the SW walls, and between 0.92 and 1.36 for the PW walls. Fig. 6.23 shows the relative ductility in the innovative shear walls to their corresponding CW walls.

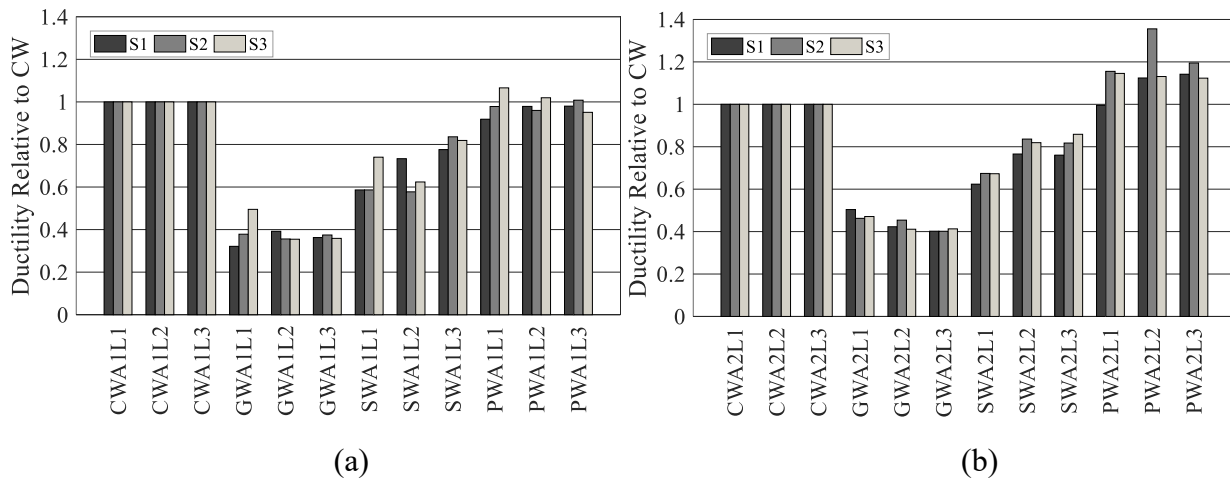


Figure 6.23. Relative ductility in shear walls to CW with an ALR of (a) 0%, (b) 5%

## 6.5.2 Inelastic Rotational Capacity

### 6.5.2.1 Yield Rotation

The yield rotation of each shear wall was calculated first to calculate the inelastic rotational capacity of the shear wall. The yield rotation of each shear wall was calculated as the rotation of the shear wall when the maximum curvature in the wall reached the yield curvature. Equation 6.1 shows the yield curvature, which was obtained, according to Priestley et al. (2007). In Eq.6.1  $\epsilon_y$  is the yield strain of longitudinal steel rebar and  $l_w$  is the length of the wall.

$$\phi_y = \frac{2\epsilon_y}{l_w} \quad (6.1)$$

Figure 6.24 shows the yield rotations of the shear walls. The yield rotations decreased as the lengths of the walls increased, which can be explained by the decrease of the yield curvature of the walls. The effect of axial loads and the reinforcement ratio was not significant on the yield rotations of the shear walls.

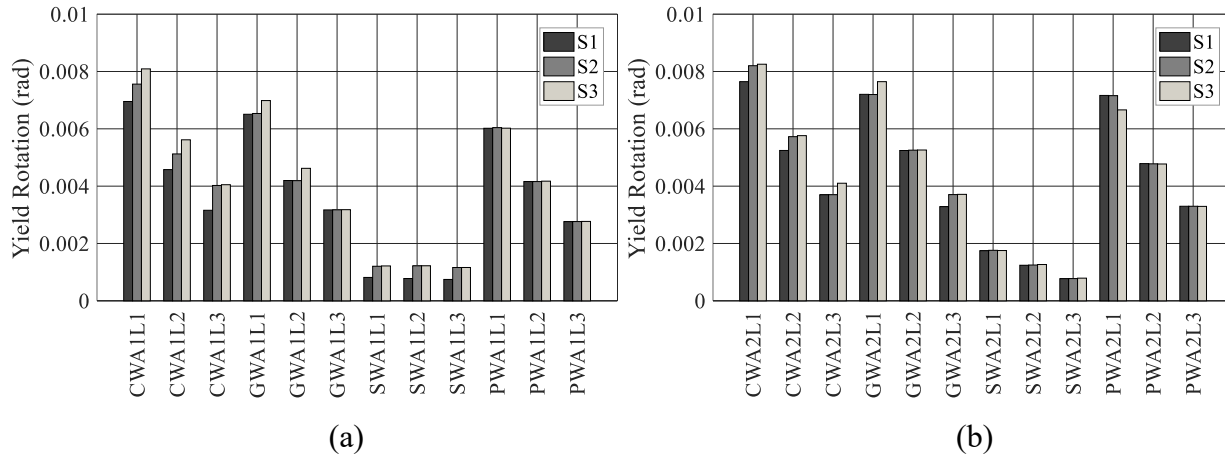


Figure 6.24. Yield Rotation in shear walls with ALRs of (a) 0%, (b) 5%

According to Fig. 6.24, the yield rotation was slightly lower in the GW walls than in their corresponding CW walls, as the GFRP bars used in the webs of the GW walls had lower stiffness compared to the steel bars used in the webs the CW walls. The PW walls also had slightly lower yield rotations than CW walls, as they had less bonded longitudinal reinforcement than the CW walls. The SW walls had the lowest yield rotations among the walls since the boundaries of the walls were reinforced with SMA bars, which had lower stiffness in comparison to the boundary reinforcement of other walls.

### 6.5.2.2 Inelastic Rotation

The inelastic rotational capacity was calculated as the rotational capacity minus the yield rotation of the shear walls. The nonlinear rotational capacity of the innovative shear walls was greater than 0.025 rad, which is the upper bound to the inelastic rotational capacity of conventional RC shear walls, according to CSA A23.3-14 (2014). According to Fig. 6.25, the shear walls with longer cross-sections had lower inelastic rotational capacities. This is because the outmost rebars of less slender shear walls fail at lower drift ratios and rotations than the outmost rebars of more slender shear walls. The effect of axial loads on the inelastic rotational capacities of the walls was insignificant, as discussed in section 6.4.3.

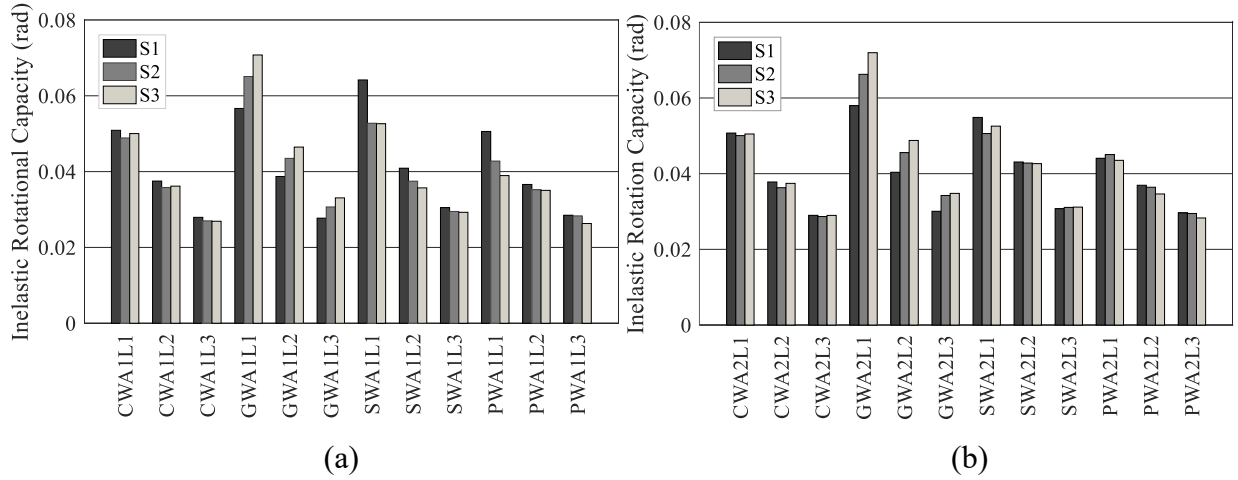


Figure 6.25. Inelastic rotational capacity in shear walls with an ALR of (a) 0%, (b) 5%.

The inelastic rotational capacity increased in GW walls with an increase in the amount of self-centering reinforcement ratios of the walls. This was because in the GFRP walls with higher GFRP reinforcement ratios, deformations were distributed more evenly along the height of the walls. On the other hand, the inelastic rotational capacity in each of the SW and PW walls was generally lower than that of their corresponding CW wall. This was due to the concentration of deformations at lower parts of the walls.

The GW and SW walls had generally higher inelastic rotational capacities than the CW walls, while the capacity of PW walls was normally comparable to those of CW walls. The ratio of the inelastic rotational capacity in the innovative walls with ALRs of 0% and 5% relative to the ratio of the inelastic rotational capacity in their corresponding CW walls was between 0.99 and 1.43 for the GW walls, between 0.99 and 1.26 for the SW walls, and between 0.78 and 1.05 for the PW walls (Fig. 6.26).

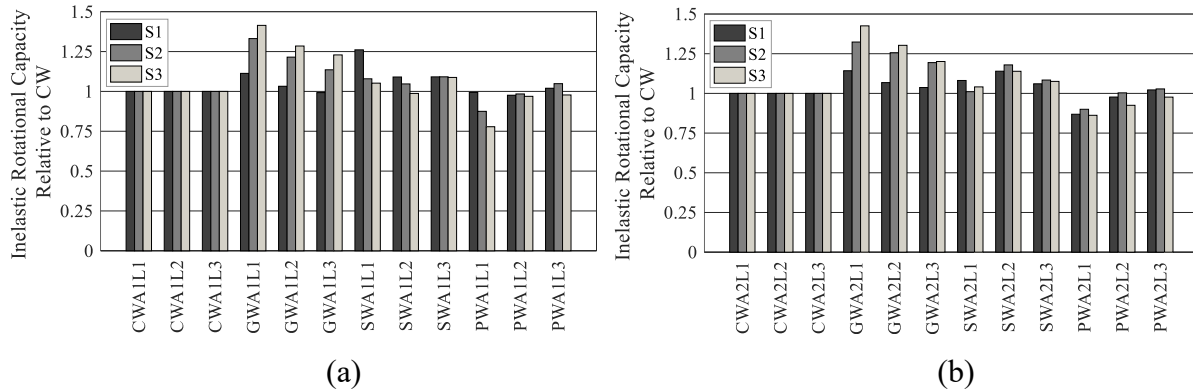


Figure 6.26. Relative Inelastic rotational capacity in the innovative shear walls to CW for ALRs of (a) 0%, (b) 5%.

## 6.5.3 Plastic Hinge Analysis

### 6.5.3.1 Curvature distribution

The distribution of curvatures in an RC element is a key parameter to quantify its deformation capacity since it allows the determination of elastic and plastic deformations through the moment-area theorem. To determine the curvature distribution of a wall, the distributions of average longitudinal strains along the horizontal rows of rectangular elements in the FE model of the wall were calculated. Then, the best fitting line to each distribution of longitudinal strains was calculated and used to determine the average curvature at the mid-height of each row of elements. For illustration purposes, the curvature distribution along the heights of the CWA1L2S3, GWA1L2S3, SWA1L2S3, and PWA1L2S3 walls is shown in Fig. 6.27.

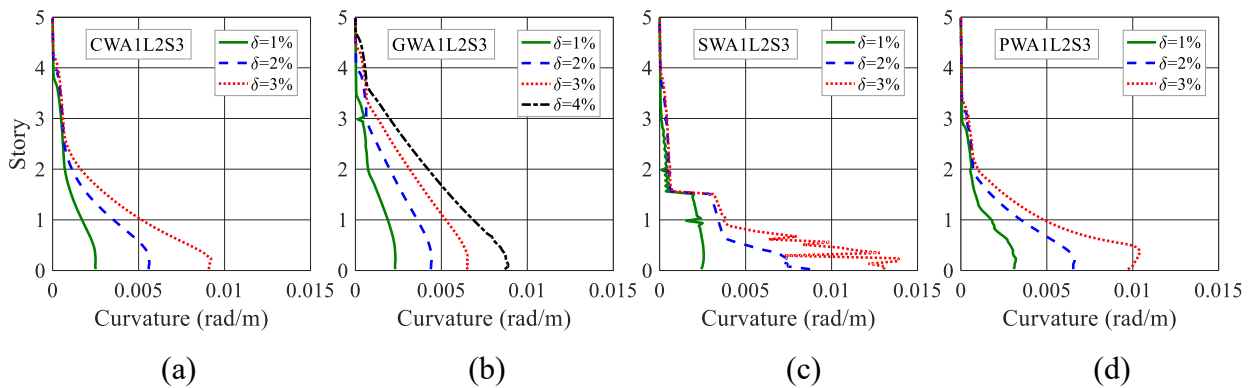


Figure 6.27. Curvature distribution of shear walls with an ALR of 0% (a) CW, (b) GW, (c) SW, (d) PW

It is seen that the curvature was more evenly distributed along the height of the GW wall in comparison to other shear walls (Fig. 6.27(b)). This is because of the linear stress-strain response of the GFRP bars, which causes deformations and damage to be better distributed along the height of the wall. On the other hand, the SW wall, which was designed to undergo nonlinear deformations mostly through its SMA-detailed plastic hinge, experienced higher curvature at its base in comparison to other shear walls at drift ratios of greater than or equal to 2% (Fig. 6.27(c)). This was because of the plateauing stress in the stress-strain response of the SMA bars of the wall, as no additional resistance was required for the sections in which SMA had reached the stress plateau to undergo extra curvatures. Also, the stress plateau was the case for SMA bars up to a strain of 6%, which resulted in the accumulation of plastic curvature around the base of the wall. The curvature distributions in the PW and CW walls were similar, although higher curvatures were developed at the base of the PW wall (Fig. 6.27(d)).

Curvature distributions of the shear walls in the presence of axial loads are shown in Fig. 6.28. The curvature had a “ragged” distribution at floor levels in the presence of axial loads. This was because the axial loads applied to each floor level restrained the cracking of the walls immediately underneath each floor level (Fig. 6.29).

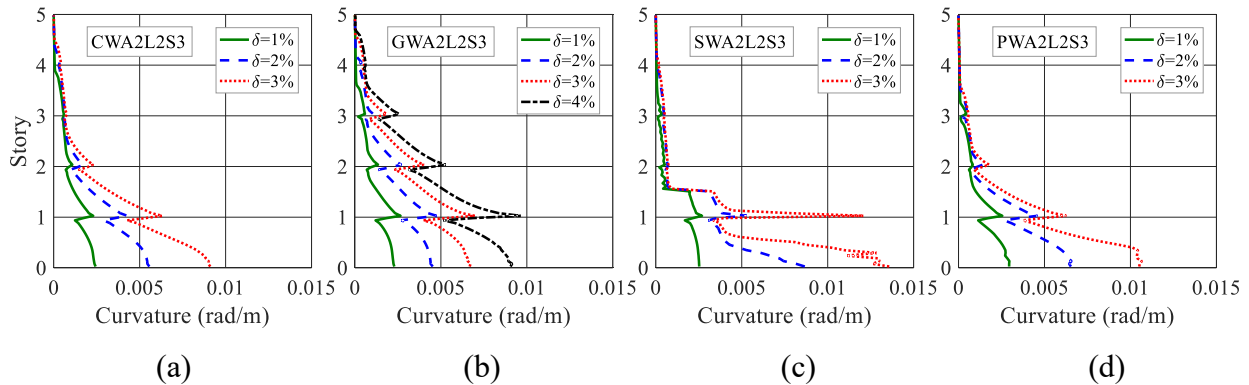


Figure 6.28. Curvature distribution of (a) CW, (b) GW, (c) SW, (d) PW under an ALR of 5%.

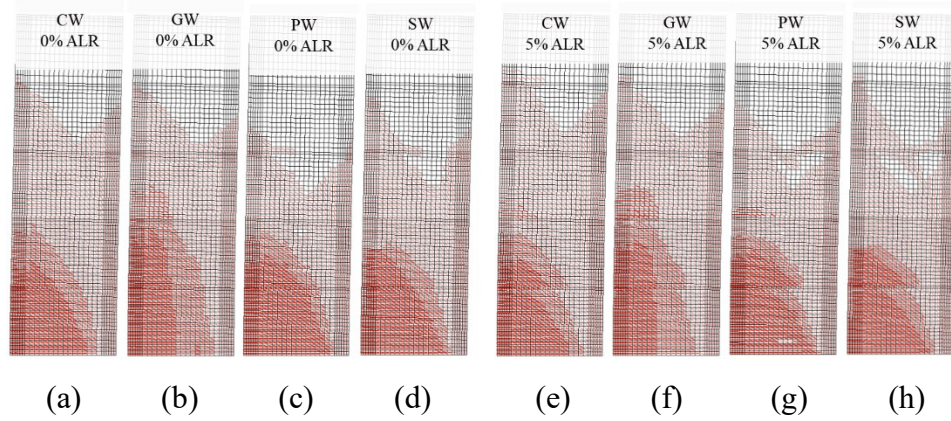


Figure 6.29. Cracking pattern at 2.0% drift in (a) CWA1L2S3, (b) GWA1L2S3, (c) PWA1L2S3, (d) SWA1L2S3, (e) CWA2L2S3, (f) GWA2L2S3, (g) PWA2L2S3, (h) SWA2L2S3

### 6.5.3.2 Base Curvature

As mentioned previously, the curvature at the base of shear walls is a useful parameter for ductility checks in walls designed to undergo seismic loading. The base curvature of each shear wall was obtained by fitting the best line to the curvature distribution along the height of the plastic zone,  $l_{pz}$ , of the shear wall, as shown in Fig. 6.30(a). The plastic zone in a shear wall was defined as the region above which curvature is smaller than yield curvature,  $\phi_y$  (Eq. 6.1).

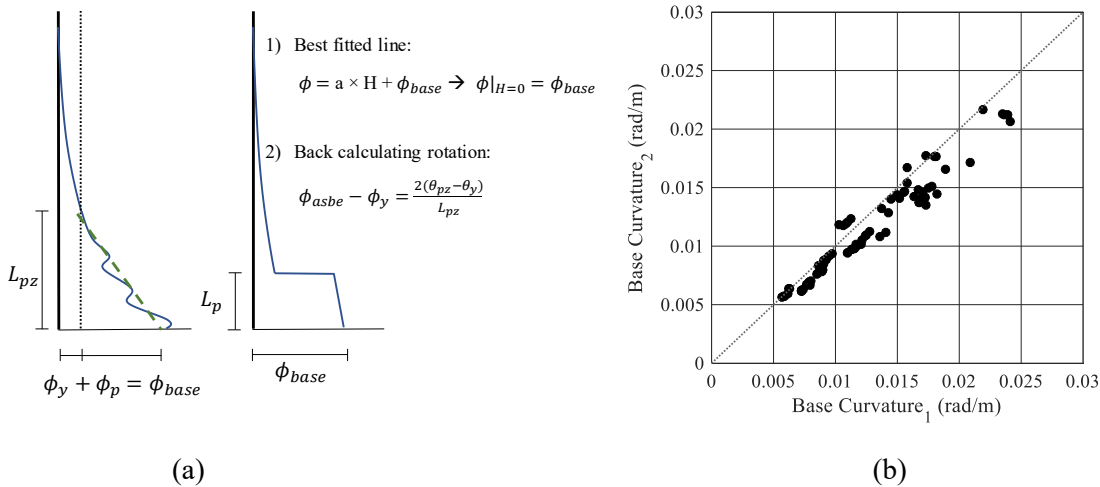


Figure 6.30. Base curvature calculation in shear walls (a) theory, (b) calculated values

Base curvature can also be back-calculated from the plastic rotation,  $\theta_{pz} - \theta_y$ , at the top of the plastic zone of each shear wall (Fig. 6.30(a)). In this approach, the yield rotation of the shear wall was

calculated as the rotation that corresponds to the yield curvature of the wall. The two approaches resulted in comparable values. However, the former method produced slightly higher base curvatures in general, as shown in Fig. 6.30(b). For this reason, the base curvatures of the walls were calculated based on the linearization of curvature along their plastic zones.

The base curvature in the shear walls decreased with the length of the walls as the walls became less slender. The axial load and reinforcement ratios did not have a notable impact on the base curvature in the shear walls. The base curvature in the shear walls slightly decreased with the increase in the axial loads of the walls. This can be attributed to the ragged distributions of the curvature along the height of the shear walls with an ALR of 5%, which corresponded to slightly steeper best lines and lower base curvatures. Figure 6.31 shows the base curvatures of the shear wall at 2% drift.

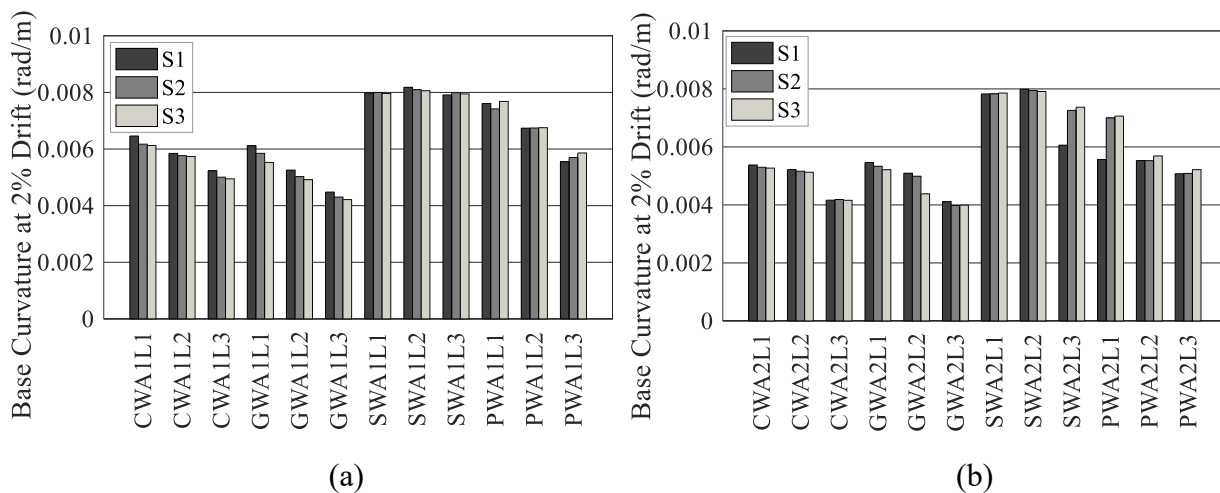


Figure 6.31. Base curvature in shear walls with ALRs of (a) 0%, (b) 5%

At 2% drift, the base curvature was larger in the SW and PW walls than in the CW the walls, while it was smaller in the GW walls than in the CW walls. The base curvature in the innovative walls relative to the base curvature in the CW walls ranged from 0.80 to 1.02 for GW walls, from 1.26 to 1.78 for SW walls, and from 1.00 to 1.28 for PW walls (Fig. 6.32). The curvature was more evenly distributed in the GW walls, while it was more concentrated at the base of the SW walls in comparison to their corresponding control walls.

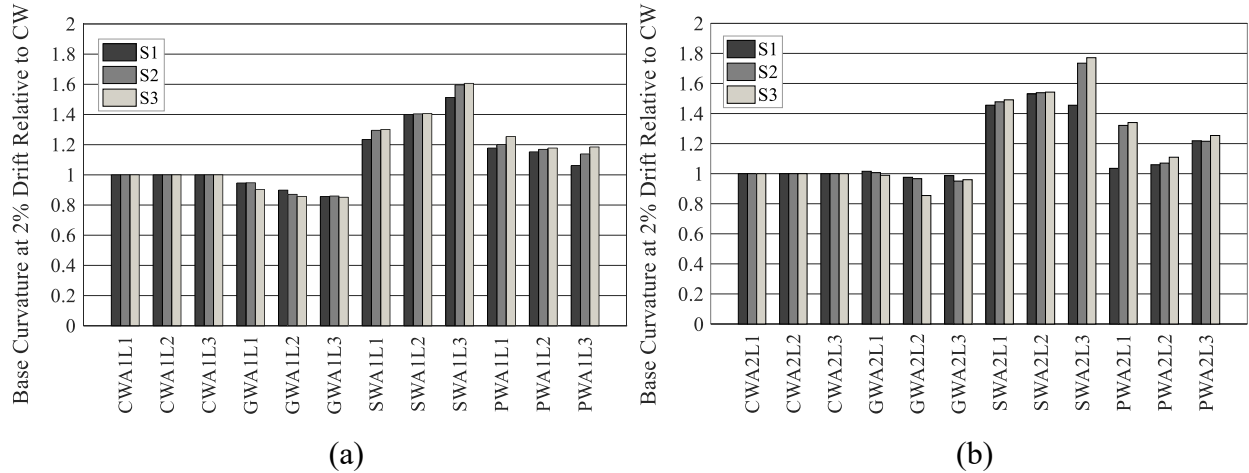


Figure 6.32. Relative base curvature to CW in shear walls with an ALR of (a) 0%, (b) 5%

### 6.5.4 Plastic Hinge Length

The plastic hinge length,  $L_p$ , of each wall was obtained from the idealization of the curvature distribution of the shear wall, as shown in Fig. 6.32(a). To calculate the plastic hinge length of the shear walls, Eq. 6.2 was solved for  $L_p$  in terms of the plastic flexural displacement ( $\Delta_f - \Delta_{fy}$ ) the plastic base curvature ( $\phi_{base} - \phi_y$ ), and height ( $H$ ) of each shear wall.

$$\frac{(\phi_{base} - \phi_y)}{2} L_p^2 - (\phi_{base} - \phi_y) H L_p + (\Delta_f - \Delta_{fy}) = 0 \quad (6.2)$$

In general, the plastic hinge length of the shear walls increased as the length and reinforcement ratio in the walls increased. This was because the base curvature was lower for the less slender shear walls, shown in Fig. 6.31. The ratio of reinforcement did not have a notable impact on the drift ratios of the walls since the effect of the parameter was also minor on the base curvatures of the walls. The axial load caused a slight increase in the plastic hinge lengths of the walls as it caused a small decrease in the base curvatures of the walls.

The length of the plastic hinge in the CW walls was relatively constant for different drift ratios applied to the walls. In the case of GW walls, plastic hinge length increased as the walls underwent higher drift ratios. This can be attributed to the elastic response of the GFRP bars of the walls, which resulted in more evenly curvature distributions along the height of the GW walls in comparison to other shear walls. On the other hand, plastic hinge length was generally decreasing in the SW walls as the drift ratios increased. This is because the curvature distributions of the SW

walls concentrated at their bases as the SMA material is significantly more flexible than conventional steel reinforcement. The change in the plastic hinge lengths of PW and CW walls was similar. However, plastic hinge length in PW walls was slightly shorter than in CW walls, which was a result of higher curvature values at the bases of PW walls compared to CW walls. The plastic hinge length for the shear walls with ALRs of 0% and 5% is shown in Figs. 6.33 and 34.

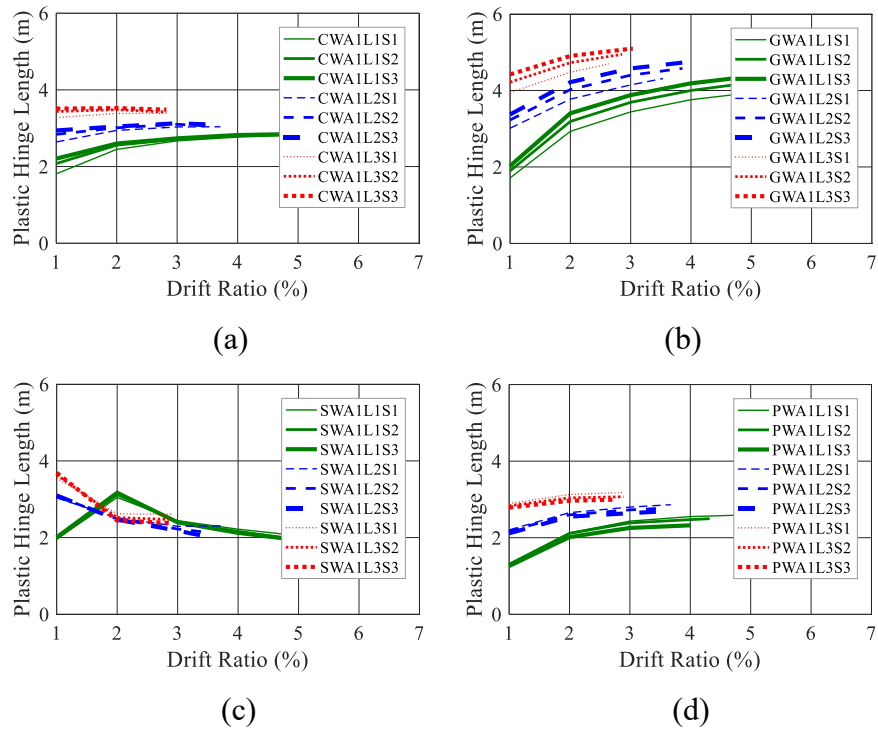


Figure 6.33. Plastic hinge length of (a) CW, (b) GW, (c) SW, (d) PW, with an ALR of 0%

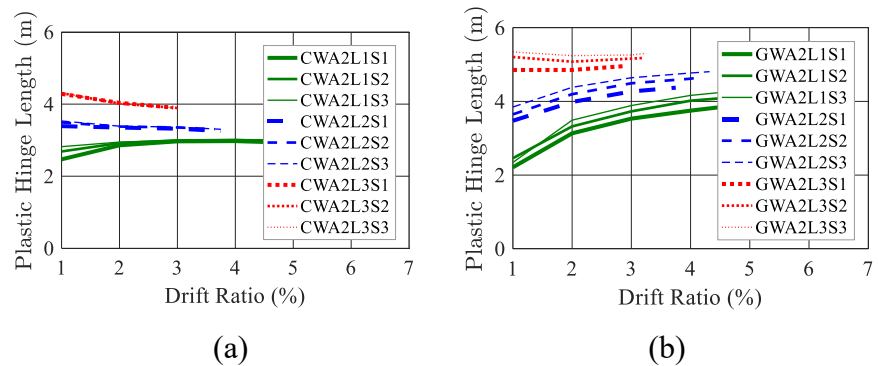


Figure 6.34. Plastic hinge length of (a) CW, (b) GW, (c) SW, (d) PW, with an ALR of 5%

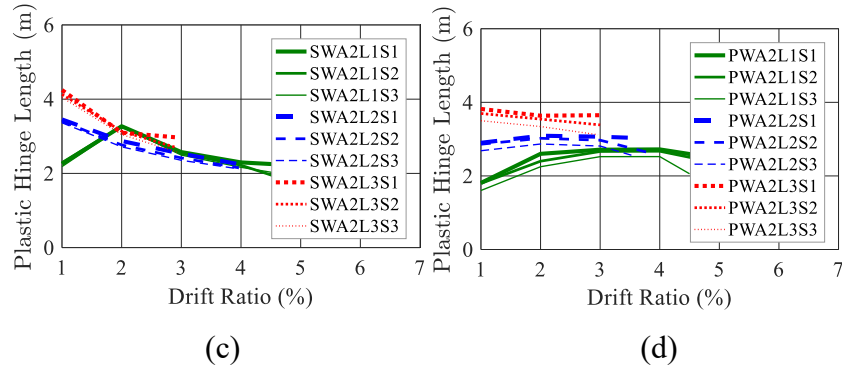


Figure 6.34. Continued

To put the plastic hinge length of the innovative specimens into perspective, the ratio of the plastic hinge length of each shear wall over that of its corresponding CW wall is shown in Figs 6.35 and 36. The plastic hinge in GW walls was generally larger than that of the corresponding CW walls. The relative plastic hinge length ratio of the GW walls to the CW walls was between 1.27 and 1.48 at ultimate drift ratios. In the SW walls, the plastic hinge was larger than in CW walls at first but became smaller at ultimate drift ratios. The relative plastic hinge length of SW walls to CW walls was between 0.63 and 0.75 at ultimate drifts. The plastic hinge in the PW walls was shorter than in their corresponding CW walls. The ratio of the plastic hinge length in the PW walls to that in the CW walls was between 0.77 and 0.93 at ultimate drifts.

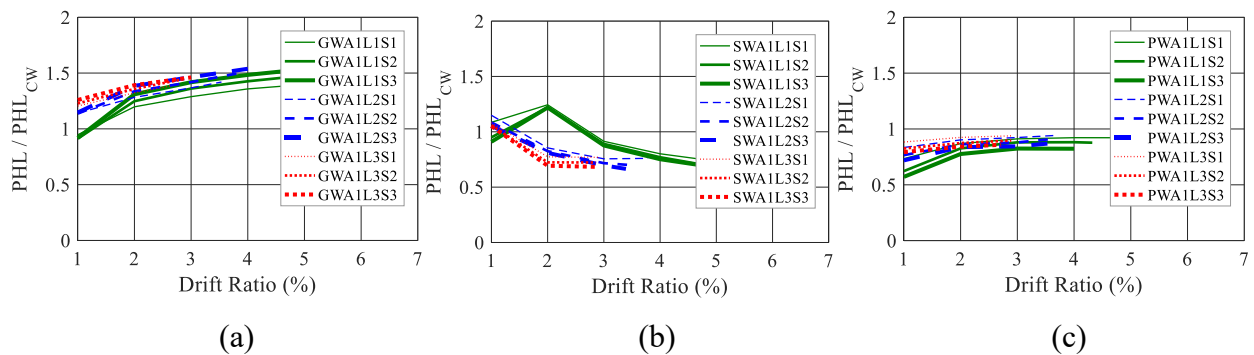


Figure 6.35. Relative plastic hinge length in the innovative walls with an ALR of 0% to CW walls for (a) GW, (b) SW, (c) PW

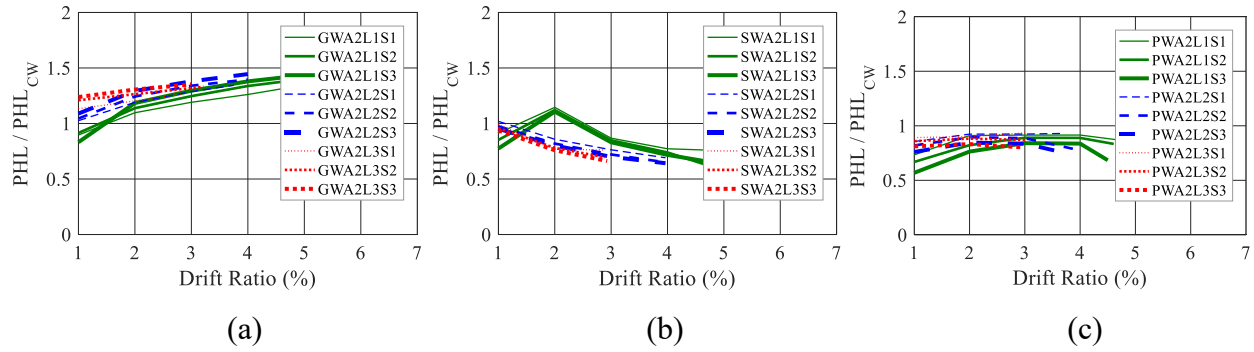


Figure 6.36. Relative plastic hinge length in the innovative walls with an ALR of 5% to CW walls for (a) GW, (b) SW, (c) PW

Figure 6.37(a) compares the plastic hinge lengths obtained from the FEM analyses of shear walls with  $0.5L_w$  proposed by Park and Paulay (1975), which is widely used in the plastic hinge analysis of RC shear walls. The plastic hinge length in the CW and GW walls was greater than  $0.5L_w$ , which means using  $0.5L_w$  in the design of the CW and GW walls could be conservative. However, in the cases of SW and PW walls, the plastic hinge length can be overestimated if  $0.5L_w$  is used. Overestimating the plastic hinge length results in the overestimation of flexural displacement capacities in the shear walls, which is unsafe. For this reason, the lower bounds to the ratio of plastic hinge length in the innovative walls at the ultimate drift ratio over  $0.5L_w$  can be used in the plastic hinge length analysis of innovative walls. These lower bounds are equal to 1.4, 0.7, and 0.9 for GW, SW, and PW walls and can be used as modification factors when a plastic hinge length of  $0.5L_w$  based on Park and Paulay (1975) is used in design equations (Fig. 6.37(b)).

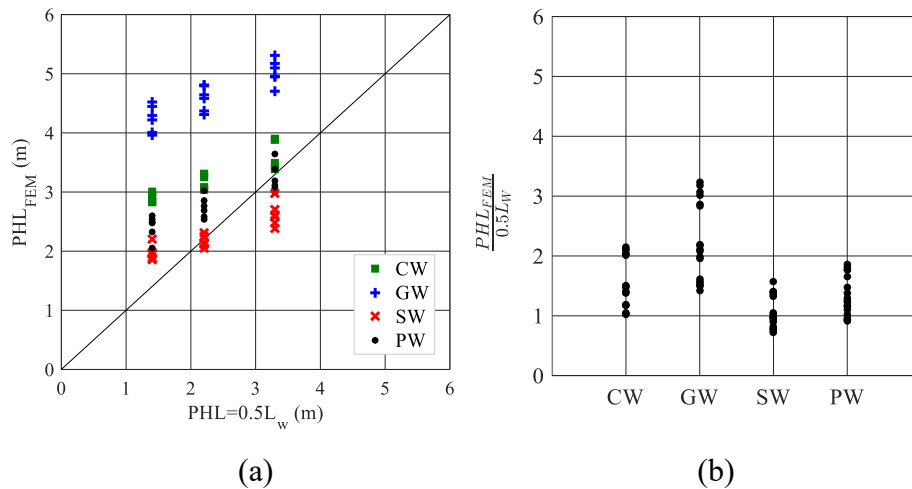


Figure 6.37. Plastic hinge length of shear walls (a) compared to  $0.5L_w$  (b) normalized to  $0.5L_w$

## 6.5.5 Self-Centering Analysis

### 6.5.5.1 Drift Ratio Recovery

Under no axial loads, the drift ratio recovery in CW walls with different aspect ratios and reinforcement layouts was between 0.47 and 0.73 at 1% drift and decreased to below 0.40 at their ultimate drift ratios (Fig. 6.38(a)). Similar self-centering with some improvements were identified for GW and PW walls (Fig. 6.38(b) and (d)). On the other hand, SW walls showed highly improved self-centering with drift ratio recoveries of between 0.62 and 0.82 at 1% drift, and between 0.61 and 0.93 at ultimate drifts (Fig. 6.38(c)).

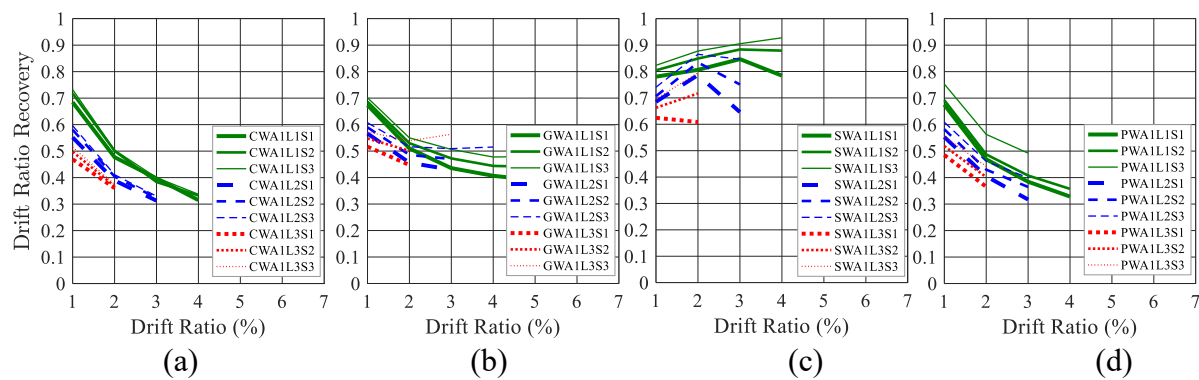


Figure 6.38. Drift ratio recovery of shear walls with 0% ALR (a) CW (b) GW (c) SW (d) PW

All of the shear walls with an ALR of 5% had significantly elevated drift ratio recoveries, as shown in Fig. 6.39. Drift ratio recovery in the CW walls was between 0.79 and 0.95 at drift a ratio of 1%; then, it ranged from 0.55 to 0.76 at ultimate drift ratios of the walls. In SW walls, drift ratio recovery was above 0.97 during the whole deformation range of the walls, while it was above 0.93 for PW walls and above 0.79 in the case of GW walls.

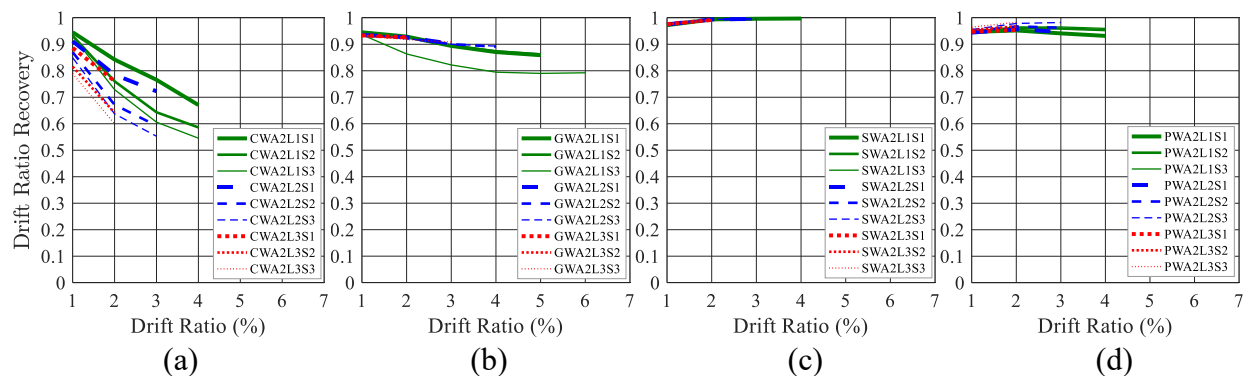


Figure 6.39. Drift ratio recovery of shear walls with 5% ALR (a) CW, (b) GW, (c) SW, (d) PW

### 6.5.5.2 Self-Centering Moment

The restoring moment produced by the self-centering reinforcement and axial loads in shear walls was studied to identify a relationship between the self-centering moment and the drift ratio recovery of each type of the shear walls. To calculate self-centering moments in a shear wall, the distance,  $c$ , between the neutral axis and the extreme compression fiber at the base of the wall was determined based on the average vertical strains at the wall boundaries. The distance of the neutral axis to the extreme compression fiber in shear walls normalized to the length of the walls was generally decreasing (Fig. 6.40). For walls with 5% ALR,  $c/L$  was slightly higher than the no-axial-load case, in general.

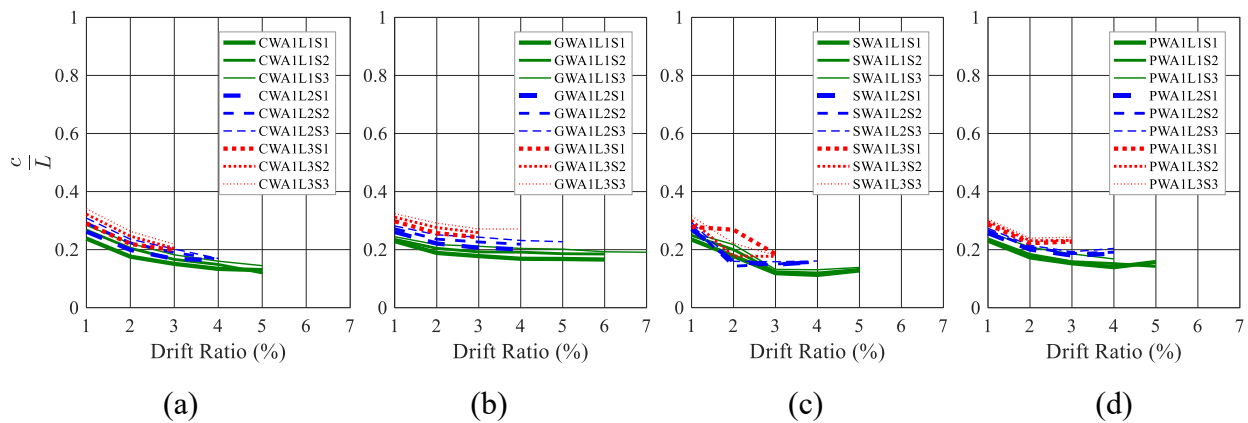


Figure 6.40. Distance between neutral axis to the extreme compression fiber in the shear walls normalized to wall lengths for (a) CW, (b) GW, (c) SW, (d) PW

After the determination of the neutral axis in each shear wall, the location of the resultant compressive force at the toe of the wall was calculated based on the compressive stresses of concrete elements. Then, the self-centering moments of shear walls were calculated based on the stress of self-centering reinforcement and the distance between the reinforcement and the resultant compressive force of each wall at peak displacement demands. When lateral loads were released, self-centering moments in shear walls reduced permanent drift ratios, which increased the drift ratio recovery of the walls. The increase in the drift ratio recovery of each innovative shear walls with no axial load to its corresponding CW walls versus the ratio of the self-centering moment over the resisting moment of the innovative wall is shown in Fig. 6.41. The resisting moments of

shear walls were calculated by multiplying the lateral resisting forces of the walls by the height of the walls.

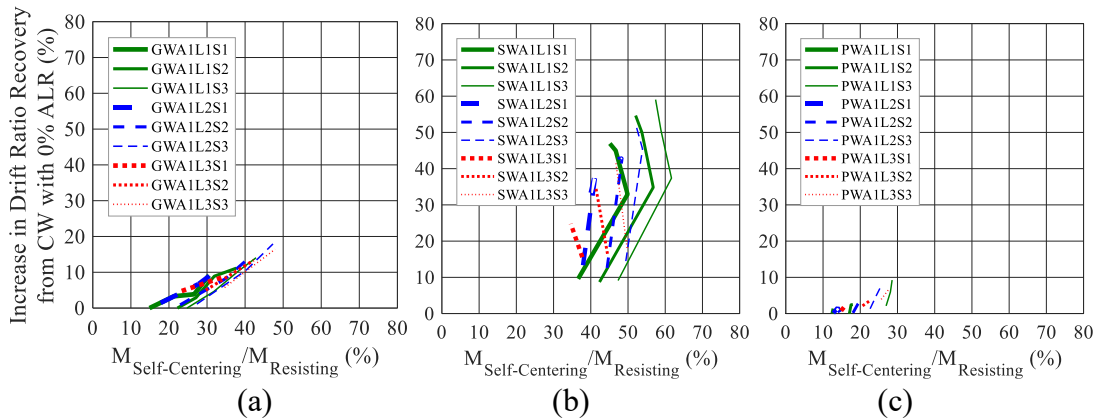


Figure 6.41. Increase in drift ratio recovery of innovative shear walls with an ALR of 0% compared to their control walls with 0% ALR for (a) GW, (b) SW, (c) PW

As shown in Fig 6.41, the ratio of the self-centering to resisting moments in the PW and GW walls with an ALR of 0% was less than 30% and 50%, respectively. On the other hand, the ratio of the self-centering to the resisting moments in the SW wall with no axial load was between 35% and 62%, which resulted in a higher increase in the drift ratio recovery of the wall in comparison to the PW and GW walls. The increase in the drift ratio recovery of the SW walls was between 25% to 59%, while it was below 20% and 10% for the GW and PW walls, respectively.

The lower self-centering moments in the GW and PW walls compared to the SW walls were mainly because of the lower ratios of self-centering reinforcement used in the GW and PW walls with respect to the SW walls. This was because of the fact that the GFRP bars and high-strength steel strands had higher ultimate stresses in comparison to the steel and SMA bars, and comparable lateral resisting forces were desirable in the innovative and control walls. Also, a shorter distance between the self-centering reinforcement and the resultant compressive forces at the toes of the GW and the PW walls in comparison to the SW walls contributed to the lower self-centering moments of the GW and the PW walls.

The axial load also produced a self-centering moment in the shear walls. As shown in Fig 6.42, the CW walls with an ALR of 5% showed an increase of 20% to 42% in their drift ratio recovery

with respect to the CW walls with no axial loads. The ratio of self-centering to resisting moments in the CW walls with an ALR of 5% was between 29% and 44%.

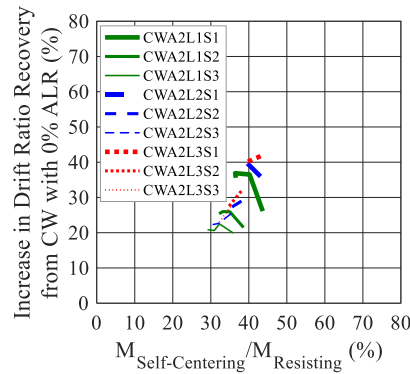


Figure 6.42. Increase in drift ratio recovery of CW walls with 5%ALR of compared to the control walls with ALR 0%

When both the self-centering reinforcement and the axial load were incorporated in CW walls, higher increases in the drift ratio recoveries obtained (Fig. 6.43). For instance, the increase in the drift ratio recovery of the innovative walls with an ALR of 5% with respect to the CW walls with no axial loads was between 46% and 59% for the GW walls, between 62% and 68% for the SW walls and between 59% and 65% for the PW walls. This was because the ratio of the self-centering to resisting moments at peak drift ratios was great enough to trigger a high permanent drift ratio recovery in the innovative walls with a 5% ALR.

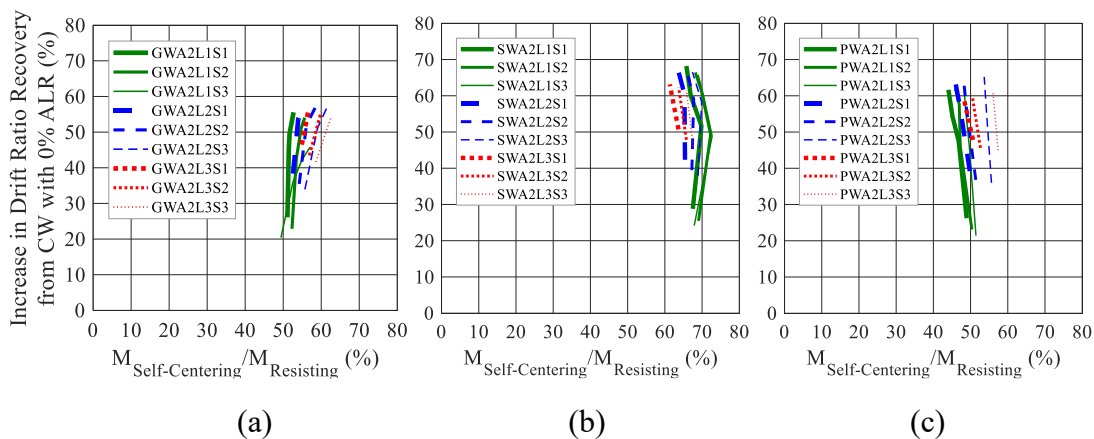


Figure 6.43. Increase in drift ratio recovery of innovative shear walls with an ALR of 5% compared to the control walls with 0% ALR for (a) GW (b) SW (c) PW

## **6.5.6 Effects of Independent Parameters on Design Parameters**

### **6.5.6.1 Effects of Axial Loads**

As discussed above, the axial loads slightly increased the ductility levels of the shear walls. This was because the axial loads decreased the yield drift ratios of the shear walls without decreasing the ultimate drift ratios of the walls. The axial load caused a slight increase in the plastic hinge lengths of the walls, as the base curvature in the shear walls with an ALR of 5% was slightly lower compared to the no axial load case (section 6.5.3.2). The effect of axial loads on the inelastic rotational capacity of the walls was insignificant since the axial loads were not great enough to initiate concrete crushing at the toes of the walls. The reason for this was the adequate confinement of the wall boundaries.

### **6.5.6.2 Effects of Wall Lengths**

As discussed above, the increase in the length of the shear walls did not have a notable effect on the ductility of the walls. This was since the shear walls were slender, and the yield and ultimate drift ratios of the walls changed proportionately. The increase in the length of the shear walls increased the plastic hinge length of the walls. This was because the walls with longer cross-sections had lower base curvatures in comparison to the walls with shorter lengths. The increase in the length of the shear walls decreased the inelastic rotational capacity of the shear walls. This is because the outmost rebars in the less slender walls experience higher values of tensile strains than the outmost rebars of the most slender walls at the same curvature values.

### **6.5.6.3 Effects of Reinforcement Ratio**

As discussed above, the increase in the reinforcement ratio of the walls caused a decrease in the ductility of the walls. This was because the yield drift ratio in the shear walls increased by the increase in the reinforcement ratios of the walls, while the ultimate drift ratios of the walls did not have a significant increase. The increase in the reinforcement ratio of the walls had no significant impact on the inelastic rotational capacity of the shear walls but the GW walls. This can be explained by the fact that the curvature was more evenly distributed along the GW walls compared to the other shear walls. As a result, the increase in the GFRP reinforcement of the GW walls improved the curvature distributions of the walls, leading to higher inelastic rotational capacities. This reason can be used to explain that the increase in the reinforcement ratio of the walls had an

insignificant effect on the plastic hinge length of the shear walls except for the GW walls, on which the reinforcement ratio had an increasing impact.

#### **6.5.6.4 Effects of Self-Centering Reinforcements**

As discussed above, the type of self-centering reinforcement of the shear walls had an impact on some of the design parameters of the shear walls. The steel-GFRP reinforced walls had lower ductility levels compared to the control walls, as the GW walls had higher yield drift ratios than the CW walls. The GW walls had higher inelastic rotational capacity than the CW walls, as a result of the more evenly curvature distribution and lower base curvature in the GW walls than in the CW walls. Also, the GW walls had longer plastic hinges than the CW walls because of their more evenly curvature distribution in comparison to the CW walls.

The steel-SMA reinforced walls had lower ductility compared to the control walls as a result of the higher yield drift ratios in the SW walls. The SW walls had comparable inelastic rotations to the CW walls. This can be explained by the comparable rotational capacities and ultimate drift ratios of the SW and CW walls. The SW walls had shorter plastic hinges than the CW walls, as the base curvature was higher in the SW walls than in the CW walls.

The partially post-tensioned walls showed higher levels of ductility compared to the control walls. This was because the yield drift ratio was lower in the walls compared to the CW walls, while the ultimate drift ratio in the PW and CW walls was comparable. The PW walls had comparable inelastic rotational capacities to the CW walls. This was because the PW and CW walls the walls had comparable ultimate drift ratios and rotational capacities. The PW walls had shorter plastic hinges compared to the CW walls since the PW walls had higher base curvatures than the CW walls.

### **6.6 Seismic Response**

To see the response of the innovative shear walls under seismic loads, the walls with a length of 4500 mm, a self-centering reinforcement arrangement of S3 and ALR levels of 0.0%, 2.5%, and 5.0% were subjected to four earthquake acceleration histories. The selected earthquakes were comprised of 1989 Loma Prieta, 1985 Nahanni, 1994 Northridge, and 1978 Tabas earthquakes,

which are introduced in Table 6.5 The acceleration history of each earthquake in terms of gravitational acceleration is also shown in Fig. 6.44.

Table 6.5. Specifications of the earthquakes.

Earthquake Name	Year	Magnitude (Mw)	Mechanism	PGA (g)	Distance (km)	Station Name
Loma Prieta	1989	6.9	Reverse Oblique		17.5	WAHO
Nahanni	1985	6.8	Reverse		9.6	Site 1
Northridge	1994	6.7	Reverse		8.6	Rinaldi
Tabas	1978	7.4	Reverse		2.1	Tabas

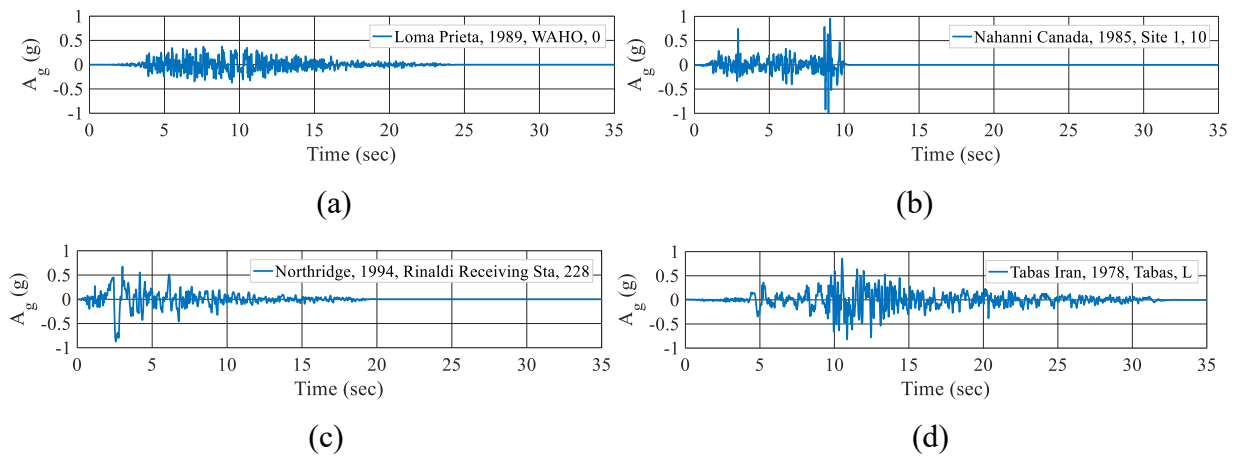


Figure 6.44. Acceleration history of (a) 1989 Loma, (b) 1985 Nahanni, (c) 1994 Northridge, (d) 1978 Tabas earthquakes.

The pseudo-spectral acceleration and spectral displacement of the earthquakes are shown in Fig. 6.45. As can be seen in the figure, the Northridge earthquake exerts higher acceleration and displacement demands on structures with a fundamental period of 0.3 sec or greater in comparison to the Tabas, Nahanni, and Loma Prieta earthquakes. To obtain the seismic response of the shear walls, five equal lumped masses were assigned to the floor levels of each shear walls. The mass of each wall was tuned so that all the shear walls had a fundamental period of 0.5 sec. A fundamental period of 0.5 sec was chosen since the walls had five stories, and based on a simple rule-of-thumb,

the fundamental period of an RC building is in the order of 0.1 sec per story. A damping ratio of 5% was specified for the first and the second modes of vibration of each shear wall.

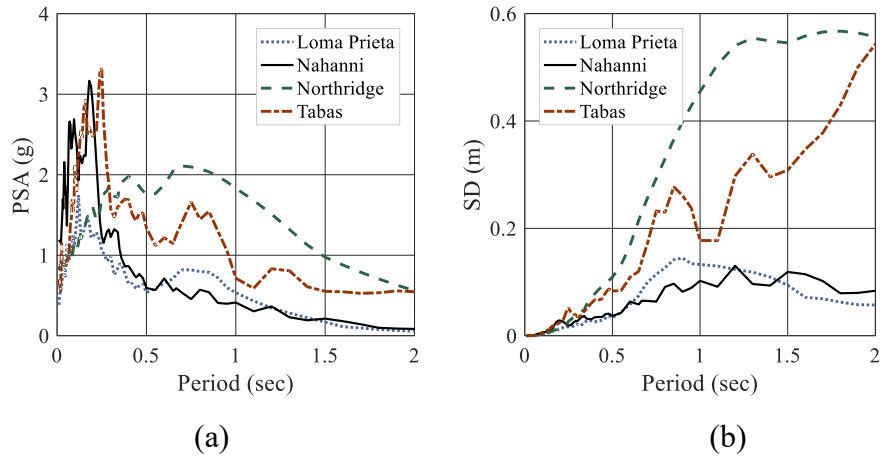


Figure 6.45. Selected earthquake (a) pseudo-spectral acceleration (b) spectral displacement

### 6.6.1 Response History

The response history of each shear walls under the selected earthquakes and zero axial loads is shown in Fig. 6.46. As can be seen in the figure, displacement demands exerted on the shear walls during Loma and Nahanni earthquakes were well below 1% drift. As a result, the shear walls underwent small nonlinear deformations and, consequently, small permanent drift ratios. On the other hand, in the case of the Northridge and Tabas earthquakes, the shear walls experienced displacement spikes of 3% drift or greater, after which the CW wall sustained considerable residual displacements.

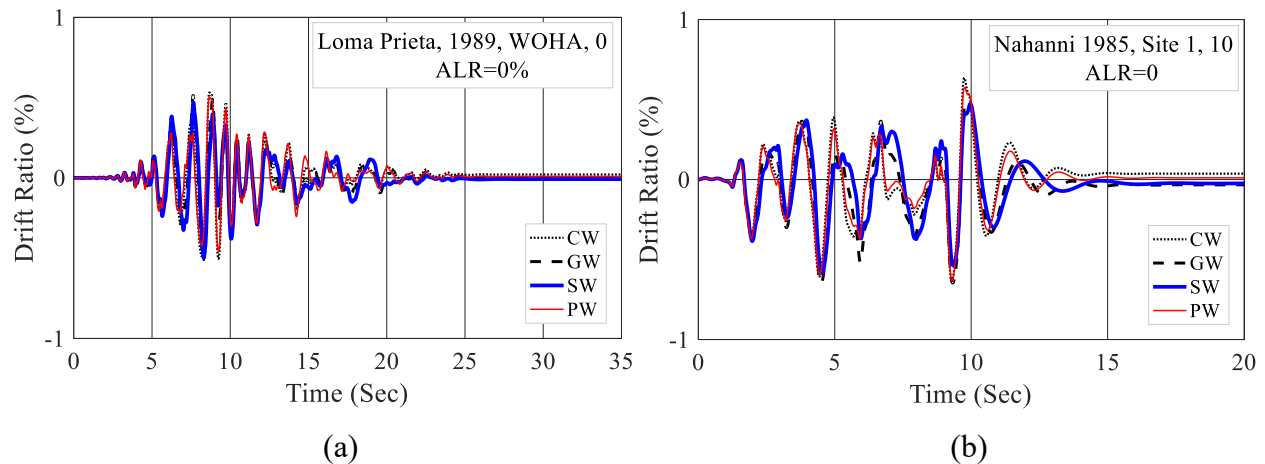


Figure 6.46. Response histories under (a) Loma Prieta (b) Nahanni (c) Northridge (d) Tabas

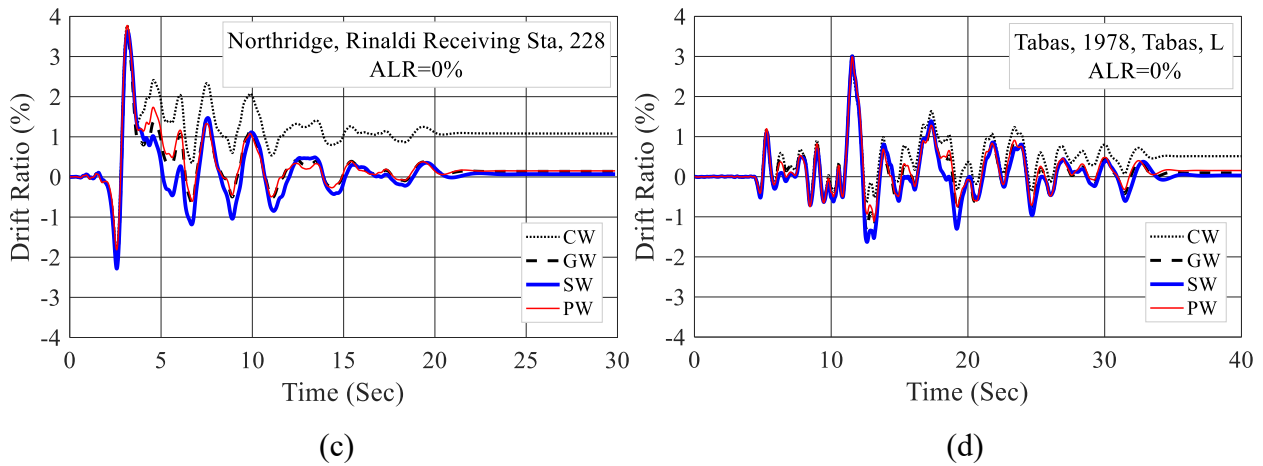


Figure 6.46. Continued

### 6.6.2 Peak Drift Ratio

Peak drift ratio of each shear wall under different axial loads and ground motions is shown in Fig. 6.47. The peak drift ratios of the shear walls were comparable during each earthquake. The peak drift ratios of shear walls under the Loma and Nahanni earthquakes were under 1.0% drift, while it was between 2.0% and 3.0% drifts for the Tabas earthquake and between 3.0% and 4.0% drifts for the Northridge earthquake.

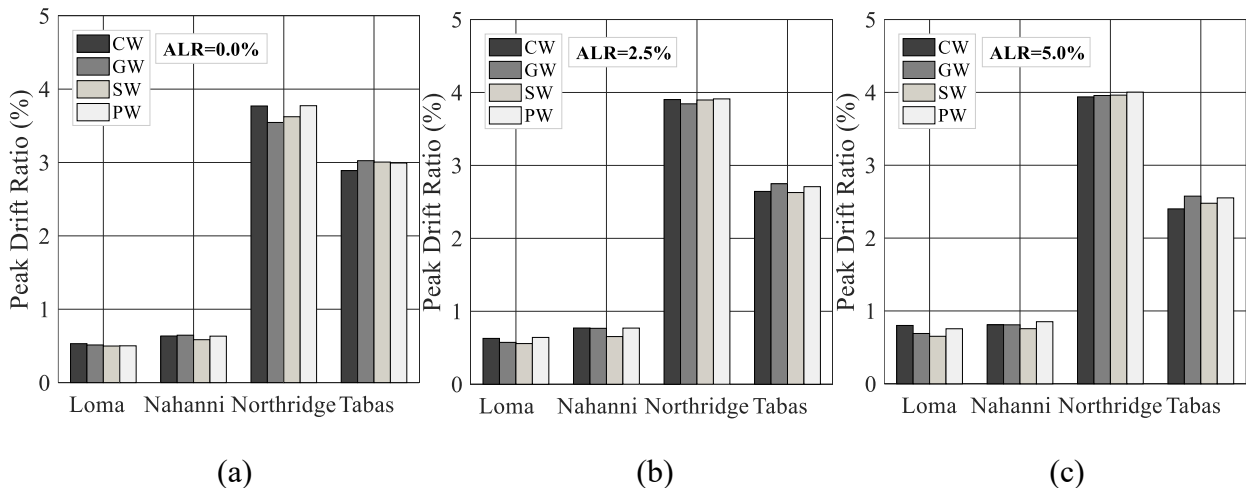


Figure 6.47. Peak drift of walls under seismic loads and an ALR of (a) 0%, (b) 2.5%, (c) 5%

### 6.6.3 Residual Drift Ratio

The residual drift ratio of each shear wall under different axial loads and earthquake histories is shown in Fig. 6.48. In general, the shear walls sustained higher residual drift ratios after the Northridge and Tabas earthquakes in comparison to the Nahanni and Loma earthquakes. The CW wall sustained larger residual drift ratios than the innovative walls. For instance, CW sustained a permanent drift ratio of 1.1% and 0.51% under the Northridge and Tabas earthquakes and zero axial loads, while the residual drift ratios of the innovative walls were below 0.2%. The permanent drift ratio of the shear walls decreased and became insignificant as their axial load ratios increased to 5%.

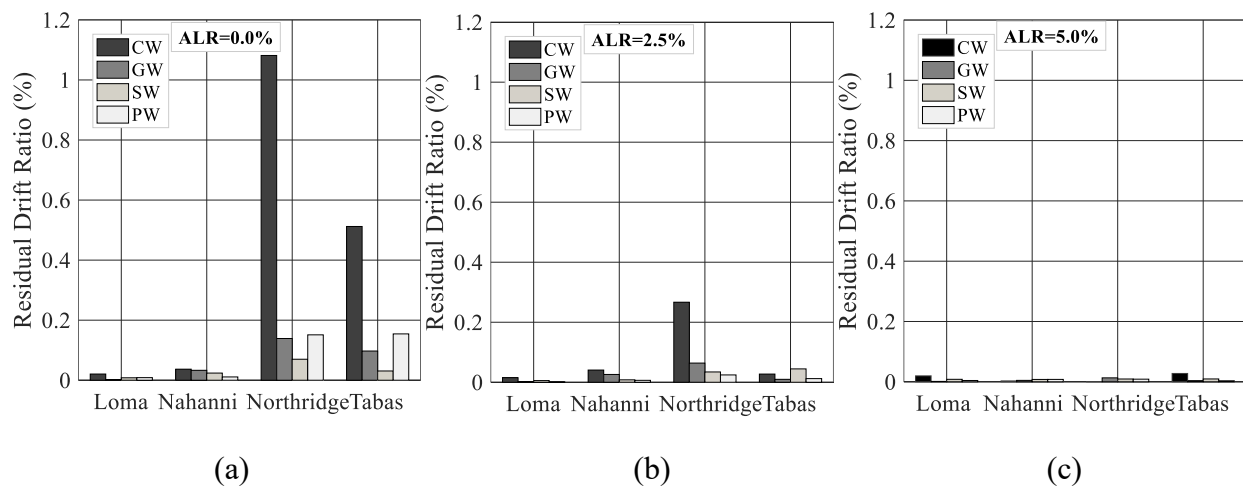


Figure 6.48. Residual drift of walls under seismic loads and an ALR of (a) 0%, (b) 2.5%, (c) 5%

### 6.6.4 Energy Dissipation

The amount of energy dissipated by each shear wall during different earthquakes and levels of ALR is shown in Fig. 6.49. The walls dissipated more energy during the Northridge and Tabas earthquakes since more energy was induced to the shear walls. The amount of energy dissipated by the shear walls increased with an increase in their axial loads. This can be attributed to the additional resistance that shear walls gained in the presence of axial loads.

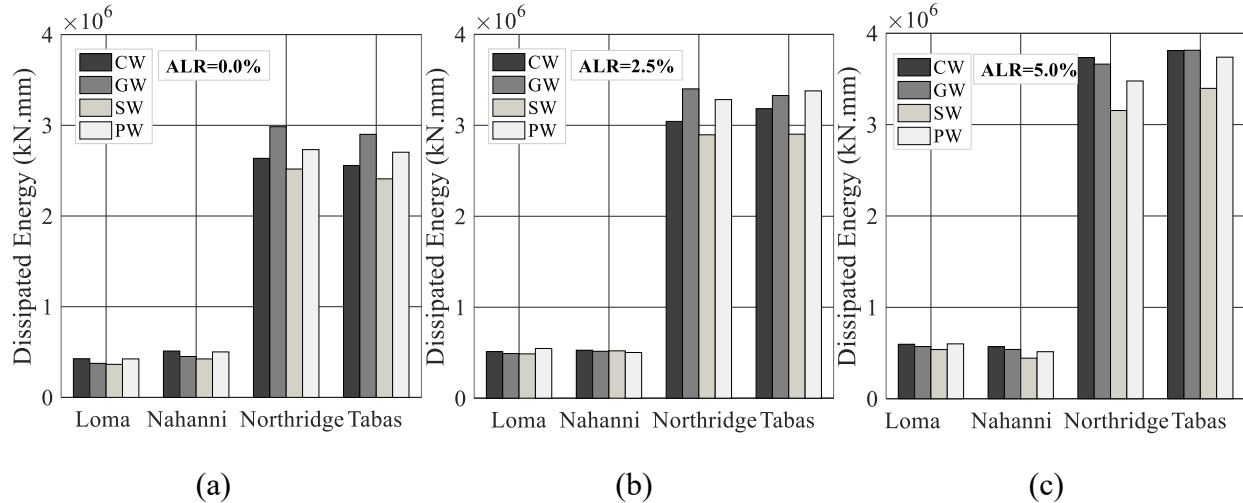


Figure 6.49. Dissipated energy of walls under seismic and an ALR of (a) 0% (b) 2.5% (c) 5%

For ALRs of 0% and 2.5%, the energy dissipated by the CW was slightly lower than that of GW and PW walls during The Northridge and Tabas earthquakes. This can be explained by the fact that each innovative wall dissipated an extra amount of energy for returning to its original position after a major spike happened in the response history of the wall, while it was not completely the case for the CW wall. As can be seen in Fig. 6.49(c), the lower energy dissipation of CW was compensated at 5% ALR when all the walls had sufficient self-centering properties.

## 6.6.5 Effects of Independent Parameters on Seismic Properties

### 6.6.5.1 Effects of Axial Loads

As discussed above, the increase in the axial loads of the walls did not significantly change the peak drift ratios of the shear walls. This was since the fundamental period, which is the most important parameter in the seismic analysis, was the same in the shear walls. The increase in the axial loads of the walls significantly decreased the permanent drift ratio of the shear. This was due to the increasing effect of axial loads on the self-centering moment of the shear walls. The amount of energy dissipated by the shear walls increased with an increase in their axial loads. This can be attributed to the increased resistance of that shear walls in the presence of axial loads.

### 6.6.5.2 Effects of Self-Centering Reinforcements

As discussed above, the type of self-centering reinforcement did not significantly change the peak drift ratio of the shear walls. This can be attributed to the fact that the shear walls had the same

fundamental period, and the fundamental period is the parameter, on which the response of a structure under dynamic loads depends. Different types of self-centering reinforcement decreased the permanent drift ratios of the shear walls. This was because the self-centering reinforcement increased the self-centering moments of the walls. The type of self-centering reinforcement did not significantly change the dissipated energy of the shear walls. This can be attributed to the fact that the response histories of the shear wall had few cycles with high peaks.

### **6.6.5.3 Effects of Earthquake Accelerations**

As discussed above, different earthquakes exerted different amounts of energy into the shear walls, which resulted in the walls reaching different levels of peak drift ratio. The shear walls experienced low peak drift ratios (less than 1%) during Nahanni and Loma earthquakes, while the walls had peak drift ratios of greater than 2% during the Tabas and Northridge earthquakes. Also, due to the same reason, the shear walls dissipated lower amounts of energy during the Nahanni and Loma earthquakes than during the Tabas and Northridge earthquakes. The effect of different earthquakes on the residual drift ratios of the shear walls was significant. The shear walls suffered higher residual drift ratios after the Northridge and Tabas earthquakes compared to the Nahanni and Loma earthquakes. This was because the walls sustained higher peak drift ratios in the Northridge and Tabas earthquakes.

## **6.7 Conclusions**

The following conclusions were made from a parametric study performed on the design parameters of innovative shear walls with different self-centering reinforcement types and ratios, different aspect ratios, and different axial load ratios.

- The ultimate drift ratio in SW walls, PW walls, and in RC shear walls was comparable. In GW walls, the ultimate drift ratio was generally higher than in RC shear walls. This was because nonlinear deformations were spread along the height of GW walls rather than being accumulated close to their bases. For this reason, the ultimate drift ratio in GW walls increased with an increase in the self-centering reinforcement ratio of the walls, while the opposite was true for the other types of innovative walls.

- The drift ratio recovery in the SW walls was higher than in GW and PW shear walls when there was no axial load carried by the walls. The drift ratio recovery of the innovative walls increased with an increase in the aspect ratio and self-centering reinforcement ratio of the walls. However, with an ALR of 5% at the base of each wall, the drift ratio recoveries of the innovative walls with different aspect ratios, self-centering reinforcement types and ratios were comparable. This was because of the high self-centering moments of the shear walls.
- The energy dissipation capacity in the innovative walls was lower in comparison to the conventional RC shear walls. The ratio of normalized dissipated energy in the innovative walls relative to CW walls was between 0.69 and 0.96 for GW walls, 0.34 and 0.72 for SW walls and 0.79 and 1.04 for PW walls. For that reason, the innovative shear wall should not be overly slender in order to have enough longitudinal steel reinforcement to provide adequate energy dissipation capacity to the walls.
- The displacement ductility in CW walls was between 3.1 to 4.9, while it was between 1.3 to 2.3 for GW walls, between 2.2 and 3.8 for SW walls, and between 3.3 and 5.6 for PW walls. The relative ductility indices of the innovative walls to CW walls were between 0.32 and 0.5 for GW walls, between 0.58 and 0.86 for SW walls and between 0.92 and 1.36 for PW walls.
- In general, GW and SW walls had higher inelastic rotational capacities than CW walls, while the capacities of PW walls were generally equal or lower than those of CW walls. The inelastic rotational capacity of the innovative walls relative to the CW walls was from 0.99 to 1.43 for the GW, from 0.99 to 1.26 for the SW and from 0.78 to 1.05 for the PW walls.
- The plastic hinge lengths were relatively constant in CW walls, increasing in GW walls and generally decreasing in SW walls as higher peak drift ratios were applied to the walls. For PW walls, the plastic hinge lengths changed in a similar manner to CW walls; however, it was slightly shorter in the PW walls. The ratio of plastic hinge lengths of the GW walls to the plastic hinge lengths of the control walls was between 1.27 and 1.48 at ultimate drift ratios. On the other hand, the relative plastic hinge length ranged between 0.63 and 0.75 for SW walls and between 0.77 and 0.93 for PW walls. The lower bounds to the plastic hinge lengths of GW, SW, and PW walls over  $0.5L_w$ , which is generally used as the plastic hinge length of RC walls, were equal to 1.4, 0.7 and

0.9. These ratios can be used in the estimation of plastic hinge lengths of the shear walls in the design process of the innovative walls.

- The innovative shear walls with an ALR of 5% showed significant improvement in terms of drift ratio recovery with respect to the CW walls that had no axial loads. Drift ratio recovery of the GW walls increased between 46% and 59%, while it was between 62% and 68% in the SW walls and between 59% and 65% in the PW walls. The reason for the significant improvement in the self-centering properties of the walls was the high self-centering to resisting moments of the shear walls from the beginning of analyses.
- The shear walls with a fundamental period of 0.5 sec and a comparable lateral resistance experienced comparable levels of maximum drift ratio and energy dissipation under the Northridge, Tabas, Nahanni, and Loma earthquakes. The residual drift ratios of the innovative specimens were notably lower in comparison to that of the control wall of the study when the walls were not bearing axial loads. However, in the presence of 5% ALR, the residual drift ratios of all the shear walls were negligible.

## CHAPTER 7 CONCLUSIONS

### 7.1 Conclusions

#### 7.1.1 Experimental Study

Three different innovative walls were designed with advanced materials and details to reduce the damage and the permanent displacement in conventional RC shear walls. The innovative walls were cast with fiber-reinforced concrete and were reinforced with conventional steel rebars and a type of self-centering reinforcement consisting of SMA bars, GFRP walls, and post-tensioned high-strength steel strands. The walls were tested as cantilevers under in-plane lateral displacement reversals while carrying no axial loads.

- The experimental tests showed that the innovative walls achieved improved damage tolerance characteristics compared to the control wall of the study. For instance, the innovative walls formed fewer cracks, less spalling, and no concrete crushing compared to the control wall. However, the crack opening in the innovative walls was intensified due to the resistance of the fiber-reinforced concrete of the walls to form more cracks. In addition, the fact that the response of the innovative walls had a rocking nature was a contributing factor to the higher crack opening in the innovative walls. The fiber-reinforced concrete of the innovative shear walls did not promote crack closure after unloading and, to some extent, reduced the self-centering capability of the walls.
- In addition to higher damage tolerance in the innovative shear walls, the experimental tests showed that the innovative shear walls achieved higher initial stiffness compared to the control wall. An improvement in the initial stiffness of the steel-SMA and steel-GFRP reinforced walls is important since the shear walls can be prone to low stiffness as a result of lower elastic modulus of SMA and GFRP compared to steel.
- The experimental tests showed that the innovative shear walls achieved different levels of self-centering at different levels of drift ratio demand during testing. It was after a drift ratio of 1% that the GFRP-ECC and SMA-SFRC walls showed improved self-centering properties compared to the control wall. As a result, it can be concluded that the walls are suitable for improving the LS and CP seismic performance levels of shear walls. The partially post-tensioned SFRC specimen

showed self-centering from the beginning of testing, which makes it appropriate for improving all performance levels of shear walls, especially the IO and LS performance levels.

- As a result of the experimental tests, three improved self-centering objectives for the design of innovative shear walls with improved seismic performance levels were introduced. The new objectives improved upon the self-centering limits of FEMA for steel-reinforced RC shear walls. The self-centering objective-I improves the self-centering of innovative shear walls at the drift ratios between 1% and 2%. The objective requires the LS permanent drift ratio limit of FEMA when the transient drift ratio is between 1% and 2%. The improved self-centering design objective-II improves the self-centering of the innovative shear walls at the drift ratios between 0.5% and 2%. The objective requires the IO permanent drift ratio limit of FEMA when the transient drift ratios are between 0.5% and 1%, and the LS permanent drift ratio limit of FEMA when the transient drift ratios are between 1% and 2%. And finally, the improved self-centering objective-III requires the IO self-centering limit of FEMA at the drift ratios between 0% and 2%.

- The experimental tests showed that the placement of the self-centering reinforcement used in the innovative walls was successful in increasing the restoring moment of the walls and protecting the self-centering reinforcement from high tensile strains. High-strength, brittle reinforcement, such as GFRP bars and high-strength steel strands, should be placed between the middle thirds of the web of an innovative shear wall. On the other hand, the boundary elements of an innovative shear wall should be reinforced with ductile reinforcement, such as steel and SMA bars.

- The post-testing analysis revealed the relationship between the self-centering reinforcement of each innovative shear wall and the self-centering effectiveness of the wall. The relationships were displayed in terms of the self-centering to the resisting moments of each innovative wall versus the increase in the drift ratio recovery of the innovative wall with respect to the control wall. The relationships showed that there was not enough self-centering reinforcement generated in the SMA-SFRC and GFRP-ECC walls at the beginning of testing to illustrate improved drift ratio recovery levels.

### **7.1.2 Numerical Study**

The finite element models for the shear walls tested in this study and in the recent studies on

innovative shear walls were successfully developed and verified with experimental results. Then, the verified FE models were used to perform a parametric analysis on multi-story innovative shear walls. The walls were made up of normal concrete and were reinforced with mild steel rebars and a type of self-centering reinforcement consisting of SMA bars, GFRP bars, and post-tensioned high-strength strands. The design parameters of innovative RC shear walls, such as the stiffness, ductility, inelastic rotational capacity, and plastic hinge length were closely studied.

- The numerical study showed that VecTor2, which is an FE analysis software specializing in the analysis of RC elements, can be successfully used to simulate the response of conventional and innovative RC shear walls. The built-in materials and elements of VecTor2 can capture the behavior of the innovative reinforcements, simulate their bond properties, and model fiber-reinforced concrete accurately.
- The numerical study provided some insight into the ductility of innovative shear walls since the ductility index is commonly used to identify the force reduction factors of the forced-based design of structures. It was shown that the steel-GFRP and steel-SMA reinforced concrete walls had lower ductility indices in comparison to conventional walls. It was shown that this finding was due to the lower effective stiffness and, consequently, the higher yield drift ratios of the shear walls compared to conventional RC shear walls. On the other hand, the ductility indices of partially post-tensioned concrete walls were comparable to those of conventional RC walls despite the fact the walls had lower amounts of bonded reinforcement than the conventional control walls. This was since the post-tensioned strands exerted compressive stresses to the partially post-tensioned walls.
- The numerical study sheds some light into the inelastic rotational capacity of innovative shear walls. This was because the inelastic rotational capacity can be used to check the adequacy of RC shear walls according to seismic design codes for RC structures, such as CSA A23.3-14 (2014). It was shown that the steel-GFRP walls and the steel-SMA walls had generally higher inelastic rotational capacities than conventional RC shear walls. On the other hand, the inelastic rotational capacity of the partially post-tensioned wall could be lower than that of conventional steel-reinforced shear walls.

- The numerical study showed that the plastic hinge in the steel-SMA and partially post-tensioned reinforced concrete shear walls was shorter compared to conventional RC shear walls. On the other hand, the study showed that the reverse was the case for steel-GFRP walls. Since overestimating plastic hinge length is not conservative, the lower bounds to the plastic hinge length in the innovative walls relative  $0.5L_w$  in the shear walls were suggested to be used in the estimation of the plastic hinge length of innovative walls. The calculated lower bands were equal to 1.4, 0.7, and 0.9 in the case of the steel-GFRP reinforced walls, the steel-SMA reinforced walls and the partially post-tensioned walls. These values can be used as modification factors to  $0.5L_w$ , the plastic hinge length of RC shear walls proposed by Park and Paulay (1975).

## **7.2 Suggestions for Further Studies**

The following suggestions were made to further the present study, which investigated the seismic performance and design of innovative RC shear walls.

### **7.2.1 Experimental Studies**

This study was one of the first studies that incorporated self-centering reinforcement and fiber-reinforced cementitious composites in shear walls. It is suggested that more experimental studies are performed on the innovative shear wall to enrich the database of shear walls incorporating high-performance materials. This is because the number of such studies is very limited, and more data is required for the concept of damage-resistant shear walls to be practically used.

This study investigated the cyclic response of three innovative damage-resistant shear walls. Due to the limitations of the study, the specimens were designed and tested as one-story long shear walls carrying no axial loads. For this reason, more experimental studies on multi-story innovative shear walls bearing typical axial loads of such walls are suggested. In the next step, it is suggested that the seismic response of the innovative shear walls as a part of RC building structures be tested using a shake table or a hybrid testing system.

### **7.2.2 Numerical Study**

The present study included a parametric investigation on the seismic properties and design parameters of innovative shear walls. To further the study, it is suggested that separate parametric

studies are performed on each type of innovative shear walls to find the optimum design criteria for each type. In addition, it is suggested that a comprehensive study including different types of earthquake records is performed on the seismic response of each type of the innovative shear walls. In the next step, it will also be a huge leap if full RC structures that include innovative shear walls are studied under cyclic and seismic loads.

## REFERENCES

- Abdulridha, A. (2013). "Performance of Superelastic Shape Memory Alloy Reinforced Concrete Elements Subjected to Monotonic and Cyclic Loading." University of Ottawa.
- Abdulridha, A., and Palermo, D. (2014). "Response of a Hybrid-SMA Reinforced Concrete Shear Wall." *Tenth U.S. National Conference on Earthquake Engineering: Frontiers of Earthquake Engineering*, Anchorage, Alaska.
- Abdulridha, A., Palermo, D., Foo, S., and Vecchio, F. J. (2013). "Behavior and Modeling of Superelastic Shape Memory Alloy Reinforced Concrete Beams." *Engineering Structures*, 49, 893–904.
- ACI-ASCE Joint Committee 423. (1999). *423.5R-99: Report on Partially Prestressed Concrete*.
- Adebar, P., Ibrahim, A. M. M., and Bryson, M. (2007). "Test of high-rise core wall: effective stiffness for seismic analysis." *ACI Structural Journal*, American Concrete Institute, 104(5), 549.
- Akkaya, Y., Guner, S., and Vecchio, F. J. (2019). "Constitutive Model for Inelastic Buckling Behavior of Reinforcing Bars." *ACI Structural Journal*, 116(2), 195–204.
- Aly, N., AlHamaydeh, M., and Galal, K. (2018). "Quantification of the impact of detailing on the performance and cost of RC shear wall buildings in regions with high uncertainty in seismicity hazards." *Journal of Earthquake Engineering*, Taylor & Francis, 1–26.
- American Concrete Institute (ACI). (2002). *Building Code Requirements for Structural Concrete ACI 318*. Farmington Hills, MI.
- American Concrete Institute (ACI). (2014). *Building Code Requirements for Structural Concrete ACI 318*. Farmington Hills, MI.
- ASTM A370-14. (2014). *Standard Test Methods and Definitions for Mechanical Testing of Steel Products*. ASTM International, West Conshohocken, PA, ASTM International, West Conshohocken, PA.
- ASTM C39. (2015). *Standard Test Method for Compressive Strength of Cylindrical Concrete Specimens*. ASTM International, West Conshohocken, PA, ASTM International, West

Conshohocken, PA.

- ASTM F2516-14. (2014). *Standard Test Method for Tension Testing of Nickel-Titanium Superelastic Materials ASTM*. ASTM International, West Conshohocken, PA.
- Athanasopoulou, A., and Parra-montesinos, G. (2014). “Experimental Study on the Seismic Behavior of High- Performance Fiber-Reinforced Concrete Low-Rise Walls.” (110), 767–778.
- Baena, M., Torres, L., Turon, A., and Barris, C. (2009). “Experimental Study of Bond Behaviour Between Concrete and FRP Bars Using a Pull-Out Test.” *Composites Part B: Engineering*, Elsevier Ltd, 40(8), 784–797.
- Bohl, A., and Adebar, P. (2012). “Plastic Hinge Lengths in High-Rise Concrete Shear Walls.” *ACI Structural Journal*, 108(2), 148–157.
- Canadian Precast/Prestressed Concrete Institute (CPCI). (2007). *Design Manual*. CPCI, Ottawa, Ontario.
- Canadian Standards Association (CSA). (2012). *Design and Construction of Building Structures with Fibre-Reinforced Polymers CSA S608-12*. Mississauga, Ontario, Canada.
- Canadian Standards Association (CSA). (2014). *Design of Concrete Structures CSA A23.3-14*. Mississauga, Ontario, Canada.
- Canbolat, B. A., Parra-montesinos, G. J., and Wight, J. K. (2005). “Experimental Study on Seismic Behavior of High- Performance Fiber-Reinforced Cement Composite Coupling Beams.” *Concrete*, (102), 159–166.
- Del Carpio Ramos, M., Mosqueda, G., and Lignos, D. G. (2014). *Hybrid Simulation of the Seismic Response of a Steel Moment Frame Building Structure Through Collapse*. Buffalo, NY.
- Cederstrom, J., and Humbeeck, J. Van. (1995). “Relationship Between Shape Memory Material Properties and Applications.” *J. Phys. IV France*, 5, C2 335-C2 341.
- Cheng, C. T., and Mander, J. B. (1997). “Seismic Design of Bridge Columns Based on Control and Reparability of Damage.” *Technical Rep. No. NCEER 97-0013*.
- Choi, J., and Lee, B. Y. (2015). “Bonding Properties of Basalt Fiber and Strength Reduction

- According to Fiber Orientation.” *Materials*, 8, 6719–6727.
- Cruz Noguez, C. A., Saiidi, M. S., and Asce, F. (2012). “Shake-Table Studies of a Four-Span Bridge Model with Advanced Materials.” *Journal of Structural Engineering*, 138(2), 183–192.
- Desroches, R., Asce, M., McCormick, J., and Delemont, M. (2004). “Cyclic Properties of Superelastic Shape Memory Alloy Wires and Bars.” *Journal of Structural Engineering*, 130(1), 38–46.
- Driver, R. G., Kulak, G. L., Laurie Kennedy, D. J., and Elwi, A. E. (1998). “Cyclic Test of Four-Story Steel Plate Shear Wall.” *Journal of Structural Engineering*, 124(2), 112–120.
- Erkmen, B., and Schultz, A. E. (2009). “Self-Centering Behavior of Unbonded, Post-Tensioned Precast Concrete Shear Walls.” *Journal of Earthquake Engineering*, Taylor & Francis Group, 13(7), 1047–1064.
- Escolano-Margarit, D., Klenke, A., Pujol, S., and Benavent-Climent, A. (2012). “Failure Mechanism of Reinforced Concrete Structural Walls with and without Confinement.” *15th World Conference on Earthquake Engineering*, Lisboa.
- FEMA. (1997). *NEHRP Guidelines for the Seismic Rehabilitation of Buildings*. Washington, D.C.
- FEMA. (2000). *Prestandard and Commentary for the Seismic Rehabilitation of Buildings. FEMA 356*, Washington, D.C.
- fib. (2013). *fib Model Code for Concrete Structures 2010*. Lausanne, Switzerland.
- Fischer, G., Fukuyama, H., and Li, V. C. (2002). “Effect of Matrix Ductility on the Performance of Reinforced Ecc Column Members Under Reversed Cyclic Loading Conditions.” *Proceedings of the JC/ International Workshop on Ductile Fiber Reinforced Cementitious Composites (DFRCCJ - Application and Evaluation)*, 269–278.
- Gan, Y. (2000). “Bond Stress and Slip Modeling in Nonlinear Finite Element Analysis of Reinforced Concrete Structures.” University of Toronto.
- Gao, X. D. (1999). “Framed shear walls under cyclic loading.” University of Houston.
- Ge, J., Saiidi, M. S., and Varela, S. (2019). “Computational studies on the seismic response of

- the State Route 99 bridge in Seattle with SMA/ECC plastic hinges.” *Frontiers of Structural and Civil Engineering*, 13(1), 149–164.
- Ghazizadeh, S. (2017). “Behavior of Low-Rise Shear Walls with Hybrid GFRP-Steel Reinforcement and Steel Fiber-Reinforced Concrete.” University of Alberta.
- Ghazizadeh, S., and Cruz-Noguez, C. A. (2018). “Damage-Resistant Reinforced Concrete Low-Rise Walls with Hybrid GFRP-Steel Reinforcement and Steel Fibers.” *Journal of Composites for Construction*, 22(2).
- Ghazizadeh, S., Cruz-Noguez, C. A., and Talaei, F. (2018). “Analytical model for hybrid FRP-steel reinforced shear walls.” *Engineering Structures*, Elsevier, 156, 556–566.
- Ghosh, S., Hawkins, N. M., and Emeritus, P. (2004). “Acceptance Criteria for Special Precast Concrete Structural Walls Based on Validation Testing.” *PCI Journal*, 49(5), 78–92.
- Henager, C. H. (1977). “Steel Fibrous, Ductile Concrete Joint for Seismic-Resistant Structures.” *From the American Concrete Institute Annual Convention, Symposium on Reinforced Concrete Structures in Seismic Zones*, San Francisco, 371–386.
- Hidalgo, P. A., Ledezma, C. A., and Jordan, R. M. (2002). “Seismic Behavior of Squat Reinforced Concrete Shear Walls.” *Earthquake Spectra*, 18(2), 287–308.
- Holden, T., Restrepo, J., and Mander, J. B. (2003). “Seismic Performance of Precast Reinforced and Prestressed Concrete Walls.” *Journal of Structural Engineering*, 129(3), 286–296.
- Kerry Clines. (2016). “The engineering behind the new earthquake-proof bridge near Seattle’s SR99 tunnel project | Equipment World | Construction Equipment, News and Information | Heavy Construction Equipment.” <<http://www.equipmentworld.com/the-engineering-behind-the-new-earthquake-proof-bridge-near-seattles-sr99-tunnel-project/>>.
- Kunieda, M., and Rokugo, K. (2006). “Recent Progress on HPFRCC in Japan Required Performance and Applications.” *Journal of Advanced Concrete Technology*, 4(1), 19–33.
- Kurama, Y. (2000). “Seismic Design of Unbonded Post-Tensioned Precast Concrete Walls with Supplemental Viscous Damping.” *ACI Structural Journal*, 97(4), 648–658.
- Kurama, Y. (2002). “Hybrid Post-Tensioned Precast Concrete Walls for Use in Seismic Regions.” *PCI Journal*, 47(5), 36–59.

- Kurama, Y. C. (2005). "Seismic Design of Partially Post-Tensioned Precast Concrete Walls." *PCI Journal*, 50(4), 100–125.
- Kurama, Y., Sause, R., Pessiki, S., and Lu, L.-W. W. (1999). "Lateral Load Behavior and Seismic Design of Unbonded Post-Tensioned Precast Concrete Walls." *ACI Structural Journal*, 96(4), 622–632.
- Lee, S. C., Cho, J.-Y., and Vecchio, F. J. (2014). "Crack model for steel fiber-reinforced concrete members containing conventional reinforcement." *ACI Structural Journal*, 110(4), 639–648.
- Lee, S., Oh, J., and Cho, J. (2015). "Compressive Behavior of Fiber-Reinforced Concrete with End-Hooked Steel Fibers." *Materials*, 8(4), 1442–1458.
- Li, M., Luu, H., Wu, C., Mo, Y., and Hsu, T. (2014). "Seismic Performance of Reinforced Engineered Cementitious Composite Shear Walls." *Earthquake and Structures*, 7(5), 691–704.
- Li, V. C. (1993). "From Micromechanics To Structural Engineering -- The Design Of Cementitious Composites For Civil Engineering Applications." *JSCE Journal of Structural Mechanics and Earthquake Engineering*, 10(2), 37–48.
- Li, V. C. (1998). "Engineered Cementitious Composites for Structural Applications." *Materials in Civil Engineering*, 10(2), 6–69.
- Li, V. C. (2003). "On Engineered Cementitious Composites (ECC) A Review of the Material and Its Applications." *Journal of Advanced Concrete Technology*, 1(3), 215–230.
- De Luca, A., Matta, F., and Nanni, A. (2009). "Behavior of Full-Scale Concrete Columns Internally Reinforced with Glass FRP Bars under Pure Axial Load." *Composites & Polymers American Composites Manufacturers Association*.
- Maciel, M., Palermo, D., and Abdulridha, A. (2016). "Seismic Response of SMA Reinforced Shear Walls." *Special Topics in Structural Dynamics*, 185–192.
- Mallick, P. K. (2007). *Fiber-Reinforced Composites : Materials, Manufacturing, and Design*. CRC/Taylor & Francis.
- Martinelli, P., and Filippou, F. C. (2009). "Simulation of the Shaking Table Test of a Seven-

- Story Shear Wall Building.” *EARTHQUAKE ENGINEERING AND STRUCTURAL DYNAMICS*, 38, 587–607.
- Mohamed, N. (2013). “Strength and Drift Capacity of GFRP- Reinforced Concrete Shear Walls.” Université de Sherbrooke.
- Mohamed, N., Farghaly, A. S., Benmokrane, B., and Farghaly, A. (2013). “Strength Reduction Factor of GFRP-Reinforced Shear Walls.” *4th Asia-Pacific Conference on FRP in Structures (APFIS2013)*, Melbourne.
- Mohamed, N., Farghaly, A. S., Benmokrane, B., and Neale, K. W. (2014a). “Numerical simulation of mid-rise concrete shear walls reinforced with GFRP bars subjected to lateral displacement reversals.” *Engineering Structures*, 73, 62–71.
- Mohamed, N., Sabry Farghaly, A., Benmokrane, B., and Neale, K. W. (2014b). “Experimental Investigation of Concrete Shear Walls Reinforced with Glass Fiber–Reinforced Bars under Lateral Cyclic Loading.” *J. Compos. Constr.*, 18(3), 1–10.
- Montoya, E. (2000). “Modeling of Confined Concrete.” University of Toronto.
- Morgen, B. G., and Kurama, Y. C. (2004). “A Friction Damper for Post-Tensioned Precast Concrete Moment Frames.” *PCI Journal*, 49(4), 112–133.
- Muntasir Billah, A. H. M., and Alam, M. S. (2016). “Bond Behavior of Smooth and Sand-Coated Shape Memory Alloy (SMA) Rebar in Concrete.” *Structures*, Elsevier B.V., 5, 186–195.
- Nagae, T., Ghannoum, W. M., Kwon, J., Tahara, K., Fukuyama, K., Matsumori, T., Shiohara, H., Kabeyasawa, T., Kono, S., Nishiyama, M., Sause, R., Wallace, J. W., and Moehle, J. P. (2015). “Design Implications of Large-Scale Shaking Table Test on Four-Story Reinforced Concrete Building.” *ACI Structural Journal*, 112(2), 135–146.
- Nagai, S., Kanda, T., Maruta, M., Corporation, K., and Miyashita, T. (2002). “Shear Capacity of Ductile Wall with High Performance Fiber Reinforced Cement Composite.” *1st FIB Congress on Concrete Structures in the 21st Century*, Osaka, Japan, 767–774.
- Nemat-Nasser, S., and Guo, W. G. (2006). “Superelastic and Cyclic Response of NiTi SMA at Various Strain Rates and Temperatures.” *Mechanics of Materials*, 38(5–6), 463–474.
- Oosterle, R. G., Fiorato, A. E., Johal, L. S., Carpenter, J. E., and Russell, H. G. (1976).

- Earthquake Resistant Structural Walls-Tests of Isolated Walls*. Washington, D. C.
- Palermo, D., and Vecchio, F. (2007). "Simulation of Cyclically Loaded Concrete Structures Based on the Finite-Element Method." *Journal of Structural Engineering*, 133(5), 728–738.
- Park, R. (1988). "Ductility Evaluation from Laboratory and Analytical Testing." *Ninth World Conference on Earthquake Engineering*, Tokyo-Kyoto, 605–616.
- Park, R., and Paulay, T. (1975). *Reinforced Concrete Structures*. John Wiley & Sons, Inc., Hoboken, NJ, USA.
- Park, R., Priestley, M. J. N., and Gill, D. W. (1982). "Ductility of Square Confined Concrete Column." *Journal of Structural Division*, 108(4), 929–950.
- Parra-montesinos, G. J. (2005). "High-Performance Fiber-Reinforced Cement Composites: An Alternative for Seismic Design of Structures." *ACI Structural Journal*, 102(5).
- Parra-Montesinos, G. J., and Kim, K. Y. (2004). "Seismic Behavior of Low-Rise Walls Constructed With Strain-Hardening Fiber Reinforced Cement Composites." *13th World Conference on Earthquake Engineering*, Vancouver, B.C., Canada.
- Popovics, S. (1973). "A Numerical Approach to the Complete Stress-Strain Curve of Concrete." *Cement and Concrete Research*, 3(4), 583–599.
- Prakash, V., Powell, G., and Campbell, S. (1993). *DRAIN-2DX Base Program Description and User Guide; Version 1.10 Report No. UCB/SEMM-93/17*. Berkeley, Calif.
- Priestley, M., Calvi, G., and Kowalsky, M. (2007). *Displacement Based Seismic Design of Structures*. IUSS Press, Pavia, Italy.
- Ramirez, C. M., and Miranda, E. (2012). "Significance of residual drifts in building earthquake loss estimation." *Earthquake Engineering & Structural Dynamics*, John Wiley & Sons, Ltd, 41(11), 1477–1493.
- Saenz, L. P. (1973). "Equation for the Stress-Strain Relation for Concrete." *Cement and Concrete Research*, 3(5), 583–599.
- Saiidi, M. S., Asce, F., Sadrossadat-Zadeh, M., Ayoub, C., and Itani, A. (2007). "Pilot Study of Behavior of Concrete Beams Reinforced with Shape Memory Alloys."
- Saiidi, M. S., O'Brien, M., and Sadrossadat Zadeh, M. (2009). "Cyclic Response of Concrete

- Bridge Columns Using Superelastic Nitinol and Bendable Concrete.” *ACI Structural Journal*, 106(1), 69–77.
- Saiidi, M., and Wang, H. (2006). “An Exploratory Study of Seismic Response of Concrete Columns with Shape Memory Alloys Reinforcement.” *ACI Structural Journal*, 103(3), 436–443.
- Sakai, J., and Mahin, S. (2004). “Mitigation of Residual Displacements of Circular Reinforced Concrete Bridge Columns.” *13th World Conference on Earthquake Engineering*, Vancouver, Canada, 1–13.
- Schultz, A. E., Cheok, G. S., and Magana, R. A. (1998). “Performance of Precast Concrete Shear Walls.” *Sixth U.S. National Conference on Earthquake Engineering*, Oakland, CA.
- Seismosoft. (2010). *SeismoStruct 2010 – A computer program for static and dynamic nonlinear analysis of framed structures*. available from <http://www.seismosoft.com>.
- Shahria Alam, M., Moni, M., and Tesfamariam, S. (2012). “Seismic Overstrength and Ductility of Concrete Buildings Reinforced with Superelastic Shape Memory Alloy Rebar.” *Engineering Structures*, 34, 8–20.
- Shahria Alam, M., Nehdi, M., and Youssef, M. A. (2009). “Seismic performance of concrete frame structures reinforced with superelastic shape memory alloys.” *Smart Structures and Systems*, 5(5), 565–585.
- Su, R. K. L., and Wong, S. M. (2007). “Seismic Behaviour of Slender Reinforced Concrete Shear Walls under High Axial Load Ratio.” *Engineering Structures*, 29, 1957–1965.
- Tazarv, M., and Saiidi, M. S. (2015). “Reinforcing NiTi Superelastic SMA for Concrete Structures.” *American Society of Civil Engineers*, 141(8), 1–10.
- Tehrani, A. M., Shahrokhshahi, H., Parvin, N., and Brgoch, J. (2015). “Influencing the Martensitic Phase Transformation in NiTi through Point Defects.”
- Thomas, J., and Ramaswamy, A. (2007). “Mechanical Properties of Steel Fiber-Reinforced Concrete.” *J. Mater. Civ. Eng.*, 9(5), 385–392.
- Tolou Kian, M. J., and Cruz-Noguez, C. (2018). “Reinforced Concrete Shear Walls Detailed with Innovative Materials: Seismic Performance.” *Journal of Composites for Construction*,

22(6), 04018052.

- Tolou Kian, M. J., Ghazizadeh, S., and Cruz Noguez, C. (2018). “An Experimental Investigation of FRCC Shear Walls Reinforced with Steel and GFRP Bars.” *Journal of Composites Science*, 2(3), 55.
- Vecchio, F. J. (1989). “Nonlinear finite element analysis of reinforced concrete membranes.” *ACI Structural Journal*, 86(1), 26–35.
- Vecchio, F. J. (2001). “Distributed Stress Field Model for Reinforced Concrete: Implementation.” *Journal of Structural Engineering*, 127(1), 12–20.
- Vecchio, F. J., and Collins, M. P. (1986). “The Modified Compression-Field Theory for Reinforced Concrete Elements Subjected to Shear.” *ACI Journal*, 8(22), 219–231.
- Walraven, J. C. (1981). “Fundamental Analysis of Aggregate Interlock.” *Journal of the Structural Division*, ASCE, 107(11), 2245–2270.
- Wei, Z. G., Sandstrom, R., and Miyazaki, S. (1998). “Shape-memory materials and hybrid composites for smart systems - Part I Shape-memory materials.” *Journal of Materials Science*, 33(15), 3743–3762.
- Whyte, C. A., and Stojadinovic, B. (2012). “Hybrid Simulation of the Seismic Response of Squat Reinforced Concrete Shear Walls.” *15th World Conference on Earthquake Engineering*, Lisboa.
- Wong, P. S., and Vecchio, F. J. (2002). *VecTor2 and FormWorks user’s manual (Publication No. 2002-02)*. : University of Toronto, Toronto, ON.
- Yamamoto, T. (1999). “Nonlinear Finite Element Analysis of Transverse Shear and Torsional Problems in Reinforced Concrete Shells.” University of Toronto.
- Yu-Fei Wu, Tao Liu, D. J. O. (2006). “Fundamental Principles that Govern Retrofitting of Reinforced Concrete Columns by Steel and FRP Jacketing.” *Advances in Structural Engineering*, 9(4), 507–533.
- Zhang, Y., and Wang, Z. (2000). “Seismic Behavior of Reinforced Concrete Shear Walls Subjected to High Axial Loading.” *ACI Structural Journal*, 97(97), 739–750.